Development of Evaluation Procedures for Evaporative Transport Based Deterioration

Andrew John Karol Komar, Department of Civil Engineering and Applied Mechanics

June 2017

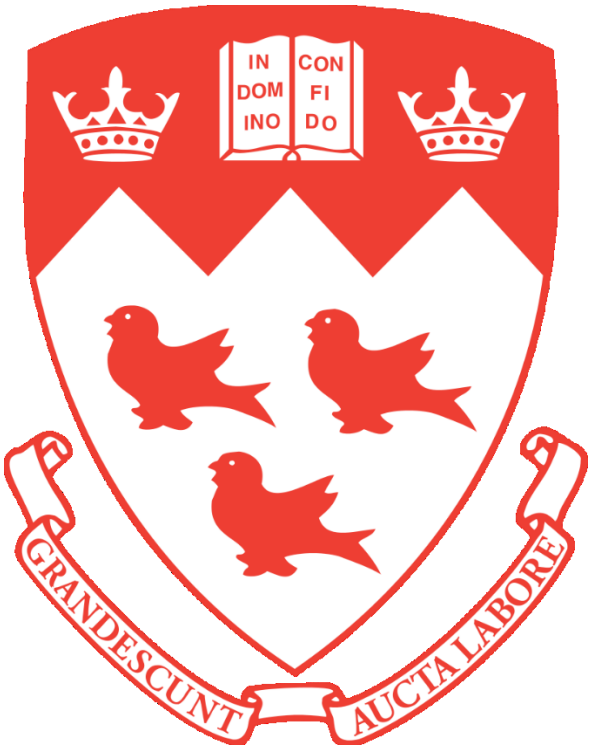

A thesis submitted to McGill university in partial fulfillment of the requirements of the degree of

Doctorate of Civil Engineering

Table of Contents

Development of Evaluation Procedures for Evaporative Transport Based Deterioration 1
Table of Contents 2
List of Figures 9
List of Tables 13
List of Equations 14
List of Symbols 16
Abstract 22
Acknowledgements 27
Preface and Contribution of Authors 29
Publications 32
Expected List of Contributions 33
Chapter 1: Introduction 36
1.1. Background 36
1.1.1. Pressure tension 37
1.1.2. Nondestructive testing 39
1.1.3. Magnetic resonance imaging 41
1.2. Research objectives 44
Chapter 2: Literature Review 46
2.1. Mass transport in porous media 46
2.1.1. Sorptivity 48
2.1.2. Wicking action 49
2.2. Magnetic resonance imaging of cement materials 50
2.2.1. Basic principles 50
2.2.2. Spatial imaging with NMR techniques 56
2.2.3. Applications to concrete durability and water mass transport 60
2.3. Tension testing 66
2.3.1. Direct tension tests 66
2.3.2. Flexural tests 67
2.3.3. Splitting tension test 68
2.3.4. Other indirect tension tests 71
2.3.5. Pressure tension test 74
2.3.5.1. Pressure tension effect 74
2.3.5.2. Boundary conditions 79
2.3.5.3. Failure mechanism 80
2.3.5.4. Moisture content 81
2.3.5.5. Durability studies 83
2.4. References 85
Foreword to Chapter 3 94
Chapter 3: Single Point Ramped Imaging with T1 Enhancement (SPRITE) Imaging of 1 Dimensional Sorptive Flow in White Portland Cement Pastes 96

3.1. Abstract....96
3.2. Introduction....97
3.2.1. Moisture transport....97
3.2.2. Sorptivity....97
3.2.3. SPRITE imaging technique....99
3.2.3.1. Relaxation times....100
3.3. Materials and Methods....101
3.3.1. Paste preparation....101
3.3.2. MRI parameters....102
3.3.2.1. Magnetic sensitivity reference....102
3.3.2.2. Fiduciary markers....103
3.3.3. Sorptivity....103
3.3.4. Steady state....103
3.4. Results and Discussion....104
3.4.1. Sorptivity Imaging of 45 mm samples....104
3.4.1.1. Steady state imaging of 45 mm samples....106
3.4.1.2. Imaging of 100 mm length samples....108
3.5. Conclusions....112
3.6. References....112
Foreword to Chapter 4....116
Chapter 4: Comparison of Temperature Correction Methods for Surface Resistivity Measurements for Portland Cement Concretes....118
4.1. Background....118
4.1.1. Surface resistivity....118
4.1.2. Electrical conductivity....120
4.1.3. Temperature effect....120
4.2. Materials and Methods....123
4.2.1. Mixture design....123
4.2.2. Surface resistivity - temperature testing....125
4.2.3. Data analysis....127
4.2.3.1. Method 1....127
4.2.3.2. Method 2....128
4.2.3.3. Method 3....128
4.2.4. Temperature correction....129
4.2.4.1. Correction factor method....129
4.2.4.2. Arrhenius method....130
4.3. Results and Discussion....131
4.3.1. Method 1....131
4.3.2. Method 2....132
4.3.3. Method 3....133
4.3.4. Comparison between the 3 methods....134
4.3.5. Activation energy vs time....137
4.3.6. Surface resistivity temperature time....139
4.3.7. Surface resistivity temperature correction....145

4.4. Conclusions 149
4.5. Acknowledgements 151
4.6. References 151
Forward to Chapter 5 155
Chapter 5: Pressure Tension and the Effect of Variable Moisture Content 157
5.1. Abstract 157
5.2. Background 158
5.2.1. Pressure tension 158
5.2.2. Effect of moisture content on pressure tension 159
5.2.3. Moisture content calculations 163
5.3. Materials and Methods 165
5.3.1. Mixture design 165
5.3.2. Conditioning 167
5.3.2.1. Saturated 167
5.3.2.2. Vacuum saturation 167
5.3.2.3. Air drying 169
5.3.2.4. Oven drying 169
5.3.3. Destructive testing 170
5.3.3.1. Pressure tension testing 170
5.3.3.2. Compression testing 171
5.3.4. Nondestructive test monitoring 171
5.3.4.1. Surface resistivity 171
5.3.4.2. Ultrasonic pulse velocity 172
5.4. Results and Discussion 173
5.4.1. Nondestructive monitoring 173
5.4.1.1. Surface resistivity 173
5.4.1.2. Ultrasonic pulse velocity 175
5.4.2. Destructive testing 176
5.4.2.1. Compressive strength 176
5.4.2.2. Absorption and void space 177
5.4.2.3. Variable moisture content and pressure tension 178
5.4.2.4. Exposure conditions and pressure tension 179
5.4.3. Visual observations 182
5.5. Conclusions 184
5.6. Acknowledgements 186
5.7. References 186
Foreword to Chapter 6 189
Chapter 6: Pressure Tension Test: Reliability for Assessing Concrete Deterioration 191
6.1. Abstract 191
6.2. Introduction 192
6.3. Materials and Methods 194
6.3.1. Control system calibration 194
6.3.2. Sample preparation 194
6.3.3. Experimental setup 196

6.4. Results and Discussion....198
6.4.1. Pressure tension test reliability....198
6.4.2. Destructive testing....199
6.5. Conclusions....202
6.6. References....202
Foreword to Chapter 7....204
Chapter 7: Pressure-Tension Testing in the Evaluation of Freeze-Thaw Deterioration....205
7.1. Abstract....205
7.2. Background....206
7.3. Materials and Methods....208
7.3.1. Concrete mix design....208
7.3.2. Exposure conditions....209
7.3.3. Test methods....209
7.3.3.1. Nondestructive test methods....209
7.3.3.2. Destructive test methods....210
7.4. Results and Discussion....211
7.4.1. Nondestructive testing....211
7.4.1.1. Surface resistivity....211
7.4.1.2. Ultrasonic pulse velocity....213
7.4.2. Destructive test results....214
7.4.2.1. Compressive strength....214
7.4.2.2. Pressure tension strength....215
7.5. Conclusions....217
7.6. References....218
Foreword to Chapter 8....220
Chapter 8: The Influence of Freeze-Thaw Damage in Pressure Tension Testing....222
8.1. Abstract....222
8.2. Background....222
8.2.1. Nondestructive testing....224
8.2.1.1. Ultrasonic pulse velocity....224
8.2.1.2. Surface resistivity....225
8.2.1.3. Expansion prisms....225
8.2.2. Destructive testing....225
8.2.2.1. Compressive strength....225
8.2.2.2. Pressure tension....226
8.3. Materials and Methods....228
8.3.1. Mix design....228
8.3.2. Exposure conditions....229
8.3.3. Destructive testing....232
8.3.3.1. Compressive strength....232
8.3.3.2. Pressure tension....232
8.3.4. Nondestructive testing....233
8.3.4.1. Surface resistivity....233
8.3.4.2. SR-temperature curves....234

8.3.4.3. Ultrasonic pulse velocity 235
8.3.4.4. Expansion prisms 236
8.4. Results and Discussion 236
8.4.1. Visual observations 236
8.4.2. Destructive testing 238
8.4.2.1. Compressive strength 238
8.4.2.2. Pressure tension 239
8.4.3. Nondestructive testing 242
8.4.3.1. Surface resistivity 242
8.4.3.2. SR-temperature correction 243
8.4.3.3. Ultrasonic pulse velocity 247
8.4.3.4. Expansion prisms 249
8.5. Conclusions 250
8.6. Acknowledgements 251
8.7. References 252
Foreword to Chapter 9 254
Chapter 9: Tensile Strength of Plain Concrete under Sustained Load by Pressure Tension 255
9.1. Abstract 255
9.2. Background 255
9.2.1. Creep testing 255
9.2.2. Tension testing 261
9.3. Materials and Methods 266
9.3.1. Mix design 266
9.3.2. Exposure conditions 267
9.3.3. Destructive testing methodology 268
9.4. Results and Discussion 269
9.4.1. Destructive testing for set point 269
9.4.2. Decrease of long-term pressure tension strength 270
9.4.3. Prediction of original strength 273
9.4.4. Comparison with previous studies 275
9.4.5. Analysis of failure patterns 276
9.5. Conclusions 280
9.6. Acknowledgements 282
9.7. References 282
Chapter 10: Conclusions & Recommendations 286
10.1. Magnetic resonance imaging 286
10.1.1. Contributions 286
10.1.1.1. Sorptivity 287
10.1.1.2. Steady-state evaporative flow 287
10.1.2. Suggested future studies 288
10.2. Surface resistivity 290
10.2.1. Contributions 290
10.2.2. Suggested future studies 292
10.3. Pressure tension 293

10.3.1. Contributions 293
10.3.1.1. Creep 295
10.3.1.2. Freeze-thaw 296
10.3.1.3. Sulphate attack 297
10.3.1.4. Moisture content 297
10.3.2. Suggested future studies 298
10.4. Conclusion 301
Master Reference List 302
Appendix A: Pressure Tension Specification Manual 319
1.1. Operating principle 319
1.2. Compressed air system 320
1.2.1. Air compressor 320
1.2.2. Compressed air reservoir 320
1.3. Loading system 321
1.3.1. Blowout valve 321
1.3.2. ¼ turn safety valve 321
1.3.3. Regulator valve 322
1.3.4. Downstream cut-off valves 323
1.3.5. Flow regulating valve 324
1.3.6. Automated needle valve and actuator 325
1.3.7. Pressure sensors 326
1.3.8. Pressure safety switch 327
1.3.9. DAQ 328
1.4. Testing chamber 328
1.4.1. Connections 328
1.4.2. Confining rings 329
1.4.3. O-rings 330
1.4.4. Testing chamber frame 331
1.4.5. Safety interlock system 331
1.5. Unloading system 332
1.6. Safety systems 334
1.6.1. Redundant safety circuit 334
1.6.1.1. Emergency stop button 334
1.6.1.2. Arming button 335
1.6.1.3. Emergency safety valves 335
1.6.1.4. Frame lid locking mechanism 336
1.6.2. Computer controlled safety system 336
1.6.2.1. Automated load detection shutoff 336
1.6.2.2. Manual override switch 337
1.6.3. Manually operated ¼ turn valves 337
1.6.3.1. Upstream discharge valve 337
1.6.3.2. Upstream cut-off valve 338
1.6.3.3. Downstream discharge valve 338
1.6.4. Maximum pressure blowout valve 338

1.7. Software.....339
1.7.1. Operation input parameters 339
1.7.2. Control loop..... 340
1.7.3. Error detection 341
1.7.4. Output 341
1.8. Operation.....341

List of Figures

Figure 2.1- “The static magnetic field B_0 splits the energy of the spin parallel and spin anti parallel energy states."- From Balcom et al. [11] 52
Figure 2.2-"Water consumed(a), and total surface area, S_0(b), as a function of hydration time expressed in terms of the weight of the initial dry cement powder" From Halpern et al. [12]... 55
Figure 2.3- "Schematic description of the Single-Point Imaging (SPI) method.”- From Balcom et al. [11] 58
Figure 2.4- “Schematic description of the Single-Point Ramped Imaging with T_1 Enhancement (SPRITE) imaging method.” From Balcom et al. [11] 59
Figure 2.5- “Drying profiles of cement samples with (a) w/c =0.6 and (b) w/c =0.4 following a moist cure period of 90 days” From Beyea et al. [16] 61
Figure 2.6- “Plot of average $1/T_1$ (ms^{-1}) versus relative humidity (%) for the average of three mortar disks with a w/c ratio of (a) 0.6 and (b) 0.4, and an initial hydration period of 90 days.”- From Beyea et al. [17] 62
Figure 2.7- “Capillary water uptake profiles into 96-day-old 0.5 w/c ratio samples.” – From Bohris et al. [18] 63
Figure 2.8- “2D Spiral SPRITE images of a mortar cylinder insulated on the sides and bottom, with the top face exposed to cold nitrogen vapor, -20°C.” From Balcom et al. [11] 66
Figure 2.9- “Schematic representation of test set-up for (a) center point loading and (b) third point loading” – From Carrasquillo and Carrasquillo [29]. 68
Figure 2.10- "Brazilian concrete splitting tension test" From Lin and Wood [33] 69
Figure 2.11- “Horizontal stress, σ_x, distributions along vertical diameter of cylinder during loading up to failure”, from Lin and Wood [33] 70
Figure 2.12- "(a) The specimen for the biaxial flexure (BFT) method and (b) the uniform principal stress on the bottom surface" From Zi et al. [36] 72
Figure 2.15- Pressure tension effect. From Clayton and Grimer [38] 76
Figure 2.16- "Demonstration experiment details". From Clayton and Grimer [39] 77
Figure 2.17- "Summary of fluid-pressure test results" From Clayton [40] 78
Figure 2.18- "Surface and internal strain gauges" -From Uno et al. [43] 80
Figure 2.19- "Fracture plane in Mix-A a) solid specimen, b) hollow specimen"- From Fujikake et al. [44] 81
Figure 3.1- ^1H Signal intensity from sorptive flow in a 0.35 White Portland Cement Paste 104
Figure 3.2- ^1H Signal intensity from sorptive flow in a 0.60 White Portland Cement Paste 105
Figure 3.3- Steady state moisture content profiles of saturated cement paste. Each W/C profile is comprised of at least three images 106
Figure 3.4- Effect of relative humidity on steady state condition for 0.35 and 0.60 W/C 107
Figure 3.5- Moisture profile for dry 0.6 W/C paste using encoding time t_p of 90 µs 108
Figure 3.6- Moisture profile for dry 0.60 W/C paste using encoding time t_p of 400 µs 109
Figure 3.7- Sorptivity and steady state, 100 mm sample, 0.60 w/c, 90µs encoding time 110
Figure 3 8- Sorptivity and Steady State, 100 mm sample, 0.6 w/c, 400µs 111
Figure 4.1- Activation Energy of Conduction. From Spragg et al. [13,14] 122

Figure 4.2- Surface resistivity markings on the side of a typical cylinder 125
Figure 4.3- 0.35 w/c 7-day hydration surface resistivity vs temperature, ... 132
Figure 4.4- 0.35 W/C 7-day hydration surface resistivity vs temperature, Method 2 133
Figure 4.5- 0.35 W/C 7-day hydration ln(SR) 1/K diagram, method 3 134
Figure 4.6- Activation energy of conduction for ordinary concrete mixtures 138
Figure 4.7- Activation energy of conduction for 10% silica fume mixtures 139
Figure 4.8- SR-T-Hydration relationship for 0.30 OPC concrete 140
Figure 4.9- SR-T-Hydration relationship for 0.35 OPC concrete 140
Figure 4.10- SR-T-Hydration relationship for 0.40 OPC concrete 141
Figure 4.11- SR-T-Hydration relationship for 0.45 OPC concrete 141
Figure 4.12- SR-T-Hydration relationship for 0.30 10% SF replacement concrete 142
Figure 4.13- SR-T-Hydration relationship for 0.35 10% SF replacement concrete 143
Figure 4.14- SR-T-Hydration relationship for 0.40 10% SF replacement concrete 143
Figure 4.15- SR-T-Hydration relationship for 0.45 10% SF replacement concrete 144
Figure 4.16- Normalized surface resistivity readings of ordinary portland cement concretes at 20 °C over time 148
Figure 4.17- Normalized surface resistivity readings of 10% silica fume cementitious replacement concretes 20 °C over time 148
Figure 5.1- Pressure tension effect 158
Figure 5.2- Configuration of vacuum saturation apparatus 168
Figure 5.3- Relationship between curing time and measured surface resistivity on six mixes.. 174
Figure 5.4- The effect of curing time on stress wave propagation 176
Figure 5.5- Relationship between moisture content and pressure tension failure level for six mixtures 179
Figure 5.6- The effect of different exposure conditions on the pressure tension failure level for six mixtures 180
Figure 5.7- Normalized pressure tension failure stresses after different durations of air dry .. 181
Figure 5.8 - Typical tensile crack for high moisture content specimens 182
Figure 5.9- Volumetric paste failure of typical low moisture content specimens 183
Figure 5.10- Distinctive partially saturated crack surface face 183
Figure 6.1- Cross section of pressure chamber 192
Figure 6.2- Partial immersion of concrete blocks [8] 196
Figure 6.3- Location of cores taken from concrete blocks [8] 196
Figure 6.4- Coefficient of determination versus load rate 198
Figure 7.1- (Left) Exploded view of the PT apparatus with concrete cylinder in machine. (Right) Cross section of PT apparatus and concrete cylinder. 207
Figure 7.2- Average surface resistivity measurements as a function of freeze thaw cycles 212
Figure 7.3- Surface resistivity measurements from 0.45 w/c control sample #3 from four separate locations on the surface 213
Figure 7.4- Average ultrasonic pulse velocity measurement as function of freeze-thaw cycle for two mixtures 214
Figure 7.5- ASTM C 39 average compressive strength results from 0 and 20 freeze-thaw cycles for the two mixtures 215
Figure 7.6- PT average failure levels as function of freeze thaw cycle for both mixes 216

Figure 7.7- Tensile failure comparison between splitting tension (ST) and pressure tension (PT) for two mixes after 20 cycles of freeze-thaw damage 217
Figure 8.1- Pressure tension apparatus 227
Figure 8.2- Pressure tension effect [5,6,7] 227
Figure 8.3- 0.45 W/C specimens as cast 229
Figure 8.4-Samples and containers inside refrigerator 230
Figure 8.5- Heating element on circulating water bath 231
Figure 8.6- Undamaged failure plane from pressure tension test 237
Figure 8.7- Damaged failure plane from pressure tension test 237
Figure 8.8- Compressive strength deterioration as function of freeze thaw cycle 239
Figure 8.9- Pressure tension strength deterioration versus freeze thaw cycle for two mixtures 240
Figure 8.10- Average tensile to compressive ratio as a function of F/T cycling 241
Figure 8.11- Surface resistivity versus freeze thaw cycle for two mixtures and 3 samples per mixture. 242
Figure 8.12- Surface resistivity versus temperature from different freeze-thaw cycles 243
Figure 8.13- Surface resistivity as function of temperature and cycles, 0.45 w/c 244
Figure 8.14- Surface resistivity as function of temperature and cycles, 0.65 w/c 244
Figure 8.15- Corrected surface resistivity versus freeze thaw cycle for two mixtures for three samples per mixture 246
Figure 8.16- Comparison between calibrated and uncalibrated surface resistivity measurements as a function of freeze-thaw cycles 247
Figure 8.17- Average ultrasonic pulse velocity measurements as a function of freeze thaw cycles for two mixtures 248
Figure 8.18- Ultrasonic pulse velocity versus freeze thaw cycles from three samples per mix. 248
Figure 8.19- Linear expansive behavior during F/T cycles 249
Figure 9.1-Tension testing specimen configuration and results from Al-Kubaisy et al. [17] 259
Figure 9.2- Relationship between relative sustained stress level and time to failure for concentric tensile tests (a) and eccentricity of .167 (b). From Shkoukani et al. [18] 260
Figure 9.3- Sustained load levels versus failure in lifetime creep testing. Arrow indicates that failure did not occur during testing. From Carpinteri et al. [19] 261
Figure 9.4- Pressure tension effect 263
Figure 9.5- Schematic view of a fluid-pressurized tensile test system for concrete. From Cantillo and Andrés [17] 264
Figure 9.6- Photograph of pressure tension testing machine 265
Figure 9.7- Frozen and oven-dried sample conditions 268
Figure 9.8- Creep test results for group 1 (saturated specimens of W/C 0.45) 271
Figure 9.9- Creep test results for group 2 (saturated specimens of W/C 0.65) 271
Figure 9.10- Creep test results for group 3 (oven dried specimens of W/C 0.65) 272
Figure 9.11- Comparison of the three exposure conditions, normalized with respect to instantaneous failure level 272
Figure 9.12- Explanation of predicting original strength 274
Figure 9.13- Comparison of groups 1 through 3 with previous studies [17, 18, 19] 275
Figure 9.14- Typical failure pattern of saturated samples 276

Figure 9.15- Failure adjacent to sealing O-ring 277
Figure 9.16- Typical failure pattern of dry samples 278
Figure 9.17- Air bubbles observed on outer surface of sample 280
Figure 1- Schematic overview 319
Figure 2- Detail on the T-Junction including the tank regulator, quick connects, adaptor tubing and 17 MPa emergency blowout valve 321
Figure 3- Manual ¼ valve and regulating valve to control the maximum pressure levels in the pressure tension machine 322
Figure 4-Regulator valve. The gauge on the right corresponds to the indicator that represents the current pressure of the compressed air within the tank. The gauge on the right indicates the set point of the pressure tension machine and can be changed by rotating the dial on the regulator valve 322
Figure 5- (left) solenoid cut-off valve and needle-tip valve. The automated actuator is the red box at the bottom, which operates a needle-tip valve that controls the flow rate into the PT machine 325
Figure 6- 12 V DC power supplies. Each actuator runs on an independent supply, and the third unit supplies power for sensors 326
Figure 7- A) Pressure tension chamber loaded with simulated concrete cylinder B) chamber without sample. The two confinement rings, O-rings and the nuts and bolts to provide the sealing found in figure 7B. 329
Figure 8- Cross section of pressure tension chamber with sample inside 329
Figure 9- A) Safety interlock switch system,open button B) detail of safety lock key from lid.. 332
Figure 10- Unloading system. Clockwise from upper left is the computer controlled actuator (red box), the quick disconnect, a ¼ turn valve for manual venting, and the solenoid valve (lower left) which opens the pressure line when the system is not armed 333
Figure 11- Emergency stop system. 335

List of Tables

Table 3.1- Paste mixtures 101
Table 4.1- Mixture design 124
Table 4.2- Regular concrete SR-T curves and activation energy 134
Table 4.3- 10% silica fume replacement concrete SR-T curves and activation energy 135
Table 4.4- Comparison between correction factor method and Arrhenius method for temperature correction 145
Table 5.1- Mixture design 166
Table 5.2-Fresh concrete properties 166
Table 5.3- Compressive strength results 177
Table 5.4- Permeable void space for mixtures 178
Table 5.5- Normalized pressure tension stress failure values for different exposures 181
Table 6.1- Concrete mixture designs 194
Table 6.2- Tensile strength of concrete exposed to ambient conditions for two years 199
Table 6.3- Tensile strength of cores taken from exposure blocks 200
Table 7.1- Mixture designs for freeze-thaw study 208
Table 8.1- Mixture designs 228
Table 8.2- Fresh concrete properties 229
Table 9.1- Mixture design of concrete samples 266
Table 9.2- Classification of the long-term testing samples 269
Table 9.3- 'Instantaneous' strength testing results for 4 MPa per minute strain rate 269
Table 9.4- Comparison between predicted strength and instantaneous failure levels 274

List of Equations

Equation 2.1- Gravimetric mass ratio, from Hall [1] 46
Equation 2.2- Reduced water content, from Hall [1], Lockington [2] 47
Equation 2.3- Darcy's law, from Hall, and Gummerson et al. [1,3] 47
Equation 2.4- Unsaturated flow through porous media, from Lockington et al. [2] 48
Equation 2.5- Exponential and power law definitions of hydraulic diffusivity, from Lockington et al. [2] 48
Equation 2.6- Differential equation definition for water penetration front [2] 49
Equation 2.7- Mass uptake solution for sorptive flow conditions, from Gummerson et al. [3] .. 49
Equation 2.8- Lockington model for steady state flow under evaporative conditions [10] 50
Equation 2.9- Exponential recovery of magnetic moment in Z direction from Balcom et al.[11] 53
Equation 2.10- Transverse magnetic decay, from Balcom et al. [11] 53
Equation 2.11- Definition of the 'k-space' variable. From Balcom et al. [11] 56
Equation 2.12- NMR signal definition using k. From Balcom et al. [11] 56
Equation 2.13- Nuclei spatial function from FFT in k space. From Balcom et al. [11] 57
Equation 2.14- Sample magnitude in the SPI method. From Balcom et al. [11] 58
Equation 2.15- Local signal intensity for SPI method, simplified with sufficiently long TR time. From Balcom et al. [11] 58
Equation 2.16- Splitting tension stress magnitude [32] 70
Equation 2.17- Peak tension stress on bottom face in the disc, from Zi et al. [36] 72
Equation 2.18- Tangential stress in fluid pressure test, from Cantillo and Guzman [37] 73
Equation 3.1- Formulation of 1 dimensional flow of water through a porous medium 97
Equation 3.2- Integral form of sorptive flow 98
Equation 3.3- Sorptive flow 98
Equation 3.4- Geometric formulation of sorptive flow 98
Equation 3.5- Definition of variable change for SPRITE method of signal analysis, from Balcom et al. [12] 99
Equation 3.6- Magnetic resonance signal definition 100
Equation 3.7- Fast Fourier transform 100
Equation 3.8- Decay signal perpendicular to applied magnetic field 100
Equation 3.9- SPRITE signal intensity definition 101
Equation 4.1- Modified Hinrichson-Rasch Law, from Whittington et al. [3] 121
Equation 4.2- Arrhenius equation for surface resistivity temperature correction, from Spragg et al. [13] 121
Equation 4.3- Best fit curve form 127
Equation 4.4- Best fit curve for Arrhenius function 129
Equation 4.5- Correction factor form 129
Equation 4.6- Correction factor alternative form 129
Equation 4.7- Corrected surface resistivity measurement 130
Equation 5.1- Work function of adiabatic gas pressurization 161
Equation 5.2- Work function of adiabatic water pressurization 161

Equation 5.3- Calculated volume of specimen from bulk density 163
Equation 5.4- Mass of water in whole sample lost because of duration in exposure condition 164
Equation 5.5- Mass of fragments lost during testing 164
Equation 5.6- Mass of water lost after testing until oven dry condition 164
Equation 5.7- Estimated mass of water in fragments lost during testing 164
Equation 5.8- Total mass of water in sample calculation 164
Equation 5.9- Estimated moisture content at time of testing 164
Equation 5.10- Moisture content due to vacuum saturation 165
Equation 5.11- Estimated suspended mass of sample 165
Equation 5.12- Pulse velocity calculation for UPV 173
Equation 8.1: Ultrasonic pulse velocity..... 235
Equation 8.2- Surface resistivity correction factor 245
Equation 8.3- Correction factor calculation..... 245
Equation 9.1- Empirical best-fit relationship for variable sustained loading. From Carpinteri et al. [19] 261
Equation 9.2- Logarithmic best fit curve form 270

List of Symbols

a	curve fitting parameter for surface resistivity correction method
a	radius of sample disk in biaxial flexure method
AEA	air entraining admixture
α	curve fitting parameter for creep test
ASR	alkali silicate reaction
ASTM	American Society for Testing and Materials
B	curve fitting parameter for creep test
b	curve fitting parameter for surface resistivity correction method
b	radius of bearing disk in biaxial flexure method
BFT	biaxial flexure method
B_0	externally applied magnetic field strength
BRC	building research council
C	constant reference temperature value in temperature correction method
Ca	calcium
°C	degrees Celsius
d	depth of slab
1D	one dimension
2D	two dimensional
3D	three dimensional
ΔSR	surface resistivity temperature correction value
D_0	experimentally derived fitting parameter for hydraulic diffusivity
$D(\Theta)$	moisture content dependant hydraulic diffusivity
e	base of the natural logarithm
$E_{A\text{-}cond}$	activation energy of conduction
$E(P)$	work function

exp	base of the natural logarithm
η	Boltzmann transform variable
FFT	fast Fourier transform
F/T	freeze-thaw
$f(T)$	best fit curve as a function of temperature
g	grams
γ	gyromagnetic ratio
γ	compressibility of gas
G_z	magnetic field gradient
h	height of liquid from reservoir in sorptive flow
h	height of sample disk in biaxial flexure test
^1H	hydrogen nuclei
I	current in amps
i	length the water has been transported in sorptivity equation
ITZ	interfacial transition zone
K	degrees Kelvin
k	capillary coefficient in sorptive flow
k	empirically derived constant describing rate of evaporation
kg	kilograms
kJ	kilojoules
$K(\Theta)$	moisture content dependant hydraulic conductivity
k_z	variable used in NMR imaging, 'k-space'
l	length
Log	logarithm
Ln	natural logarithm
m	meters
m	mass of water

m_a	mass of dry solid absent any water
$M_{fragment}$	mass of fragments lost during testing
MHz	megahertz
mm	millimetres
Mol	moles
M_0	magnet moment at equilibrium
MRI	magnetic resonance imaging
MPa	megapascals
$M_{partial\,saturation}$	mass of sample after testing
$M_{suspended}$	estimated suspended mass in water
$M_{Saturated}$	mass of saturated sample
M_{test}	mass of sample at time of testing
$M_{water,\,fragments}$	mass of water in fragments lost during testing
$M_{water,\,partial\,saturation}$	mass of water lost after testing to oven dry
$M_{water,\,test}$	mass of water in sample at the time of testing
M_{water}	mass of water in sample calculation
M_{xy}	transverse magnetic moment in xy plane spinning at Lamor frequency
M_z	magnetic moment aligned in z direction
n	experimentally derived fitting parameter for hydraulic diffusivity
NDT	nondestructive testing
NMR	nuclear magnetic resonance
v	gravimetric mass ratio
ν	Poisson's ratio
OH	hydroxide
Ω	ohms
OPC	ordinary portland cement
P	point force

Pa	Pascal
P_A	atmospheric pressure
P_B	pressure at testing
Φ	hydraulic potential
π	mathematical constant pi
P_i	pressure of fluid in fluid pressure test
psi	pounds per square inch
PT	pressure tension
Q	force applied
R^2	coefficient of determination
R	universal gas constant
R	resistance in ohms
RF	radio frequency
RH	relative humidity
ρ_1	corrected surface resistivity measurement
ρ_2	uncorrected surface resistivity measurement
$\rho_{mixture}$	apparent density of mixture
ρ_{t-ref}	corrected surface resistivity measurement in Arrhenius equation
ρ_t	surface resistivity at testing temperature
$\rho(z)$	linear distribution along z-axis of nuclei
r_i	inner diameter of cylinder in fluid pressure test
r_0	outer diameter of cylinder in fluid pressure test
s	seconds
S	sorptivity
SF	silica fume
σ_t	creep testing stress at time t
σ_θ	tangential stress in fluid pressure test

Sin	sine function
SPI	single point imaging
SPRITE	single point ramped imaging with T_1 enhancement
SR	surface resistivity
SR_{raw}	raw surface resistivity measurement
ST	splitting tension
S_t	reduced water content
t	time in seconds
$T_{measured}$	temperature at measurement in surface resistivity correction method
T_{ref}	reference temperature for Arrhenius equation
$T_{reference}$	reference temperature in surface resistivity correction method
TR	encoding time
Θ	reduced water content
θ	volumetric water content between saturated and dry
θ	off-angle axis rotation angle of sample magnetization
θ_i	initial dry water content
$\theta_{saturated}$	estimated moisture content at time of testing
θ_s	saturated water content
T_1	time constant for atomic nuclei
T_1	surface resistivity temperature measurement at corrected temperature
T_2	surface resistivity temperature measurement, uncorrected temperature
T_2*	spin-spin relaxation time
u	flow within a porous medium
UPV	ultrasonic pulse velocity
V	volts
V_B	volume of pores
$V_{Specimen}$	volume of the specimen

W/C	water to cement ratio
x	distance from wet end in sorptivity
z	spatial position along z axis

Abstract

This thesis presents a series of studies related to the transport properties of water in concrete systems. There were two primary foci for the experimental research: the use of Magnetic Resonance Imaging (MRI) techniques to directly image the distribution of ^{1}H nuclei in water during mass transport in both sorptive and evaporative flow, and the use of the pressure tension test, developed in part at McGill, to evaluate the effects of transport property-related durability issues on the tensile strength of concrete materials. The transport properties of concrete are relevant to the sustainability of the material, because many different modes of deterioration are directly related to the transport of water and ions dissolved within. The use of an indirect tension test to directly evaluate the effects of deterioration in concrete was found to be significant, especially when compared to standard destructive test methods, since many of the investigated deterioration mechanisms caused expansive damage that had a considerable effect on the tensile capacity of the material.

The Single Point Ramped Imaging with T_1 Enhancement (SPRITE) MRI technique was used to directly image the distribution of ^{1}H nuclei of water in the capillary pore structure of different W/C cement pastes and mortars in sorptive and evaporative flow conditions. An experimental technique was developed to allow SPRITE MRI imaging of longer specimens approximating the depth of concrete slabs in common use. Steady-state 1D evaporative transport imaging with different W/C mortars was also performed with SPRITE.

The pressure tension test was designed, developed, and programmed as a part of the thesis to be fully automated for a variety of loading conditions, including ramped loading at different rates,

cyclic loading, and constant loading, such as creep. The efficacy of the developed pressure tension test at evaluating tension capacity of concrete was subsequently demonstrated in a series of durability-related studies.

The pressure tension test was used to evaluate the effects of variable moisture content, including vacuum saturation and oven drying, sulphate attack from evaporative flow conditions, freeze-thaw in saturated concrete, and creep loading for both saturated and dry specimens. The moisture content had a significant effect on the failure levels of concrete, with saturated specimens failing at a higher tensile stress compared to specimens that had been partially dried and oven dried. For sulphate attack, the pressure tension test could significantly distinguish between sulphate damage in cores drilled from a slab undergoing evaporative flow of water with dissolved sulphate ions from specimens without ions. A gradient in tension resistance was found corresponding to areas with a greater concentration of sulphate ions. For freeze-thaw, the pressure tension test could detect a significant decrease of tension resistance in concrete specimens at an earlier time than any of the other destructive test methods examined, and the magnitude of the decrease was much larger than in any of the other destructive test methods. The thesis also demonstrates a novel use of the pressure tension test to evaluate the deterioration of tension capacity due to a constant load creep condition in both saturated and dried concrete. The results agreed with other tension creep tests in concrete despite the radically different method of stress application.

In concordance with the durability tests, a variety of nondestructive test (NDT) techniques were used to concurrently evaluate the change in material properties due to transport-based deterioration. Both ultrasonic pulse velocity (UPV) and surface resistivity (SR) were used to

characterize durability or hydration-related changes in concrete for different w/c and admixtures. For the surface resistivity method, a novel procedure for normalizing the results with respect to temperature was presented and compared with existing methods of temperature correction. The surface resistivity temperature method was subsequently used to normalize results from a freeze-thaw study, with the resulting variability of the SR signal being greatly decreased as a function of deterioration. The thesis demonstrated the applicability of the pressure tension test at evaluating the deterioration of tension capacity in concrete due to a variety of durability mechanisms related to the transport properties.

Français

Cette thèse présente une série d'études relatives aux propriétés de transport de l'eau dans les systèmes en béton. Il y avait deux sujets primaires pour la recherche expérimentale : l'utilisation de techniques d'imagerie par résonance magnétique (IRM) pour mettre directement en images la distribution des noyaux ^{1}H dans l'eau pendant le transport de masse dans le flux de sorption et d'évaporation et l'utilisation de l'essai de traction de pression, développé en partie à McGill, pour évaluer les effets des problèmes de durabilité liés à la propriété du transport sur la résistance à la traction des matériaux en béton. Les propriétés de transport du béton sont pertinentes pour la durabilité du matériau, car de nombreux types de détérioration sont directement liés au transport de l'eau et des ions dissous à l'intérieur. L'utilisation d'un essai de traction indirect pour évaluer directement les effets de la détérioration du béton a été jugée significative, en particulier par rapport aux méthodes d'essai destructrices standard, car de nombreux mécanismes de détérioration étudiés ont causé des dommages expansifs qui ont eu un effet considérable sur la capacité de traction du matériau.

La technique de l'IRM d'imagerie en rampe à un seul point avec la méthode T_1 (SPRITE) a été utilisée pour mettre directement en images la répartition des noyaux ^1H de l'eau dans la structure des pores capillaires de pâtes et mortiers de ciment avec différents rapports eau/ciment dans des conditions d'écoulement par sorption et par évaporation. Une technique expérimentale a été développée pour permettre l'imagerie IRM SPRITE d'échantillons plus longs approchant la profondeur des échantillons plus longs. Le transport par évaporation 1D à l'état stable dans des mortiers avec différents rapports eau/ciment a également été réalisé avec SPRITE.

L'essai de traction de pression a été conçu, développé et programmé dans le cadre de thèse afin d'être entièrement automatisé pour diverses conditions de chargement, y compris le chargement en rampe à différents taux, le chargement cyclique et le chargement constant, comme le fluage. L'efficacité de l'essai de traction de pression développé pour évaluer la capacité de traction du béton a ensuite été démontrée dans une série d'études liées à la durabilité.

L'essai de traction de pression a été utilisé pour évaluer les effets de la teneur en humidité variable, y compris la saturation sous vide et le séchage au four, l'attaque de sulfate à partir de conditions d'écoulement par évaporation, le gel-dégel dans le béton saturé et le chargement de type fluage pour les échantillons saturés et secs. La teneur en humidité a eu un effet significatif sur les niveaux de dégradation du béton, les échantillons saturés ayant échoué à une contrainte de traction plus élevée que les échantillons partiellement séchés ou ceux séchés au four. Pour l'attaque par le sulfate, l'essai de traction de pression pourrait distinguer de façon significative les dommages du sulfate dans des carottes de forage d'une dalle soumise à un écoulement évaporateur d'eau avec des ions sulfate dissous des spécimens sans ions. Un gradient de résistance à la traction a été trouvé correspondant à des zones avec une plus grande

concentration d'ions sulfate. Pour le gel-dégel, l'essai de traction de pression pourrait détecter une diminution significative de la résistance à la traction dans les échantillons de béton plus rapidement que les autres méthodes d'essai destructrices examinées, et la grandeur de la diminution était beaucoup plus grande que dans l'une des autres méthodes d'essai destructrices. La thèse démontre également une nouvelle utilisation de l'essai de traction de pression pour évaluer la détérioration de la capacité de traction due à une condition de fluage à charge constante dans le béton saturé et séché. Les résultats rejoignent ceux de d'autres essais de fluage en traction dans le béton malgré la méthode radicalement différente d'application du stress.

Conformément aux essais de durabilité, une variété de techniques d'essai non destructif (END) ont été utilisées pour évaluer en même temps la variation des propriétés du matériau en raison de la détérioration du transport. La vitesse de l'impulsion ultrasonique et la résistivité de surface ont toutes deux été utilisées pour caractériser la durabilité ou les changements liés à l'hydratation dans le béton pour différents rapports eau/ciment et adjuvants. Pour la méthode de résistivité superficielle, une nouvelle procédure pour normaliser les résultats par rapport à la température a été présentée et comparée aux méthodes existantes de correction de température. La méthode de la température de résistivité superficielle a ensuite été utilisée pour normaliser les résultats d'une étude de gel-dégel, la variabilité résultante du signal SR étant fortement diminuée en fonction de la détérioration. La thèse a démontré l'applicabilité de l'essai de traction de pression pour évaluer la détérioration de la capacité de traction dans le béton en raison de divers mécanismes de durabilité liés aux propriétés de transport.

Acknowledgements

The author acknowledges the contributions of the undergraduate student workers who have helped with data acquisition and concrete casting. Special thanks go to Charles Desjardins, Julia Bond, Susan Blackmore and Majed Karam for their contributions. The author acknowledges the contribution of the McGill technical staff John Bartczak, Damon Kiperchuk for assistance with the experimental setups and other testing. Thanks to Jorge Sayat for assistance with software and computer programming issues. Thanks as well to Dr. William Cook for his expertise in electrical systems related to the pressure tension machine, as well his training and guidance. The author acknowledges the technical, research and academic staff at the University of New Brunswick, Dr. Florin Marica and Igor Mastikhin for their contributions in the MRI imaging and analysis portion of the thesis. The MRI studies performed would be impossible without Dr. Bruce Balcom, and his contributions are acknowledged and appreciated. Thanks as well to Razieh Enjilela and Prisciliano F. de J. Cano-Barritaco, the co-authors of the wicking action MRI paper for their contributions to writing, image processing and analysis. The author acknowledges assistance of other graduate students with help in experiments. Thanks to Aifei Lu, Dr. Julie Hartell, Dominic Langelier, Yutai Liu, Sydney Milton, Gaowei Xu and Rami Ghanem. The author acknowledges the CREATE grant program from NSERC, which has provided funding throughout the course of the research program. Special thanks to supervisor Dr. Andrew Boyd at McGill, for his input, support, and guidance over the course of the program, as well as for his inestimable contributions to the editing and preparation of the thesis and papers. Final thanks go to my friends, family and

especially to my partner, Amy-Jean Mac Donald, for her love, support and dedication throughout the course of this research program.

Preface and Contribution of Authors

Andrew Komar is the author of every chapter contained within this thesis including the introduction, literature review, and conclusion chapters, as well as the appendix (Chapters 1, 2, 10). The author designed the pressure tension machine used for the research program and assisted in the build, implementation of the safety systems, and calibration of the machine before it was used in any tests. The author created blueprints used for the fabrication of the machine. The author wrote the LabView software used for the automated control system in the pressure tension machine, and designed all the loading and unloading apparatus used to control the machine. The author formulated a standardized testing protocol for pressure tension testing and created a training program which allowed others to operate the machine without supervision.

For Chapter 3, the author designed and mixed the mixtures used for the concrete specimens and created the apparatus for the one-dimensional sorptive flow conditions. The author conditioned the samples before shipping them to UNB for imaging. The author acknowledges Susan Blackmore in her assistance with the conditioning at UNB. The sealing for the one-dimensional flow condition with epoxies was performed by the author. All the MRI imaging work was performed by Dr. Balcom's research group at the University of New Brunswick and the images presented throughout were created from the data they provided. The author is the sole writer of the chapter. The contributions of Dr. Balcom and Dr. Boyd in editing of the document are acknowledged.

For the collaborative paper on steady state monitoring of wicking action, the author acknowledged the contributions of co-authors, including primary author Razieh Enjilela for her

writing and work in the experimental imaging. The author acknowledges co-author Prisciliano F. de J. Cano-Barritaco for their contribution to the modelling of steady state wicking action and calculating the diffusion parameters from the experimentally derived MRI data, which are detailed within the co-authored paper. The contributions of Dr. Balcom in developing the SPRITE technique as well as supervising the work of Razieh Enjilela during the experimental phase are also acknowledged with respect to the steady state paper. The author contributed to the paper by creating and casting the concrete mixtures used for the entirety of the paper. The author conditioned and sealed the samples for one dimensional flow, and provided the measurements of porosity used as input for modelling parameter. The author created the one-dimensional flow apparatus used for all the steady state conditioning. Input during the experimental phase as well as in analysis of the implications with respect to durability issues was also contributed by the author.

For Chapter 4, the raw surface resistivity data was collected as part of Sydney Milton's master's research program. The author acknowledges the donation of the Surface Resistivity meter from Proceq, and donations of the coarse and fine aggregates used in casting from Bauval LLC. The experimental technique used to obtain this raw data was developed by the author. The development of the temperature correction method as well as the statistical analysis of the data detailed in Chapter 4 was an original contribution of the author, with supervision from Dr. Boyd as well as the editing of the writing.

For Chapter 5, the author created the mixture design and cast all the samples. The author acknowledges Bauval LLC for the donation of the coarse and fine aggregates used in the study, and for the donation of the SR meter from Proceq. The author designed the modified vacuum

saturation system with assistance from the laboratory technicians. The NDT data and some of the pressure tension results was collected in part by a Julia Bond, a summer student properly trained and employed for this purpose, but all the analysis of the results was performed by the author. Dr. Boyd assisted in the supervision of the testing as well as the editing of the writing.

For Chapter 6, the sulphate cores were obtained from a project which had originally been a project from Scott Cumming's master's thesis. The author performed all the pressure tension testing as well as the statistical analysis described in the chapter. Dr. Boyd and Dr. Hartell assisted in the supervision of the testing as well as the editing of the writing.

For Chapter 7, all the mixtures for the study were designed and cast by the author. The author acknowledges the coarse and fine aggregate donations by Bauval LLC and for the donation of the SR meter by Proceq. All the NDT outlined was performed by the author, as well as the conditioning of the samples in a freeze-thaw condition. All the pressure tension, compressive strength and splitting tension tests were performed by the author. Dr. Boyd assisted in the supervision of the testing as well as the editing of the writing.

For Chapter 8, all the mixtures for the study were designed and cast by the author. The author acknowledges the donation of the coarse and fine aggregates by Bauval LLC, and for the donation of the SR meter by Proceq. All the NDT outlined was performed by the author, as well as the conditioning of the samples in a freeze-thaw condition. All the pressure tension and compressive strength were performed by the author. The testing required to implement the surface resistivity temperature correction method outlined in Chapter 8 was performed by the author, and the

analysis of these results was performed by the author. Dr. Boyd assisted in the supervision of the testing as well as the editing of the writing.

For Chapter 9, Gaowei Xu assisted the author with the casting and conditioning of the samples. The author acknowledges the donation of the coarse and fine aggregates by Bauval LLC. The creep loading protocol for the pressure tension test as well as the implementation was performed by the author. Mr. Xu performed much of the testing in pressure tension with assistance from the author. The analysis of the results as well as the statistics were performed by both the author and Mr. Xu. The writing of the document was a collaborative effort from both authors. Dr. Boyd assisted in the supervision of the testing as well as the editing of the writing.

Publications

Pressure Tension Test: Reliability for Assessing Concrete Deterioration Komar, A. J. K.; Hartell, J. A.; Boyd, A. J., CONSEC 13, 2013, Nanjing China. pp 337-344

Pressure Tension Testing in the Evaluation of Freeze-Thaw Deterioration Komar, A. J. K.; Boyd, A .J., 10th fib International PhD Symposium in Civil Engineering, 2013, Universite Laval, Quebec, Canada, pp 143-148

Tensile Strength of Plain Concrete under Sustained Loading by Pressure Tension Xu, G. W.; Komar, A. J. K; Boyd, A. J. (Pre-pub)

Pressure Tension Test for Assessing Fatigue in Concrete Soleimani, S. M.; Komar, A. J. K.; Boyd, A. J. SPIE Smart Structures and Materials + Nondestructive Evaluation and Health Monitoring.

Monitoring Steady State Moisture Distribution during Wick Action in Mortar by Magnetic Resonance Imaging (MRI) Razieh E.; Prisciliano F. de J. C. B.; Komar, A. J. K.; Boyd A. K.; Balcom, B., Materials and Structures, April 2017

Effect of Varying Moisture Content on Tensile Strength of Plain Concrete in Pressure Tension Komar, A. J. K.; Boyd, A. J. (Pre-pub)

Expected List of Contributions

- Pressure tension test development
  - Designed and implemented the first automated apparatus capable of operating without direct human control.
  - Formulated standard operating procedures for enhanced repeatability.
  - Incorporated automated control of loading and unloading rates, allowing for any load/unload combination during testing, including:
    - Standard ramping at any predefined rate.
    - Cyclic loading.
    - Sustained pressure level for simulated creep behavior.
  - Developed compensation algorithm for pressure leakage during testing.
  - Digitized the control program output to provide better data acquisition and analysis.
  - Developed procedures to effectively test specimens under a wide range of sample conditions, including those with large leaks.
- Pressure tension research
  - Demonstrated tensile creep fatigue behavior

- Demonstrated detection capabilities for deterioration of concrete due to freeze/thaw cycling with greater sensitivity than existing tension methods.
- illustrated changes to the concrete failure mechanism as freeze/thaw deterioration progresses.
- Demonstrated detection capabilities for deterioration of concrete due to sulphate attack, specifically related to a damage gradient caused by an evaporative transport mechanism during exposure.
- Demonstrated and characterized the change in tensile resistance of concrete due to moisture content variations, including vacuum saturation.
- Illustrated changes to the concrete failure mechanism at different moisture contents.

- Surface resistivity
  - Developed a novel procedure for developing temperature corrections for surface resistivity measurements on concrete samples.
  - Applied temperature correction procedure to standardize characterization of the hydration behavior of concrete.
  - Applied temperature correction procedure to long-term durability testing.
- MRI testing
  - Demonstrated that the SPRITE method can distinguish between different populations of water in the nanopores (those associated with creep).
  - Used the SPRITE method to characterize sorptive behavior in cement pastes.
  - Illustrated changes in water content that could be associated with ongoing hydration during sorptivity experiments

- Developed a technique for imaging samples longer than the MRI's field-of-view, allowing for more representative samples to be imaged.
- Imaged specimens undergoing steady state wicking of water:
- Detected moisture in the larger pores which would not be reflected by commonly used predictive models.
- Illustrated a larger variance with respect to w/c for longer steady state specimens.
- Illustrated that even non-steady state specimens can incur moisture content gradients driven by evaporation.

Chapter 1: Introduction

1.1. Background

This research program was focused on the study of concrete deterioration processes driven by the evaporative transport of water and the use of newly developed test methods to study these processes. Concrete is the most used building material around the world, so an increased understanding of the mechanisms that cause the material to deteriorate is important in terms of increasing the service life of the material in practice. Integral to this pursuit are test methods which accurately and reliably determine the performance of the material under the kind of conditions to which concrete is subjected in the field, particularly under extreme conditions associated with rapid deterioration.

The experimental program followed fell into three main branches: the further development of the pressure tension test with subsequent proof-of-concept testing to demonstrate the utility of the test method on concrete, evaluation of commonly used nondestructive testing techniques and their relative efficacy at detecting ongoing changes to cement systems, and the use of Magnetic Resonance Imaging (MRI) techniques to directly examine water transport in cement systems. Although the themes are radically different in terms of experimental work, they are unified in terms of the investigation of the effect of water transport within the pore structure of concrete.

Water transport, in particular the movement of dissolved ions within the water, is directly involved in deterioration mechanisms such as sulphate attack and other durability issues. In the case of concrete with embedded reinforcing steel, ion mobility within the water in the connected

pore structure is a concern if there is a source of chlorides nearby, such as seawater or de-icing salts. These chloride ions will cause premature rusting of the reinforcing steel, which can lead to expansive cracking and a dramatic increase in the overall rate of mass transport into the concrete due to these cracks, which exacerbates the deterioration rate in a positive feedback loop. Even without dissolved ions, the presence of water within the pore structure of concrete can be a source of deterioration if there are large temperature changes such as freeze-thaw cycling.

Regardless of the specific method of deterioration, or combination thereof, having methods of accurately characterising water transport in concrete is important for making sustainable design choices that will increase the service life of concrete. In addition, it is also important to formulate experimental testing methods that will accurately quantify the extent of deterioration in concrete to allow properly informed decisions concerning repair or replacement. The research program herein was primarily concerned with these goals, as outlined in more detail in the following chapters.

1.1.1. Pressure tension

The primary focus of the research program was the further development and proof testing of the pressure tension machine as a destructive test method that specifically evaluates the tensile capacity of concrete. Although compressive tests are most commonly used to evaluate the strength of concrete mixtures in engineering practice, the tensile capacity is more relevant to durability concerns because concrete is an order of magnitude weaker in tension relative to compression. When the tensile capacity is exceeded on a microstructural level, cracks will initiate and begin to propagate, dramatically increasing the transport properties of the bulk material due to the larger flow pathways available to the water on the macrostructural level. This increase in

transport properties due to cracking will create a positive feedback loop for any durability mechanisms already underway moderated by the connectedness of the pore structure.

While other tension tests exist that can evaluate the tensile resistance of concrete (such as splitting tension and direct tension), they differ from the pressure tension test in their method of applying the stress. The pressure tension test is the only test method that applies stress directly to the connected pore structure of the concrete, whereas the other methods rely on mechanical means of stress application. Because this tensile stress field is created within the entire volume of the specimen, the specimen will fail at the weakest point within this region, instead of in regions of applied peak stress caused by the loading as is the case with the other existing tension testing methods. Pressure tension, unique among these tension tests, is sensitive to the weakening of the hydrated cement paste and the connected pore structure in concrete due to this load application on a microstructural level. This causes tensile failures wherever the material is weakest or most heavily damaged within this entire volume.

The pressure tension test has existed in a rudimentary form since the late 1970s, but a large part of the experimental research undertaken was made possible by the novel innovations implemented during the research program. The previous iterations of the test system used manually operated valves to apply the pressure to the system, which resulted in large variances in terms of applying a consistent loading rate. A novel instrumentation system was devised and implemented during the research program that allowed fully automated control of the loading rate and variety of loading protocols, including a constant loading rate and controlled unloading. These innovations allowed for novel studies to be performed, including tensile creep, using the pressure tension machine. In addition, the measurement of pressure within the system was

digitized, which allowed for an automated data acquisition of pressure application. This innovation allowed for a greater level of accuracy in the maximum applied pressure.

This new configuration of the pressure tension machine was used to specifically investigate the effect of variable moisture content on the results of the pressure tension test, since there has been previous work using a similar machine that had indicated that there was some sort of correlation between these two variables. The work performed validated and expanded on these preliminary indications, and this moisture content dependant behavior was characterized.

Based on the results of this moisture content study, a standard protocol for testing fully saturated specimens was created and a variety of studies were carried out to demonstrate the applicability and utility of the pressure tension test method for evaluating different durability issues. These issues include degradation of strength under constant uniform tension loading (tensile creep), freeze-thaw damage, and sulphate attack. For these durability issues, the evolution of the transport properties within the connected pore structure, particularly due to expansive stresses that cause cracking of the concrete, was of key importance. It was found that the pressure tension test was well suited to detecting ongoing damage for these cases. The pressure tension test was also found to be more sensitive to the paste weakening effects of durability related deterioration caused by these expansive stresses relative to any of the other test methods, destructive or nondestructive, used in the concurrent investigations.

1.1.2. Nondestructive testing

Engineers must make informed decisions about the state of deterioration in-situ without the use of destructive test methods such as the commonly used compressive strength tests. This research

program evaluated surface resistivity (SR), ultrasonic pulse velocity (UPV) and expansion prisms as nondestructive test methods for evaluating the changes in concrete systems due to durability concerns.

For surface resistivity, specifically, it was noted in previous work that temperature variations of the sample can cause extremely large anomalies in the measured values for the test, so an experimental test method designed to formulate a correction factor for these temperature variations was developed and evaluated as compared to existing correction methods. Using this technique, it was demonstrated that the large variability in SR test results can be largely controlled for, allowing temperature independent quantification of the evolution of surface resistivity measurements due to ongoing deterioration. The surface resistivity test method indirectly measures the connectivity of the pore system within concrete, so controlling for the temperature variation was found to be integral to understanding the significance of the observed changes to the pore structure. This surface resistivity correction method was used both to evaluate the changes in pore structure due to hydration for a variety of concrete mixtures as well as to normalize the measurements for concrete mixtures undergoing deterioration due to freeze-thaw damage.

The ultrasonic pulse velocity test is a measurement of the connectedness of the solid part of the concrete through which the stress waves propagate, and it is well suited for evaluating any changes to this solid structure due to ongoing deterioration. By using both surface resistivity and ultrasonic pulse velocity in conjunction, two independent measures of the state of concrete pore structure were taken to provide a more complete picture of the evolution of the pore space of concrete due to durability issues, in particular, ongoing freeze-thaw damage.

The expansion prism method was used to specifically evaluate the dimensional length change of concrete specimens due to freeze-thaw damage. Water within a concrete pore system does not all freeze simultaneously, there is a progression as the larger pores freeze first, followed by successively smaller and smaller pores. As water freezes within the confined, connected pore structure of concrete, it expands and forces unfrozen water through the ever-constricting pore structure, causing stress to develop within the solid part of the concrete. These stresses can overcome the tensile capacity of the material in the immediate area and cause cracking within the microstructure. This cracking is associated with a dimensional change that is measurable since the cracks occupy a greater volume than the previously undamaged, contiguous porous material. These cracks are pathways for increased permeability and thus water transport of deleterious agents typically carried by water, so directly measuring the change in length is an independent way to monitor the progress of ongoing freeze-thaw deterioration

1.1.3. Magnetic resonance imaging

The goal for this part of the research program was to characterise and directly image the flow of water in simple cement systems. This work was performed in association with the University of New Brunswick's Magnetic Resonance Imaging (MRI) research centre due to their expertise and facilities capable of performing the proposed research. Modelling and analysis of the resulting images was also undertaken to relate the images to more commonly used hydraulic parameters.

The primary focus of the MRI work was one dimensional sorptive flow of water into initially dried concrete, as well as the long-term change of this sorptive flow due to evaporation from a dry end, also known as wicking action. This kind of exposure condition is common in a variety of real world conditions, such as in pavements on top of wet soil, partially submerged or buried concrete

structures, or in tunnel linings built below the waterline of the surrounding soil. One of the key decisions for reinforcing concrete design is related to the minimum depth of cover for the embedded reinforcement to provide a sufficient barrier between intruding moisture and the reinforcing steel. If steel is exposed to chloride ions within water, or a low pH environment caused by carbonation, rusting and expansion will commence on the steel, possibly initiating a rapid deterioration of the composite reinforcing steel-concrete system.

The experimental work with magnetic resonance imaging was performed to directly observe the flow of water through cement systems over different lengths and water to cement ratios (W/C). The MRI procedure is particularly sensitive to magnetically active materials that are common in ordinary portland cement, aggregates and sealants. Hence, there was significant experimental work required at the outset of these studies to develop representative systems that would also be suitable for MRI. It was determined that white portland cement could be used due to its negligible portion of ferromagnetic components that would interfere with the effective acquisition of the MRI signals. In addition, pure silicate sand was used as the aggregate in the mortar samples to further minimise any included ferromagnetic impurities.

The other experimental issue that was addressed during the research program using MRI was the development of a technique that would allow for the imaging of specimens with a length larger than 45 mm. The 45-mm field of view limitation was a fundamental characteristic of the MRI equipment used for the studies, so a novel technique using fiduciary markers was developed to overcome this limitation. This development allowed samples of lengths that are more representative of concrete slab depths of 100 mm to be imaged, and sorptive flow of 100 mm pastes was undertaken using these fiduciary markers.

Implementing these developments coupled with the Single Point Ramped with T2 Enhancement (SPRITE) imaging technique originally developed by the UNB MRI centre, the sorptive flow of different W/C pastes of 45 mm lengths were imaged as they were allowed to evolve due to evaporation from the dry end. However, it was found that the rate of sorptive flow was much larger than the associated evaporation rate, and these short sample lengths did not show significant drying gradients.

The SPRITE technique was then used to image longer samples of the same W/C, but with mortars instead of pastes, in order to introduce the inclusion of the interfacial transition zone (ITZ) in the mortars that was not otherwise present in the paste samples. The inclusion of the aggregates was important to properly simulate the heterogenous distribution of connected porosity due to this ITZ. These mortar samples showed a much more pronounced effect of the evaporation from the dry end as a function of W/C, but also showed that there were still significant amounts of moisture present within the sample at a depth that would be commensurate with the reinforcing steel.

The MRI studies experimentally demonstrated that there was significant water present in the region that would nominally have embedded steel, and that this wet region was unexpected given two commonly used modelling techniques. Based on these experimental results, it could be seen that the associated deterioration of the steel would therefore begin sooner than would be otherwise anticipated by the designer. This condition of increased water near reinforcing steel would lead to a decreased service life in cement systems undergoing wicking action similar to the type simulated, and could create the conditions associated with increased deterioration.

1.2. Research objectives

While the three main themes of the research program seem somewhat disparate, they were designed to represent components of a more holistic exposure/monitoring/testing regimen for concrete exposed to deterioration induced by an evaporative moisture transport environment. The MRI work was more focused on the characterization of steady-state moisture transport properties due to evaporation and sorptivity for different W/C pastes and mortars, whereas the pressure tension and nondestructive testing methods were more focused on the macroscopic results of deterioration due to durability concerns moderated by these transport properties.

The pressure tension machine is very sensitive to differences in moisture content, even at high levels of partial saturation, so the steady-state results from the MRI studies were useful in understanding the mechanisms of water transport during drying due to evaporation. Based on the results of the MRI, it was clear that, even for low w/c concretes, there would be significant amounts of free water within the regions that would normally be considered 'dry', which could explain why there was a less severe change in pressure tension failure results at partial saturation values relative to dry values.

It was clearly demonstrated throughout the research program that the pressure tension machine was capable of reliably detecting ongoing deterioration due to freeze-thaw, creep, and sulphate attack that caused changes in the tensile strength of the material. The pressure tension test was well suited for evaluating these deterioration issues which were ultimately driven by transport properties, and the different NDT methods, surface resistivity especially, that were chosen to monitor the ongoing deterioration were ultimately successful at providing independent verification of the changes to the transport characteristics of the concretes. Testing the tensile

capacity of the material in the context of ongoing deterioration is an important factor to consider since it is directly related to the formation of cracks within the solid material. Pressure tension is uniquely suited for this endeavor since the loading mechanism uses the connected pore structure to apply the stress directly to this solid phase, and is thus more sensitive to deterioration of this solid phase compared to existing test methods.

Chapter 2: Literature Review

This thesis was compiled primarily in the form of a manuscript-based document, and as such, a more specific review of the relevant literature that concerns each paper's subject matter is included in the introduction sections of each respective chapter. The following chapter supplements those more detailed review section with a broader review of the relevant literature and general concepts referred to herein.

2.1. Mass transport in porous media

The broad theme of the research program examines the behavior of water undergoing mass transport through the porous structure of a variety of cement systems, including pastes, mortars, and concretes. In each of these cases, the material is not homogenous, it is instead best described as a heterogenous material consisting of two phases. The first is a solid phase, which is comprised of the cementitious hydrate by-products and aggregates that constitute the solid part of the material. The second is the voids between these solid materials, with a very wide distribution of void sizes present from the nanoscopic intercrystalline voids up to millimetre sized capillary pores.

It is within this void space of a variety of sizes that the mass transport occurs. The amount of water, or 'water content' within this void space is generally measured as a mass ratio, defined in Equation 2.1 as [1]

$$v = \frac{m}{m_a}$$

Equation 2.1- Gravimetric mass ratio, from Hall [1]

Where m is the mass of water and m_a is the mass of the dry solid absent any water. The values of these two variables are generally derived experimentally by a gravimetric comparison between the 'saturated' and 'dry' states achieved through conditioning. However, it is difficult to achieve a fully dried state, since water will remain tightly bound in some range of the void spaces, particularly at the smaller nanoscopic scale. Thus, a commonly used definition in mass transport literature is the reduced water content, defined in Equation 2.2 as:

$$\Theta = \frac{\theta - \theta_i}{\theta_s - \theta_i}$$

Equation 2.2- Reduced water content, from Hall [1], Lockington [2]

Where Θ is the reduced water content, θ_s is the saturated water content θ_i is the initial or 'dry' water content, and θ is the volumetric water content between these two values [1,2]. This reduced water content is also referred to in the literature as S_t or simply θ. For saturated or uniformly dry specimens, this value will be constant as a function of the depth of the material, but this research program is concerned with conditions where this value is between the saturated and dry conditions, also known as unsaturated mass transport.

The basics of mass transport into media are primarily derived from the Darcy equation, where the flow of fluid is defined in Equation 2.3 as:

$$u = -K(\Theta)\nabla\Phi$$

Equation 2.3- Darcy's law, from Hall, and Gummerson et al. [1,3]

Where flow u within a porous medium is dependant on the gradient of the hydraulic potential Φ as well as the moisture content dependant hydraulic conductivity $K(\Theta)$. This hydraulic potential takes into account both the capillary forces of the liquid from the solid phase as well as external

forces such as gravity. The hydraulic conductivity is a property of the porous medium and will also have a strong dependence on the reduced water content. [1]

When formulated as a differential equation with respect to time, darcy's equation for unsaturated flow can be represented in Equation 2.4 as:

$$\frac{\partial \Theta}{\partial t} = \nabla \cdot [D(\Theta)\nabla\Theta - K(\Theta)]$$

Equation 2.4- Unsaturated flow through porous media, from Lockington et al. [2]

Where D(Θ) is the hydraulic diffusivity of the material as a function of reduced water content, and K(Θ) is the hydraulic conductivity [2]. The D(Θ) relationship is not exactly predictable from principles, and in practice is approximated in Equation 2.5 using either an exponential or a power law relationship:

$$D = D_0 e^{n\Theta}, D = D_0 \Theta^n$$

Equation 2.5- Exponential and power law definitions of hydraulic diffusivity, from Lockington et al. [2]

Where D_0 and n are experimentally derived fitting parameters. Other, more complicated models of hydraulic diffusivity can be used, which can lead to significantly more complicated analyses.

2.1.1. Sorptivity

One application of this unsaturated theory is the prediction of the ingress of water in mass transport as a function of distance from a reservoir of water. These conditions will be relatively common in field applications, such as retaining walls or tunnel structures. Lockington *et al.* define this generally in Equation 2.6 as [2]

$$\frac{\delta\Theta}{\delta t} = \frac{\delta}{\delta x}\left(D(\Theta)\frac{\delta\Theta}{\delta x}\right), 0 < \mathrm{x} < \infty$$

Equation 2.6- Differential equation definition for water penetration front [2]

In the simplest case, this differential equation can be used to predict the 1D uptake of water due to capillary action of an initially dry porous media with exposure to a water reservoir. By using a Boltzmann transform variable $\eta = xt^{-1/2}$, this differential equation can be formulated as seen in Equation 2.7 to directly solve for the mass of the water uptake:

$$\mathrm{i} = \mathrm{t}^{1/2} \cdot \int_{\Theta_\mathrm{i}}^{\Theta} \eta \, \mathrm{d}\Theta = \mathrm{S} \cdot \mathrm{t}^{1/2}$$

Equation 2.7- Mass uptake solution for sorptive flow conditions, from Gummerson et al. [3]

Where *i* is the length the water has been transported in distance/area, and sorptivity is in length·$t^{-1/2}$. Sorptivity is a useful first step in looking at the mass transport of water in porous media as it is relatively simple to experimentally evaluate. Since the water penetration distance is directly proportional to the square root of time of the flow, the mass of the cumulative water uptake will also be proportional to the root of time. This type of sorptive flow will have a sharp wetting front, and a boundary between the wet and dry regions will often be evident by visual observation. However, finer examination of the exact distribution of the reduced moisture content is difficult to perform due to the complications in precisely measuring the moisture content as a function of distance [4,5,6,7,8].

2.1.2. Wicking action

When considering the nature of mass transport of water with boundary conditions more complicated than simple sorptivity, a much more complex analysis is required to account for the

observed behavior of the water. For example, the previous analysis of sorptivity neglects the effect of evaporation of water from within the void space of the porous material, but coupled vapor-liquid flow will occur within the unsaturated regions of the material. If this evaporation is accounted for at the dry end of one-dimensional flow, it will create additional mass transport due to wicking action. Since vapor is a gas and has different sensitivities to temperature and pressure conditions, the inclusion of evaporation in the unsaturated region considerably increases the computational difficulties of this highly nonlinear differential equation analysis [9]

Some experimental models have been developed to look at the long term steady state conditions of this evaporation condition from the dry end. Lockington *et al.* [10] used the formulation of Equation 2.6 and added an additional sink term, to account for the moisture lost due to the evaporation at the dry end. Equation 2.8, which was used in their analysis, is formulated as: [10]

$$\frac{\partial \Theta}{\partial t} = \frac{\partial}{\partial x}\left(D(\Theta)\,\frac{\partial \Theta}{\partial x}\right) - k\Theta$$

Equation 2.8- Lockington model for steady state flow under evaporative conditions [10]

Where constant *k* is an empirically derived constant that determines the rate of evaporation. The exact analytical form of the solution to this differential equation is highly dependant on the form that the diffusivity function takes.

2.2. Magnetic resonance imaging of cement materials

2.2.1. Basic principles

A major component of the experimental work in terms of characterizing the moisture content profiles of cement systems undergoing both sorptivity and wicking action is only made possible by using magnetic resonance imaging (MRI) techniques. Magnetic resonance imaging is used in a

multitude of subject areas other than materials engineering, such as chemical structure determination or for medical imaging. The approach used for both experimental studies within this research thesis employed a specific technique more specifically tailored for use in cementitious systems, and to imaging the distribution of specific nuclei within a porous media. The theory of this nuclear magnetic resonance (NMR) technique will be outlined in more detail.

The basic principle behind NMR imaging is via manipulation of the spin angular momentum of atomic nuclei. This spin angular momentum of nuclei is a fundamental quantum mechanical property, which can be in either a parallel or anti-parallel configuration. This spin angular momentum is related to the magnetic moment of the nuclei and essentially determines the magnitude and reactivity of the individual nuclei to magnetism. Thus, this fundamental property will be different for different nuclei, and is particularly strong for nuclei relevant to the study of mass transport, namely the ^{1}H nuclei present in H_2O molecules [11].

In the presence of an externally applied magnetic field with field strength B_0 aligned in the z-direction (on an x, y, z coordinate system), the magnetic moments of nuclei will split into different orientations, which is dependant on the quantum numbers of the nuclei. For the case of the ^{1}H nuclei, there will be two possible orientations relative to the applied magnetic field, either parallel to the magnetic field or opposite. These two orientations have a difference in terms of their energy states, as denoted in Figure 2.1 [11].

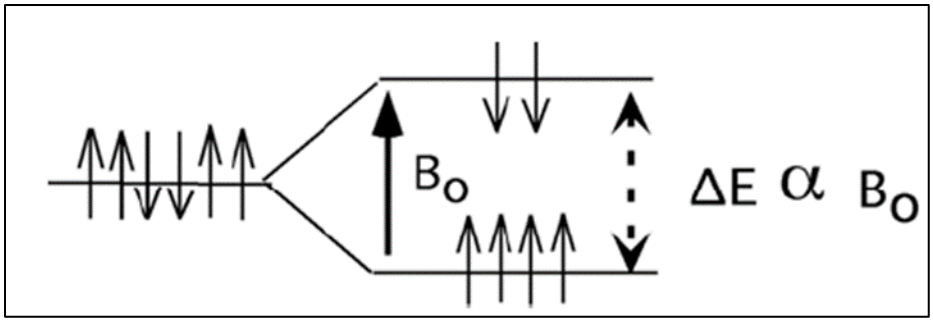

Figure 2.1- "The static magnetic field B_0 splits the energy of the spin parallel and spin anti parallel energy states. The energy gap between the two states increases with the field strength. The lower energy, spin parallel, state is preferentially occupied"- From Balcom et al. [11]

Crucially, the magnitude of the difference in the energy between the two states is on the same order of energy as electromagnetic radiation of radio wave frequencies. The energy required to cause an energy transition between the two energy states is proportional to the externally applied magnetic field B_0, and will correspond to radio waves of frequencies between tens and hundreds of MHz, depending on the magnitude of B_0 [11]. While in this state, there will also be some development of the magnetic moment in the x and y direction, but they will cancel each other out due to symmetry, leaving a net magnetic moment in the nucleus. When all the nuclei in each population of a sample are exposed to the same condition (i.e. the ^1H nuclei of water within the void structure of concrete) there will be a net magnetization M_0 of the sample, which is aligned with the magnetic field.

When a population of nuclei is in this coherent state aligned with the external magnetic field, it can be manipulated using the electromagnetic radiation of the appropriate radio frequencies. Essentially, by shooting Radio Frequency (RF) photons of the correct energy at the population in this aligned state, the net magnetic moment M_0 can be 'knocked off' the alignment with the z direction, causing it to rotate in the x-y plane. This rotation about the z-axis will cause an induced

magnetic moment with magnitude M_{xy} which will, due to Faraday's law, induce a voltage within the RF emitter. It is this induced voltage that is the detected signal and that forms the basis of the magnetic resonance imaging techniques in use for this research program [11]. This signal from the induced voltage caused by the transverse magnetic moment spinning is referred to as the Free Induction Decay (FID) signal, which is a time domain signal that can be converted into the frequency domain spectrum via a Fast Fourier transform.

This off-axis rotation is not in equilibrium due to the applied external magnetic field B_0, and the spin will return to the parallel state over time in an exponential fashion. The magnitude of the magnetic moment in the z direction during this return to the equilibrium state can be described by Equation 2.9 [11].

$$M_z = M_0(1 - e^{\frac{-t}{T_1}})$$

Equation 2.9- Exponential recovery of magnetic moment in Z direction from Balcom et al. [11]

Where M_0 is the magnitude of the magnetic moment in the equilibrium position, t is the time after the RF pulse which caused the non-equilibrium state (here taken to be at a 90° angle from the z-axis), and T_1 is a time constant for the nuclei or population of nuclei. Since the signal which is measured by the NMR equipment is the magnitude of the transverse magnetic moment of these nuclei or population of nuclei M_{xy}, it is useful to look at the decay signal of this magnetic moment as well, shown in Equation 2.10:

$$M_{xy} = M_0 e^{-\frac{t}{T_2*}}$$

Equation 2.10- Transverse magnetic decay, from Balcom et al. [11]

In Equation 2.10, T_2^* is a constant referred to as the spin-spin relaxation time, and the magnitude of this parameter will differ depending on the conditions of the population nuclei. Since the transverse axis has nuclei spinning about the z-axis in the x-y plane, individual nuclei will interact with their neighbors electromagnetically, leading to some partial signal cancellation that will affect the net magnitude of the population signal M_{xy}. T_2^* will also be affected by the specific condition of the nuclei in the sample so, for example, nuclei which are in molecules tightly bound up within a crystalline structure will have a different T_2^* magnitude than for nuclei which are present in larger void spaces such as capillary pores. The T_1 an T_2^* signals can also be affected by the kinematics of the population, so temperature, viscosity and phase will all affect these values [11].

Due to the sensitivity of this T_2^* measurement to the surrounding environment in which the nuclei are located, the T_2^* measurement has been used to make an approximate measurement of the pore size distribution in cement systems. Halpern *et al.* could distinguish between the relaxation times of water that was tightly bound between hydrates and water that was free to move through the voids of the concrete because of their different relaxation times [12]. By tracking the evolution of these two signals, Halpern *et al.* documented a simultaneous decrease in free water and increase in total surface area, as seen in Figure 2.2.

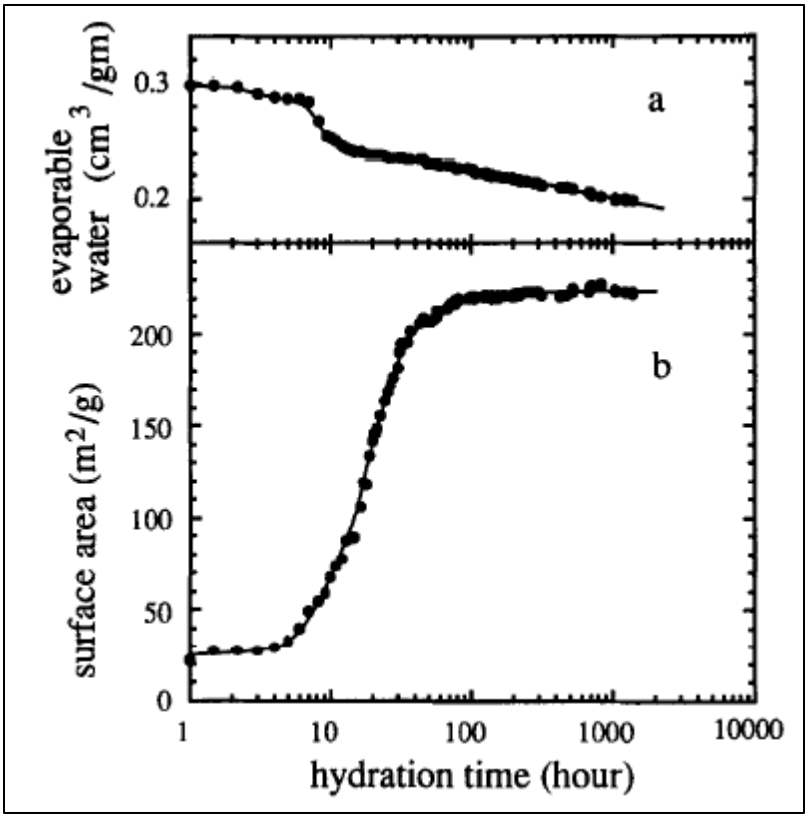

Figure 2.2-"Water consumed(a), and total surface area, S_0(b), as a function of hydration time expressed in terms of the weight of the initial dry cement powder" From Halpern et al. [12]

Others have used a mapping of T_1 values to look at the evolution of hydrating cement paste pore sizes. Plassais *et al.* [13] documented a 'bifurcation' of T_1 values as a function of curing time. These two different relaxation times were hypothesized to be belonging to non-confined, or 'free' water which would participate in mass transport through larger pores, and protons within water that were confined due to adsorption from hydration by-products in much smaller pores.

Other, independent systems of measuring the distribution of pore sizes such as using mercury intrusion porosimetry have shown that there is a wide distribution of pore sizes from the micron to the nanometer scale [15]. Kumar and Bhattacharjee divide these into roughly four types, corresponding to gel pores between cement hydrates on the nanometer scale, capillary

'mesopores' which range from the nanoscopic to microscopic scale, as well as entrained air bubbles on the micron scale and larger entrapped air due to inadequate compaction [14]. The different lengths of the T_1 and T_2* relaxation times as documented by Halpern, Plassais and others correspond to the nuclei of water populations within the nano and meso sized pores.

2.2.2. Spatial imaging with NMR techniques

The basis of the NMR spatial imaging technique involves changing the time domain signal into a frequency domain signal via Fast Fourier transform. The common practice within NMR is to use 'k-space', which is a mathematical formalism that allows for analysis with units of k, in cm^{-1}. Thus, the Fourier transform will produce results in cm. The variable is introduced in Equation 2.11 [11].

$$k_z = \frac{\gamma G_z t}{2\pi}$$

Equation 2.11- Definition of the 'k-space' variable. From Balcom et al. [11]

Where *G* is the magnetic field gradient in the z-direction at position z, γ is the gyromagnetic ratio in radians·s^{-1}·T^{-1} and *t* is the time in seconds after the RF pulse. The whole of k-space is in a rotating reference frame at the Lamour frequency, which is the frequency at which the magnetic moment rotates about the z-axis when it is knocked out of alignment by the Radio Frequency pulse. If linear distribution along the z-axis of nuclei being imaged is represented by the function ρ(z), the NMR signal can be formulated as Equation 2.12: [11]

$$\mathrm{S}(\mathrm{k_z}) = \int \rho(\mathrm{z}) e^{\mathrm{i}2\pi \mathrm{k_z}\,\mathrm{z}}\,\mathrm{dz}$$

Equation 2.12- NMR signal definition using k. From Balcom et al. [11]

To determine the distribution of nuclei as a function of length ρ(z), the Fast Fourier transform is performed with the variable k_z, resulting in Equation 2.13

$$\rho(z) = \int S(k_z) e^{-i2\pi k_z z}\, dk_z$$

Equation 2.13- Nuclei spatial function from fast Fourier transform in k space. From Balcom et al. [11]

With the definition of k, it is important to note that k-space analysis is valid for changes in time with a constant field gradient, as well as for a constant time in a changing field gradient. Techniques which sample the signal as a function of time are referred to as frequency encoding, and techniques which vary the magnetic gradient with constant time are called phase encoding techniques [11]. Varying both the time and gradient is also possible, and is a commonly used method of MRI imaging called spin warp imaging. However, this class of technique is not applicable to concrete materials because the total encoding time required to produce the required sequence of RF pulses is much longer than the T_1 and T_2* times of ^{1}H nuclei found in cement systems.

One relevant class of imaging techniques for cement imaging is the Single-Point Imaging (SPI) technique, which is a phase encoding technique. A single, broad band RF pulse is applied to a ^{1}H population in the presence of constant magnetic field gradients in all thee direction. This RF pulse causes the magnetic moments of the ^{1}H nuclei to be knocked off of the alignment with the magnetic field in the z direction, and the magnetic moments rotate about the z-axis at the Lamour frequency. This creates the free induction decay signal in the ^{1}H, which decays exponentially at the rate T_2*. After the encoding time t_p, a single data point of this induction signal is recorded. The whole SPI method is schematically outlined in Figure 2.3 [11].

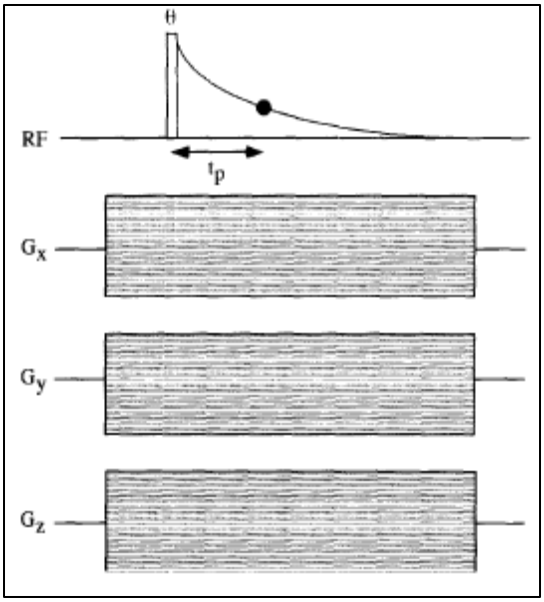

Figure 2.3- "Schematic description of the Single-Point Imaging (SPI) method."- From Balcom et al. [11]

Thus, the magnitude of the signal is proportional to the magnetic moment of the ^1H nuclei. This local signal intensity can be formulated as Equation 2.14

$$S = M_0 e^{\frac{-t_p}{T_2*}} \left(\frac{1 - e^{-\frac{TR}{T_1}}}{1 - cos\ \theta\ e^{-\frac{TR}{T_1}}} \right) sin\theta$$

Equation 2.14- Sample magnitude in the SPI method. From Balcom et al. [11]

The angle θ is the off-axis rotation angle of the sample magnetization, which is assumed constant throughout the sample, and *TR* is the time in between successive RF pulses. As the equation shows, if TR is sufficiently longer than T_1, Equation 2.14 will reduce to the comparatively simpler Equation 2.15

$$S = M_0 e^{\frac{-t_p}{T_2*}} sin\theta$$

Equation 2.15- Local signal intensity for SPI method, simplified with sufficiently long TR time. From Balcom et al. [11].

A similar technique to SPI is the Single Point Ramped Imaging with T_1 Enhancement (SPRITE) method, which is also a phase encoding technique. The key difference between SPI and SPRITE is that the magnetic field gradient G_z is varied in between successive RF pulses (hence the 'ramping'). In general, SPRITE is performed much quicker than a comparable SPI technique, due to differences in the application of the magnetic field gradients. Figure 2.4 shows the comparative scheme for the SPRITE technique, from Balcom *et al*. [11]

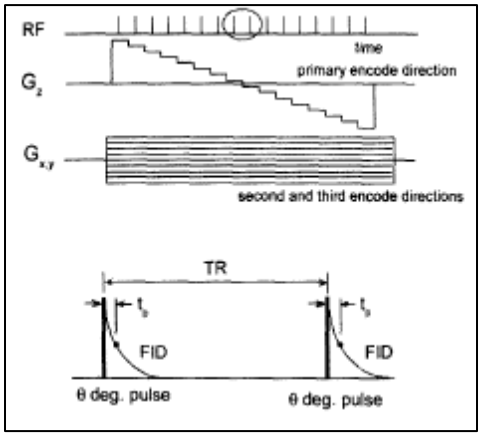

Figure 2.4- "Schematic description of the Single-Point Ramped Imaging with T_1 Enhancement (SPRITE) imaging method. The primary phase-encode gradient, G_z in this case, is stepped with an RF excitation at each gradient level. Sixty-four steps, each on the order of 1 ms duration are typically employed. The second and third gradients, G_x and G_y, are amplitude cycled to phase encode the X and Y dimensions. (b) A magnification of two pulse-encode events (circled) from (a). A single point on the MR signal is recorded at an encoding time t_p after each RF pulse. A short duration, low-flip angle (θ) pulse ensures a uniform excitation of spins throughout the specimen. The RF pulses are applied at intervals of TR" From Balcom et al. [11]

The SPRITE image signal has the exact same formulation as Equation 2.15. When combined with the rapid acquisition time of the signal and relative ease of signal analysis, the SPRITE method has been used to study the ^1H nuclei in a variety of cement systems under different conditions. The SPRITE method is different from the SPI method in that it can perform imaging in 2 and 3 dimensions by varying the direction of the ramping magnetic field gradient direction.

2.2.3. Applications to concrete durability and water mass transport

The ability to directly image the location of various nuclei within cement systems has many implications with regards to the study of mass transport of water in concretes, especially for durability issues related to mass transport. The SPI method has been used to examine the evolution of the pore structure and mass transport through hydrating cement systems for many years. Beyea *et al.* used SPI to investigate the drying behavior of white portland cements and concrete [16]. The researchers let cylindrical samples of 0.40 and 0.60 w/c cure for 90 days in moist curing conditions before sealing all the faces except one and allowing them to dry for up to 90 days. The drying profiles obtained from this procedure are reproduced in Figure 2.5. They show a steady gradient of water evaporation from the face exposed to the atmosphere, which they correlated directly to the evaporable water content due to simultaneous gravimetric mass measurements. The shrinkage cracking associated with this drying was confirmed both visually, with macroscopic sized cracks being observed on the paste samples after 90 days, but also using T_1 mapping. There was a slight decrease in the T_1 parameter which grew larger as a function of drying time. This evolution of the T_1 parameter was more prominent in the larger pore structure of the 0.6 w/c sample, and this evolution was correlated with changes in the mass transport rate that was hypothesized to be additional capillary porosity caused by microcracks. Essentially, Beyea *et al.* observed an initial increase in water transport properties at early ages of drying which corresponded to the presence of microcracks. The addition of aggregates, and therefore additional weaker paste-aggregate interface zones, exacerbated this behavior [16]

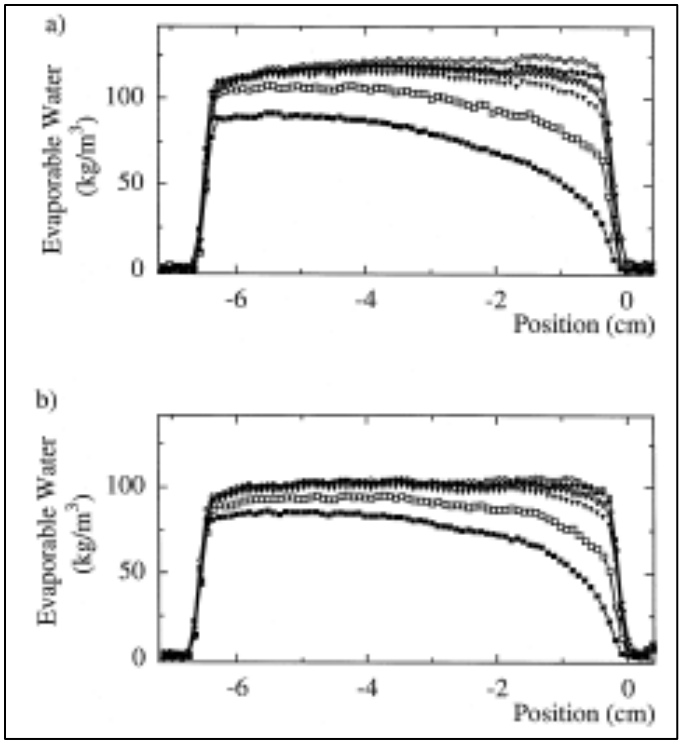

Figure 2.5- "Drying profiles of cement samples with (a) w/c =0.6 and (b) w/c =0.4 following a moist cure period of 90 days: profiles shown for 0, 1, 3, 7, 28 and 90 days of drying. The MN(II)-doped water calibration standard used, is not shown. Drying occurs from the open face (0 cm) due to a mixture of capillary flow and diffusion. The profiles were obtained using SPI with a t_p of 130 µs." From Beyea et al. [16]

The effect of relative humidity on these drying processes was additionally investigated by Beyea *et al.*, with an emphasis on the increase in transport properties due to the drying microcracks [17]. Figure 2.6 shows the inverse of T_1 measurements from two different samples from Beyea *et al*.

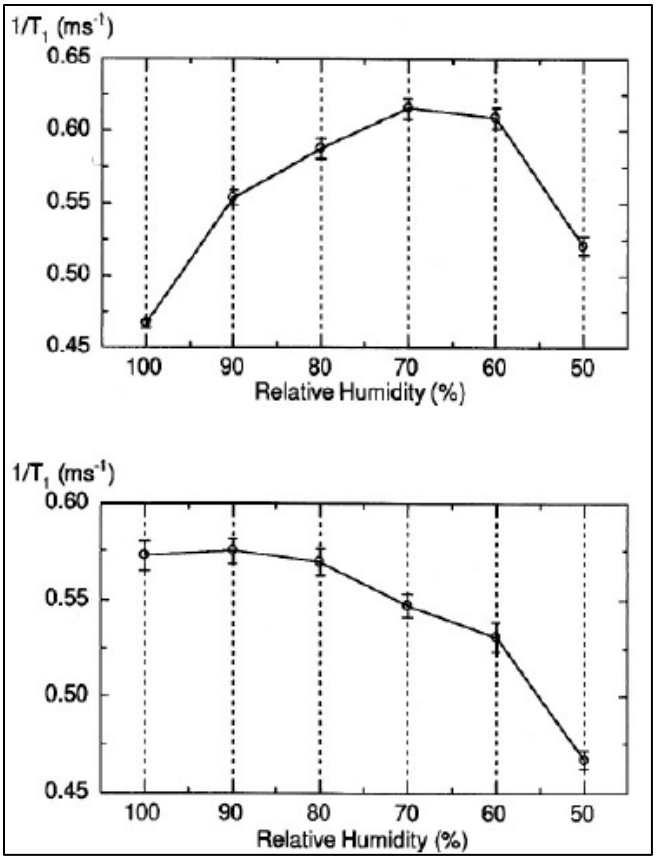

Figure 2.6- "Plot of average $1/T_1$ (ms^{-1}) versus relative humidity (%) for the average of three mortar disks with a w/c ratio of (a) 0.6 and (b) 0.4, and an initial hydration period of 90 days. Results shown are the average of the three measurements, with error bars given as the average deviation"- From Beyea et al. [17]

As Figure 2.6 shows, there is anomalous behavior in terms of the T_1 values for relative humidities below 60% in the higher porosity sample. The meaning of this decrease was hypothesized by Beyea *et al*. to correspond to the additional microcracks which affected the spin-lattice relaxation (T_1) value, which is correlated with the surface area to volume ratio of the water occupied regions. For low relative humidify conditions and high porosity, there was more shrinkage cracking that lead to additional transport pathways becoming available, which was detected by both T_1 mapping as well as the average saturation levels of the drying samples at different relative humidities [17].

Others have examined the evolution of pore water due to curing processes. Bohris *et al.* examined the curing behavior of different w/c pastes and different curing conditions, including underwater curing, sealed curing and open curing [18]. They directly imaged the evolution of the water within the volume as it was consumed during hydration processes. Subsequently, the different samples were exposed to a 1D sorptive flow process and the differences between the curing conditions and w/c was characterized. Figure 2.7 shows the subsequent 1D sorptive moisture content profiles for these three different curing conditions at different times after initial exposure

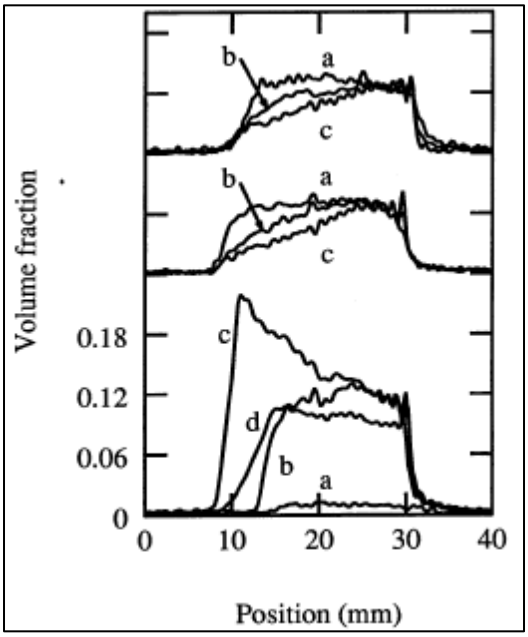

Figure 2.7- "Capillary water uptake profiles into 96-day-old 0.5 w/c ratio samples. The basal source of water (wet sponge, removed for imaging) is to the right, and the top of each sample is left open. Upper traces show sealed cure after 0 (a), 1 (b), and 7 (c) days of exposure to water. Middle traces show underwater cure after 0 (a), 1 (b), and 7 (c) days of exposure to water. Bottom traces show open cure after 0 (a), 1 (b) and 6 (c) h and 7 days (d) of exposure to water. In each case, the last trace represents a dynamic equilibrium" – From Bohris et al. [18].

Interestingly, the open cured sample shows a remarkably different sorptive flow behavior than either the sealed cure or underwater cured specimens for this w/c. Bohris *et al.* believed that this

inverse concentration gradient seen in Figure 2.7 on the open cure specimen was due to hydration causing a densification of the pore structure after it had initially dried out due to an open cure. This had the net effect of decreasing the net pore volume and creating a profile more in line with the other curing methods [18]. These drying profiles are very similar to those observed by other groups, such as Beyea *et al.* on samples with very similar curing and conditioning [19].

Leech *et al.* demonstrated the use of SPI profiles from samples undergoing a sorptive flow process to estimate the hydraulic diffusivity of the samples [20]. They used least-squares fitting after a Boltzmann transformation technique to fit the observed moisture profiles to both exponential and power law functions of diffusivity, and therefore derive experimentally determined diffusivity parameters from a simple sorptivity test.

Cano-Barrita *et al.* obtained profiles by SPI to simulate the effect of curing and drying on samples exposed to a hot, dry climate for both high performance and ordinary concretes [21]. They compared an immediate exposure to a severe condition of 38°C and 40% RH with samples which had been moist cured for 28 days. They found that, for high performance concretes incorporating silica fume, additional curing did not significantly affect the moisture loss, but this was not the case for ordinary concretes. Cano-Barrita *et al.* applied the Boltzmann transform method of estimating the hydraulic diffusivity from these profiles, and derived relationships for moisture diffusivity as a function of water content for the different mixtures examined and curing conditions used. There was a marked difference between the long-term curing behavior and the short-term curing regimes, with the increased curing time and higher performance mixtures

exhibiting a greatly decreased diffusivity behavior at all moisture contents then when compared to the short curing.

The effect of phase transitions of water during freeze-thaw has also been characterized with MRI methods. Prado *et al.* used SPRITE along with a temperature control system to image concrete samples in a range of temperatures between +12 °C and -50 °C, with a profile being obtained at approximately every 0.5 °C step [22]. They found a decrease in the T_2* time for both pastes and mortars, with the values at-50 °C being about 40% of what they were at 12 °C. However, they did not observe a significant change in the T_2* value associated with a phase transition, indicating that there was some amount of non-frozen water present even at -50 °C. The relaxation time of frozen water is considerably shorter than for liquid water, and this behavior has the net effect of making frozen water invisible to imaging with SPRITE and SPI methods.

Prado *et al.* similarly looked at the T_2* evolution during a thawing event from -50 °C to above 0 °C [23]. They found a T_2* dependence which agreed with their previous work, which seemed to correspond with the unfrozen water remaining in the capillary pores [21]. At temperatures above zero, the T_2* change was found to be minimally dependant on the temperature, showing that the phase transition from liquid to solid has a strong influence on the T_2* behavior.

Balcom *et al.* used a 2D SPRITE method to examine this T_2* change under a phase transition to image the propagation of a freezing front as a mortar sample dropped below zero [11]. Figure 2.8 shows a 1-day cured mortar specimen at different times after exposure to a sub-zero temperature condition.

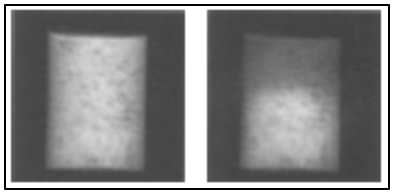

Figure 2.8- "2D Spiral SPRITE images of a mortar cylinder insulated on the sides and bottom, with the top face exposed to cold nitrogen vapor, -20°C. The image at right was acquired 10 minutes after the image at left. The cylinder examined had w/c=0.5, 1 day moist cure with a diameter of 3.3 cm. The images clearly show the presence of a freezing front which propagates through the material. The velocity directly depends on the thermal properties of the mortar. More extensively cured samples do not reveal a sharp moving boundary in similar experiments" From Balcom et al. [11]

2.3. Tension testing

2.3.1. Direct tension tests

There are a few varieties of direct tension testing in use, all of which involve applying a mechanical force directly to a concrete specimen and measuring the effective stress required to induce a failure. There are some variations in the exact mechanism of load application; mechanical grips or clamps, chemical adhesives, or embedded steel reinforcement. One of the earliest demonstrations of this direct tension testing was performed by Gonnerman and Shuman in 1928 [24], where the ends of a uniaxial test specimen were gripped via compression and friction, and a net stress was applied to the uniaxial test coupon through this mechanical connection. A key issue with this type of mechanical testing is the effect of the mechanical compressive stress on the material, since it can cause damage via crushing and may affect the net tensile capacity of the material [25].

A study on asphalt cement systems by Bolzan *et al.* from the University of Austin found that the repeatability of these types of direct tension tests are not particularly high. They reported testing difficulties resulting from the alignment of the stress application with the test specimens, which

created eccentric loading conditions that significantly decreased the net tensile capacity of the material [26]. They also found a non-trivial portion of the observed test specimens had failures in the region directly affected by the higher localized stress concentrations from the mechanical grips.

In general, it is difficult to correctly position tension test specimens to render them free from eccentric tension loading or localized mechanical damage from grip friction forces. This experimental difficulty makes the direct tension test method of tension testing largely unsuitable for practical evaluation of tension resistance given the large amount of uncertainty that results from these complications. This is the main reason that direct tension tests of this nature are not recognized as ASTM standards.

2.3.2. Flexural tests

However, ASTM has recognized two methods of creating a tensile loading condition indirectly by way of flexural load application, in ASTM C 293 and ASTM C78 [27,28]. These test methods use a rectangular prism specifically cast for the test method. The two standards differ mainly in the locations of loading points and the resulting moment distribution, but both test methods result in a loading condition that produces a maximum tensile stress on the bottom face of the beam, as seen in Figure 2.9. The test methods apply a point load either in one or two locations depending on whether it is center-point or third-point. The main difference between these two methods is that the maximum bending moment is applied only on a single plane directly beneath the load application in the case of center-point loading, and over a region between the two load points in the case of third-point loading. In either case, a tensile crack on the bottom face results

from this bending moment, and beam theory is applied to the moment distribution in order to derive the magnitude of the maximum tensile stresses at failure.

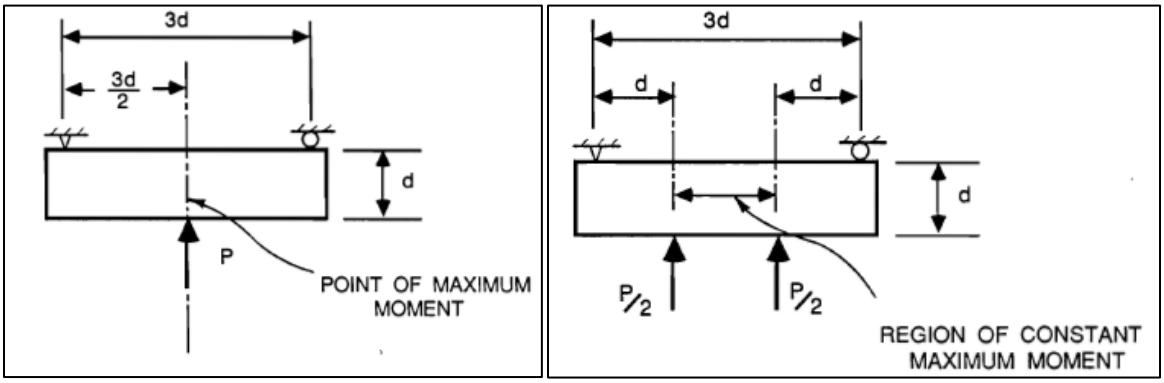

a) b)

Figure 2.9- "Schematic representation of test set-up for (a) center point loading and (b) third point loading" – From Carrasquillo and Carrasquillo [29].

One issue with these tests is that the limited volume of the concrete exposed to maximum moment could lead to an overestimation of the true tensile capacity of the material. In an investigation of different flexural loading applications at the University of Texas at Austin, it was found that the third-point loading configuration resulted in rupture stresses that were, on average, 85% of those obtained on identical specimens tested in one-point loading [29]. The study also showed that larger sized specimens failed at a lower rupture stress, a phenomenon known as 'size-effect'. The size effect essentially states that larger specimens will fail at a lower stress due to an increased probability of a critical weaknesses in the larger volume, particularly in larger members which will generally be subject to a larger stress [30].

2.3.3. Splitting tension test

A different ASTM test which is the most common currently accepted method of determining tension strength of concrete, is the splitting Brazilian or splitting tension test ASTM C 496 [31].

The splitting tension, or Brazilian test was invented in the 1940s and uses an ordinary concrete cylinder as the test specimen [32]. A line load is applied parallel to the long axis of the cylinder through its center, so that it is being compressed along a single axis which passes through the centre of the volume, as depicted in Figure 2.10 [33].

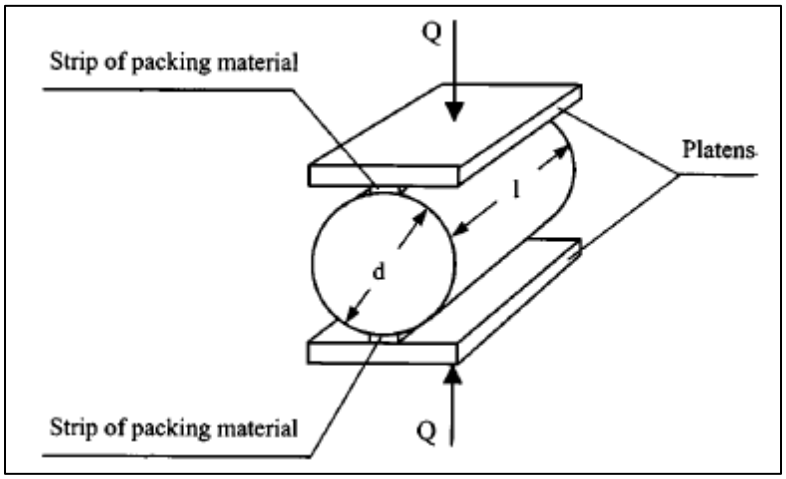

Figure 2.10- "Brazilian concrete splitting tension test" From Lin and Wood [33]

Based on linear elastic theory of materials, this loading configuration results in a stress distribution as depicted in Figure 2.11 [33,34]

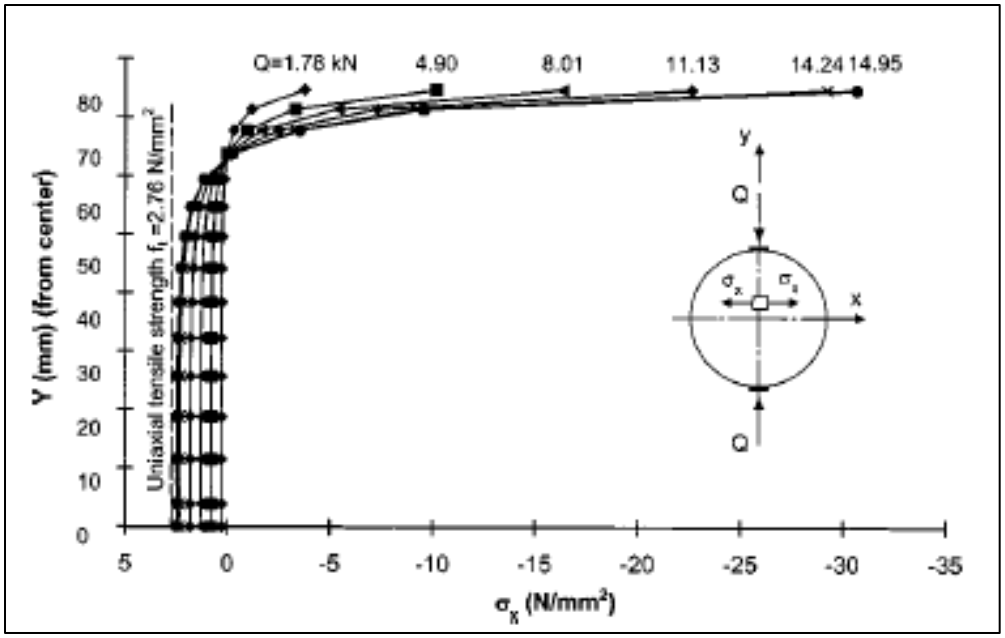

Figure 2.11- "Horizontal stress, σ_x, distributions along vertical diameter of cylinder during loading up to failure", from Lin and Wood [33]

As Figure 2.11 shows, there is a large plane concurrent with the centroid of the cylinder for which there is a roughly uniform uniaxial tensile stress perpendicular to the applied stress *Q*. The magnitude of this tensile stress can be calculated from linear elastic material behavior as shown in Equation 2.16.

$$f_t' = \frac{2Q}{\pi l d}$$

Equation 2.16- Splitting tension stress magnitude [32]

Where *Q* is the force applied, *l* is the length of the cylinder, and *d* is the depth. However, this calculated uniaxial tension force is not the true distribution of stress states as depicted in Figure 2.11. The region directly adjacent to the load application exhibits large compressive stresses many times greater than the net tension stress, which could result in localized crushing that might precipitate tension cracking. The specific thickness of the loading strip which applies Q to the

cylinder has also been found to affect these peak compressive stress, with wider strips being generally correlated with lower measured tension stresses [33].

Splitting tension tests will generally measure tensile resistances higher than those obtained by direct tension methods but lower than those derived from the flexural loading methods [31]. This may be due to the limited region at which the peak tensile stress is applied, which is only on the plane concomitant with the loading plane. Due to the application of these peak stresses within a limited volume, the splitting test may overestimate the tensile strength of the material, especially if a critical flaw does not coincide with this peak stress volume. Hence, if the concrete sample is susceptible to cracking due to material defects or durability issues, the splitting tension test would not necessarily detect these issues due to the nature of the test [25,35].

2.3.4. Other indirect tension tests

There have been other attempts by researchers to create a tension test which does not suffer from the experimental complications of direct tension testing or the systematic overestimation of tensile strength from the splitting tension or flexural tension tests. Zi *et al.* described an indirect biaxial flexure test (BFT) method that, like the flexural systems, that incorporates a biaxial distribution of the bending moment [36]. The test specimen and uniform principal stresses on the bottom face of the specimen are depicted in Figure 2.12 [36].

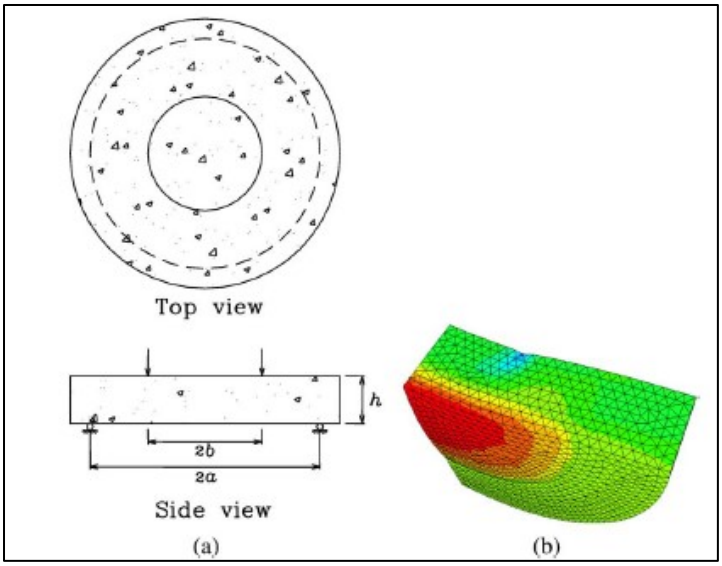

Figure 2.12- "(a) The specimen for the biaxial flexure (BFT) method and (b) the uniform principal stress on the bottom surface" From Zi et al. [36]

The test consists of a circular cast ring of concrete or other brittle material, which is bearing on two rollers. A bearing ring applies an axisymmetric stress on a smaller cross section of the ring, which results in a flexural moment which is axially symmetric. This loading condition results in a peak tensile stress from the bending moment located in the ring section underneath the bearing plate at the extreme tensile face of the disc. Plate elastic theory was applied to this condition, and the peak stress on the bottom face was calculated as depicted in Equation 2.17

$$\sigma = \frac{3}{4\pi h^2}\left\{(1-v)\left[1-\left(\frac{b}{a}\right)^2\right]-2(1+v)\log\left(\frac{b}{a}\right)\right\}P$$

Equation 2.17- Peak tension stress on bottom face in the disc, from Zi et al. [36]

Where *h* is the height of the sample disc, *b* is the radius of the bearing disc, *a* is the radius of the sample disc, *v* is Poisson's ratio, and *P* is the force applied to the bearing disc.

They found that the BFT results were on average, higher than the tension results from uniaxial tests, and with a higher standard deviation between test results [36]. These results were in line

with those from uniaxial flexural tests, which also tend to be higher on average than uniaxial tension tests.

Cantillo and Guzman described an indirect tension test that was performed by pressurizing water inside a hollow cylinder of concrete [37]. The test setup as well as the radial and tangential stresses that develop within this hollow cylinder are depicted in Figure 2.13.

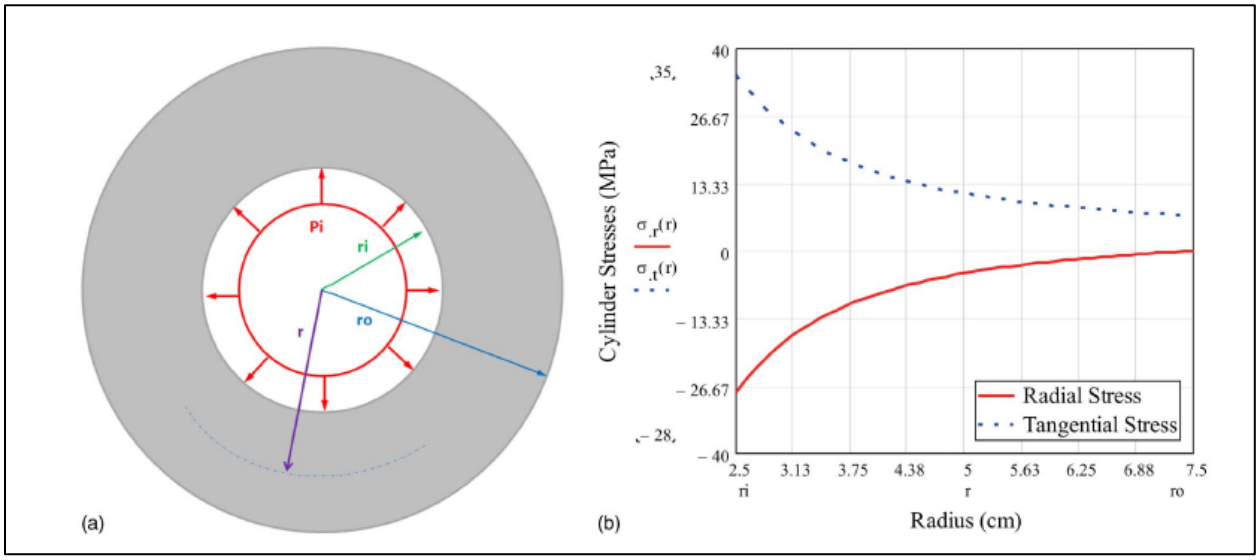

Figure 2.13- "(a) Geometrical parameters for Lame's Equations; (b) stress distribution through a cylinder wall subjected to Pi=28 MPa" From Cantillo and Guzman [37]

This stress state has the two boundary conditions at the interior wall of the cylinder being equal to the fluid pressure of the water, and the exterior wall being zero. Thus, by applying Lame's equations, Cantillo and Guzman calculated the theoretical stress tangential to the load using Equation 2.18 [37]

$$\sigma_\theta = \frac{P_i(r_0^2 + r_i^2)}{r_0^2 - r_i^2}$$

Equation 2.18- Tangential stress in fluid pressure test, from Cantillo and Guzman [37]

Where P_i is the pressure of the fluid, r_0 is the outer diameter of the cylinder and r_i is the inner diameter for the cylinder. For the geometry used in the testing system, they found a simple equation where the calculated maximum tensile stress was equal to 1.25 P_i. Cantillo and Guzman performed tests on different w/c mixtures and correlated the results with splitting tension and compressive strength tests. The fluid pressure test produced tension resistance values at about 10% of the compressive strength, and were a 17% greater in magnitude than results from the splitting tension test [37].

2.3.5. Pressure tension test

2.3.5.1. Pressure tension effect

The behavior of materials under high pressure in biaxial loading conditions has long been investigated by engineers. Bridgeman performed various experiments in the 1930s and found what was then considered to be a paradoxical result; an apparent tension failure occurred transverse to the applied biaxial loading direction despite there being no direct loading in that direction [38]. Depending on the material characteristics, ductile materials such as metals would produce a necking effect as one might expect from a biaxial load, but brittle materials such as glass failed in 'paradoxical manner'.

It was not until the 1970s that this paradoxical behavior was investigated in detail with respect to concrete materials. Clayton and Grimer performed a series of novel experiments to examine this 'pressure tension effect' [39]. The basic configuration of their primary test chamber is found in Figure 2.14.

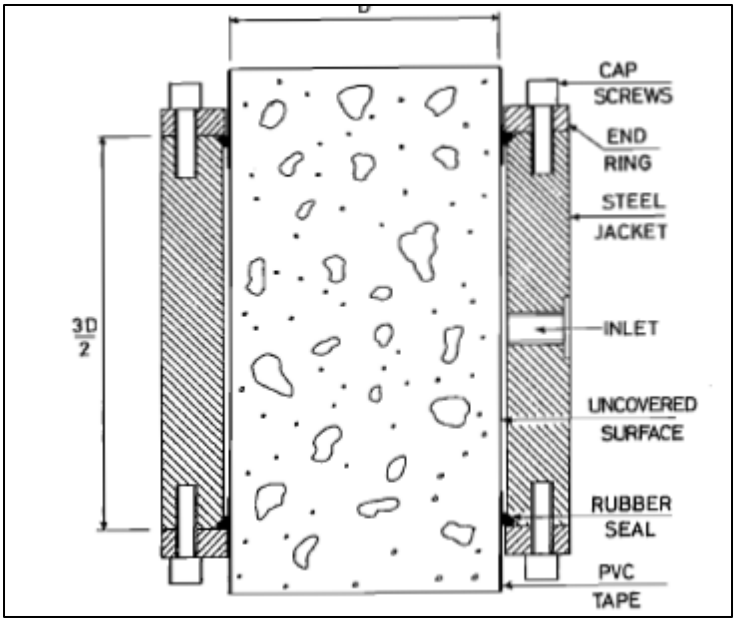

Figure 2.14- "Water pressure experiment details" From Clayton and Grimer [39]

The basic test configuration was a cylindrical steel jacket in which a concrete specimen could be fitted. At either end of the jacket, two sealing end rings provided a confinement pressure by compressing rubber sealant onto the specimens. A PVC tape was adhered to the ends of the concrete specimen to provide better sealant with the rubber seals. In this configuration, the ends of the concrete cylinder were exposed to the atmosphere and a differential pressure could be applied to the curved surface of the concrete cylinder, resulting in a biaxial loading condition. Clayton and Grimer used both water and a nitrogen gas as the medium of load application for their experiments [39].

The explanation that Clayton and Grimer arrived on to explain this 'paradoxical' tension failure behavior in this configuration was related to the porous nature of the concrete. They termed this analysis the 'diphase approach', and it simply reflects that concrete has both a solid phase and a fluid phase which is related to the permeable porosity of the material. All of the connected pores

and voids in concrete can be filled with either a liquid, or gas, or combination of the two depending on the moisture content, and this interconnected system is referred to as the 'fluid'. The key to the diphase approach is that the fluid phase responds differently to an applied pressure than a solid phase, where the fluid will develop a triaxial 'hydrostatic' pressure whereas this is not true of the solid phase. Thus, when considering the biaxial loading condition of a diphase material, Clayton and Grimer proposed the net stress state to be of that found in Figure 2.15 [39].

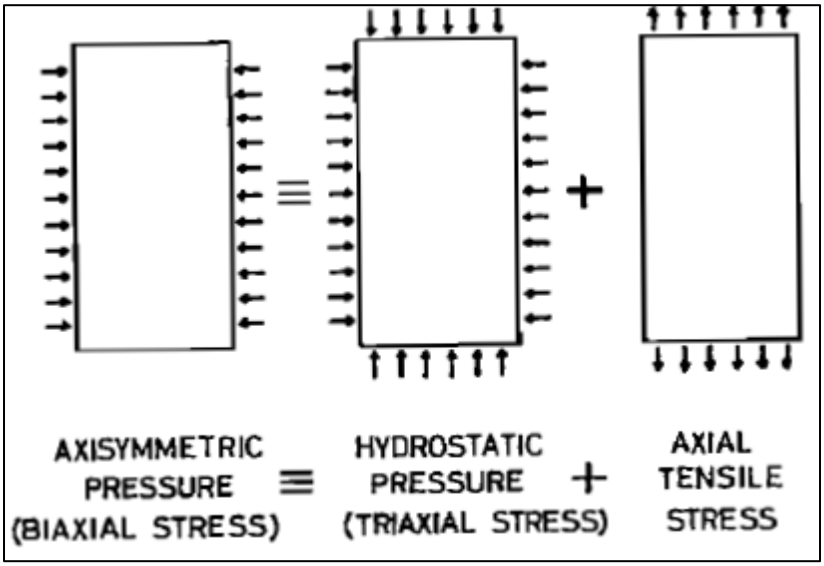

Figure 2.15- Pressure tension effect. From Clayton and Grimer [38]

This explanation solves the supposed paradox, as the net axial tensile stress develops perpendicular to the applied biaxial stress as a direct result of the hydrostatic pressure of the fluid phase. In other words, the fluid develops a hydrostatic pressure because of the biaxial stress applied to the exterior of the concrete cylinder. However, since there is no compression in the z-direction, the fluid pushes on the solid phase at a magnitude equal to the applied biaxial stress, creating an equivalent tensile stress despite no direct load application [39].

Clayton and Grimer demonstrated the validity of this approach with a modified direct tension test carried out within a water pressure chamber, as depicted in Figure 2.16. A concrete cylinder is suspended within a water pressure vessel, and two end caps are fitted at either end. Critically, no mechanical clamps or adhesives are used to keep the caps on the concrete sample, with the only pressure coming from the hydrostatic pressure of the water.

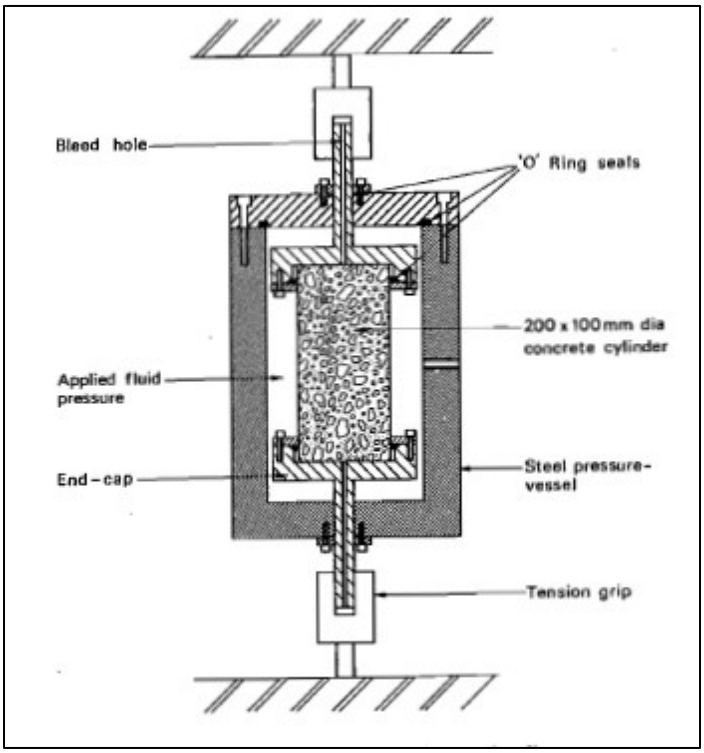

Figure 2.16- "Demonstration experiment details". From Clayton and Grimer [39]

The experiment consists of pressurizing the water to a point which would cause a failure in the pressure tension configuration. Tension forces are then applied to the end caps to pull them off the ends of the cylinder, and the magnitude of the force required to do so is compared. Clayton and Grimer found that the specimens failed in a transverse manner similar to that seen in tension tests as they decreased the external stress on the solid phase, which was an identical condition to increasing the internal stress on the solid phase [39].

The parameters of the loading medium were also investigated by Clayton and Grimer. They found that pressure tension specimens tested with water as the loading medium failed at a higher stress than those tested with nitrogen gas. Figure 2.17 shows the effect of the two different loading mediums as a function of load rate, with the water having a higher failure value than the same mixture tested with nitrogen [40]

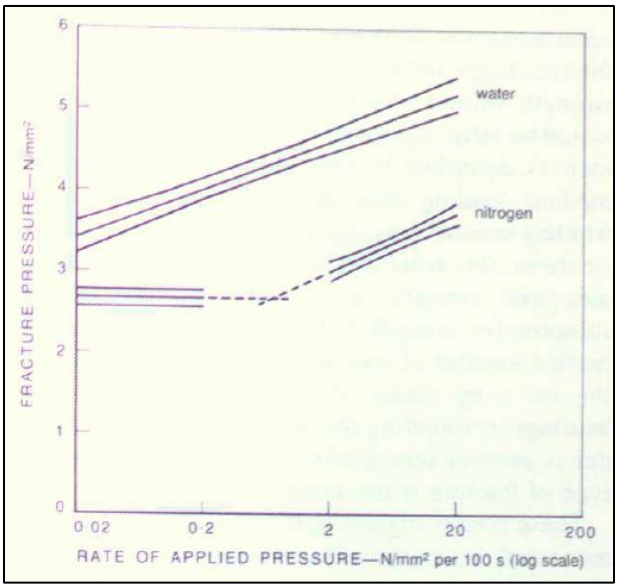

Figure 2.17- "Summary of fluid-pressure test results" From Clayton [40]

They attributed this difference to the fact that the gas can more easily transmit the pressures as compared to water [39]. Clayton and Grimer also examined a solid material which transferred a biaxial stress to the concrete cylinder, which was hypothesized to be less effective at transferring the stresses to the internal fluid phase, by using ball bearings. The failure due to this biaxial loading with ball bearings was found to be 2-3 times higher than that found with water, though the fracture pattern found with ball bearings was identical to the tension failure. Langan and Garas used wire winding to apply biaxial stresses on similar cylinders, and they found tension failures at a pressure approaching half of the compressive strength of the mixture [41].

Clayton and Grimer further validated this indirect axial tension effect on the solid phase by embedding longitudinal strain gauges in the concrete specimens undergoing pressure tension testing and detected an axial strain on the solid material. They also performed pressure tension tests with the ends of the concrete cylinder in an axial compression machine, and by varying the rates of both the applied fluid pressure and axial compression they could create conditions somewhere between a biaxial and triaxial condition. If the rate of loading in the fluid phase was higher than the rate of loading from the compression machine, they found axial elongation via the strain gauges which indicates tension on the solid phase [39,42].

2.3.5.2. Boundary conditions

Uno *et al.* performed a variety of different tests to further explore the pressure tension system in more analytical detail, by examining the boundary conditions, axial strain response and failure mechanism using modern crack theory [43,44]. Using solid mechanics assumptions, they demonstrated that the restraining force of the O-ring on the pressure specimen was equal to about 4% of the gas pressure, which was considered negligible. Uno *et al.* then cast several standard concrete cylinders with both external and embedded strain gauges, as depicted in Figure 2.18. They found that there was no detectable difference between the internal and external strain gauge measurements, demonstrating that the types of loading eccentricities typical of the direct tension methods are not present in the pressure tension configuration. In other words, insofar as could be discerned from strain gauges, the pressure tension configuration produces a uniform tension field that applies the same stress uniformly through the cross section of the material and creates a uniform strain response in the material.

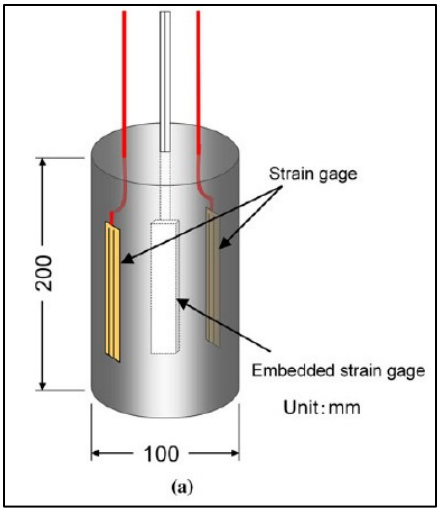

Figure 2.18- "Surface and internal strain gauges" -From Uno et al. [43]

Furthermore, they found that the axial strain response of the material agreed with Clayton and Grimer's 'diphase' concept of the material, and the initial modulus of elasticity was more correctly predicted by using effective stress theory [43].

2.3.5.3.Failure mechanism

Fujikake *et al.* looked at the failure mechanism in more detail using concrete samples that were hollow, as well as examining the fracture behavior using samples with notches of various depths and widths. The hollow concrete samples were very similar to the type of specimen used in Cantillo and Guzman's setup except the pressure was being applied from the exterior surface instead of from the interior surface [37]. However, the test results were markedly different between the two setups. All of the hollow specimens failed in a tensile crack perpendicular to the applied loading at a stress statistically indistinguishable from the solid cylinders. The typical failure modes are shown in Figure 2.19.

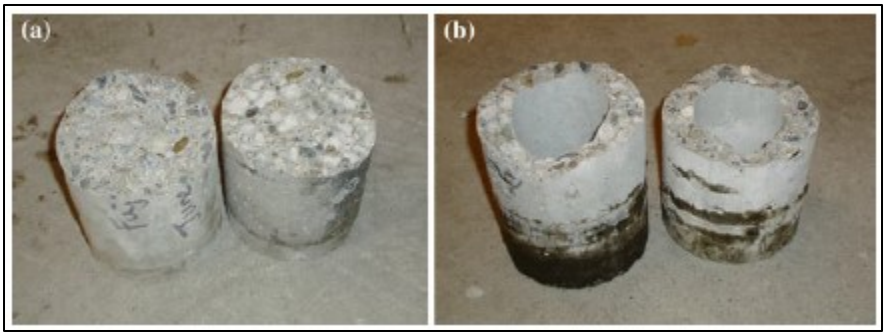

Figure 2.19- "Fracture plane in Mix-A a) solid specimen, b) hollow specimen"- From Fujikake et al. [44]

Interestingly, Fujikake *et al.* found a difference in terms of the failure mechanism for mixtures of different strengths. For the lower strength concrete, the failure planes in both the hollow and solid cylinders passed around the aggregate and through the ITZ, whereas the failure passed directly through the aggregates for the high strength mixture. This type of disparate behavior due to differences in the paste strength had been noted by Boyd *et al.* using pressure tension to examine paste-weakening durability mechanisms, for ASR and sulphate attack [25,45,46].

Fujikake *et al.* used linear elastic fracture mechanics (LEFM) to examine the failure behavior. They found that, if microcracks and flaws or cracks were smaller than the critical notch depth of the specimen, the failure of the section would be controlled by the tensile strength of the material. If the cracks were larger then this critical notch depth, then the ultimate tensile stress would be inversely proportional to the size of the cracks relative to the overall radius of the cylinder [44]. There was no significant relationship between the notch width and the failure pressure.

2.3.5.4. Moisture content

Uno *et al.* noted a distinct moisture content dependency on the pressure tension tests, with there being a difference between saturated specimens and partially saturated specimens which had

been dried [43]. The fully saturated specimens had tensile capacities which were measured at a greater magnitude than those from splitting tension tests, whereas the partially saturated specimens had failure values which were much more comparable to splitting tension. Uno *et al.* hypothesized that this difference in moisture content failure values was due to the differences in viscosity between nitrogen gas and water, with the compressed gas being more easily able to intrude into cracks and therefore apply their stress onto the crack faces.

Li performed a series of experiments using pressure tension in which moisture content was controlled via drying and a defined period of re-immersion [47]. The results were in contradiction to the moisture-content dependency found by Uno *et al.* [43]. Li found that the specimens which were drier (i.e. were exposed to a shorter period of immersion) exhibited a higher tensile strength compared to those which were 'wetter'. However, when Li examined the behavior of oven-dried specimens, the failure stress was significantly lower. Li attributed this to microstructural damage caused by the high temperatures associated with oven drying, leading to a weakening of the paste. However, the moisture content was not directly measured in any case by Li, nor was the load rate controlled, so there were large variances expected within this data and it is difficult to draw firm conclusions.

Lu performed a set of moisture content studies where the moisture content was controlled via timed drying of the specimens from a saturated moisture content, and found a weak linear relationship between the pressure tension failures and the moisture content which contradicted Li's observations, but was in line with those of Uno *et al.* [48]. Lu also had difficulty exactly measuring the moisture content of the samples, so the conclusions drawn were preliminary. Another part of Lu's work examined the variability inherent in the pressure tension test method,

and found that it was comparable to that of existing standard test methods. This low variability of the test method is corroborated by other studies as well [43, 47].

2.3.5.5. Durability studies

Pressure tension has been used to examine the effects of expansive processes due to durability issues on the tensile capacity of concretes. Bremner *et al.* looked at the effect of ASR on mechanical properties of concrete using both pressure tension and compressive strength [25]. They found that the tension-to-compression ratio significantly decreased because of ASR damage, within time periods that were shorter than those associated with the standard test method for detecting ASR.

ASR creates expansive damage in concrete because of soluble alkali ions within the pore water solution reacting with aggregates. This aggregate reaction creates a new material, called alkali-silica gel, which has a greater volume than the original reactants, causing an expansive stress to develop within the pores of the concrete system. This ASR gel will then imbibe water present in the pore system of concrete, expanding and causing further expansive stresses. These expansive stresses can exceed the tensile capacity of concrete, thereby causing cracks which increase the transport properties in a positive feedback loop [48,49]

The pressure tension machine has also been used to measure deterioration of the tensile capacity of concrete due to sulphate attack. Boyd *et al.* used the tensile capacity of concrete to examine the effect of ongoing sulphate attack, and the effect on the tensile to compressive strength ratio [45]. They found that pressure tension results could distinguish the ongoing sulphate attack at early ages. Further studies by Boyd *et al.* attempted to correlate the tension damage due to

sulphate attack in both pressure tension and splitting tension with non-destructive test methods [51]. Later testing by Hartell *et al.* looked at the effect of sulphate attack due to an evaporative transport condition on pressure tension results [35].

Sulphate attack is essentially caused by the reaction of sulphates present in ionic formation within the pore water of concrete with some cementitious hydrate compounds, namely the calcium hydroxide to form gypsum, or calcium sulphate. The subsequent reaction of the calcium sulphate with tricalcium aluminate (C_3A in cement chemistry shorthand) crystals produces another cement hydrate called ettringite, with a significantly different morphology to the gypsum or calcium hydroxide crystals. The ettringite is a long and thin crystal, and the growth of this crystal within the confined environment of the pore structure in concrete leads to expansive damage in concrete [53]. There are multiple possible types of crystals formed during sulphate attack due to different combinations of ion concentration and temperature of the material, most notably Thaumasite [53,54]. While the specifics of ongoing sulphate attack are complex, the deterioration of the tensile capacity on concrete is considerably easier to characterise with pressure tension testing.

A third deterioration mechanism that is the subject of study in this document is freeze-thaw damage. Freeze-thaw damage is due to the action of water expanding due to the phase change between a liquid and solid that occurs when the material drops below its freezing point. When this phase change occurs within the connected void structure of concrete, expansive stresses will be created on the connecting solid material. These expansive stresses can exceed the tension capacity of concrete, leading to cracking [55]. Due to the confinement pressure caused by the small spaces within the smallest pores of concrete, not all the water will freeze at the same

temperature, with the water within the largest pores freezing first and smaller pores progressively freezing as the temperature decreases. This progression creates a freezing front that moves through the pore system from the larger pores to successively smaller pores, pushing unfrozen water ahead of it and generating a hydraulic pressure [56,57,58,59]. In either case, the expansive stresses will cause significant damage to the solid phase of the material, leading to deterioration due to cracking. This degradation of the tensile capacity due to the creation of new cracks is well suited to detection with the pressure tension machine.

For these durability mechanisms, expansion within the confined void structure causes damage which changes to the pore structure and simultaneously weakens the tension capacity of the material due to paste weakening. For this reason, the pressure tension machine is well suited for the detection of this damage due to the loading mechanism being applied from within the pore structure. Changes to this pore structure also has important implications in terms of the transport properties of the material. Additional pathways will open due to this damage, which causes a positive feedback loop which will make the transport of water and deleterious ions contained within more severe. For this reason, quantifying the deterioration of tension capacity and the predilection for cracking is directly related to the transport properties of the material, especially for deterioration caused by water transport through the porous material.

2.4. References

[1] Hall, C. "Water Movement in Porous Building Materials—I. Unsaturated Flow Theory and Its Applications." Building and Environment 12, no. 2 (1977): 117-25.

[2] Lockington, D.A., J.-Y. Parlange, and P. Dux. "Sorptivity and the Estimation of Water Penetration into Unsaturated Concrete." Materials and Structures 32, no. 5 (1999): 342-47.

[3] Gummerson, R. J., C. Hall, and W. D. Hoff. "Water Movement in Porous Building Materials—II. Hydraulic Suction and Sorptivity of Brick and Other Masonry Materials." Building and Environment 15, no. 2 (1980/01/01 1980): 101-08.

[4] Carpenter, T.A., E.S. Davies, C. Hall, L.D. Hall, W.D. Hoff, and M.A. Wilson. "Capillary Water Migration in Rock: Process and Material Properties Examined by NMR Imaging." Materials and Structures 26, no. 5 (1993): 286.

[5] Fischer, N., R. Haerdtl, and P.J. McDonald. "Is Colour Change a Good Measure of a Water Penetration Front?". Magazine of Concrete Research 67, no. 19 (2015): 1048-53.

[6] Hall, C. "Water Sorptivity of Mortars and Concretes: A Review." Magazine of Concrete Research 41, no. 147 (1989): 51-61.

[7] Hall, C., and W.D. Hoff. Water Transport in Brick, Stone and Concrete. Spon Press, London: Routledge, 2002. doi:10.4324/9780203301708.

[8] Hanzic, L., and R. Ilic. "Relationship between Liquid Sorptivity and Capillarity in Concrete." [In English]. Cement and Concrete Research 33, no. 9 (2003): 1385-88.

[9] Bažant, Z.P., and L.J. Najjar. "Nonlinear Water Diffusion in Nonsaturated Concrete." Matériaux et Construction 5, no. 1 (1972): 3-20.

[10] Lockington, D. A., J.-Y. Parlange, and M. Lenkopane. "Capillary Absorption in Porous Sheets and Surfaces Subject to Evaporation." Transport in Porous Media 68, no. 1 (2007): 29-36.

[11] Balcom, B.J., J.C. Barrita, C. Choi, S.D. Beyea, D.J. Goodyear, and T.W. Bremner. "Single-Point Magnetic Resonance Imaging (MRI) of Cement Based Materials." Materials and Structures 36, no. 3 (2003): 166.

[12] Halperin, W. P., J-Y Jehng, and Y-Q Song. "Application of Spin-Spin Relaxation to Measurement of Surface Area and Pore Size Distributions in a Hydrating Cement Paste." Magnetic Resonance Imaging 12, no. 2 (1994): 169-73.

[13] Plassais, A., M.-P. Pomiès, N. Lequeux, P. Boch, J.-P. Korb, and D. Petit. "Micropore Size Analysis in Hydrated Cement Paste by NMR." Comptes Rendus de l'Académie des Sciences - Series IIC - Chemistry 4, no. 11 (2001): 805-08.

[14] Kumar, Rakesh, and B. Bhattacharjee. "Porosity, Pore Size Distribution and in Situ Strength of Concrete." Cement and Concrete Research 33, no. 1 (1// 2003): 155-64.

[15] Winslow, D., and Di. Liu. "The Pore Structure of Paste in Concrete." Cement and Concrete Research 20, no. 2 (1990): 227-35.

[16] Beyea, S.D., B.J. Balcom, T.W. Bremner, P.J. Prado, A.R. Cross, R.L. Armstrong, and P.E. Grattan-Bellew. "The Influence of Shrinkage-Cracking on the Drying Behaviour of White Portland Cement Using Single-Point Imaging (SPI)." Solid State Nuclear Magnetic Resonance 13, no. 1–2 (1998): 93-100.

[17] Beyea, S.D., B.J. Balcom, T.W. Bremner, R.L. Armstrong, and P.E. Grattan-Bellew. "Detection of Drying-Induced Microcracking in Cementitious Materials with Space-Resolved 1h Nuclear

Magnetic Resonance Relaxometry." Journal of the American Ceramic Society 86, no. 5 (2003): 800-05.

[18] Bohris, A.J., U. Goerke, P.J. McDonald, M. Mulheron, B. Newling, and B. Le Page. "A Broad Line NMR and MRI Study of Water and Water Transport in Portland Cement Pastes." Magnetic Resonance Imaging 16, no. 5–6 (1998): 455-61.

[19] Beyea, S.D., B.J. Balcom, T.W. Bremner, P.J. Prado, D.P. Green, R.L. Armstrong, and P.E. Grattan-Bellew. "Magnetic Resonance Imaging and Moisture Content Profiles of Drying Concrete." Cement and Concrete Research 28, no. 3 (1998): 453-63.

[20] Leech, C., D. Lockington, and P. Dux. "Unsaturated Diffusivity Functions for Concrete Derived from NMR Images." Materials and Structures 36, no. 6 (2003): 413.

[21] Cano-Barrita, P.F. de J., B.J. Balcom, T.W. Bremner, M.B. MacMillan, and W.S. Langley. "Moisture Distribution in Drying Ordinary and High Performance Concrete Cured in a Simulated Hot Dry Climate." Materials and Structures 37, no. 8 (2004): 522.

[22] Prado, P.J., B.J. Balcom, S.D. Beyea, R.L. Armstrong, T.W. Bremner, and P.E. Grattan-Bellew. "Concrete/Mortar Water Phase Transition Studied by Single-Point MRI Methods." Magnetic Resonance Imaging 16, no. 5–6 (1998): 521-23.

[23] Prado, P.J., B.J. Balcom, S.D. Beyea, R.L. Armstrong, and T.W. Bremner. "Concrete Thawing Studied by Single-Point Ramped Imaging." Solid State Nuclear Magnetic Resonance 10, no. 1 (1997): 1-8.

[24] Gonnerman, H., and E. Shuman. "Compression, Flexural and Tension Tests of Plain Concrete." ASTM Proceedings 28 (1928): 527-64.

[25] Bremner, T.W., A.J. Boyd, T.A. Holm, and S.R. Boyd. "Tensile Testing to Evaluate the Effect of Alkali-Aggregate Reaction in Concrete." In Proceedings, International Workshop on Alkali-Aggregate Reactions in Concrete, 311-26. Dartmouth, Canada: CANMET/ACI, 1995.

[26] Bolzan, Pablo E, and Gerald A. Huber. "Direct Tension Test Experiments." Strategic Highway Research Program, National Research Council Washington, DC, 1993.

[27] ASTM. "Standard Test Method for Flexural Strength of Concrete (Using Simple Beam with Center-Point Loading)." West Conshohocken, PA: ASTM International, 2016.

[28] ASTM "Standard Test Method for Flexural Strength of Concrete (Using Simple Beam with Third-Point Loading)." West Conshohocken, PA: ASTM International, 2016.

[29] Carrasquillo, P.M., and R.L. Carrasquillo. "Improved Concrete Quality Control Procedures Including Third Point Loading." Center for Transportation Research, The University of Texas at Austin, 1987.

[30] Bažant, Z.P. "Size Effect in Blunt Fracture: Concrete, Rock, Metal." Journal of Engineering Mechanics 110, no. 4 (1984): 518-35.

[31] ASTM. "Standard Test Method for Splitting Tensile Strength of Cylindrical Concrete Specimens." West Conshohocken, PA, ASTM International, 2004.

[32] Carneiro, F.L.L.B. "A New Method to Determine the Tensile Strength of Concrete. In:" Paper presented at the Proceedings of the 5th meeting of the Brazilian Association for Technical Rules, 1943

[33] Lin, Z., and L. Wood. "Concrete Uniaxial Tensile Strength and Cylinder Splitting Test." Journal of Structural Engineering 129, no. 5 (2003): 692-98.

[34] Davies, J. D., and D. K. Bose. "Stress Distribution in Splitting Tests." J. Am. Concr. Inst. 65 (1968): 662.

[35] Hartell, J.A., A.J. Boyd, and C.C. Ferraro. "Sulfate Attack on Concrete: Effect of Partial Immersion." Journal of Materials in Civil Engineering 23, no. 5 (2011): 572-79.

[36] Zi, G., H. Oh, and S.-K. Park. "A Novel Indirect Tensile Test Method to Measure the Biaxial Tensile Strength of Concretes and Other Quasibrittle Materials." Cement and Concrete Research 38, no. 6 (2008): 751-56.

[37] Cantillo, V., and Andrés G. "Fluid-Pressured Test to Measure Tensile Strength of Concrete." Journal of Materials in Civil Engineering 26, no. 4 (2014): 776-80.

[38] Bridgman, P.W. The Physics of High Pressure. Dover Publications, 1931.

[39] Clayton, N., and F. Grimer. "The Diphase Concept, with Particular Reference to Concrete." Chap. 7 In Developments in Concrete Technology, 283-317. Waterford, UK: Elsevier Science & Technology, 1979.

[40] Clayton, N. "Fluid-Pressure Testing of Concrete Cylinders." Magazine of Concrete Research 30, no. 102 (1978): 26-30.

[41] Langan, D., and F.K. Garas. "The Failure of Concrete under the Combined Action of High Shearing Forces and Biaxial Restraint." Paper presented at the International Conference of Structure, Solid Mechanics and Engineering Design in Civil Engineering, Southampton, 1969.

[42] Grimer, F., and R.E. Hewitt. "The Form of the Stress-Strain Curve of Concrete Interpreted with a Diphase Concept of Material Behavior." 681-91. Building Research Station: Ministry of Public Building and Works, 1968.

[43] Uno, T., K. Fujikake, S. Mindess, and H. Xu. "The Nitrogen Gas Tension Test of Concrete. Part 1: Effect of Boundary Conditions and Axial Strain Response." Materials and Structures 44, no. 4 (2011): 857-64.

[44] Fujikake, K., S. Mindess, T. Uno, and H. Xu. "The Nitrogen Gas Tension Test. Part 2: Failure Mechanism." Materials and Structures 44, no. 4 (2011): 865-77.

[45] Boyd, A.J., and S. Mindess. "The Effect of Sulfate Attack on the Tensile to Compressive Strength Ratio of Concrete." In Proceedings of Third International Conference on Concrete Under Severe Conditions, 789-96. Vancouver, Canada: ACI/CSCE, 2001.

[46] Boyd, A.J., and S. Mindess. "The Use of Tension Testing to Investigate the Effect of W/C Ratio and Cement Type on the Resistance of Concrete to Sulfate Attack." Cement and Concrete Research 34, no. 3 (2004): 373-77.

[47] Li, G. "The Effect of Moisture Content on the Tensile Strength Properties of Concrete." University of Florida, 2003.

[48] Lu, Aifei. "Preliminary Assessment of the Base Variables for Standardizing the Pressure Tension Test." McGill University, 2015.

[49] Fournier, B., and M.-A. Bérubé. "Alkali-Aggregate Reaction in Concrete: A Review of Basic Concepts and Engineering Implications." Canadian Journal of Civil Engineering 27, no. 2 (22000): 167-91.

[50] Gillott, J. E. "Alkali-Aggregate Reactions in Concrete." Engineering Geology 9, no. 4 (1975): 303-26.

[51] Cumming, Scott R., Andrew J. Boyd, and Christopher C. Ferraro. "Tensile Strength Prediction in Concrete Using Nondestructive Testing Techniques." Research in Nondestructive Evaluation 17, no. 4 (2006): 205-22.

[52] Neville, A.M. "The Confused World of Sulfate Attack on Concrete." Cement and Concrete Research 34, no. 8 (2004): 1275-96.

[53] Crammond, N. "The Occurrence of Thaumasite in Modern Construction – a Review." Cement and Concrete Composites 24, no. 3 (2002): 393-402.

[54] Marchand, J., I. Odler, and J.P. Skalny. Sulfate Attack on Concrete. CRC Press, 2003.

[55] Cai, H., and X. Liu. "Freeze-Thaw Durability of Concrete: Ice Formation Process in Pores." Cement and Concrete Research 28, no. 9 (1998): 1281-87.

[56] Banthia, N., M. Pigeon, and L. Lachance. "Calorimetric Study of Freezable Water in Cement Paste." Cement and Concrete Research 19, no. 6 (1989): 939-50.

[57] Mindess, S., J.F. Young, and D. Darwin. Concrete. 2 ed.: Pearson, 2002.

[58] Neville, A.M. Properties of Concrete. 4 ed. Harlow Essex, England: Longman Group Limited, 1996.

[59] Kosmatka, S.H., B. Kerkhoff, W.C. Panarese, N.F. MacLeod, and R.J. McGrath. Design and Control of Concrete Mixtures. Vol. 5420, Ottawa, Ontario, Canada: Cement Association of Canada, 2002.

Foreword to Chapter 3

Chapter 3 details the preliminary work done using the SPRITE MRI technique in directly evaluating the mass transport of water in simple cement systems. Both simple sorptive flow and the development of a quasi-steady state evaporative flow were examined in this chapter. A new technique allowing for the imaging of samples with lengths more representative of concrete in field conditions was also demonstrated. This chapter is relevant to the study of evaporative transport implicated in durability issues, as the distribution of the water during mass transport under these conditions is directly related to the severity of the ensuing deterioration. The steady state condition in the 100 mm samples confirmed that there was a non-uniform distribution of the water in the dry end, which showed evaporation was occurring, indicative of wicking action. The effect of hydration was also observed in this chapter, where the total amount of free water in the pore space decreased the longer the specimen was exposed to water in the pores. In addition, the MRI imaging revealed that all the pore space was not being immediately filled by water entering the pore system, instead showing a 'backfilling' of the pore space as the sorptive flow progressed. This 'backfilling' process could be related to a kind of mass transport of water that occurs during freeze thaw, where the water freezes in the largest pores first, hydraulically forcing water into smaller pores. The thesis later explores freeze thaw damage and the implications to the tensile resistance of the solid phase in Chapters 7 and 8 respectively.

The work in Chapter 3 also demonstrated a bi-exponential T_2* distribution, essentially showing that there was free water in different types of pore spaces. The larger pore spaces were associated with the capillary flow detailed in the chapter and all evaporative transport conditions.

The smaller pore spaces, however, corresponded to the water in nanopores, which remained constant. Migration of water from these nanopores directly detected with MRI techniques is associated with creep deterioration, as investigated with tensile properties in Chapter 9.

The preliminary results detailed in Chapter 3 were used as the basis for a more detailed study of one-dimensional evaporative flow in pastes and mortars, on which the author collaborated. The results were published in a paper not included in this thesis:

Enjilela, R., P.F. de J. Cano-Barrita, A.J.K. Komar, A.J. Boyd, and B.J. Balcom. "Monitoring Steady State Moisture Distribution During Wick Action in Mortar by Magnetic Resonance Imaging (MRI)." Materials and Structures 50, no. 2 (2017): 151.

This paper directly builds on the work outlined in Chapter 3. In this paper, it was demonstrated that common methods used to predict the total depth of the liquid water penetration in evaporative flow conditions do not capture the true nature of the transport behavior as revealed by MRI. The depth of penetration of this wetting front is relevant to many durability related issues, so accurately characterizing the nature of this behavior is important for making design choices that will result in sustainable concrete structures.

This paper also showed is that there is a significant amount of water present, even at low moisture contents that common diffusion based models would have overlooked. This water in samples undergoing evaporative mass transport could explain the experimental difficulties encountered in Chapter 5 during conditioning for lower moisture contents. More appropriate estimations of the hydraulic conductivity were obtained by taking the moisture content profiles from the MRI and deriving the parameters from an inverse modelling procedure.

Chapter 3: Single Point Ramped Imaging with T1 Enhancement (SPRITE) Imaging of 1 Dimensional Sorptive Flow in White Portland Cement Pastes

Komar, A.J.K., Boyd, A.J, Balcom, B.J.

3.1. Abstract

The authors performed studies investigating transport properties of cement pastes undergoing one dimensional sorptive and evaporative flow using Single Point Ramped Imaging with T_1 Enhancement (SPRITE) as well as Single Point Imaging (SPI) Magnetic Resonance Imaging techniques. The wetting front of the water undergoing both sorptive and evaporative flow was directly imaged using these techniques and the variations in results between different water/binder ratios was observed. Two different populations of ^1H nuclei with different T_2* values were observed, corresponding to water found in different pore sizes. Variations in steady state moisture profiles were observed due to ongoing evaporation from one end of 100 mm length samples. A procedure for imaging longer samples was also developed and the results of this imaging technique for both sorptive and evaporative water transport are presented.

Suggested Keywords: Cement Paste, Transport Properties, Image Analysis, Adsorption, Magnetic Resonance

3.2. Introduction

3.2.1. Moisture transport

The transport properties of cementitious materials are of great importance when considering the life cycle of concrete infrastructure. Water ingress, driven primarily by capillary absorption and molecular diffusion, can carry deleterious ions such as chlorides through the pore structure, which can cause serious degradation to embedded reinforcement or to the cementitious matrix itself [1]. The distribution of pore water within cementitious material is also critical when considering the ongoing hydration reaction. Understanding this distribution and the kinetics of water as a function of water binder ratio, as well as relative humidity boundary conditions during transport through a cementitious matrix can lead to better design choices that will result in more durable concrete infrastructure.

3.2.2. Sorptivity

The uptake of water into an unsaturated porous material driven by capillary action is deemed to be sorptivity. The mathematical formulation herein is adapted from Hall *et al.* [2-6]. When considering a one-dimensional flow of water from a reservoir through a porous medium, the behavior can be modelled by Equation 3.1:

$$\frac{\delta\Theta}{\delta t} = \frac{\delta}{\delta x}\left(D(\Theta)\frac{\delta\Theta}{\delta x}\right)$$

Equation 3.1- Formulation of 1 dimensional flow of water through a porous medium

Where $\Theta = \frac{\theta-\theta_i}{\theta_s-\theta_i}$, x is distance from the water to a chosen point in the sample, D is moisture diffusivity and the boundary conditions are $\Theta = \theta_s$ at $x=0$, $t\geq 0$; $\Theta = \theta_i$ for $x>0$, $t=0$. [6]

Using the Boltzmann transformation variable $\eta = xt^{-\frac{1}{2}}$, Equation 3.1 can be converted into an ordinary differential equation. The results of solving this ODE yields Equation 3.2:

$$D(\Theta) = -\frac{1}{2} \cdot \left(\frac{d\eta}{d\Theta}\right) \int_{\Theta_i}^{\Theta} \eta \, d\Theta$$

Equation 3.2- Integral form of sorptive flow

Solving for the cumulative amount of liquid absorbed as a function of time, *i* (in mm/area) we get Equation 3.3, where *S* is the sorptivity (mm/min^1/2) and *t* is time in minutes

$$i = t^{1/2} \cdot \int_{\Theta_i}^{\Theta} \eta \, d\Theta = S \cdot t^{1/2}$$

Equation 3.3- Sorptive flow

Measuring the change in mass of a sample as a function of time is referred to as the gravimetric method. Another formulation of sorptivity, based on the geometric location of the wetting front due to this capillary absorption, can also be formulated as Equation 3.4:

$$h = k \cdot t^{1/2}$$

Equation 3.4- Geometric formulation of sorptive flow

Where *h* is the height of the liquid from the reservoir to the wetting front, *k* is the capillary coefficient and *t* is time in minutes [2,3]. The imaging techniques employed in this study can use both of these formulations of sorptivity because the images provide both volumetric and spatial information regarding the location of the water.

3.2.3. SPRITE imaging technique

Many different magnetic resonance based imaging techniques have been used to image the movement of water through porous materials such as cement mortars and pastes [7-11]. The magnetic resonance imaging technique used in this study was originally developed by Balcom *et al.* [12-22] and is applicable to samples containing hydrogen ^{1}H nuclei exposed to a controlled series of Radio Frequency (RF) pulses in the presence of a strong magnetic field [12]. The analysis described herein contains results using the Single Point Ramped Imaging with T_1 Enhancement (SPRITE) technique [12,15,16,19,22]. A series of RF pulses rotates the sample magnetic moments of the ^{1}H nuclei out of alignment with the applied magnetic field, and the resulting MR signal is detected via electromagnetic induction of these field changes as the perturbed magnetic moments decay back into alignment with the strong magnetic field. These detected signatures can be processed to show information about the ^{1}H nuclei and their surrounding environment. The spatial analysis of this RF signal is made possible by introducing a new variable shown in Equation 3.5:

$$k_z = \frac{\gamma \cdot G_z \cdot t}{2 \cdot \pi}$$

Equation 3.5- Definition of variable change for SPRITE method of signal analysis, from Balcom et al. [12]

Where γ is the gyromagnetic ratio in radians$\cdot s^{-1} \cdot T^{-1}$, G_z is the gradient of the in the z-direction, t is the time elapsed since the initial RF pulse. Note that both the magnetic field gradient and the time after the initial RF pulse are included in the definition of k_z variable, which has units of cm^{-1}. The signal S as a function of k_z can then be described as shown in Equation 3.6:

$$S(k_z) = \int \rho(z) \exp(i2\pi k_z z)\, dz$$

Equation 3.6- Magnetic resonance signal definition

Where ρ(z) is the concentration of the ^{1}H nuclei as a function of length, *i* is the imaginary number, and *z* is the spatial position in cm. This is the signal *s(k)* that is detected by the RF probe. To convert this data into spatial and volumetric information, a Fast Fourier transform (FFT) is required to resolve ρ(z). The results of the FFT of Equation 3.6 can be described in Equation 3.7:

$$\rho(z) = \int S(k_z) \exp(-i2\pi k_z z)\, dk_z$$

Equation 3.7- Fast Fourier transform

Since k_z is a function of both magnetic field gradient and encoding time, this allows for two different techniques, only one of which is used in this paper. The first, SPRITE, will vary the gradient of the z-direction magnetic field in 64 step increments while keeping the gradients in the x and y-direction, as well as the encoding time, constant [18]. The second, Single Point Imaging (SPI), keeps the magnetic field gradient constant.

3.2.3.1. Relaxation times

The magnitude of the induced nonequilibrium magnetic moments in the ^{1}H molecules via RF pulses will naturally return to an unperturbed condition in alignment with the applied magnetic field in the z-direction by relaxation. The observed signal depends on transverse magnetization M_{xy}, which is given by Equation 3.8:

$$M_{xy} = M_0 \cdot \exp(-t/T_2^*)$$

Equation 3.8- Decay signal perpendicular to applied magnetic field

Where M_0 is the sample magnetization, t is time in seconds, and T_2^* is a time constant related to the environment of the ^{1}H nuclei are in. Different populations of ^{1}H nuclei, for example water within large and small pores, will have different T_2^* decay rates and can therefore be imaged by varying the time between the RF pulse application and detection of the signal. The final signal intensity using SPRITE methods will therefore be proportional to both the characteristics of the population being excited T_2^*, the RF rotation angle θ as well as the encoding time t_p, as is described in Equation 3.9:

$$S = M_0 \cdot \exp(-t_p/T_2^*) \cdot \sin(\theta)$$

Equation 3.9- SPRITE signal intensity definition

3.3. Materials and Methods

3.3.1. Paste preparation

The imaging techniques used are very sensitive to differences in the magnetic response of materials [20,21]. Therefore, ferromagnetic materials including the C_4AF found in ordinary Portland cement as well as certain types of ferrous aggregates cannot be used in MRI studies of this kind. For that reason, a white portland cement with no ferrous components was used as the binder.

To accommodate the interior diameter of the magnets (50 mm), cylindrical samples were cast with a diameter of 45 mm. The samples were then cut into constant lengths of either 45 mm or 100 mm. The following mixes in Table 3.1 were prepared and cured in saturated limewater solution for 28 days.

Table 3.1- Paste mixtures

MIXTURE (w/c)	0.35	0.4	0.45	0.6
White Cement	725.0	726.5 g	725.0	725.0
Water	253.5	290.5 g	326.0	435.0

After curing, the samples were dried in an oven at 85 °C until the masses reached a constant state, meaning all the evaporable water had left the permeable pore structure. An epoxy sealant, selected to be unobservable in MRI images (Devcon 2 Tone Epoxy 14260) was applied to the sides of the samples to limit the absorption of water from anywhere other than the top and bottom face of the samples during the sorptivity experiments and promote 1-dimensional flow.

3.3.2. MRI parameters

Before the SPRITE method of imaging was performed on the samples, a Free Induction Decay (FID) was signal taken to determine the characteristics of the decay signals present within the samples. Two magnets of different field strengths were used in the study (2.21 MHz and 8.51 MHz) but, in both cases, the field of view (FOV) in the image was about 96 mm. Irregularities of the magnetic field at the extreme edges of this FOV caused signal artifacts to be detected when the sample was imaged in this region.

3.3.2.1. Magnetic sensitivity reference

During imaging, the sensitivity of the magnet could change in a way that would affect the captured images. To compensate for this known effect, a constant reference was created (comprised of water, copper sulphate and deuterium) which was imaged at the same time as any moisture content profile was taken. Since the reference remained constant during imaging, the resulting moisture content profiles could be normalized with respect to the reference so that the magnitude of the signal from different images could be directly compared.

3.3.2.2. Fiduciary markers

To overcome the field inhomogeneities that would be unavoidable when imaging samples larger than the FOV, a new technique was developed to work around this limitation. A small diameter tube made of material without ^{1}H nuclei was selected (made of non-magnetically active fluorinated ethylene propylene) that could be wrapped around the exterior of the samples while they were placed in the magnets during imaging. To allow the presence of these markers to be spatially encoded during imaging, a saturated solution of copper sulphate with 1 part heavy water to 20 parts regular water was prepared and sealed inside the tubes. The tubes were then wrapped around the sample and held in place with PTFE tape. Thus, samples larger than the FOV could be imaged in the region not affected by field inhomogenities by using the markers to 'stitch together' multiple images of a sample obtained within the field of view, with the longer samples being spatially displaced within the magnet to image the entire profile.

3.3.3. Sorptivity

The sorptivity experiments were performed on both the 45 mm and 100 mm samples in accordance with the technique used by Hall *et al.* [3-5], including gravimetric measurements. Time intervals were selected so that the $t^{1/2}$ values would produce equal steps. The samples were imaged using the MRI techniques and the progression of the wetting front from the reservoir toward the end exposed to the atmosphere was recorded.

3.3.4. Steady state

After the samples had been imaged during the sorptivity process, the exposed ends of the samples were placed in either a high relative humidity condition (RH > 80%) or a low relative humidity (RH < 20%) atmosphere. The 'wet' end of the samples remained in contact with the

water reservoir at all times. Over subsequent weeks, the distribution of the ^{1}H nuclei in the samples was imaged to determine whether the evaporation from the dry end would be detectible using the MRI techniques.

3.4. Results and Discussion

3.4.1. Sorptivity Imaging of 45 mm samples

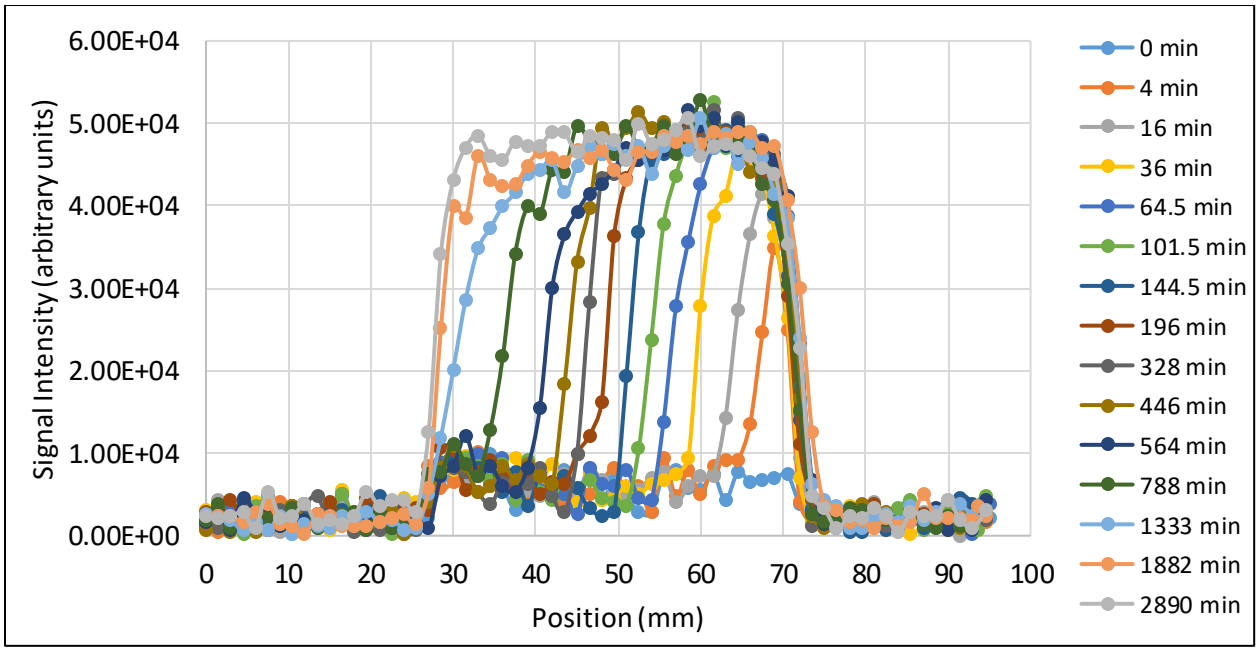

Figure 3.1- ^{1}H Signal intensity from sorptive flow in a 0.35 White Portland Cement Paste

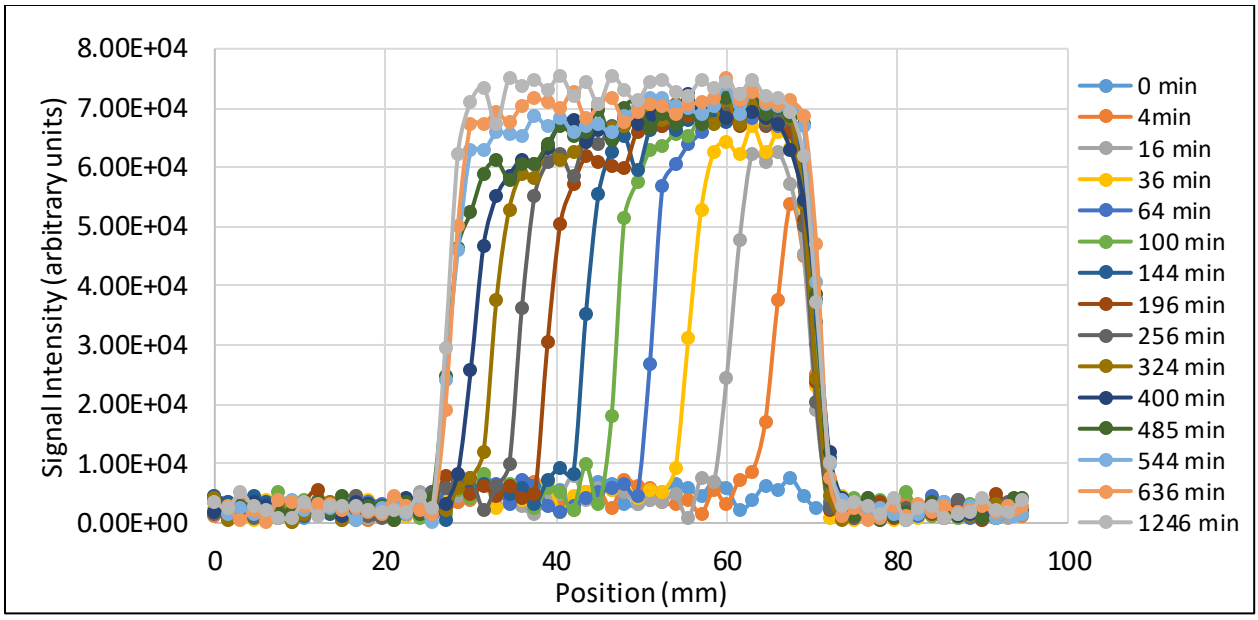

Figure 3.2- ^{1}H Signal intensity from sorptive flow in a 0.60 White Portland Cement Paste

Figures 3.1 and 3.2 show the results of the sorptivity imaging for both a 0.35 and a 0.60 w/c paste of 45 mm length, scaled in all cases by the copper sulphate/deuterium reference sample. The 'wet' end of the samples is on the right side of the images, approximately at the 75-mm area for both samples. Both the rate of water transport and absolute magnitude of water imbibed is dependent on the water to cement ratio. The 0.60 w/c paste clearly shows a greater amount of ^{1}H signal intensity throughout the entire material volume as well as increased sorptivity, since the wetting front reaches the dry end of the sample at around 485 minutes, whereas the 0.35 w/c paste takes at least 1882 minutes.

Another feature also evident from the figures are the signal intensity of the ^{1}H nuclei, which are not at a maximum at the point of the wetting front. This implies that not all the pore space available within the cement paste are immediately saturated via the capillary absorption process. This additional 'backfilling' process occurs while the wetting front is progressing. Note that

neither the traditional 'height based' sorptivity measurements nor gravimetric methods would be able to show this time-dependant process.

3.4.1.1.Steady state imaging of 45 mm samples

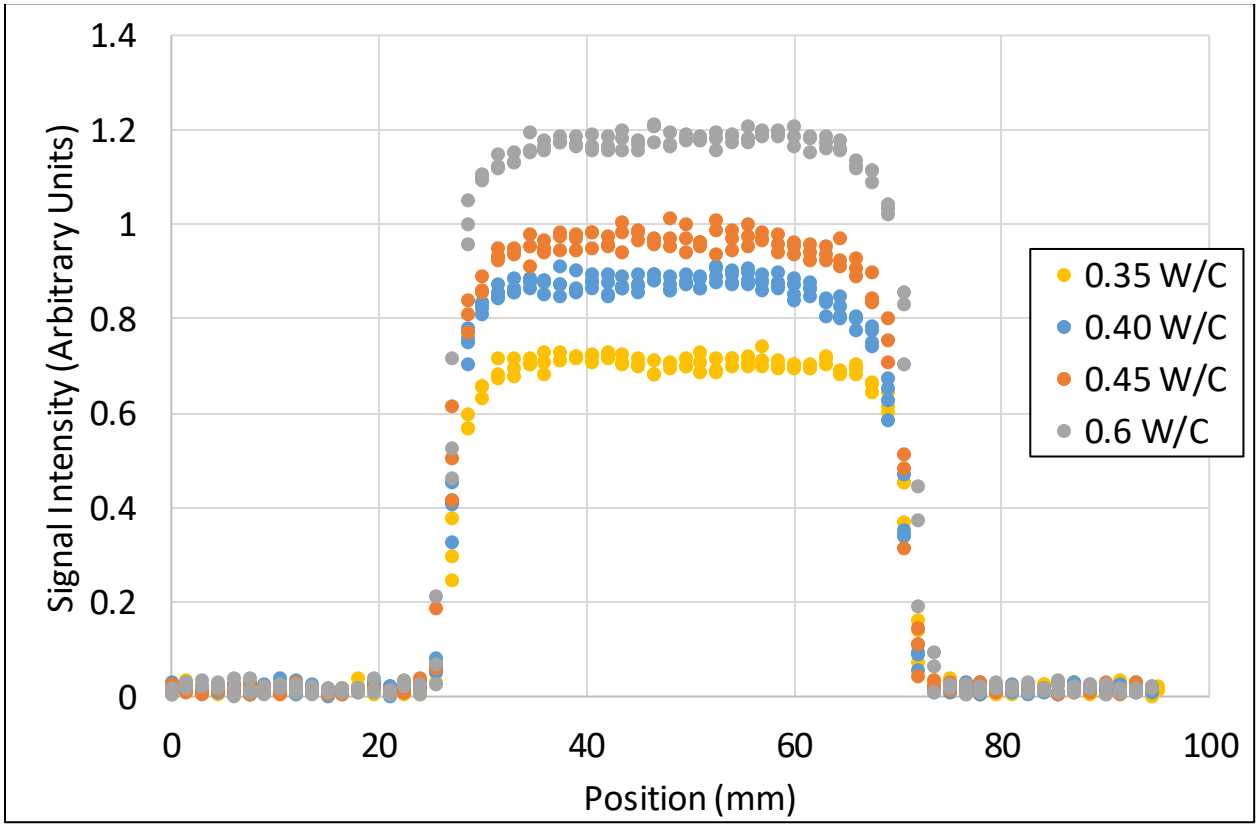

Figure 3.3- Steady state moisture content profiles of saturated cement paste. Each W/C profile is comprised of at least three images

For the different w/c paste mixtures, Figure 3.3 shows the moisture content profiles taken after 14 days of constant 1-dimensional sorptive flow in a steady state condition. For all w/c mixes, no significant loss of moisture was detectable at the dry end subject to evaporation. This strongly suggests that the rate of evaporation for all of these mixes was much less than the replenishment of the pore water via capillary forces at this length of the sample. The overall magnitude of the

^{1}H signal was used to distinguish between the absolute amount of water within the capillary pores, even being able to distinguish between the 0.40 and 0.45 mixes with great accuracy.

For the 45 mm samples, the effect of both high and low humidity environments on the ^{1}H distribution at the drying end in steady state flow was also imaged after 14 days. Figure 3.4 shows the result of this experiment. As was the case with all the other mixes investigated at this length, there was no significant difference between the high and low humidity samples for either the 0.60 or 0.35 paste samples. For both high and low humidity conditions, which were expected to promote differences in the evaporation rate at the dry end, it appears that the magnitude of the mass transport due to sorptive flow through the pore structure is much larger than the magnitude of the mass transport due to evaporation from the dry end which resulted in virtually identical moisture profiles despite the different sample conditioning.

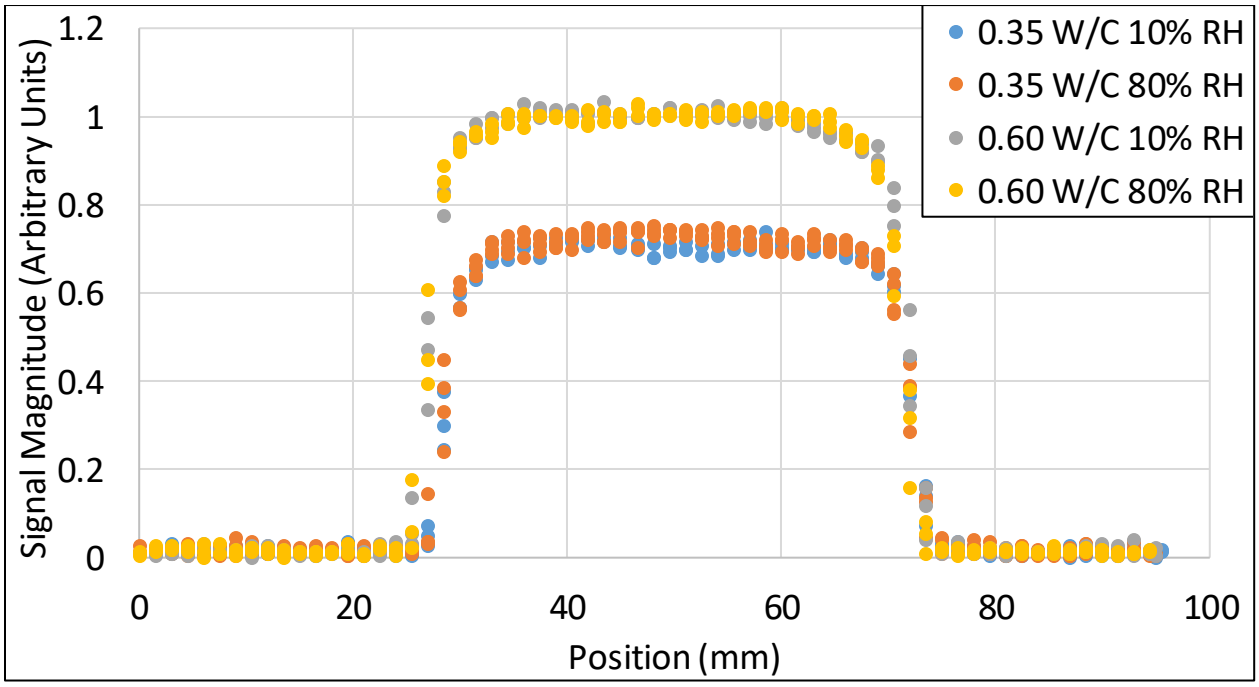

Figure 3.4- Effect of relative humidity on steady state condition for 0.35 and 0.60 W/C pastes. Each profile is comprised of three separate images

3.4.1.2.Imaging of 100 mm length samples

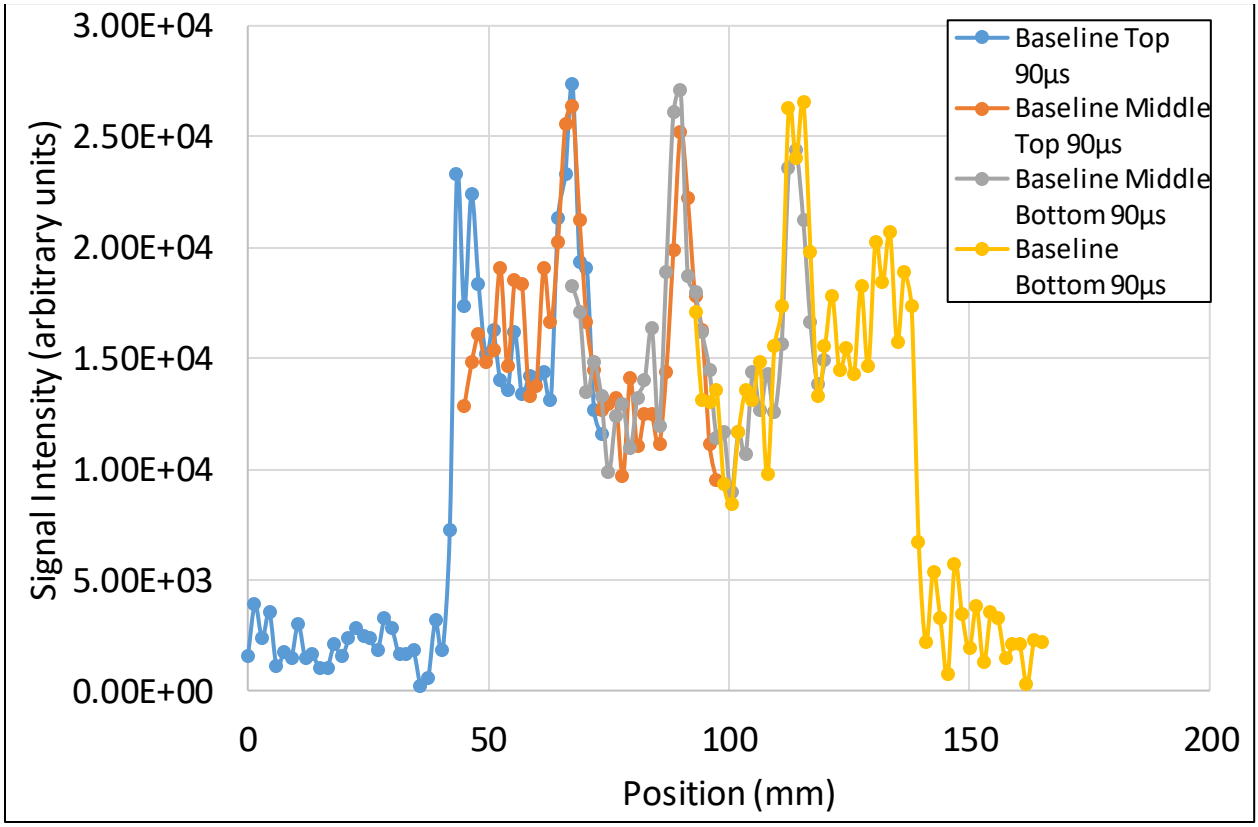

Figure 3.5- Moisture profile for dry 0.6 W/C paste using encoding time t_p of 90 µs

Figure 3.5 shows the imaging from the dry 100 mm sample of w/c 0.60 imaged with an encoding time of 90 µs. Four profiles were required to image the entire length of the sample. These four profiles have been overlaid in the figure corresponding to where the fiduciary markers overlap. Two features are notable from Figure 3.5, one being the three prominent spikes in the data which correspond to the fiduciary markers located at approximately 65, 90 and 115 mm on the axis of the figure. Figure 3.6 shows the same sample imaged with a longer encoding time of 400 µs. When comparing Figures 3.5 and 3.6, it is clear that the fiduciary markers are much more prominent in the shorter encoding time of 90 µs than in the longer encoding time of 400 µs. The second prominent feature is the ^{1}H signal between the fiduciary marker spikes found in Figure

3.5. This ^{1}H signal corresponds to some amount of free water trapped in smallest pore spaces, perhaps intercrystalline layers within the cementitious hydrates that are still present in the sample despite an extensive drying regime.

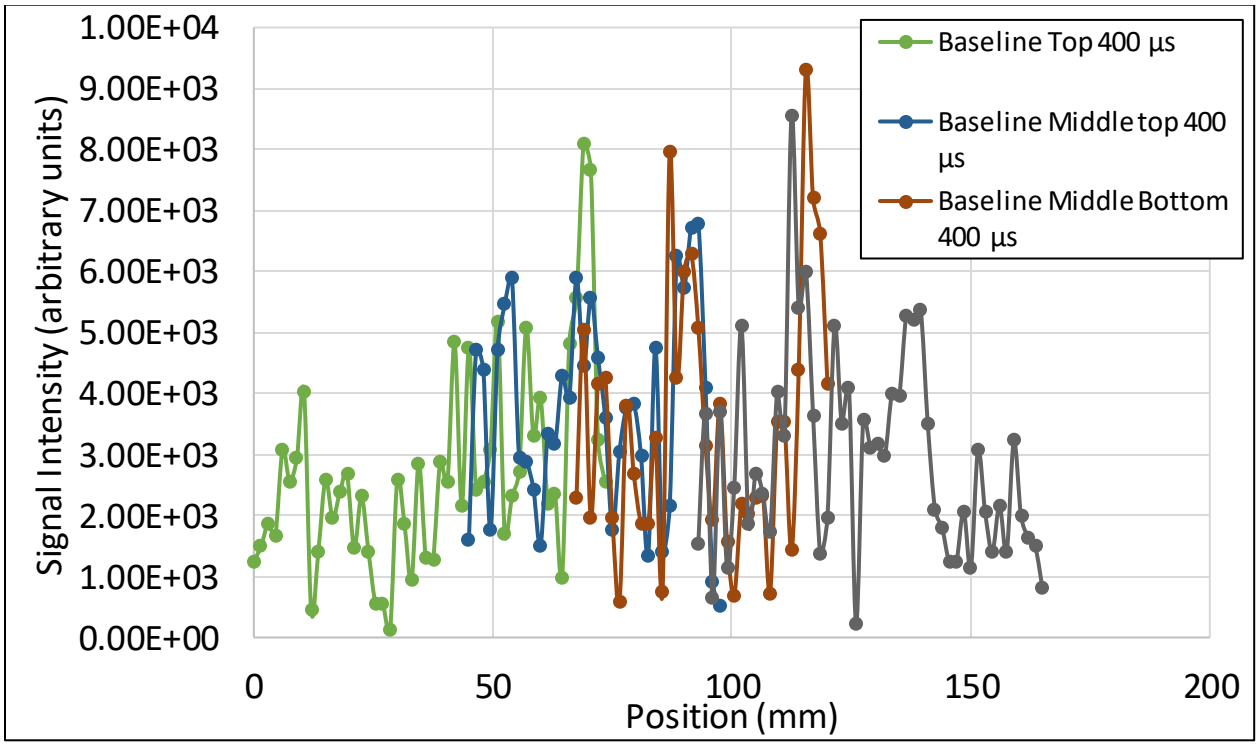

Figure 3.6- Moisture profile for dry 0.60 W/C paste using encoding time t_p of 400 µs

The longer encoding time of 400 µs used for the imaging in Figure 3.6 does not show this same signal from the ^{1}H nuclei since the longer encoding time is much larger than the decay time T_2*, and thus the longer encoding time effectively masks the signal from this population. The fiduciary markers are also much less prominently displayed in this figure relative to Figure 3.5, which demonstrates that this signal is also being partially masked at this encoding time. The difference between the two encoding times is that the shorter encoding time is more sensitive to ^{1}H nuclei which are present in these small intercrystalline voids, whereas the longer encoding time is more

sensitive to the water existing in the larger permeable pores associated with sorptive capillary flow.

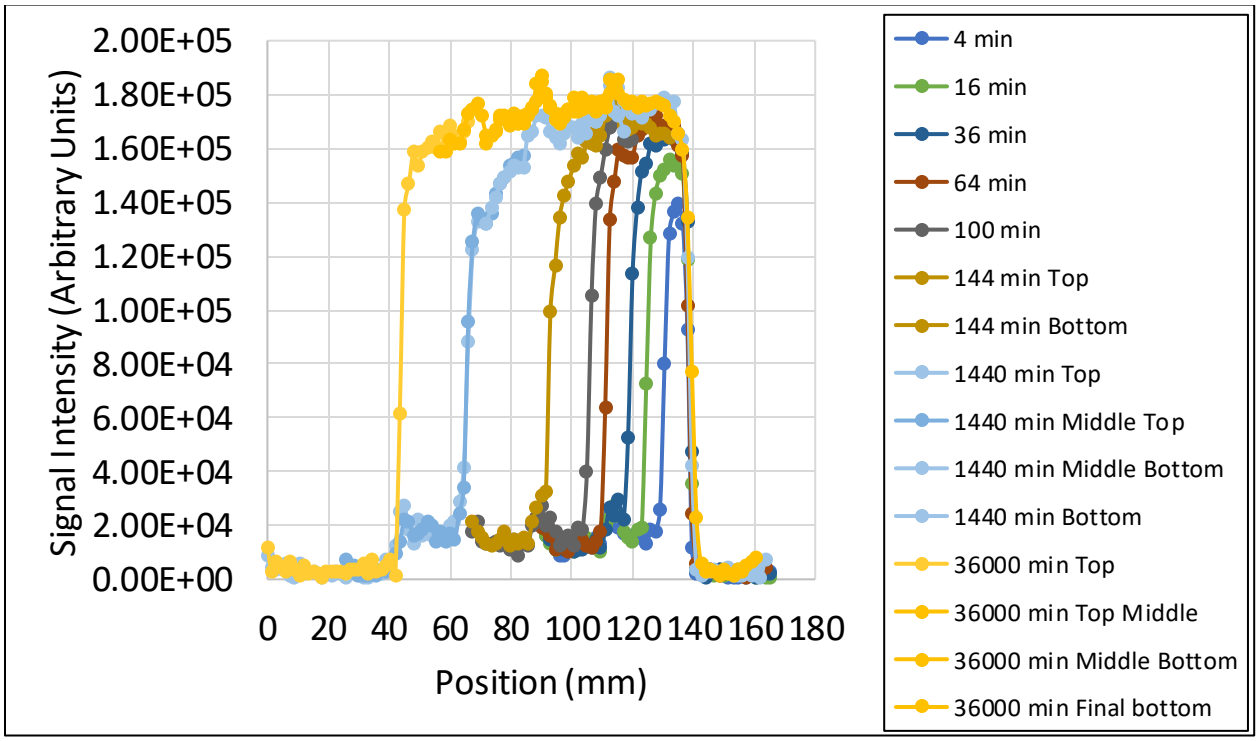

Figure 3.7- Sorptivity and steady state, 100 mm sample, 0.60 w/c, 90µs encoding time

Figure 3.7 shows the wetting front progression through the 100-mm sample at various times with one end exposed to a relative humidity of 80%. It took approximately 11 days for the wetting front to progress from the reservoir (at approximately 140 mm in Figure 3.7) to the dry end of the sample (approximately 40 mm in Figure 3.7). The final image at 36000 min was taken 11 days after the wetting front had progressed to the end of the specimen to allow for sufficient time for steady state conditions to be reached. The fiduciary markers are clearly visible at this encoding time. There is a significant difference in moisture content between the reservoir end and the dry end, showing a gradient from a fully saturated to partially saturated moisture condition that begins at around the 90-mm mark. The moisture content at the end exposed to evaporation has

approximately 12% less ^{1}H signal as compared to the wet end. In addition, the 'backfilling' behavior previously described is also present in this material, as the pores even in the first 20 mm of the material take over a day to fill to their apparent saturation point.

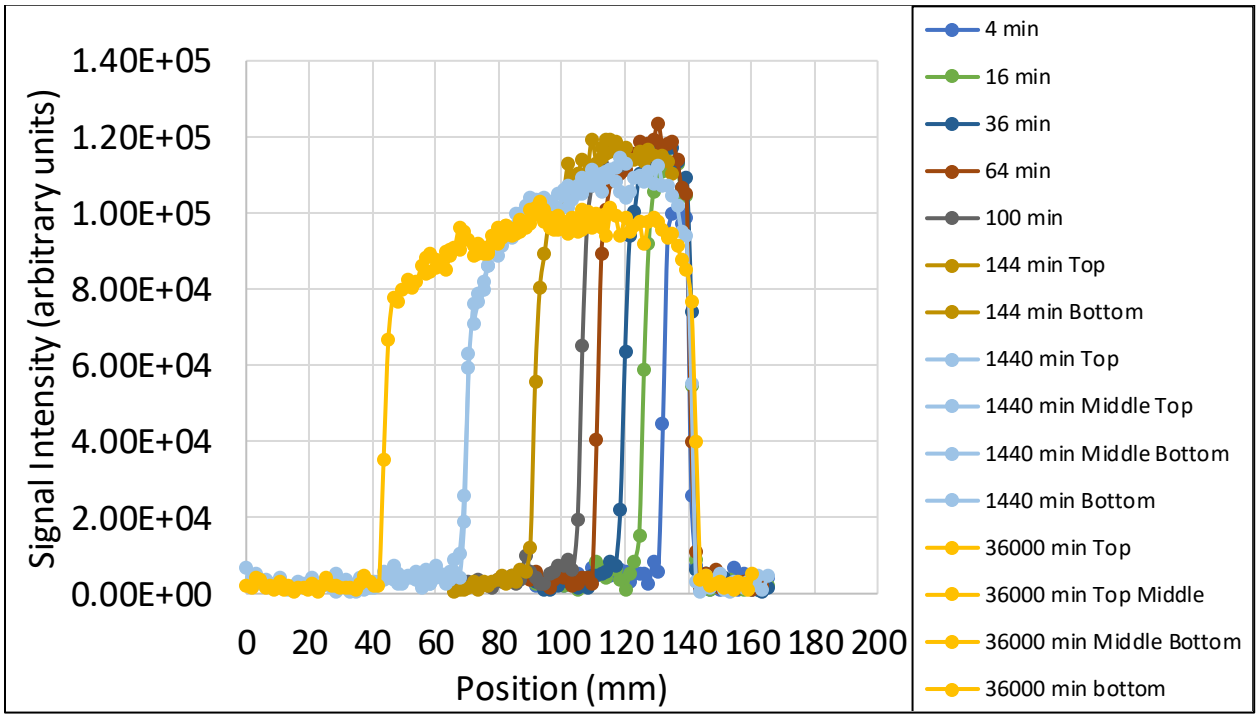

Figure 3 8- Sorptivity and Steady State, 100 mm sample, 0.6 w/c, 400µs

Figure 3.8 shows moisture content profiles of the same sample from Figure 3.7 with a different encoding time. As was the case with the baseline comparison, the fiduciary marker locations are more prominent in this figure. The moisture gradient at the steady state profile of 36000 seconds is also visible at this encoding time, with the difference that it is more prominent in this case. The difference between the wet and the dry end is nearly 20% at this encoding time. Another notable feature in Figure 3.8 is the change in the signal intensity at the wet end (approximately 100 mm - 140 mm) between the early profiles and the later ones. The magnitude of the signal from the ^{1}H population at earlier times, for example at 64 and 144 minutes, is greater than when compared

to the magnitude after 36000 minutes. The signal at this encoding time corresponds to ^{1}H from water in the larger capillary pores of the material, so a decrease in the magnitude of the signal for saturated moisture content suggests a change in the absolute volume of pores. The absolute magnitude of this signal decreased as a function of continuing exposure to water, so the author suggests that this behavior may be associated with continuing hydration in the cement paste causing a decrease in the available pore space.

3.5. Conclusions

The MRI techniques used to image the sorptive and steady state processes investigated could resolve details regarding the mass transport of water that would not be possible using either a gravimetric or height based approach to measure sorptive processes. The 45 mm samples were of insufficient length to detect any apparent evaporation from the dry end in 1-dimensional sorptive flow, even at low relative humidity. However, when imaging the 100 mm samples, a significant gradient of the moisture content was detected between the wet and dry end. Furthermore, by using different encoding times, a change in the distribution of the water as a function of time was also detected which is possibly the result of continuing hydration changing the pore structure of the materials. Thus, MRI techniques such as SPRITE are excellent tools with which to investigate mass transport of water, and furthering understanding of this complex process will allow for more accurate modelling of this important behavior.

3.6. References

[1] Hanzic, L., and R. Ilic. "Relationship between Liquid Sorptivity and Capillarity in Concrete." [In English]. Cement and Concrete Research 33, no. 9 (2003): 1385-88.

[2] Bažant, Z.P., and L.J. Najjar. "Nonlinear Water Diffusion in Nonsaturated Concrete." Matériaux et Construction 5, no. 1 (1972): 3-20.

[3] Hall, C., and T.K.M. Tse. "Water Movement in Porous Building Materials—Vii. The Sorptivity of Mortars." Building and Environment 21, no. 2 (1986): 113-18.

[4] Hall, C. "Water Movement in Porous Building Materials—I. Unsaturated Flow Theory and Its Applications." Building and Environment 12, no. 2 (1977): 117-25.

[5] Hall, C. "Water Sorptivity of Mortars and Concretes: A Review." Magazine of Concrete Research 41, no. 147 (1989): 51-61.

[6] Lockington, D.A., J.-Y. Parlange, and P. Dux. "Sorptivity and the Estimation of Water Penetration into Unsaturated Concrete." Materials and Structures 32, no. 5 (1999): 342.

[7] Phillipson, M.C., P.H. Baker, M. Davies, Z. Ye, A. McNaughtan, G.H. Galbraith, and R.C. McLean. "Moisture Measurement in Building Materials: An Overview of Current Methods and New Approaches." Building Services Engineering Research and Technology 28, no. 4 (2007): 303-16.

[8] Koptyug, I.V. "MRI of Mass Transport in Porous Media: Drying and Sorption Processes." Progress in Nuclear Magnetic Resonance Spectroscopy 65 (2012): 1-65.

[9] Carpenter, T.A., E.S. Davies, C. Hall, L.D. Hall, W.D. Hoff, and M.A. Wilson. "Capillary Water Migration in Rock: Process and Material Properties Examined by NMR Imaging." Materials and Structures 26, no. 5 (1993): 286.

[10] Leech, C., D.R. Lockington, and P. Dux. "Unsaturated Diffusivity Functions for Concrete Derived from NMR Images." Materials and Structures 36, no. 6 (2003): 413.

[11] Gummerson, R.J., C. Hall, W.D. Hoff, R. Hawkes, G.N. Holland, and W.S. Moore. "Unsaturated Water Flow within Porous Materials Observed by NMR Imaging." Nature 281, no. 5726 (1979): 56-57.

[12] Balcom, B.J., J.C. Barrita, C. Choi, S.D. Beyea, D.J. Goodyear, and T.W. Bremner. "Single-Point Magnetic Resonance Imaging (MRI) of Cement Based Materials." Materials and Structures 36, no. 3 (2003): 166.

[13] Prado, P.J., B.J. Balcom, S.D. Beyea, R.L. Armstrong, and T.W. Bremner. "Concrete Thawing Studied by Single-Point Ramped Imaging." Solid State Nuclear Magnetic Resonance 10, no. 1 (1997): 1-8.

[14] Prado, P.J., B.J. Balcom, S.D. Beyea, T.W. Bremner, R.L. Armstrong, and P.E. Grattan-Bellew. "Concrete Freeze/Thaw as Studied by Magnetic Resonance Imaging." Cement and Concrete Research 28, no. 2 (1998): 261-70.

[15] Prado, P.J., B.J. Balcom, S.D. Beyea, R.L. Armstrong, T.W. Bremner, and P.E. Grattan-Bellew. "Concrete/Mortar Water Phase Transition Studied by Single-Point MRI Methods." Magnetic Resonance Imaging 16, no. 5–6 (1998): 521-23.

[16] Beyea, S.D., B.J. Balcom, T.W. Bremner, P.J. Prado, D.P. Green, R.L. Armstrong, and P.E. Grattan-Bellew. "Magnetic Resonance Imaging and Moisture Content Profiles of Drying Concrete." Cement and Concrete Research 28, no. 3 (1998): 453-63.

[17] Young, J.J., T.W. Bremner, M.D.A. Thomas, and B.J. Balcom. "Porous Materials." In NR Imaging in Chemical Engineering, 285-303: Wiley-VCH Verlag GmbH & Co. KGaA, 2006.

[18] Petrov, O.V., G. Ersland, and B.J. Balcom. "T2 Distribution Mapping Profiles with Phase-Encode MRI." Journal of Magnetic Resonance 209, no. 1 (2011): 39-46.

[19] Beyea, S.D., B.J. Balcom, P.J. Prado, A.R. Cross, C.B. Kennedy, R.L. Armstrong, and T.W. Bremner. "Relaxation Time Mapping of Short T*2 Nuclei with Single-Point Imaging (SPI) Methods." Journal of Magnetic Resonance 135, no. 1 (1998): 156-64.

[20] Beyea, S.D., B.J. Balcom, T.W. Bremner, P.J. Prado, A.R. Cross, R.L. Armstrong, and P.E. Grattan-Bellew. "The Influence of Shrinkage-Cracking on the Drying Behaviour of White Portland Cement Using Single-Point Imaging (SPI)." Solid State Nuclear Magnetic Resonance 13, no. 1–2 (1998): 93-100.

[21] Bohris, A.J., U. Goerke, P.J. McDonald, M. Mulheron, B. Newling, and B. Le Page. "A Broad Line NMR and MRI Study of Water and Water Transport in Portland Cement Pastes." Magnetic Resonance Imaging 16, no. 5–6 (1998): 455-61.

[22] Bogdan, M., B.J. Balcom, T.W. Bremner, and R.L. Armstrong. "Single-Point Imaging of Partially Dried, Hydrated White Portland Cement." [In 1064-1858]. Journal of Magnetic Resonance 116, no. 2 (1995).

[23] Enjilela, R., P.F. de J. Cano-Barrita, A.J.K. Komar, A.J. Boyd, and B.J. Balcom. "Monitoring Steady State Moisture Distribution During Wick Action in Mortar by Magnetic Resonance Imaging (MRI)." Materials and Structures 50, no. 2 (2017): 151.

Foreword to Chapter 4

Chapter 4 is a detailed look at the surface resistivity nondestructive test method, which is used throughout the rest of the thesis (Chapters 5-8). Surface resistivity is a method which uses the conduction of electricity through the connected pore structure of the concrete being tested. This connectivity of the pore system is directly involved in the transport properties of concrete, since it is through these connected pathways that the water must flow. Chapter 4 details the evolution of different w/c concretes during continuous hydration, with decreasing connectivity of pore structure occurring as cement hydrates are formed. This evolution of the pore structure is directly measured with surface resistivity method as changes in the resistivity as a function of hydration. The effect of a pozzolanic species is also documented in Chapter 4 using surface resistivity. The pozzolan effectively creates a denser hydrated cement paste system by a conversion of one of the reaction products (calcium hydroxide) into a denser hydrate (calcium silicate hydrate). There is a marked difference in the resistivity of specimens containing silica fume, when compared to the ordinary concrete, related to the differences in pore structure and connectivity.

Most importantly for the rest of the thesis, Chapter 4 details the development of a temperature correction procedure for surface resistivity measurements that makes the measurements temperature-independent. Without such correction, the high variability of SR due to temperature results in measurements that make conclusions about damage or changes to the pore structure difficult, as detailed in Chapter 7. Based on this temperature dependant behavior, the SR readings from Chapter 5 were taken at a constant temperature. The use of the

temperature correction technique developed in Chapter 5 as applied to durability specimens is detailed in Chapter 8.

Chapter 4: Comparison of Temperature Correction Methods for Surface Resistivity Measurements for Portland Cement Concretes

Komar, A.J.K., Milton, S., Boyd, A.J.

4.1. Background

The transport properties of concrete are a critical factor when considering the long-term durability of the material. Carbonation, sulphate attack, and chloride penetration are all different deterioration mechanisms in reinforced concrete, and their severity is directly correlated with the mobility of water and dissolved ions within the concrete. Having reliable measurements of this connected pore space is therefore of great importance to engineering since it can act as a predictive indicator of the long-term performance of the material. The surface resistivity test has proven to have significant potential as a valuable test method for estimating transport properties both in the lab and in the field. However, temperatures changes found in field conditions can cause changes to the surface resistivity measurements on the order of 80%, so reliable methods of correcting for these changes are important for engineers using surface resistivity to monitor the mass transport characteristics of concrete.

4.1.1. Surface resistivity

Surface Resistivity (SR) is a nondestructive test method that measures the electrical conductivity of saturated concrete. The technique used in the following study is the Wenner probe method, although other methods of measuring resistivity are possible, such as bulk resistivity [1]. The

Wenner probe method uses four equally spaced contact points which all contact the surface of the concrete. An alternating current is passed between the outer probes of the device through the interior of the sample, with the current being carried by dissolved ions within the pore solution. An alternating current is required so that there is no net polarization or ion flow through the medium during the test. A voltmeter measures the potential difference across the inner probes induced by this current [2,3]. Through Ohm's law, the calculated resistance of this alternating current is taken as R=V/I, where *R* is the resistance in Ω, *V* is the voltage difference in Volts, and *I* is the current in amps. The overall resistance of the material is based on the overall volume through which the current passes, so both the cross-sectional area perpendicular to the current flow as well as the length of the path between the two outer probes will be a factor. Therefore, the units for the SR method are given in $\Omega \cdot m^2 \cdot m^{-1}$, but more commonly reported as Ω·cm or kΩ·cm.

Surface resistivity is sensitive to both the size and geometry of the concrete sample being tested, and size factors that take account of this variable behavior have been previously characterized [4] Morris 1996. Results from a semi-infinite slab (such as a slab that might be found in the field) can be related to samples of a finite geometry by using a size factor which takes into account the probe spacing, the overall depth of the geometry and the total length of the specimen. Using the formula reported by Morris *et al.* [4], the samples used in the following study have a length to probe spacing ratio of 5.3 and a depth to probe spacing ratio of 2.6. The associated K factor for this particular geometry is 2.05. The Proceq Resipod surface resistivity meter used for the study automatically adjusts for this size factor, and the modified results are reported herein.

4.1.2. Electrical conductivity

The current passing through the concrete volume passes primarily by way of the dissolved ions within the pore water solution. Thus, the SR test will not function if the concrete has dried to such an extent that there is no connected pore water containing ions, since the solid portion of concrete is a very effective electrical insulator. The resistivity will vary between this point and different degrees of partial saturation [5,6,7] but the resistivity will generally increase when the moisture content is below the saturation point. The ions within the pore water of concrete primarily consist of Ca^{+} and OH^{-} ions from saturated $Ca(OH)_2$ along with a variety of other alkalis that are in equilibrium with the solid cement hydrates [8,9]. Any other ionic species in the pore water will affect the overall resistivity of the medium by increasing the ion concentration and lowering overall resistivity.

Other factors which affect ion mobility will include the overall connectivity of the pore structure, the degree of saturation of the material, the diffusivity (or concentration gradient) of ions within the pores, the absorption and adsorption properties of the ions within the concrete, and any ion migration due to thermal gradients [1].

4.1.3. Temperature effect

Fluctuations in temperature of the samples can cause variations in surface resistivity measurements of up to 80% over a range that is commonly found in the field. Early attempts to quantify this behavior modelled the effect as linear, with an approximate 2-4% decrease in resistivity for each degree C the temperature increased. [10,11,12]. This linear relationship is adequate for temperature ranges of about 5-10 degrees C but becomes increasingly inaccurate for larger ranges. Another more accurate method of normalizing resistivity behavior to a common

reference temperature can be achieved by applying the Hinrichson-Rasch law (applicable to most refractory materials), as Whittington *et al.* did [3], which is of the form in Equation 4.1:

$$\rho_1 = \rho_2 e^{a(\frac{1}{T_1}-\frac{1}{T_2})}$$

Equation 4.1- Modified Hinrichson-Rasch Law, from Whittington et al. [3]

Where T_1 and T_2 are the temperature measurements of the sample in K and a is a constant. Spragg *et al.* [13,14] proposed a modified version of this approach that was based on the Arrhenius form. Their approach is found in Equation 4.2:

$$\rho_{t-ref} = \rho_t \cdot e^{\frac{E_{A-cond}}{R}(\frac{1}{T}-\frac{1}{T_{ref}})}$$

Equation 4.2- Arrhenius equation for surface resistivity temperature correction, from Spragg et al. [13]

Where $\rho_{t\text{-}ref}$ is resistivity in Ω·m at a reference temperature, ρ_t is the resistivity at testing temperature, $E_{A\text{-}cond}$ is the activation energy of conduction in kJ·mol^{-1}, R is the universal gas constant (8.314 J·mol^{-1}·L^{-1}), T is the testing temperature in K, and T_{ref} is the reference temperature in K. The reference temperature was taken to be 23°C for their studies. [13,14,18]. The activation energy of conduction is an experimentally derived value which is equated to the slope of the best fit curve from a scatterplot of the natural logarithm of resistivity in Ω·m and the inverse of temperature in K as seen in Figure 4.1.

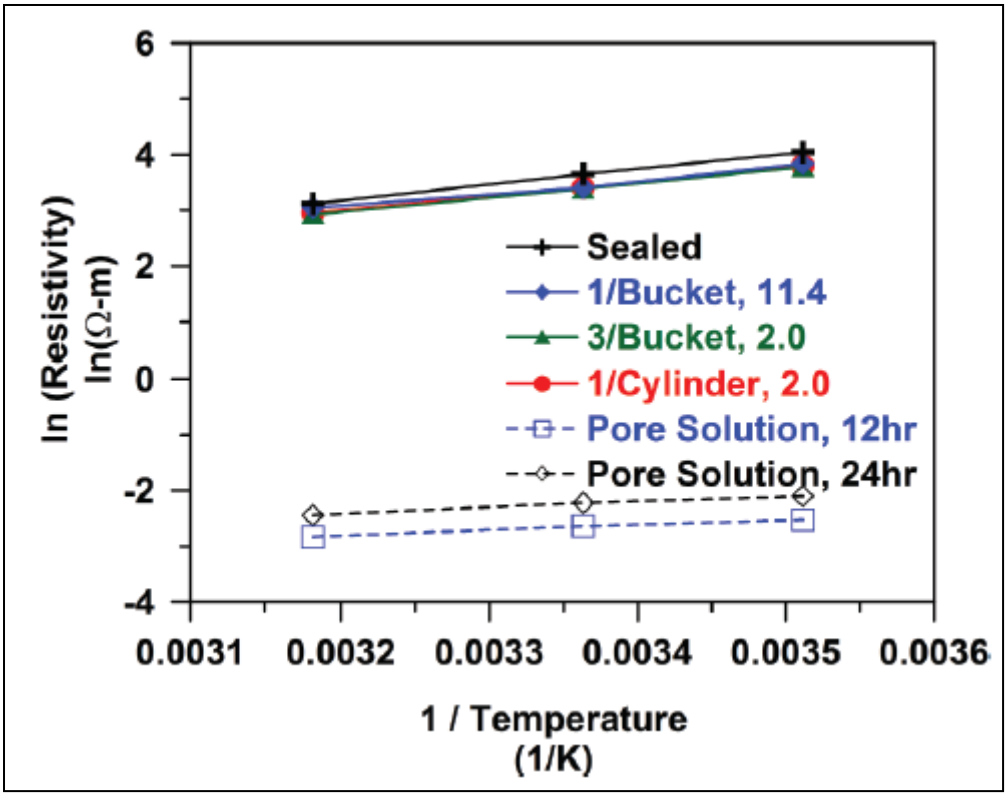

Figure 4.1- Activation Energy of Conduction. From Spragg et al. [13,14]

This slope is then multiplied by the negative of the universal gas constant to determine the activation energy of conduction. Previously reported values of $E_{A\text{-}cond}$ a for OPC - were around 18-22 kJ/mol, but some values above 30 kJ/mol have been found as well [10,13,14,15,18,19]. Similar measurements of the resistivity of the pore solution itself yield much lower values on the order of 10 kJ/mol [13,14], so the activation energy that is derived from this method must consider the combination of the resistivity of the pore water as well as the connectedness of the pathways through the concrete [3,16,17,18,20]. One issue with the method based on this Arrhenius approach is that it does not capture the large increase in resistivity associated with the freezing process. Since frozen pore water does not have freely mobile ions as is the case with its liquid form, the conductivity of ice is much lower and thus the resistivity is much higher.

The effect of different w/c and aggregate proportions are well understood in surface resistivity. The majority of the current will flow through the cement paste given that they will have a much more connected microstructure and will generally be saturated with conductive water. Concretes made with a higher w/c will have a lower electrical resistance due to the increased number of possible pathways through which the current can flow. Similarly, mixtures with a higher proportion of aggregate in their total volume will have a higher resistivity due to the decreased number of pathways.

The effect of supplementary cementitious materials on surface resistivity has also been investigated previously [3,13,14,15,20,25]. The inclusion of a pozzolanic material will affect the resistivity in two primary ways: by decreasing the permeability of the pore structure via production of additional cement hydrates, and by modifying the composition of pore water ions by changing the concentration of some ionic species. These effects on permeability and changes in the pore water chemistry have been documented elsewhere [8,9,13,17,23,24]. Other research has noted that the conductivity of concretes made with pozzolans is generally lower than as compared to OPC [9,15,17,19,22,25]

4.2. Materials and Methods

4.2.1. Mixture design

Eight mixtures in total were prepared for the study by Milton [27]. Four different water to cement ratios were prepared, ranging from 0.30 to 0.45. Half of the mixtures had 10% of the portland cement replaced with silica fume. The proportions for the eight mixtures can be found in Table 4.1

Table 4.1- Mixture design

Water to Cementitious Material Ratio	Type GU Cement (kg m^{-3})	Silica Fume (kg m^{-3})	Coarse Aggregates (kg m^{-3})	Fine Aggregates (kg m^{-3})	Water (kg m^{-3})	Water Reducing Admixture (kg m^{-3})
0.30	653.7	0.0	944.6	576.7	203.0	4.6
0.35	562.5	0.0	943.0	651.8	204.3	3.9
0.40	490.2	0.0	944.0	708.9	205.4	3.4
0.45	435.4	0.0	943.7	753.3	206.1	3.0
0.30	587.4	65.4	926.7	575.0	201.1	6.1
0.35	506.2	56.2	936.3	641.0	202.6	5.3
0.40	440.5	48.8	936.4	701.6	204.1	4.6
0.45	391.0	43.8	939.8	743.9	205.0	4.1

All samples were cast and prepared in accordance with the ASTM C39 standard. The total mixture batch was large enough to produce approximately seven 100 mm x 200 mm cylinders. A shake table was used to vibrate the cylinders in their plastic state to ensure proper consolidation and to minimize entrapped air. Granitic rock with low absorption values was used as both the coarse and fine aggregates, and the absorption of the material was accounted for in the mixture design. The absorption was measured to be 0.5% for the coarse aggregate and 1.1% for the fine aggregate, with a fineness module of 2.7 for the fine aggregate. The maximum aggregate size was 14 mm. The aggregates were obtained from a laboratory stockpile and were found to be in a dry state.

All samples were demolded after 24 hours and prepared for surface resistivity measurement. Three specimens with the highest visual consistency were selected from each batch so as to minimize any observable voids or defects that might affect the surface resistivity measurements. Figure 4.2 shows the configuration of the markings on each cylinder as to divide the curved surface into 8 equidistant positions.

Figure 4.2- Surface resistivity markings on the side of a typical cylinder

A cross-marking was placed on these equidistant lines 40 mm from the edge of the cylinders so that the centreline of the SR apparatus would coincide with the centre of the cylinder to minimize edge effects. These positions were individually labelled so that a surface resistivity measurement with the Wenner probe configuration could be taken at the exact same spot on the surface. When the samples were not being tested, they were being cured in a saturated limewater solution to minimize any calcium hydroxide leaching.

4.2.2. Surface resistivity - temperature testing

A watertight basin was set up so that it could accommodate three submerged cylinders, as well as an immersed circulating pump and heating coil. The immersion pump was used to create a circulating current within the basin to minimise any temperature gradients that could develop. The depth of the water was such that the cylinders were completely submerged within the basin

but with minimal excess water overtop. To lower the temperature initially, large ice cubes were prepared and placed within the circulating water without the heating coil so that the water could be lowered close to the freezing point. The cylinders were submerged within individual water containers and placed within a refrigerator. Both the ice water and the water in the circulating bath were obtained from the municipal water supply. At no point did any of the cylinders drop below 0 degrees, and no ice was observed on any of the individual water containers used for pre-cooling. The pre-cooled cylinders were introduced into the circulating ice water bath and the cylinders were given time to come to thermal equilibrium with the ice water, for a minimum of 10 minutes.

The heating coil was then suspended along the edge of the water within the circulating current so that a large volume of water would pass over this coil and heat the entire water basin in a uniform manner. Individual cylinders were taken out of this water bath and placed on an electrically insulated stand after excess water was wiped off of the surface to minimize any bath water on the surface. The surface temperature of the cylinder was then measured with an infrared laser thermometer pointed at roughly the same location and recorded. Eight surface resistivity measurements were taken at the pre-marked locations around the curved surface of the cylinder and the cylinder was subsequently replaced into the water bath. These eight SR readings were taken as quickly as possibly to minimise any heating in the ambient temperatures of the lab. The next of the three cylinders was then tested in the same manner.

The heating coil was activated so that the entire circulating bath and concrete cylinder system would heat at the same rate. The temperature of the water bath was independently measured with both a mercury thermometer as well as a thermocouple, and the results were consistent

with the infrared thermometer ± 0.5 °C. The overall rate of heating of the system was somewhat dependant on the laboratory conditions and the quantity of the ice cubes used for the initial cooling, but on average, one set of eight SR readings could be taken at about each 1 °C. The total temperature range of the heating bath-cylinder system was from about 4 °C to 30°C, with few outliers falling outside that range. This surface-resistivity temperature testing protocol was repeated at 1, 7, 14, 28, and 90 days after the casting date for each of the eight mixtures.

4.2.3. Data analysis

The surface resistivity data were analysed using three different curve-fitting methods to generate functions that could give surface resistivity readings which were normalized with respect to temperature effects.

4.2.3.1. Method 1

The data were separated into the results from each of the three individual samples, so that all the curve fitting results were performed on an individual sample. At each temperature point, the 8 surface resistivity readings taken from the same points along the surface were averaged together to produce a single point at that temperature. An exponential root mean square curve of the form found in Equation 4.3 was fitted to this data for each of the cylinders at each of the testing intervals for all eight of the mixtures.

$$f(T) = a \cdot e^{-b*T}$$

Equation 4.3- Best fit curve form

Where *a* is in kΩ·cm and *b* is in 1/°C, and both are derived curve fitting parameters, *f(T)* is the predicted surface resistivity measurement in kΩ·cm and T is temperature in °C. The R^2 from this

method was generally > 0.99 for each of the curves. The best-fit curve for the mixture and maturity was then derived by fitting an exponential root mean square curve of the form in Equation 4.3 to the average values from each of the three functions over a range of 0 to 35 ° C in 0.5 ° C increments.

This method was selected to minimise any sampling bias that might have resulted from more data points at any subset of the temperature range or on one sample, since all temperature ranges and cylinders were equally weighted.

4.2.3.2. Method 2

For each mixture and maturity, the individual paired SR-T data points from all three samples were plotted on a single scatterplot and an RMS exponential curve of the form in Equation 4.3 was generated. The resulting R^2 was lower for these best-fit curves because the entire range of SR values at any given temperature was represented, but a better representation of the variability was found. The lowest R^2 was 0.890, the highest was 0.995 and the average R^2 was 0.958 for Method 2.

The differences between the curves generated by Methods 1 and 2 were not statistically significant per a two-sample unequal variance paired student-t test for all mixtures and at all testing intervals.

4.2.3.3. Method 3

The modified Arrhenius method as described by Spragg *et al.* [10,11] was used to analyze the SR-T data sets for all mixtures and testing intervals. The natural logarithm of each SR measurement from each of the three cylinders in each mixture and testing interval in Ω·m was plotted against

the inverse of the temperature readings in Kelvin. A linear best-fit curve was derived for each mixture and testing interval of the form in Equation 4.4:

$$\ln(\mathrm{SR}) = \mathrm{a} * \mathrm{K}^{-1} + \mathrm{b}$$

Equation 4.4- Best fit curve for Arrhenius function

Where *a* is the slope of this curve, *b* is a constant, SR is in Ω·m and *K* is in Kelvin. The slope a of this curve was then multiplied by the negative of the ideal gas constant 8.314 $kJ \cdot K^{-1} \cdot mol^{-1}$ to give the activation energy of conduction for each mixture and each testing interval.

4.2.4. Temperature correction

4.2.4.1. Correction factor method

To determine a normalized SR reading independent of temperature effects, a correction factor was needed that would allow the SR readings to be adjusted to a common value. The methodology for calculating the correction factors derived from Method 1 and 2 are identical and found below. The magnitude of the correction factor ΔSR is defined in Equation 4.5:

$$\Delta\mathrm{SR} = \mathrm{f}(\mathrm{T}_{\mathrm{measured}}) - \mathrm{f}(\mathrm{T}_{\mathrm{reference}})$$

Equation 4.5- Correction factor form

Where $f(T_{measured})$ is the SR value in kΩ·cm from Equation 4.3 (from Method 1 or 2) at the measured temperature $T_{measured}$ in °C, $f(T_{reference})$ is the SR value in kΩ·cm from Equation 4.3. Since $f(T_{reference})$ will be constant, ΔSR can alternatively be formulated as Equation 4.6:

$$\Delta\mathrm{SR} = \mathrm{a} \cdot \mathrm{e}^{\mathrm{b} \cdot \mathrm{T}} - \mathrm{C}$$

Equation 4.6- Correction factor alternative form

Where C is the value of $f(T_{reference})$ in kΩ·cm. The temperature corrected SR value is then taken in Equation 4.7 as:

$$SR_{corrected} = SR_{raw} + \Delta SR$$

Equation 4.7- Corrected surface resistivity measurement

Where SR_{Raw} is the original SR reading in kΩ·cm taken at temperature $T_{measured}$ and ΔSR is the result from Equation 4.5.

To graphically represent this SR data, SR-T- hydration time contour maps for each of the mixtures were created by plotting the SR-T curves at each time interval. Linear interpolation was used to connect adjacent curves along isothermal lines. This method allows an arbitrary SR-T curve to be generated from any date between 1 and 90 days of hydration. The ΔSR value at any given time and temperature can be directly read from the graph by determining the SR value at the measurement temperature and the reference temperature and determining the difference.

Every paired SR-T data point from all mixtures and testing intervals were temperature corrected in this manner ($T_{reference}$ chosen to be 20 °C) so that data from all mixtures could be compared at the same temperature.

4.2.4.2.Arrhenius method

The $E_{A\text{-}cond}$ was derived for each of the mixtures and testing intervals by linear best fit techniques, and the surface resistivity readings of each paired SR-T data point were temperature corrected to $T_{reference}$ using the modified Arrhenius approach as shown in Equation 4.2. The temperature corrected results of each data point were then compared to Methods 1 and 2.

4.3. Results and Discussion

4.3.1. Method 1

40 SR-T curves from the different hydration times and eight mixtures were created based on the outlined procedure. To determine an average SR-T curve for each mixture and hydration time, a unique SR-T curve was determined for each of the three test specimens and the average of these three curves was found, as can be seen in Figure 4.3. Figure 4.3 shows typical SR-T curves from the individual cylinders as well as the average curve resultant from Method 1. The R^2 values for the individual cylinder SR-T curves were quite high, showing that the variation between different specimens of the same mixture was much higher than the variation in surface resistivity measurements from a single cylinder.

The Y-intercept in Figure 4.3 represents the highest resistivity that the specimen will have before the pore water begins to freeze. This value is more representative of the range of conditions that would be encountered in fieldwork with surface resistivity, as compared to the predicted values

which are derived from the Arrhenius method that does not account for the differences in resistivity that arise from the freezing process.

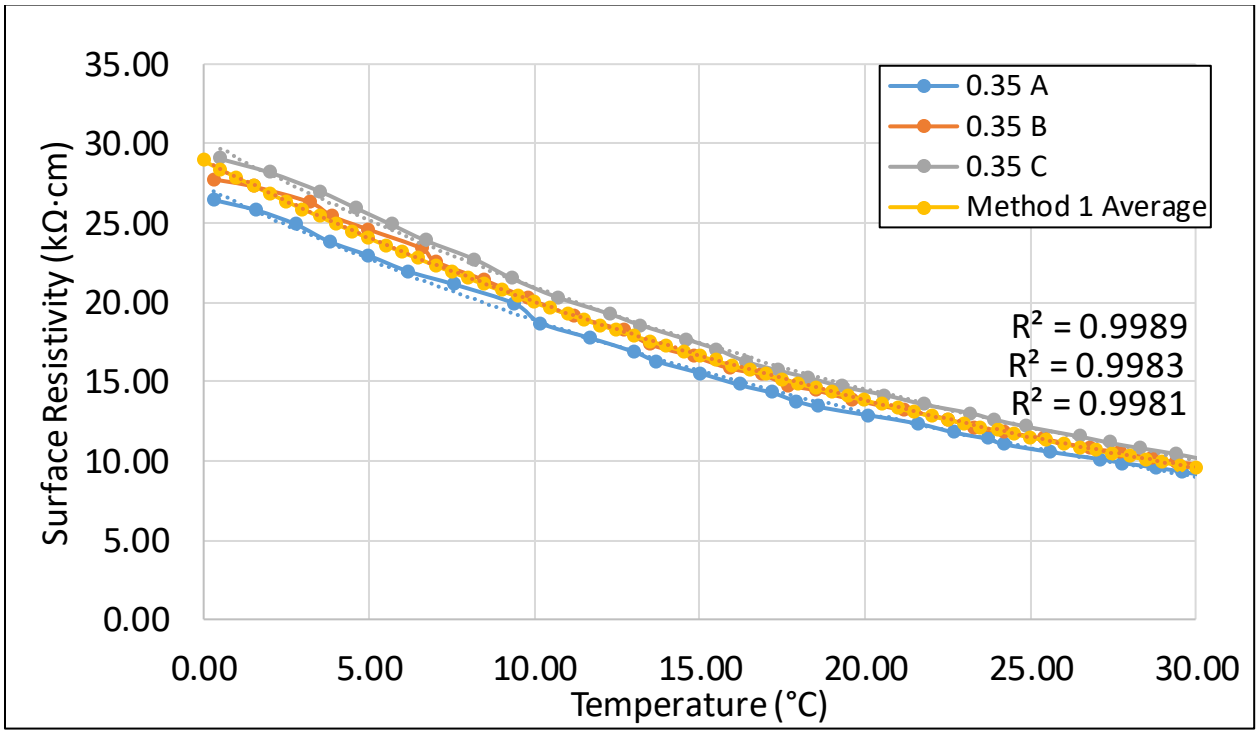

Figure 4.3- 0.35 w/c 7-day hydration surface resistivity vs temperature,

4.3.2. Method 2

Figure 4.4 shows the same mixture and hydration time as Figure 4.3, but Method 2 was used to determine the average exponential curve. Figure 4.4 shows that there is a larger variability of the raw data resulting from the 8 individual testing sites on the three cylinders. The results from each individual test site are remarkably consistent throughout the testing procedure, and the spread from each individual cylinder remains very similar across the temperature range. The eight readings from each cylinder at each temperature are clearly visible in Figure 4.4 as straight lines parallel to the y axis. There is more variability from the SR readings at lower temperatures as compared to the maximum temperature range, but the average value describing the spread of

the data remains quite consistent. The average SR-T best fit curves were not significantly different from Method 1 for any of the 40 curves generated.

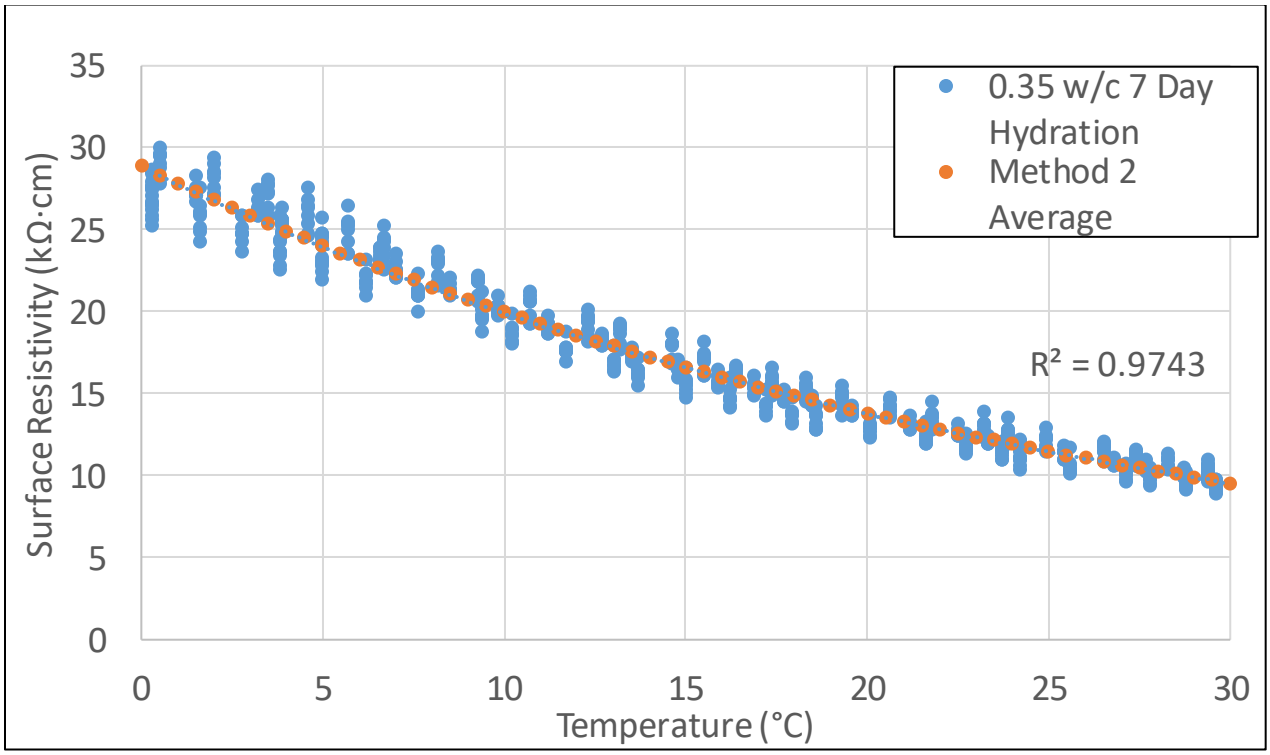

Figure 4.4- 0.35 W/C 7-day hydration surface resistivity vs temperature, Method 2

4.3.3. Method 3

The determination of activation energy was performed for each of the 40 curves. To convert the slope on the ln(SR)-1/K diagram into the activation energy of conduction used in the Arrhenius equation, the result as obtained from linear RMS curve fitting was multiplied by the ideal gas constant 8.314 $J \cdot mol^{-1} \cdot K^{-1}$. A typical example of the ln(SR)-1/K diagram used for the curve fitting is found in Figure 4.5. The same dataset used to create Figures 4.3 and 4.4 was used in Figure 4.5 to provide a basis of comparison. A 95% confidence interval on the slope was also determined for each of the curves to provide a measure of the uncertainty in the activation energy calculation.

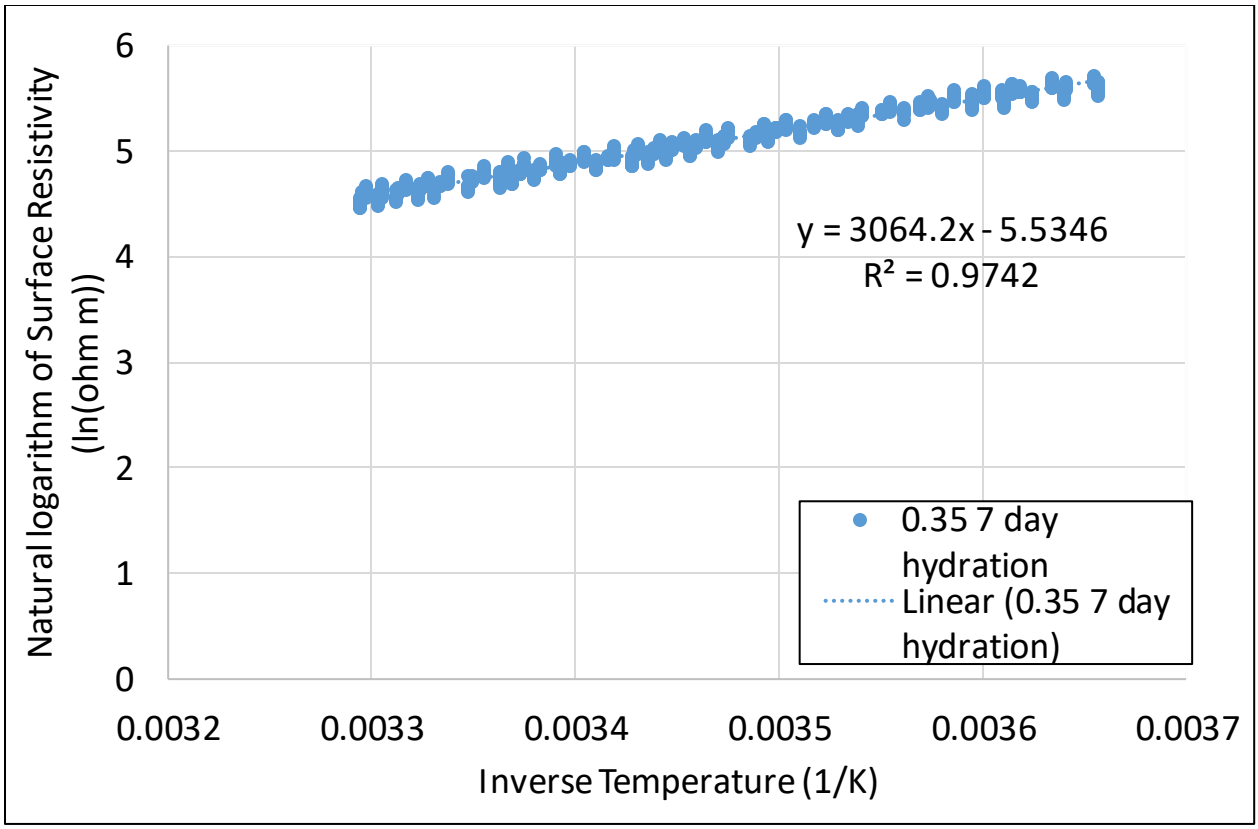

Figure 4.5- 0.35 W/C 7-day hydration ln(SR) 1/K diagram, method 3

4.3.4. Comparison between the 3 methods

The best fit curve results from the three different methods for the ordinary concrete can be found in Table 4.2 and for the 10% silica fume in Table 4.3.

Table 4.2- Regular concrete SR-T curves and activation energy

W/C	Curing Time	Method 1 Best Fit	Method 2 Best Fit		Method 3	
		Average Equation	Average Equation	R^2	Activation Energy kJ/mol	R^2
0.3	Day 1	19.83*exp(-0.03267*x)	19.85*exp(-0.03247*x)	0.9501	22.46	0.9511
	Day 7	44.7*exp(-0.03801)	44.75*exp(-0.03807*x)	0.9687	27.04	0.9714
	Day 14	52.98*exp(-0.03799*x)	53.08*exp(-0.03812*x)	0.9643	27.08	0.9707
	Day 28	63.89*exp(-0.03973*x)	63.99*exp(-0.03983*x)	0.9662	28.70	0.9731
	Day 90	82.05*exp(-0.03974*x)	82.09*exp(-0.03977*x)	0.9679	28.87	0.9748
0.35	Day 1	11.41*exp(-0.02926*x)	11.39*exp(-0.02921*x)	0.9509	19.60	0.9502
	Day 7	28.9*exp(-0.03697*x)	28.86*exp(-0.03692*x)	0.9725	25.47	0.9742

	Day 14	35.46*exp(-0.03852*x)	35.35*exp(-0.03819*x)	0.9727	26.33	0.9753
	Day 28	40.53*exp(-0.03924*x)	40.42*exp(-0.03908*x)	0.9711	26.89	0.9747
	Day 90	48.46*exp(-0.04023*x)	48.21*exp(-0.03991*x)	0.9662	27.41	0.9686
0.4	Day 1	8.575*exp(-0.02696*x)	8.584*ex(-0.02703*x)	0.9247	18.41	0.9284
	Day 7	22.93*exp(-0.03524*x)	22.94*exp(-0.03527*x)	0.9605	24.09	0.9647
	Day 14	28.53*exp(-0.03735*x)	28.55*exp(-0.03741*x)	0.9634	25.83	0.9657
	Day 28	32.39*exp(-0.03748*x)	32.39*exp(-0.0375*x)	0.9649	25.70	0.9678
	Day 90	34.69*exp(-0.03635*x)	34.67*exp(-0.0363*x)	0.9617	25.02	0.966
0.45	Day 1	11.67*exp(-0.03003*x)	11.66*exp(-0.03003*x)	0.9524	20.47	0.9517
	Day 7	25.54*exp(-0.032*x)	25.53*exp(-0.03201*x)	0.9582	22.94	0.9587
	Day 14	32.33*exp(-0.03575*x)	32.35*exp(-0.03577*x)	0.9701	24.78	0.9744
	Day 28	35.81*exp(-0.03557*x)	35.83*exp(-0.03561*x)	0.9562	24.85	0.9628
	Day 90	37.57*exp(-0.03305*x)	37.54*exp(-0.033*x)	0.9527	23.54	0.9607

Table 4.3- 10% silica fume replacement concrete SR-T curves and activation energy

W/C	Curing Time	MATLAB (method 1)	MATLAB (Method 2)		Method 3 Best Fit	
		Average Equation	Average Equation	R^2	Activation Energy (kJ/mol)	R^2
0.3	Day 1	19.27*exp(-0.03335*x)	19.36*exp(-0.03382*x)	0.8909	22.70	0.8908
	Day 7	86.36*exp(-0.03668*x)	86.41*exp(-0.03673*x)	0.9238	26.26	0.9338
	Day 14	229.6*exp(-0.04515*x)	229.3*exp(-0.04506*x)	0.9516	30.50	0.9586
	Day 28	448.8*exp(-0.04822*x)	448.6*exp(-0.04819*x)	0.9695	32.73	0.9725
	Day 90	684.6*exp(-0.0435*x)	683.7*exp(-0.04343*x)	0.99443	31.63	0.9526
0.35	Day 1	11.48*exp(-0.03053*x)	11.48*exp(-0.03056*x)	0.9462	20.54	0.9476
	Day 7	57.02*exp(-0.03817*x)	56.99*exp(-0.03816*x)	0.9792	26.15	0.9791
	Day 14	130.4*exp(-0.04148*x)	130.4*exp(-0.0415*x)	0.9843	28.70	0.9851
	Day 28	242*exp(-0.04339*x)	231.3*exp(-0.04321*x)	0.9817	29.76	0.9848
	Day 90	358.1*exp(-0.04084*x)	356.9*exp(-0.04066*x)	0.9655	29.49	0.9701
0.4	Day 1	9.386*exp(-0.02574*x)	9.389*exp(-0.02578*x)	0.8921	17.83	0.8945
	Day 7	55.48*exp(-0.03179*x)	55.55*exp(-0.03185*x)	0.9444	22.70	0.9223
	Day 14	144.8*exp(-0.03676*x)	145.1*exp(-0.03688*x)	0.942	26.16	0.9504
	Day 28	280.4*exp(-0.04359*x)	280.9*exp(-0.0437*x)	0.9717	30.06	0.9739
	Day 90	469.4*exp(-0.04648*x)	470.2*exp(-0.04656*x)	0.9706	32.18	0.9714
0.45	Day 1	4.651*exp(-0.02301*x)	4.649*exp(-0.02301*x)	0.9242	17.83	0.9282
	Day 7	28.75*exp(-0.03501*x)	28.73*exp(-0.03494*x)	0.9567	23.69	0.9602
	Day 14	75.31*exp(-0.03666*x)	75.25*exp(-0.03663*x)	0.9714	25.21	0.9736

	Day 28	137.8*exp(-0.03886*x)	137.7*exp(-0.0388*x)	0.9748	26.46	0.976
	Day 90	236.6*exp(-0.04033*x)	236.3*exp(-0.04014*x)	0.9725	28.08	0.9742

Tables 2 and 3 show that there was very little difference between the equations derived from Method 1 and Method 2. Note that the first method of curve fitting does not have an associated best-fit statistic because it exactly describes the algebraic average of three exponential curves and thus the associated R^2 value is 1. The mixtures in Table 4.3 which have 10% silica fume as a cementitious replacement show an order of magnitude higher resistivity as compared to the ordinary concrete. This was expected due to the additional densification of the pore structure due to the pozzolanic reaction as well as the change in the ion concentration of the pore water that carries the electrical current.

The effect of hydration on surface resistivity is clear from Tables 4.1 and 4.2, where a shorter curing period results in lower activation energy and a shallower surface resistivity curve for all eight mixtures. Continued curing caused all of the resistivity values and activation energy to increase as well. This was expected since continued curing is associated with increased precipitation of cementitious hydrates that would cause the densification of the microstructure and therefore decrease the number of connected pathways through which the current could flow.

The effect of w/c is also clear from Tables 4.2 and 4.3, which indicates that, in general, the mixtures with a higher binder content result in a higher resistivity. This result was expected since a lower w/c is associated with a denser microstructure and fewer connected pathways, which would allow for less current flow. This relationship between w/c and surface resistivity was relatively consistent for the eight mixtures examined.

Two exceptions to this expected w/c surface resistivity relationships occurred in the 0.40 mix and the 0.40 10% silica fume mixtures. For the former, the 0.40 w/c appeared to have lower overall resistivity as compared to the other ordinary concrete mixtures, which would seem to suggest that it had a higher effective w/c than the 0.45. In the 0.40 w/c, 10% replacement mixture, the opposite effect was observed, where the resistivity appeared to fall somewhere between the 0.30 10% and the 0.35 10% mixtures, suggesting a w/c somewhere between these two values. A possible explanation for these apparent w/c discrepancies could be related to the small size of the mixture batches. The total amount of water making up the difference between the four w/c was on the order of 5 mL, so even a small amount of evaporation or additional water added in error would have been sufficient to dramatically change the w/c values.

4.3.5. Activation energy vs time

The measured activation energy versus hydration time for the 4 ordinary concrete mixtures can be found in Figure 4.6 and Figure 4.7 for the 10% silica fume replacement. The error bars in Figures 4.4 and 4.5 represent the 95% confidence interval on the slopes as determined by the curve fitting off the Arrhenius graphs. Both figures showed that the activation energy of conduction was quite similar for all eight mixtures, between 18-22 $kJ \cdot mol^{-1}$ to begin, which agreed with reported values for this measurement. However, all eight mixtures showed a significant increase in activation energy as a function of hydration, with a larger development of this activation energy observed for the 10% SF replacement mixtures. Two of these mixtures of the lower w/c developed activation energies greater than 30 $kJ \cdot mol^{-1}$, which was on the high end of reported values for these measurements. Most this increase in this parameter occurred in the

first 14 days for the OPC mixtures and at 28 days for the SF mixtures. This slower development of activation energy for the SF mixtures is consistent with the pozzolanic effect.

Notable from Figure 4.7 is the anomalous behavior of the 0.40 10% SF mixture. The development of the activation energy was much larger for this mixture than compared to any of the other mixtures, and the final value of activation energy at 90 days was larger than the 0.30 10% mixture.

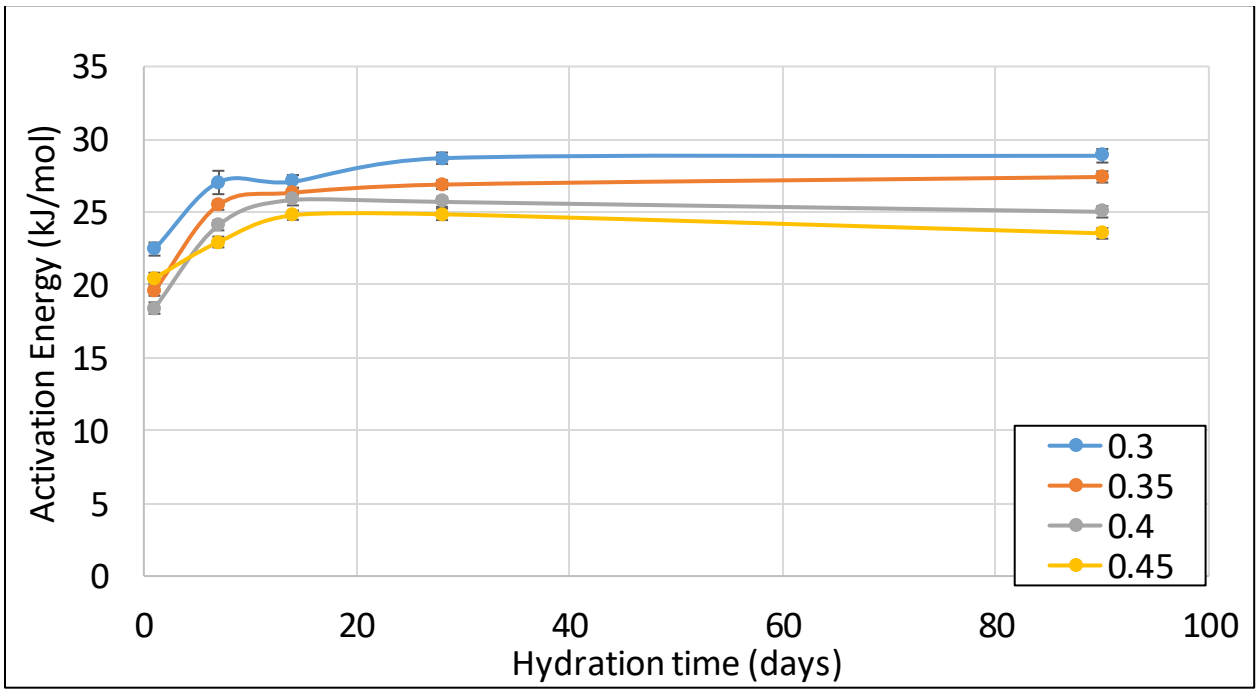

Figure 4.6- Activation energy of conduction for ordinary concrete mixtures

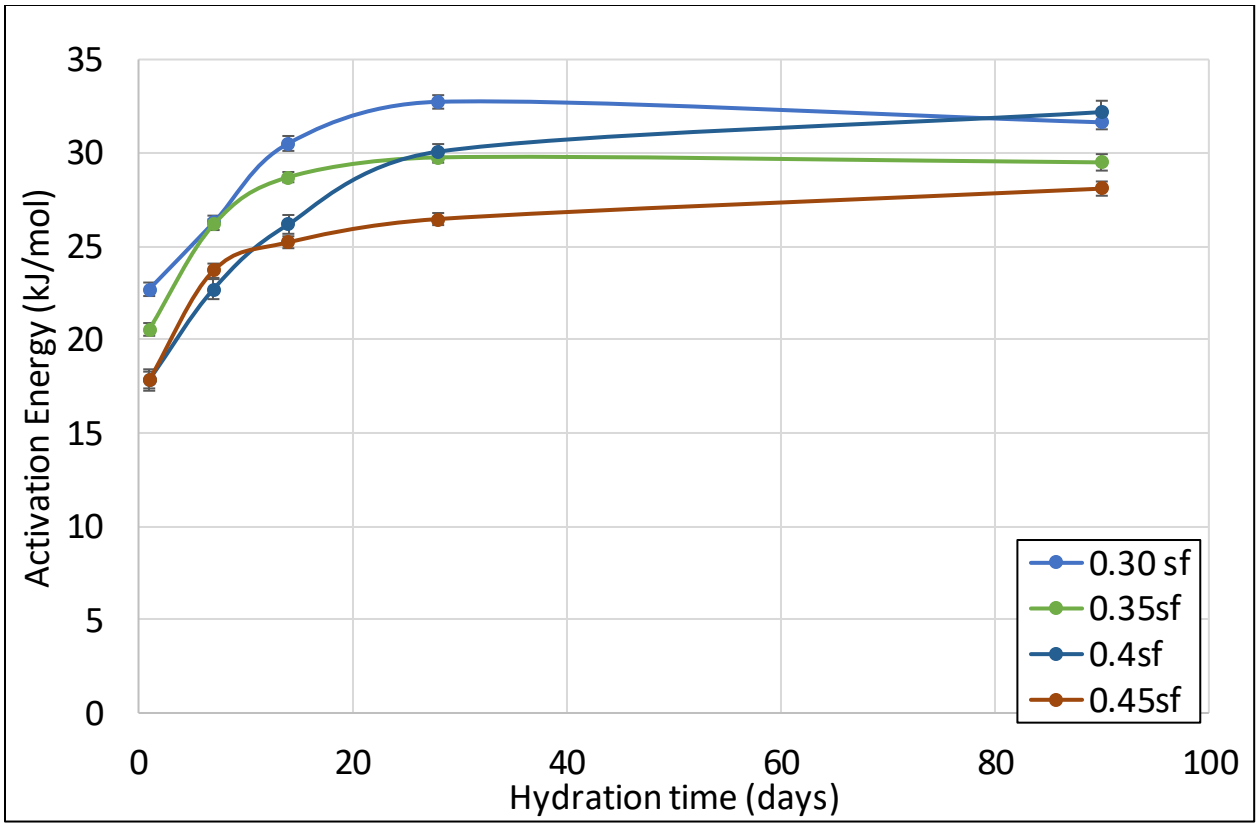

Figure 4.7- Activation energy of conduction for 10% silica fume mixtures

4.3.6. Surface resistivity temperature time

Figures 4.8 through 4.15 show the SR-T curves changing over time as contour maps of surface resistivity. The OPC mixtures in Figures 4.6 through 4.10 were all plotted with a range of 0-90 kOhm·cm values, and the 10% replacement mixtures were plotted from 0-700 kOhm·cm. Each contour line in Figures 4.8 through 4.11 is in 5 kOhm·cm increments, and for the 10% SF replacement concretes the contour lines are in 25 kOhm·cm increments. The surfaces were

created by linear interpolation between the SR-T curves from each of the 5 hydration times for all eight mixtures

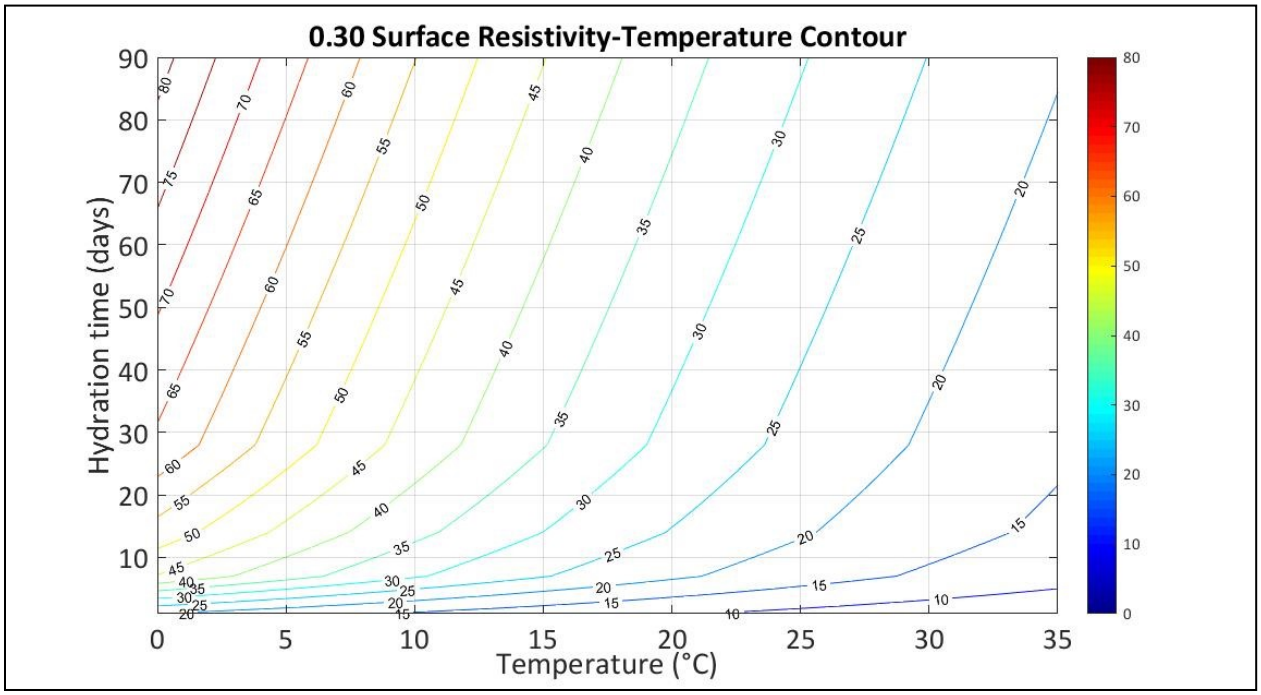

Figure 4.8- SR-T-Hydration relationship for 0.30 OPC concrete

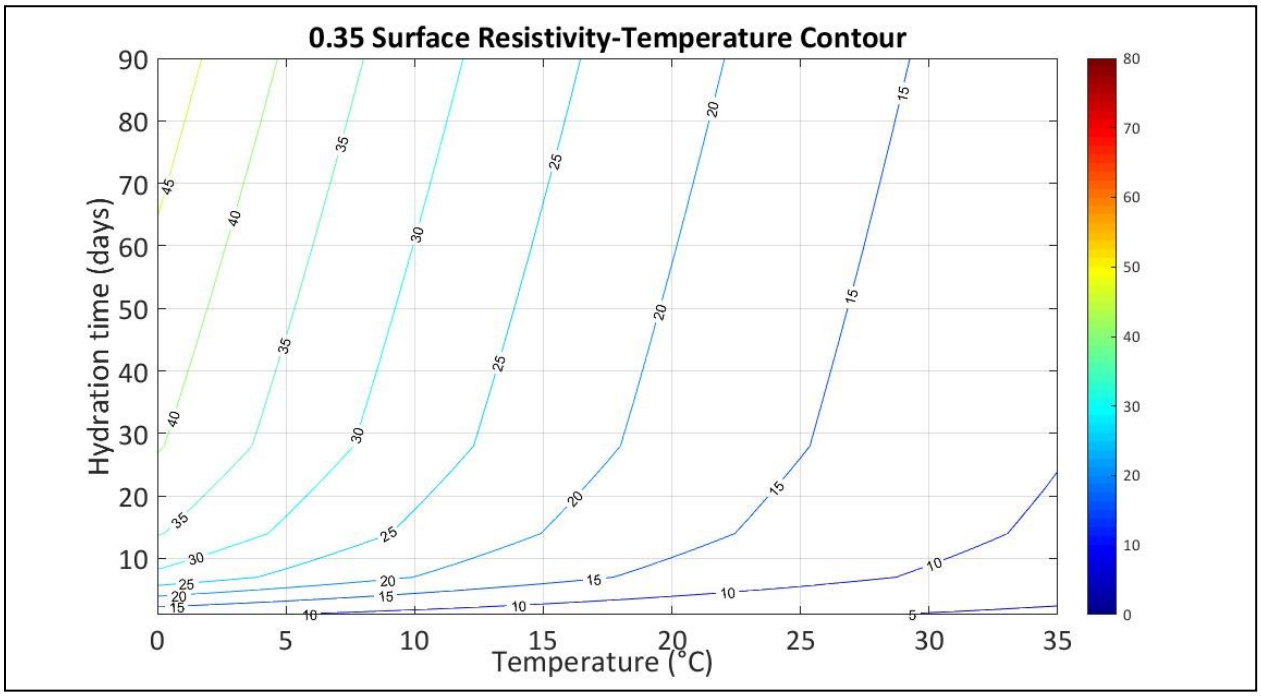

Figure 4.9- SR-T-Hydration relationship for 0.35 OPC concrete

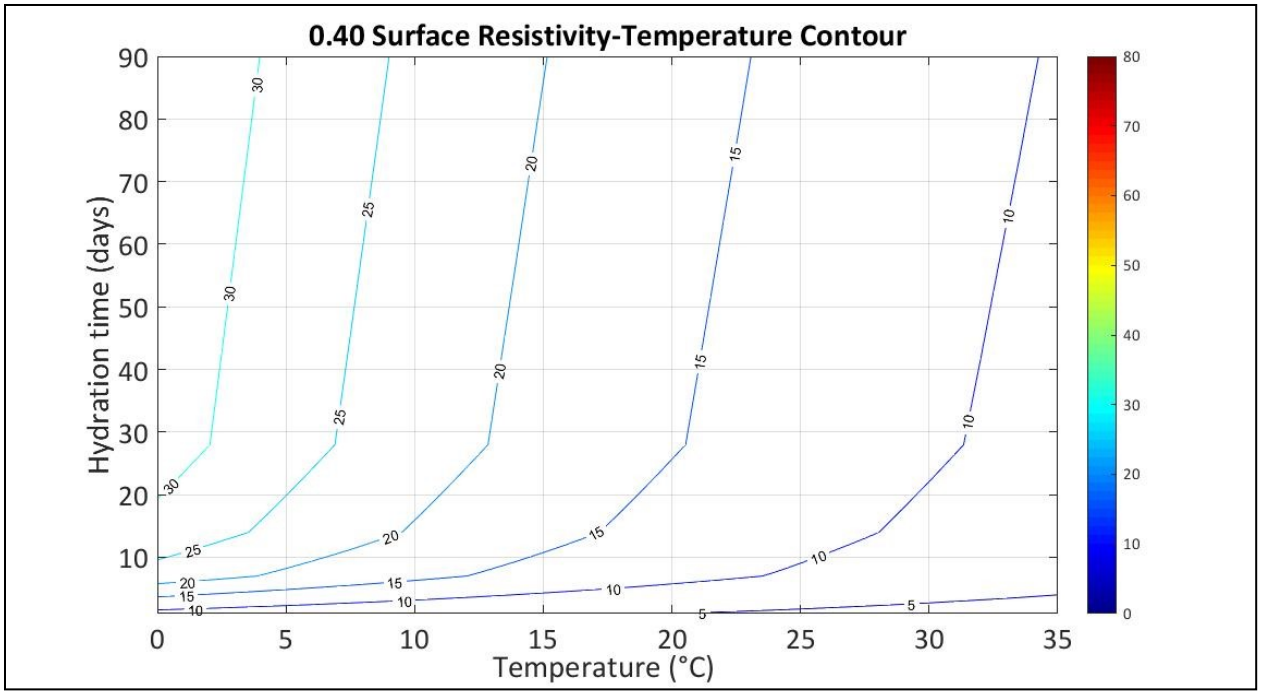

Figure 4.10- SR-T-Hydration relationship for 0.40 OPC concrete

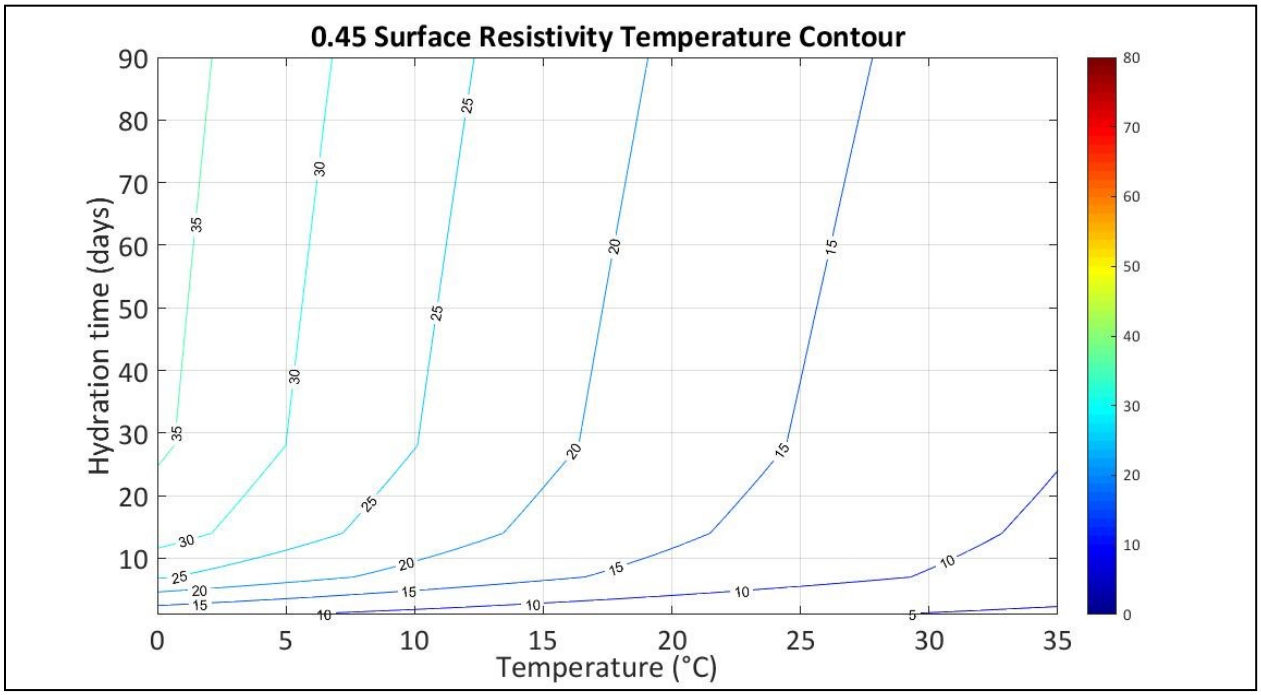

Figure 4.11- SR-T-Hydration relationship for 0.45 OPC concrete

Figures 4.8 through 4.11 show a very clear relationship between the w/c and maximum resistivity, where the lower w/c is strongly correlated with having a higher resistivity. This

behavior is consistent with the denser microstructure associated with lower w/c mixtures. Not only do the lower w/c mixtures develop a higher maximum resistivity as compared to the higher w/c mixtures, but the range of surface resistivity between 0 and 35 °C is greater. This behavior is of integral importance in the temperature correction of surface resistivity measurements since it is strongly affected by w/c ratio. When comparing Figures 4.10 and 4.11, the SR temperature - time behavior strongly suggests that the 0.40 OPC mixture had a higher effective w/c ratio as compared to the 0.45 OPC, since the maximum SR measured at 90 days of hydration for the 0.40 OPC mixture was lower than that for the 0.45 OPC mixture. This anomaly for the OPC has been discussed in other sections.

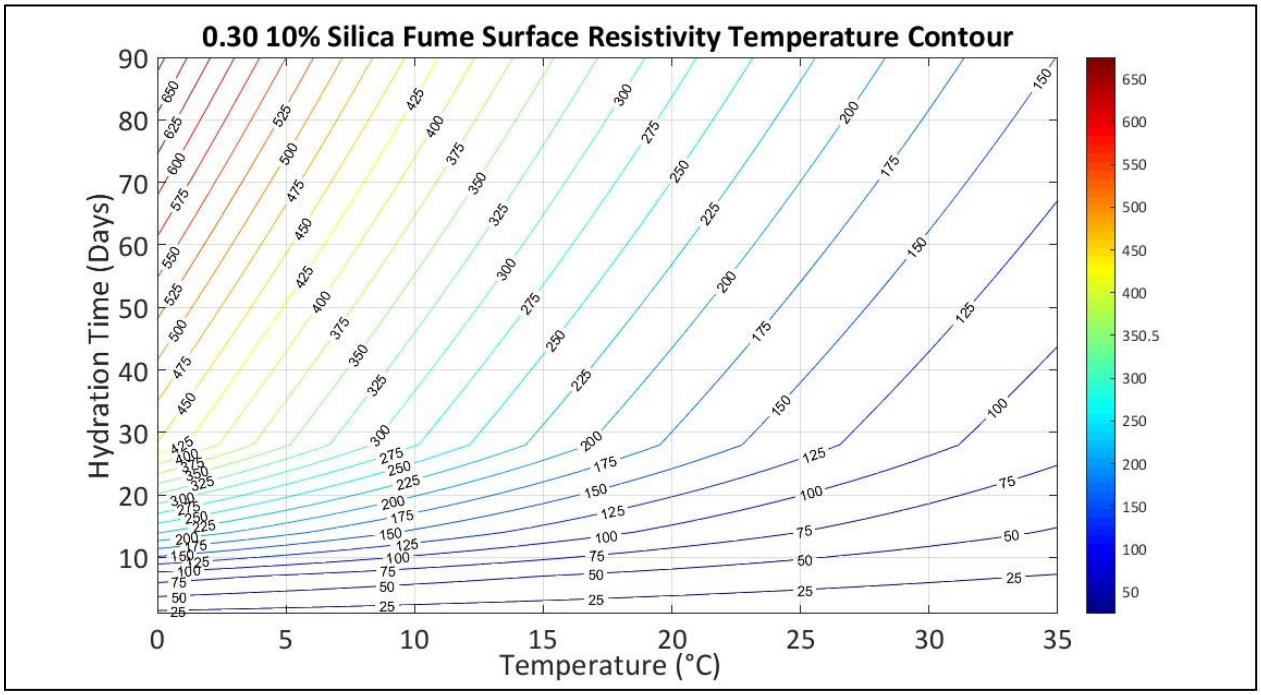

Figure 4.12- SR-T-Hydration relationship for 0.30 10% SF replacement concrete

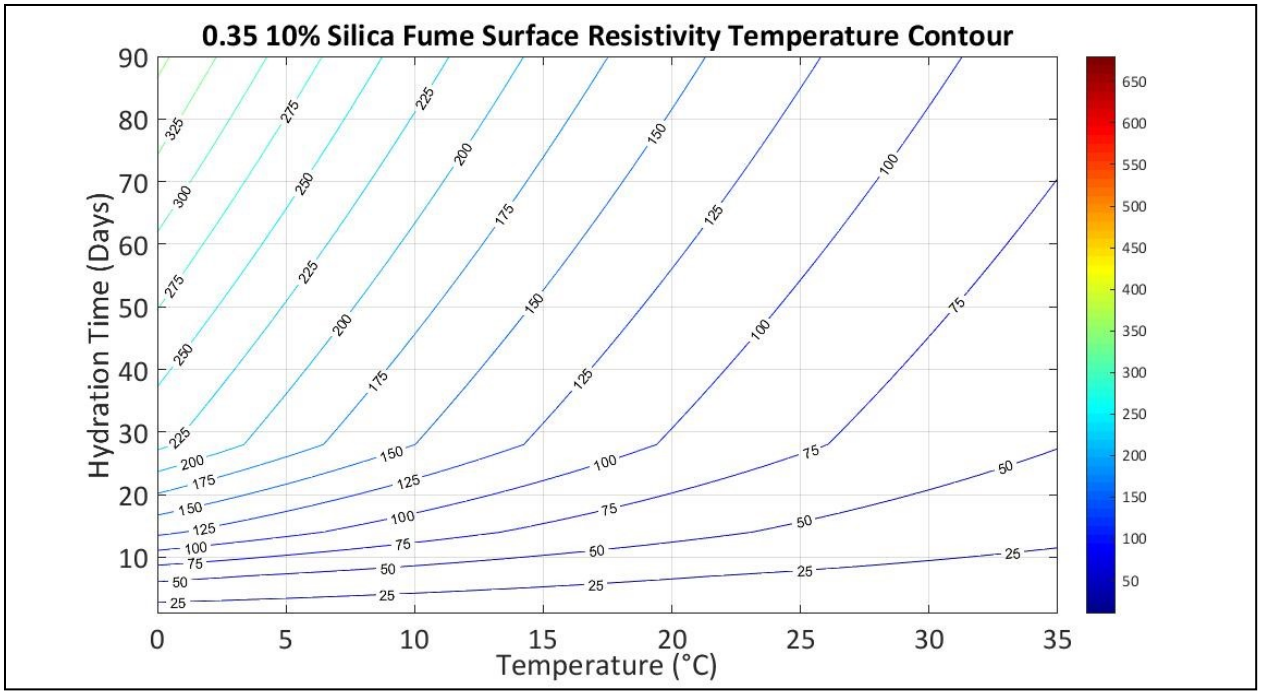

Figure 4.13- SR-T-Hydration relationship for 0.35 10% SF replacement concrete

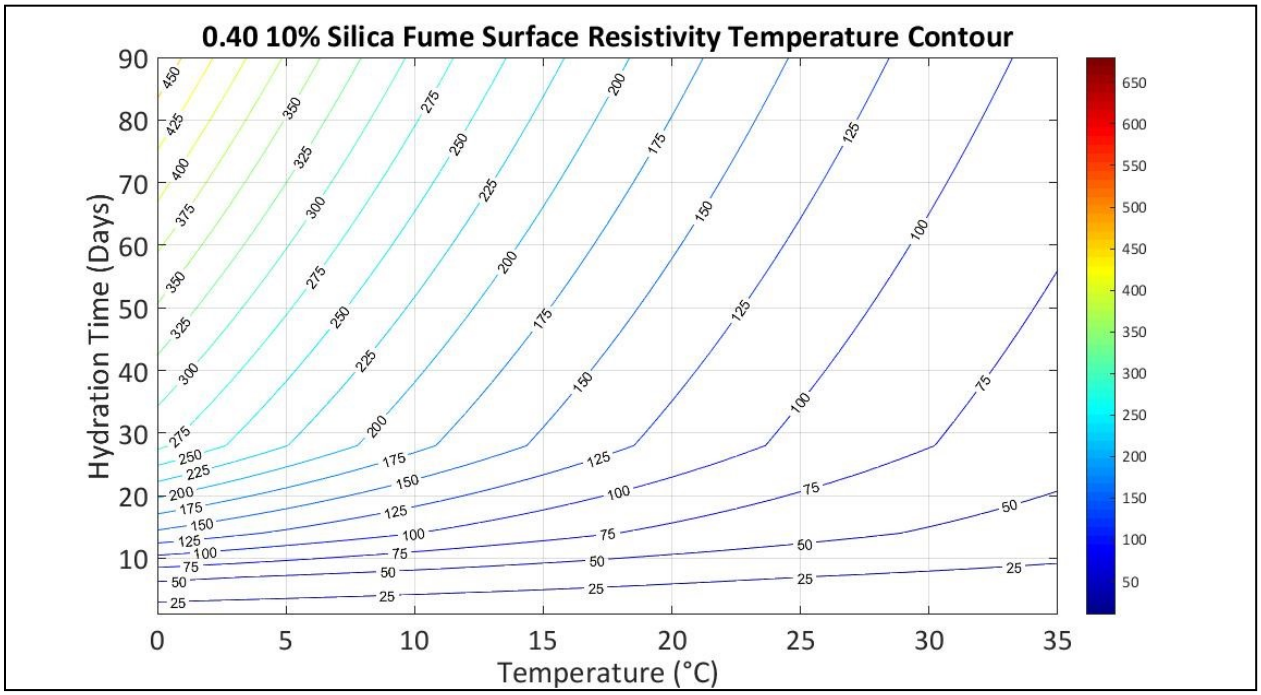

Figure 4.14- SR-T-Hydration relationship for 0.40 10% SF replacement concrete

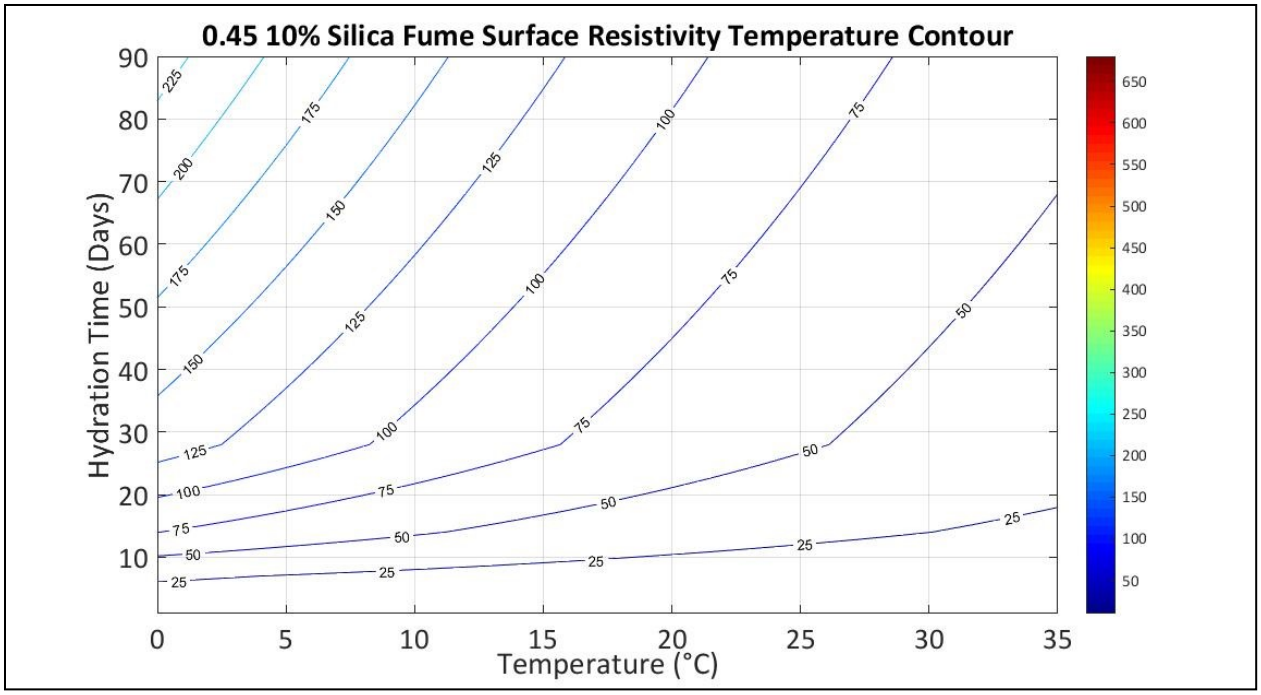

Figure 4.15- SR-T-Hydration relationship for 0.45 10% SF replacement concrete

Figures 4.12 through 4.15 show that a 10% cementitious replacement dramatically affects the resistivity behavior by an order of magnitude as compared to Figures 4.8 through 4.11. Note that the gradation for the SR contour lines is five times larger for Figures 4.12 to 4.15 than for Figures 4.8 through 4.11 due to this large change. The maximum resistivity developed by the 0.30 10% SF mixture was over 625 kΩ·cm, where the same w/c mixture without the silica fume only reached a maximum at low temperatures above 80 kΩ·cm. Figures 4.12 through 4.15 also show that the development of this resistivity proceeds at a slower rate for all the mixtures with 10% silica fume replacement as compared to the OPC. The SR contour lines are much closer to being parallel to the y axis, showing less change between 28 and 90 days for the OPC as seen in Figures 4.8 through 4.11 than for the contour lines. This observation is consistent with the hydration mechanism associated with the pozzolanic reaction creating a denser microstructure, as well as

the removal of $[OH]^-$ ions from the pore water solution leading to decreased charge carriers and thus a larger resistivity.

Figure 4.14 again demonstrates the anomalous behavior of the 0.40 10% SF replacement mixture, since the maximum SR observed at 90 days was greater than the 0.35 10% SF mixture. This is consistent with the hypothesis that the 0.40 10% SF mixture was drier than was otherwise calculated from the mix design calculations, suggesting some absorption or evaporation of water out of the mixture that would cause the effective w/c ratio to decrease somewhere between the 0.35 and 0.30 10% SF mixtures. While the exact cause of this anomalous behavior is unknown, the effect on the SR evolution is clearly evident from Figure 4.14.

4.3.7. Surface resistivity temperature correction

Using both the derived activation energies from the figures and the best fit curves generated for Figures 4.6 and 4.7, as well as the SR-T-Hydrations curves found in Figures 4.8 through 4.15, every paired SR-T measurement from the eight mixtures and hydration times was normalized to 20 °C using both the modified Arrhenius method as well as the correction factor method. The results and statistics comparing the two techniques can be found in Table 4.4. The error in Table 4.3 is the absolute value of the difference between the predicted value of surface resistivity based on the best fit curves (Method 1 and 2) derived for each as compared to the predictions from either of the methods.

Table 4.4- Comparison between correction factor method and Arrhenius method for temperature correction

Mixture	Maturity	Average SR Reading at temperature	Correction Factor			Arrhenius Method		
			SR Prediction	Error (ABS)	Standard Deviation	SR Prediction	Error (ABS)	Standard

								Deviation
0.3 OPC	1	10.369	10.369	0.000	0.742	10.314	0.055	0.624
	7	20.899	20.879	0.020	1.485	20.630	0.269	1.188
	14	24.764	24.747	0.017	1.728	24.486	0.279	1.318
	28	28.850	28.817	0.033	2.083	28.425	0.426	1.548
	90	37.055	37.002	0.054	2.565	36.452	0.603	1.924
0.35 OPC	1	6.351	6.356	0.006	0.423	6.351	0.001	0.353
	7	13.792	13.790	0.002	0.946	13.693	0.099	0.736
	14	16.469	16.472	0.002	1.116	16.372	0.097	0.858
	28	18.499	18.500	0.000	1.382	18.383	0.116	1.021
	90	21.701	21.708	0.007	1.632	21.599	0.102	1.278
0.40 OPC	1	4.999	5.000	0.001	0.373	4.988	0.012	0.313
	7	11.330	11.334	0.004	0.854	11.289	0.042	0.660
	14	13.510	13.513	0.002	1.030	13.424	0.087	0.821
	28	15.300	15.305	0.005	1.155	15.231	0.069	0.904
	90	16.775	16.779	0.004	1.221	16.690	0.085	0.964
O.45 OPC	1	6.395	6.400	0.005	0.391	6.382	0.013	0.342
	7	13.459	13.452	0.007	0.868	13.318	0.141	0.763
	14	15.819	15.818	0.001	1.076	15.699	0.120	0.816
	28	17.577	17.580	0.003	1.091	17.492	0.085	0.900
	90	19.403	19.391	0.011	1.308	19.213	0.189	1.025
0.30 10% SF	1	9.843	9.854	0.010	1.232	9.850	0.006	0.974
	7	41.451	41.422	0.029	3.941	40.997	0.454	3.133
	14	93.115	93.227	0.113	8.774	93.264	0.149	6.448
	28	171.114	171.245	0.131	16.953	170.712	0.403	11.764
	90	286.838	286.442	0.397	27.027	282.253	4.586	21.547
0.35 10% SF	1	6.230	6.234	0.004	0.454	6.233	0.003	0.365
	7	26.567	26.579	0.012	1.469	26.471	0.096	1.194
	14	56.861	56.888	0.012	3.081	56.495	0.366	2.391
	28	97.467	97.477	0.010	6.390	96.806	0.662	4.498
	90	158.263	158.091	0.171	11.420	155.830	2.433	9.215
0.40 10% SF	1	5.607	5.607	0.001	0.463	5.585	0.022	0.399
	7	29.379	29.370	0.009	1.856	29.156	0.223	1.948
	14	69.396	69.347	0.049	6.085	68.641	0.755	4.654
	28	117.214	117.217	0.004	9.996	116.361	0.852	7.205
	90	185.297	185.343	0.046	14.488	184.233	1.064	11.182
0.45 10% SF	1	2.934	2.935	0.001	0.177	2.897	0.038	0.171
	7	14.284	14.291	0.007	0.944	14.264	0.020	0.772
	14	36.169	36.177	0.007	2.401	35.969	0.200	1.873

	28	63.376	63.391	0.016	4.284	63.163	0.212	3.285
	90	105.880	105.702	0.178	7.318	104.748	1.131	5.767
		Averages	Error		0.035	Error		0.414
			Standard Deviation		3.805	Standard Deviation		2.929

Table 4.4 shows that the predictions obtained from both methods are in very close agreement with the average value determined by curve fitting. In terms of the statistics, the standard deviations of the Arrhenius method predictions were generally smaller than those resulting from the correction factor method. In terms of the error between the true average value at 20°C and the predicted value resulting from the two methods, the data shows that the average error in prediction is an order of magnitude larger for the Arrhenius method than that resulting from the correction factor method of normalizing temperatures. Table 4.4 clearly shows that both methods produce normalized temperature readouts that are in close agreement, each well within the other's standard deviations.

The normalized surface resistivity readings at 20 °C can be found in Figures 4.16 and 4.17 respectively. The differences between the two predictive methods were not sufficiently large to be visible in Figures 4.15 and 4.16 and were omitted. All mixtures exhibited increases in surface resistivity measurements over time, with the lower w/c mixtures generally having a higher resistivity. Again, the behavior of the 0.40 OPC and 0.40 10% SF replacement mixtures can be seen to be anomalous from Figures 4.16 and 4.17, with their behavior falling outside of the expected ranges. The 10% SF mixtures gained much more surface resistivity, but the relative rate at which they developed was slower than the OPC mixtures. In Figure 4.16, it is clear that there was not much change between the 28 day and 90 day points, but there was more development across the same time for the 10% SF mixtures in Figure 4.17.

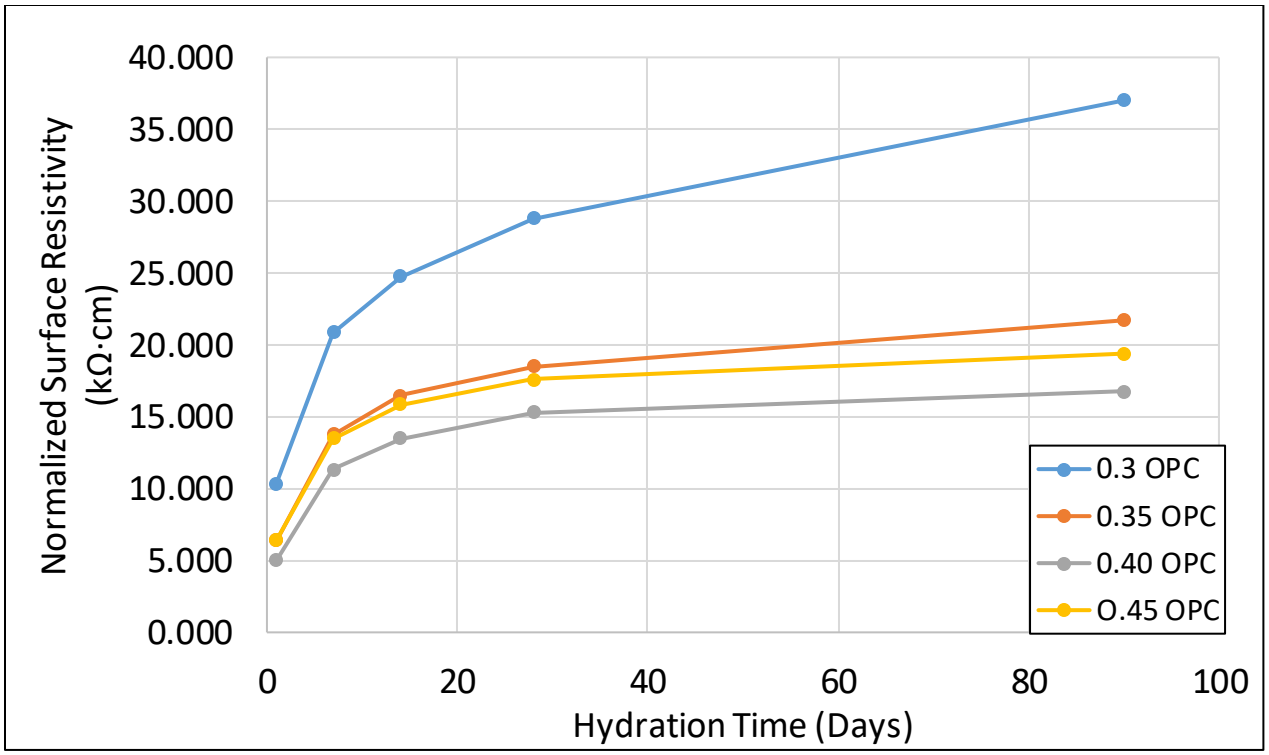

Figure 4.16- Normalized surface resistivity readings of ordinary portland cement concretes at 20 °C over time

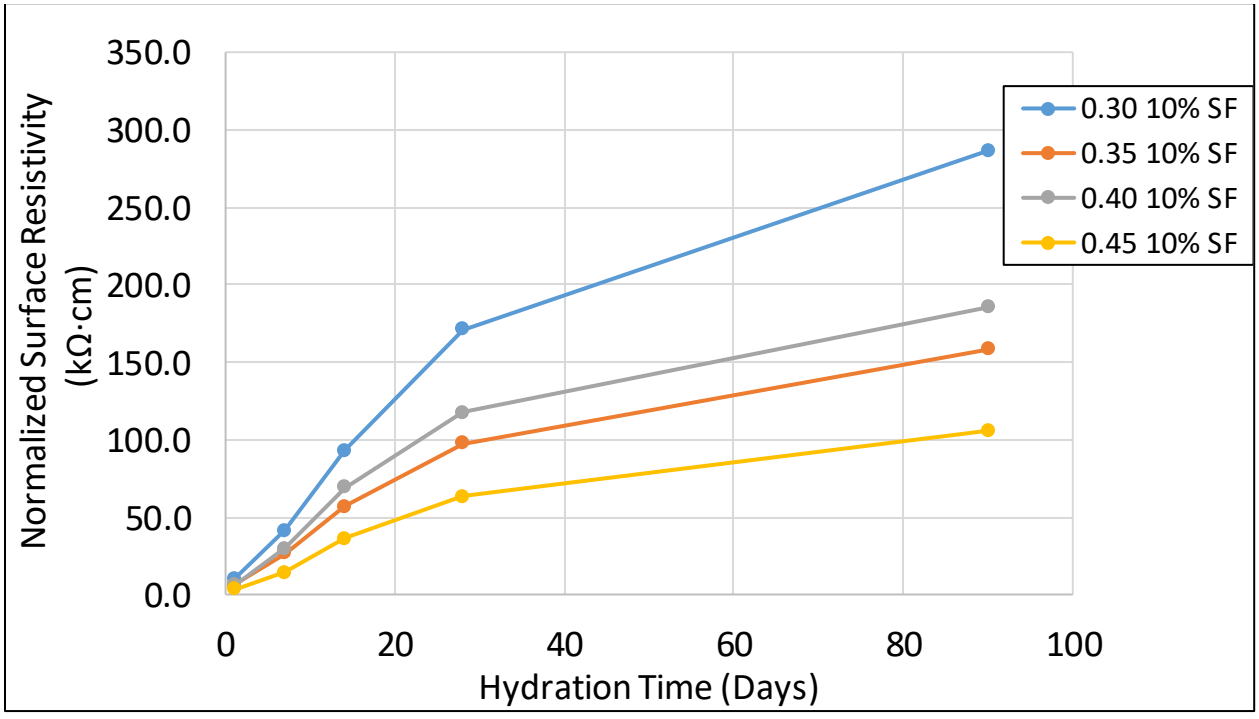

Figure 4.17- Normalized surface resistivity readings of 10% silica fume cementitious replacement concretes 20 °C over time

4.4. Conclusions

Surface resistivity measurements are strongly affected by the temperature of the concrete, which can lead to differences in measurement on the order of hundreds of kΩ·cm for the same specimen over a range that is representative of ambient field conditions. This is particularly true of mixtures which incorporate supplementary cementitious materials such as silica fume, which will change the chemistry of the pore water solution and the connectedness of the pores.

Methods to correct this variable SR-T behavior will be most accurate if this SR-T behavior is modelled as a negative exponential relationship, although methods which use a simpler linear relationship may be reasonably accurate over much smaller temperature ranges. The approach demonstrated by the author's correction factor method, as well as the modified Arrhenius method, were both effective at normalizing surface resistivity measurements. The correction factor method resulted in smaller amounts of error for normalizing the SR-T correction measurements as compared to the Arrhenius method. While the error for the correction factor method was consistently smaller than the Arrhenius method, the maximum error from either of the methods was considerably smaller than the standard deviations for the methods. Both methods produce corrected results that are not significantly different from the measured results at the temperature range, so they are both effective.

The testing procedure for deriving these SR-T relationships for the various mixtures and hydration times was very similar for both mixtures, which used curve fitting methods from the raw data. One thing that is notably different about the correction factor method as compared to the Arrhenius equation is that the empirical equations approximate the specific SR-T behavior over the temperature range, whereas the Arrhenius equation requires both an empirically determined

activation energy as well as a specific SR measurement for it to work correctly. For example, when comparing the activation energy of conductions for both the 14 day 0.4 OPC and 0.4 10% W/C (Tables 4.2 and 4.3), the values are quite similar to each other. However, the empirical curve fitting equations derived from either Method 1 or 2 demonstrate that the actual SR readings for these two mixes would be radically different despite their very similar activation energies. Another potential issue arising from using the Arrhenius method for correcting temperature is that the absolute temperature scale will give predictive results for measurements made below the freezing point of water. These corrections will not be consistent with the true behavior of pore water, which will discontinue the exponential relationship between surface resistivity and time due to the phase change. The correction factor method does not make these potentially erroneous predictions since the functions are not defined below 0 ^{o}C.

Examining this normalized SR-T behavior at a variety of hydration points can allow for an NDT examination of the evolution of the pore structure. The differences in hydration behavior were clearly evident when comparing both the different w/c mixtures as well as those which contained a pozzolan substitute in the cementitious content. The pozzolanic effect had a very strong influence on the overall measured resistivity, differing by an order of magnitude from the OPC mixtures despite the overall mixture proportions being quite similar. Even anomalous results that may have resulted from errors during the initial casting were in evidence when examining the differences in SR between mixtures of different W/C.

The large variations in surface resistivity over temperatures commonly encountered in field conditions make it clear that it is of integral importance to correct the measurements to a reference temperature to reduce this variability. SR is a very powerful tool for observing the

evolution of the pore structure during hydration, as well as the effects of different admixtures and cementitious content, but the signal that characterizes these processes would be not be evident if the temperature was not corrected. The methods outlined in this paper show that this correction procedure can be reliably performed on ordinary concrete cylinders.

4.5. Acknowledgements

The authors wish to thank Proceq for their donation and assistance with the Resipod Surface Resistivity meter as well as Bauval LLC for the donation of the granitic aggregates used for the study.

4.6. References

[1] Stanish, K.D.; Hooton, R.D.; Thomas, M.D.A.; "Testing the Chloride Penetration Resistance of Concrete: A Literature Review", FHWA Contract DTFH61-97-R-00022 “Prediction of Chloride Penetration in Concrete”, (1997)

[2] Vivas, E., A. J. Boyd, H.R. Hamilton III, and M. Bergin. "Permeability of Concrete—Comparison of Conductivity and Diffusion Methods." FDOT, 2007.

[3] Whittington, H.W.; McCarter, J.; Forde, M.C.; “The Conduction of Electricity Through Concrete”, Magazine of Concrete Research, Vol. 33 No. 114, pp 48-60, (1981)

[4] Morris W.; Moreno, E.I.; Sagues, A.A.; "Practical Evaluation of Resistivity of Concrete in Test Cylinders using a Wenner Array Probe," Cement and Concrete Research, Vol. 26, No. 12, pp. 1779-1787, (1996)

[5] Rajabipour, F., and J. Weiss. "Electrical Conductivity of Drying Cement Paste." *Mater. Struct.* 40 (2007): 1143-1160

[6] Tumidajski, P.J., A.S. Schumacher, S. Perron, P. Gu, and J.J. Beaudoin. "On the Relationship between Porosity and Electrical Resistivity in Cementitious Systems." Cem. Concr. Res. 26 (1996): 539-544.

[7] Weiss, J., K. Snyder, J. Bullard, and D. Bentz. "Using a Saturation Function to Interpret the Electrical Properties of Partially Saturated Concrete." Journal of Materials in Civil Engineering 25, no. 8 (2013): 1097-106.

[8] Larbi, J.A.; Fraay, A.L.A.; Bijen, J.M.J.M.; "The Chemistry of the Pore Fluid of Silica Fume-Blended Cement Systems", Cement and Concrete Research. Vol.20 No. 4 pp. 506-516, (1990)

[9] Shi, C.; "Effect of Mixing Proportions of Concrete on its Electrical Conductivity and the Rapid Chloride Permeability Test (ASTM C1202 or ASSHTO T277) Results", Cement and Concrete Research Vol. 34 No. 3, pp 537-545, (2004)

[10] Julio-Betancourt, G.A.; Hooton, R.D.; "Study of the Joule Effect on Rapid Chloride Permeability Values and Evaluation of Related Electrical Properties of Concretes", Cement and Concrete Research, Vol. 34, pp. 1007-1015, (2003)

[11] Polder, R.B.; "Test Methods for On Site Measurement of Resistivity of Concrete – A RILEM TC-154 Technical Recommendation", Construction and Building Materials. Vol. 15, No. 2—3, (2001)

[12] Gowers, K.R.; Millard, S.G.; “Measurement of Concrete Resistivity for Assessment of Corrosion Severity of Steel Using Wenner Technique”, ACI Materials Journal Vol. 96 No. 5 (1999)

[13] Spragg, R.; Chiara, V.; Snyder, K.; Bentz, D.; Bullard, J.W. and Weiss, J.; “Factors That Influence Electrical Resistivity Measurements in Cementitious Systems”, Transportation Research Record: Journal of the Transportation Research Board Vol 2342, pp 90-98, (2013)

[14] Spragg, R.; Bu, Y; Snyder, K.; Bentz, D. and Weiss, J.; “Electrical Testing of Cement-Based Materials: Role of Testing Techniques, Sample Conditioning, and Accelerated Curing” Publication FHWA/IN/JTRP-2013/28. Joint Transportation Research Program, Indiana Department of Transportation and Purdue University, West Lafayette, Indiana, 2013

[15] McCarter, W.J.; Starrs, G.; Chrisp, T.M.; “Electrical Conductivity, Diffusion, and Permeability of Portland Cement-Based Mortars” Cement and Concrete Research Vol. 30, No.9, pp. 1395-1400, (2000)

[16] Wei, X.; Xiao, L.; “Electrical Resistivity Monitoring and Characterization of Early Age Concrete” Magazine of Concrete Research Vol. 65, No. 10, pp 600-607 (2013)

[17] Morsy, M.S.; “Effect of Temperature on Electrical Conductivity of Blended Cement Pastes” Cement and Concrete Research, Vol 29, No.4 pp. 603-606 (1999)

[18] Zaccardi, Y.A.V., J. Fullea García, P. Huélamo, and A.A. Di Maio. "Influence of Temperature and Humidity on Portland Cement Mortar Resistivity Monitored with Inner Sensors." Materials and corrosion 60, no. 4 (2009): 294-99.

[19] Bürchler D, Elsener B, Böhni H. “Electrical resistivity and dielectric properties of hardened cement paste and mortar” Page CL, Bamforth PB, Figg JW. Proc. Fourth Int. Symp. on Corrosion of Reinforcement in Concrete Construction. Society of Chemical Industry. pp 283–293. (1996)

[20] Bentz, D.P.; Sant, G., Weiss, J.; “Early-Age Properties of Cement-Based Materials. 1: Influence of Cement Fineness” Journal of Materials in Civil Engineering Vol. 20, No.7 (2008)

[21] Ramezanianpour, A.A.; Pilvar, A.; Mahdikhani, M.; Moodi, F.; “Practical Evaluation of Relationship Between Concrete Resistivity, Water Penetration, Rapid Chloride Penetration and Compressive Strength” Construction and Building Materials, Vol. 25, No. 5, pp. 2472-2479 (2011)

[22] Tumidajski, P.J; “Electrical Conductivity of Portland Cement Mortars” Cement and Concrete Research, Vol. 26, No. 4, pp 529-534, (1996)

[23] King, D; “The Effect of Silica Fume on the Properties of Concrete as Defined in Concrete Society Report 74, Cementitious Materials” 37th Conference on Our World in Concrete & Structures, Singapore, pp 29-31, August 2012

[24] Fraay, A.L.A.; Bijen, J.M.; de Haan, Y.M.; “The Reaction of Fly Ash in Concrete. A Critical Examination” Cement and Concrete Research, Vol. 19, No.2, pp 235-246 (1989)

[25] Nokken, M.R., A. Boddy, X. Wu, and R.D. Hooton. "Effects of Temperature, Chemical, and Mineral Admixtures on the Electrical Conductivity of Concrete." Journal of ASTM International 5, no. 5 (2008): 1-9.

[26] Milton, S. "Evaluation of Various Parameters Affecting the Surface Resistivity Test." edited by A.J. Boyd. Montreal, Quebec: McGill University, 2016.

ASTM. "Standard Test Method for Compressive Strength of Cylindrical Concrete Specimens." West Conshohocken, PA: ASTM International, 2017.

Forward to Chapter 5

Chapter 5 is a direct investigation of the effect of variable moisture content on the pressure tension test. This topic is directly related to the evaporative transport theme of the thesis because of the conditioning used to vary the moisture content that is based on evaporative transport from the concrete cylinders. The NDT methods used in other chapters to monitor the deterioration due to durability issues were also used for Chapter 5 to monitor the changes in the pore structure and solid phases during hydration. These NDT methods of UPV and SR directly measure the connectivity of the solid phase or pore phase of concrete, respectively, and are good NDT measures of the nature of the pore structure. The SR results were all performed at the same temperature in order to minimise the temperature effect and ignore the temperature correction method detailed in Chapter 4.

During air drying, the only loss of moisture possible was due to an evaporation of water from the pore system of the concrete, which was observed through testing to proceed from the surface towards the interior of the specimens. Thus, the one-dimensional evaporative flow conditions explored in Chapter 3 and related evaporative transport paper were present for drying detailed in Chapter 5. The use of oven-drying as a conditioning method caused microstructural damage in the concrete pore system, similar to the type of damage that occurred due to sulphate attack and freeze-thaw damage (Chapters 6-8). This damage to the pore structure was detected as a weakening of the solid phase that resulted in lower tensile stress resistance. Additionally, the relative transport properties of gas and water were explored in terms of the effectiveness of applying the tensile stresses to the solid phase, with differences in the failure mechanism being

observed for the saturated and unsaturated specimens. Differences in the morphology of the pore system were explored via the addition of air-entraining admixtures, which created additional voids without necessarily being connected to the rest of the pore structure. Different pore structures involved in transport properties were also created by varying the w/c across different mixtures. The results from Chapter 5 substantiated the standardized pressure tension procedure developed and detailed in Appendix A. The recommendation of testing specimens that are saturated due to this value being conservative is directly based on the results detailed in Chapter 5.

Chapter 5: Pressure Tension and the Effect of Variable Moisture Content

Komar, A.J.K., Boyd, A.J., McGill University, Montreal, QC

5.1. Abstract

The tensile failure stress level of specimens tested by pressure tension has been previously found to change as a function of moisture content of the concrete, but the nature of this effect is not well characterized. This study used pressure tension testing to examine this moisture content dependency for six concrete mixtures of different w/c, half of which contained air entrainment to provide additional porosity. NDT methods of surface resistivity and ultrasonic pulse velocity were used to characterize changes during hydration associated with changes in the porosity. Four different methods of conditioning were used to control the moisture content of cured samples: vacuum saturation, air drying, oven drying, and submersion. Gravimetric methods were used to estimate the volume of evaporable pores as well as the moisture content of each sample. It was found that the difference between fully and partially saturated concretes can cause a decrease in the measured tensile failure stress of more than 50%. Air entrainment also increased the magnitude of this drop as compared to mixtures without air entrainment of a similar w/c. Pressure tension is a reliable method for assessing this decrease in tensile capacity, and further studies are in order to fully characterise this phenomenon.

5.2. Background

5.2.1. Pressure tension

The pressure tension testing method was originally developed by the building research council (BRC) as a method for applying uniaxial tension stress to a variety of specimens [1]. The basic test uses a pressure chamber made to fit around a cylindrical test specimen. O-Rings are then placed at the ends and a sealing ring is put into place to provide a pressure seal encapsulating the curved surface of the specimen. The ends of the cylinder are exposed to the ambient atmospheric pressures. The test consists of injecting a pressurized loading fluid into the space between the test chamber and the curved surface of the cylinder. The internal equilibrium of the specimen caused by this applied stress results in a net tensile stress field to develop, perpendicular to the applied biaxial loading stress, as seen in Figure 5.1.

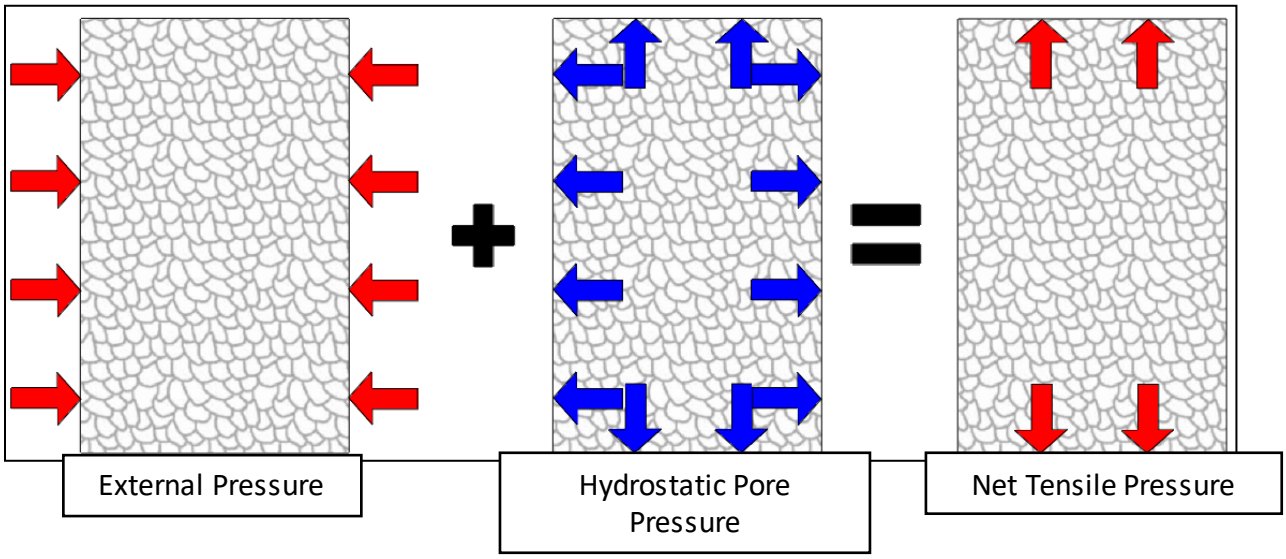

Figure 5.1- Pressure tension effect

In the case of porous materials such as concrete, the fact that there are two phases within the composite specimen is critical to this pressure tension effect. One must use the effective stress theory originally developed for use in soil mechanics to properly analyze the behavior [2, 3, 4].

The key is that stress develops differently between the solid phase and the liquid phase. The stresses within the solid phase in any direction will be a summation of the externally applied stresses as the pore pressure. The liquid phase will react in a hydrostatic manner with an isotropic stress state at the pore pressure. Since, in the pressure tension testing configuration, the externally applied stress state is biaxial, a net effective tension stress develops along the axis of the cylinder. The tensile stress along this axis is driven internally by the pressure of the pore phase, which is cancelled in all other directions by the biaxial loading. When the loading pressure reaches the value of the tensile capacity of the material, the net effective stress within the solid phase of the material is zero, and the specimen will fail due to a tension crack developing perpendicular to the applied biaxial load.

5.2.2. Effect of moisture content on pressure tension

In the first experiments by the BRC, pressurized water and compressed air were used as the loading medium [1]. Further tests using this configuration have used pressurized nitrogen gas, with the same tension failure being reported throughout [3,4]. The pressure tension apparatus used for the entirety of the following study used compressed air as the loading medium. In the studies by Uno *et al.* [3,4], one factor that had a large effect on the measured tensile capacity was the moisture content of the concrete. That study did not look at the moisture content in detail, but did make note of a significant effect related to moisture content, where the specimens that had been recently saturated as a side effect of curing were measured to have up to 3 times as much tensile strength capacity as that which was measured using the more traditional Splitting Brazilian Test (ASTM C496). The study used two concrete mixtures, both of which were dried out under ambient laboratory conditions for either 43 or 100 days after curing. They found that the

tensile strength of the former mixture was measured to be about 30% higher than in the splitting tension test, whereas the mixture that had been left to dry for 100 days had results that were more like the splitting tension results.

To explain this disparate tensile capacity for the same material, Uno *et al.* used fracture mechanics to explore the sequencing of the crack propagation. All concrete will have some pre-existing microcracks or flaws present within the volume of the sample. When the pressure of the loading medium is close to the tensile capacity of the material, one of these microcracks will begin to fracture and open up. As this crack begins to propagate from the surface to the interior, the PT loading medium will intrude on both of the crack faces and continue the propagation of the crack. The explanation that Uno *et al.* posed for the difference in tensile capacity due to moisture content was based on the differences in viscosity between gas and liquid. If there is pre-existing pore water already within the vicinity of this failure crack, the intrusion of the gas, and thus the transfer of the forces onto the failure surface, will be impeded due to the viscosity of the water. Hence, when the moisture content of the samples is high, a higher net pressure of the loading medium is required to create a tension failure because the viscosity of the water and transfer of forces through the liquid will limit the propagating forces on the crack faces. Conversely, in areas with low existing pore water, there will be nothing to impede the pressurized gas from intruding into these pre-existing microcracks and voids. Thus, the minimum pressure required to cause a tension failure would be lower for dry specimens since the forces being delivered by the pressurized voids to the surrounding material would be unmoderated by water. These results showed that moisture content strongly affects the tensile capacity as measured by the pressure tension test method.

Another possible explanation for the mechanism causing differences in pressure tension failure between high and low moisture content would be changes in the density of the material in the pore volumes and a subsequent change in the stored potential energy within that medium. Water is essentially incompressible, only varying very slightly in its density over isothermal pressure ranges of 0-5 MPa from about 998 $kg \cdot m^{-3}$ to 1000.5 $kg \cdot m^{-3}$. Over the same isothermal pressure range, air will increase in density from 1.2 $kg \cdot m^{-3}$ to 60.6 $kg \cdot m^{-3}$. Therefore, not only will the gas intrude more easily into existing cracks due to its lower viscosity, there will be a greater change in the mass of the air occupying the same void space as compared to water. This can be considered by calculating the potential energy storage of this compressed air as compared to compressed water. If the process is assumed to be adiabatic, a derivation of the ideal gas law assuming a constant volume of the pressurized pore spaces yields a work function found in Equation 5.1.

$$E(P) = P_B \cdot V_B \cdot ln\left(\frac{P_A}{P_B}\right) + (P_B - P_A) \cdot V_B$$

Equation 5.1- Work function of adiabatic gas pressurization

where P_A is atmospheric pressure of 0.1 MPa, P_B is the pressure at failure, V_B is the volume of pores in m^3, and E is in joules. For a failure at 5 MPa, the work done on the gas is calculated at -3.313 kJ. Conversely, when we consider an adiabatic compression of water, assuming the compressibility does not change over the pressure ranges, we can derive an expression for the energy contained in the compressed water in Equation 5.2.

$$E(p) = \frac{\gamma}{2} \cdot V_B \cdot (P_B - P_A)^2$$

Equation 5.2- Work function of adiabatic water pressurization

where γ is compressibility in pa^{-1}, V_B is the volume of the voids in m^3, P_B is the pressure at failure in Pa, and P_A is the atmospheric pressure in Pa. For regular water, this expression yields a result of 2.6 J, which is negligible compared to the large value of the energy contained in the compressed gas. In physical terms, there is much more potential energy stored within a compressed gas as compared to compressed water. For the same operating pressure, there is more energy required to bind the solid phase together at a lower moisture content than at a higher moisture content. Thus, when we compare the failures of saturated and unsaturated concrete, we would expect the unsaturated concrete to fail at a lower pressure due to this additional energy performing work on the surrounding pore environment.

A third possibility that has not been previously explored in the literature to explain this effect would be the contribution of molecular adhesion due to surface tension of the pore water. Concrete has a variety of pore sizes, ranging from millimetre to nanometre scales, corresponding to a variety of pore sizes for the capillary system down through the voids between hydration crystals [5,6]. This pore space will also change as a function of hydration as the cementitious crystals grow to occupy the formerly empty space. The water within the larger capillary voids is more free to change environment relative to the water in the smaller pores, which is tightly bound within intercrystalline layers. The mechanics and kinematics of the water mobility from these smaller pores are considerably more complex, being associated with shrinkage and creep phenomenon [7].

Some of this pore space, however, will remain empty even in exposure conditions we normally associate with saturation [8, 9, 10]. In any pore space that has a degree of empty space occupied by a gas, a meniscus will form on the gas-liquid interface, and this meniscus will also 'pull' on the

surrounding solid phase at the liquid-solid boundary, imparting some degree of internal tensile forces that will resist deformations of this solid phase. Thus, during a pressure tension test, the net tensile stresses for a saturated or partially saturated specimen would have to overcome both the internal cohesive stresses of the solid phase and these adhesive forces driven by surface tension, which could explain why the observed failure stresses for these specimens are higher than drier specimens. Furthermore, if additional empty voids could be partially filled through external means, such as vacuum saturation, then the net expected tensile resistance would increase because additional menisci would form in these otherwise empty voids.

5.2.3. Moisture content calculations

The following study uses a modified ASTM standard procedure for measuring the pore volume of the specimens. The bulk density of the specimens was taken at the time of casting and is used as the basis for the apparent bulk density after immersion value as per ASTM C642. More detailed information regarding the volumes of the specimens used in testing was not available, and an approximate value for each specimen's volume was calculated by Equation 5.3

$$V_{Specimen} = M_{saturated} / \rho_{mixture}$$

Equation 5.3- Calculated volume of specimen from bulk density

where $M_{saturated}$ is the saturated mass of the specimen and $\rho_{mixture}$ is the apparent density of the mixture obtained from fresh concrete properties. The mass of all the specimens was taken in a saturated state before testing or conditioning commenced. After the designated exposure duration had concluded, all samples were measured before (M_{test}) and after testing ($M_{partial\ saturation}$) to account for the mass loss due to evaporation from the exposure condition. $M_{water,\ test}$ was calculated in Equations 5.4 and 5.5

$$M_{water,test} = M_{saturated} - M_{test}$$

Equation 5.4- Mass of water in whole sample lost because of duration in exposure condition

$$M_{fragment} = M_{test} - M_{partial\ saturation}$$

Equation 5.5- Mass of fragments lost during testing

The moisture content of the fragments lost in $M_{fragment}$ was assumed to be the same as the moisture content of the sample at the time of testing. The test specimens were then subsequently dried in an oven at 105 °C as per the ASTM standard until the values stabilized within 0.5 g over successive 24 hour periods to derive the value M_{dry}. The total mass of the water within the tested specimen $M_{partial\ saturation}$ was calculated per Equation 5.6

$$M_{water,partial\ saturation} = M_{partial\ saturation} - M_{dry}$$

Equation 5.6- Mass of water lost after testing until oven dry condition

The proportion of water relative to the total fragment mass was then calculated as Equation 5.7

$$M_{water,fragments} = M_{fragment} \cdot \left(\frac{M_{water,partial\ saturation}}{M_{partial\ saturation}}\right)$$

Equation 5.7- Estimated mass of water in fragments lost during testing

Therefore, the total amount of water in the sample could be calculated as in Equation 5.8

$$M_{water} = M_{water,test} + M_{water,partial\ saturation} + M_{water,fragments}$$

Equation 5.8- Total mass of water in sample calculation

With this total amount of evaporable water, the moisture content at the time of testing could then be calculated as Equation 5.9

$$\theta_{partial} = \frac{(M_{water,partial\ saturation} + M_{water,fragments})}{M_{water}} \cdot 100\%$$

Equation 5.9- Estimated moisture content at time of testing

which is a percentage of the total amount of water in the free pore water space as a fraction of the total amount of pore water. In the special case of the vacuum saturated specimens, the moisture content was calculated as Equation 5.10

$$\theta = \frac{M_{vacuum\ saturated}}{M_{saturated}}$$

Equation 5.10- Moisture content due to vacuum saturation

It should be noted that this moisture content would be > 100 %, which corresponds to those additional pores that would not otherwise be filled under normal saturation conditions.

Using these values, the calculations for apparent empty pore volume could be undertaken as per ASTM C642, with two exceptions. The first was that no measurement of absorption mass after immersive boiling was performed, so the regular bucket saturation value was assumed for those calculations. The second exception was that the apparent mass while suspended in water was calculated as Equation 5.11, due to the incomplete density information available.

$$M_{suspended} = M_{saturated} - V_{specimen} \cdot \rho_{water}$$

Equation 5.11- Estimated suspended mass of sample

5.3. Materials and Methods

5.3.1. Mixture design

Six mixtures of three different water to cement ratios (w/c) were selected, either with or without air entrainment, which can be found in Table 5.1. Air entrainment was used to create additional porosity in half of the mixtures, although the air entraining bubbles were not expected to contribute to the permeability of the concrete. More void spaces in total would be created in the air-entrained concrete, without these voids necessarily being accessible to the movement of water within the capillary structure of the concrete.

The aggregates were regular granitic aggregates that had been dried before casting. The absorption potential of the aggregates was previously measured at 1.1% and 0.5% for the coarse and fines respectively, and this aggregate absorption of water was accounted for in the mixture design. The fine aggregate had a fineness module of 2.7.

Table 5.1- Mixture design

Mixture	Coarse Aggregate ($kg \cdot m^{-3}$)	Fine Aggregate ($kg \cdot m^{-3}$)	Cement ($kg \cdot m^{-3}$)	Water ($kg \cdot m^{-3}$)	AEA ($kg \cdot m^{-3}$)
0.45	952.97	754.77	436.30	200.87	0.00
0.45 AEA	973.80	713.49	434.85	208.32	2.29
0.55	812.10	938.03	353.86	203.80	0.00
0.55 AEA	972.08	776.44	355.19	208.85	1.86
0.65	936.76	855.30	299.02	209.20	0.00
0.65 AEA	970.92	819.93	300.27	209.17	1.58

Empirical properties of the fresh concrete mixtures were measured during the casting procedure, which produced about 20 100 mm x 200 mm samples per cast. The mixtures for the 0.45 and 0.55 w/c mixtures resulted in a much smaller yield than anticipated, so not all the exposure conditions were performed on these two mixtures. Slump was measured per ASTM C 143. Both the air content and density of the fresh mixtures were empirically measured using a pressure air content meter per ASTM C 231. Table 5.2 shows the results of these empirical tests for all the mixtures used in the study.

Table 5.2- Fresh concrete properties

Mixture	Slump (mm)	Air Content (%)	Density ($kg \cdot m^{-3}$)
0.45	23	1.5	2458
0.45 AEA	81	9.5	2216
0.55	75	2.0	2433
0.55 AEA	180	10.5	2140
0.65	90	2.0	2337

0.65 AEA	175	13.0	2096

All mixtures were demolded after 24 hours and put into a saturated limewater solution at 24 °C for 28 days before the beginning of the moisture content conditioning and subsequent destructive testing.

5.3.2. Conditioning

Four different conditioning methods were used to create variable moisture contents in the different samples. Before any of these conditions were applied to any of the mixtures, both PT and compressive testing were performed on a representative subset of the saturated 28 day cured cylinders to provide a control.

5.3.2.1.Saturated

The samples that had been curing for 28 days in a saturated limewater solution were rinsed, dried-off, weighed and then tested in pressure tension. These specimens were taken as representative of 'bucket-saturated' since they had continuous exposure to water throughout the hydration process. The samples were maintained in a saturated condition right up until the moment of testing using a small bucket that could hold the sample and enough water to fully immerse the specimen to ensure that negligible evaporation into the atmosphere could occur between weighing and pressure tension testing.

5.3.2.2.Vacuum saturation

Previous work has indicated that simple submersion does not necessarily saturate all the available pore space [8,9,10]. Weiss *et al.* found that filling of this additional porosity that would not otherwise be filled with water can be induced via an exposure to water in an appropriately

strong vacuum. Other work by Safiuddin *et al.* found that vacuum saturation methods produced higher measured porosities than any other saturation technique.

Two vacuum chambers capable of accommodating a concrete cylinder were set up in the manner depicted in Figure 5.2. The two chambers were filled with tap water obtained from the municipal supply and sealed with pressure gaskets capable of resisting the applied vacuum. These sealed chambers were then pneumatically connected to a Venturi tube attached to a 6.9 bar pressure line so that the flow of the pressurized air through the Venturi device caused a partial vacuum to develop within the vacuum chamber. The partial vacuum was measured with a vacuum gauge, and the setup reliably reached a vacuum of -28 Hg, or about 3 kPa. The setup was run for at least 48 hours continuously to remove any dissolved gases within the vacuum chamber water before any samples for vacuum saturation were introduced. Valves were placed in such a manner that the regular atmospheric pressure could be introduced back into the chamber by turning a ¼ ball valve installed on the pressure line.

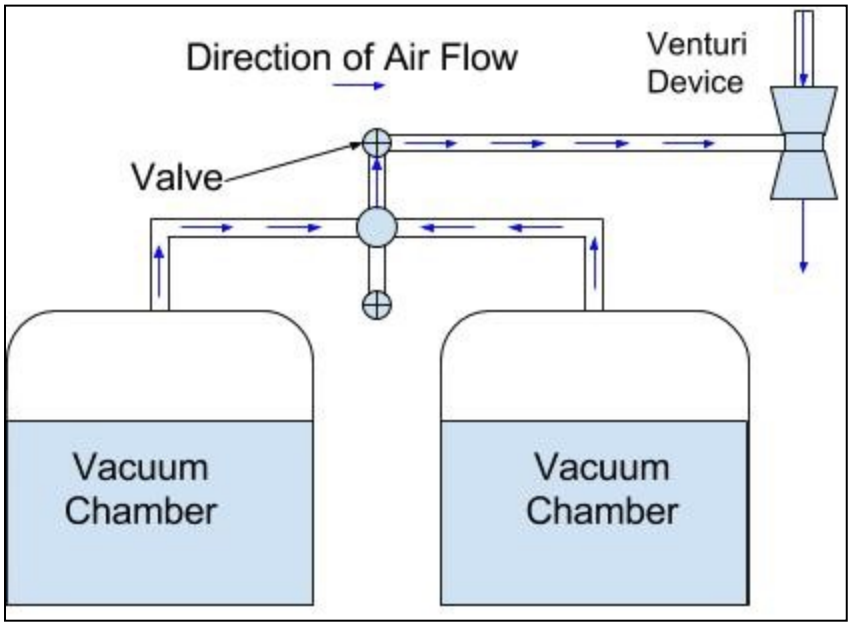

Figure 5.2- Configuration of vacuum saturation apparatus

Saturated concrete samples from the six mixtures were placed within these chambers and exposed to the vacuum for at least 2 days up to a maximum of 4 days. Every 24 hours, the samples were removed from the vacuum, wiped dry of excess surface moisture, and then measured with a scale with an accuracy to 0.1 g to measure the additional water absorbed by the sample due to the vacuum. These specimens were then tested in pressure tension after a final weighing after the exposure period.

5.3.2.3.Air drying

After curing, samples for the air-dried condition were weighed and then exposed to ambient laboratory conditions of 22 °C ± 2 °C for a variety of exposure times from 6 hours to 10 days. Every 24 hours, their mass was measured with a 0.1 g scale to track the mass loss due to moisture migration. The specimens were placed on a table in such a manner that the top and sides of the concrete cylinders were exposed to the ambient conditions. After the exposure period, the samples were weighed a final time, and then tested in pressure tension.

5.3.2.4.Oven drying

After the samples had been weighed, the oven dried samples were placed within a commercially available oven that was used to achieve the oven dried condition. The ovens were set to 105°C ± 5 °C as per the recommendations of ASTM C 642. Every 24 hours, the samples were taken out of the oven and weighed using a gravimetric scale with a 0.1 g accuracy to track the moisture loss from the sample. Unlike the other exposure conditions, which were applied for a pre-determined time, the oven dried specimens were maintained in the oven environment until successive 24-hour mass readings were less than 0.5 g from each other, indicating that all the evaporable water

had escaped from the voids of the samples. At this point, the samples were allowed to cool to ambient temperature and then tested in pressure tension.

For those samples that had already been tested in pressure tension, the mass of the remaining sample was measured directly after the test and then placed within the oven. Subsequent mass measurements were taken every 24 hours until the mass readings stabilized in the manner recommended by ASTM C 642.

It should be noted that the temperature of the oven was set to above the boiling point of water, so additional expansive pressures from the phase transition of water into steam within the confined environment of pores could have caused damage to the pore structure that may have been detectable using pressure tension testing. Previous work showed that the expansion caused by the phase transition of liquid water into ice can induce damage that is detectable by pressure tension [11,12]. Expansive damage due to severe sulphate attack was similarly detected using pressure tension [13,14]. Other previous work has shown that the porosities of specimens that have been oven dried are measured to be higher than the same mixtures that have not been exposed to this environment [9,10], indicating that the oven drying method may be causing additional voids to develop that would have an adverse effect on the solid material cohesion and thus the tensile capacity of the material.

5.3.3. Destructive testing

5.3.3.1. Pressure tension testing

All specimens were tested in pressure tension after their respective conditioning regimes. Compressed air from a tank connected to a compressor was used as the loading medium. A constantly increasing chamber pressure, at a rate of 2.0 MPa/minute, was maintained by

computer-controlled actuator valves. The chamber pressure was measured every 0.1 s using a pressure transducer attached to the pressure line leading into the chamber. The peak pressure load was obtained from this signal as measured by a data acquisition system, and the ultimate chamber pressure was taken as the tensile failure stress of the specimen.

5.3.3.2.Compression testing

Compressive strength tests in accordance with ASTM C 39 were performed on 3 samples per mixture. The ends of these samples were ground parallel using a commercially available sample grinder. The diameter of the sample was measured using a caliper with an accuracy to 0.01 mm so that a representative stress could be calculated from this surface area. Peak loads in N were taken from the testing apparatus and the representative compressive stress was calculated using these peak loads and the measured surface area of the ground ends.

5.3.4. Nondestructive test monitoring

5.3.4.1.Surface resistivity

A commercially available Proceq Resipod surface resistivity (SR) meter with 50 mm spacing between the probes was used for all the NDT monitoring. From each of the mixtures, seven specimens were randomly selected for daily monitoring throughout curing. On each of these specimens, four lines were drawn on the curved surface so that the SR measurements would be taken in the same place at every testing interval. These lines were equidistant from each other, and positioned so that there would be no surface voids beneath the probe contact points during the testing. The SR meter was positioned so that the distance to the edge of the specimen was equal on either end to minimize edge effects. An average of these four SR readings per sample was determined, and then the averages from each of the seven controls were calculated to

produce an average SR for every day during the curing for each of the mixtures. After 28 days of curing, and before any specific conditioning could commence, the rest of the specimens were tested to make sure that they agreed with the values found from the control readings. If possible, SR readings were taken at the time of PT testing, but this was only possible for the saturated and vacuum saturated specimens, due to the necessity for near-saturated conditions required by the SR test.

5.3.4.2. Ultrasonic pulse velocity

A commercially available ultrasonic pulse velocity (UPV) measuring device was used in the end-to-end configuration as an alternative NDT monitoring system during the curing of the specimens. Before every test, the device was calibrated to ensure that the measured travel times were as accurate as possible. A water-based gel was used to ensure a sound connection between the transducers and the flat surfaces of the ends of the concrete sample. In some cases, surface roughness of the specimen caused some difficulties in creating a sound connection, which necessitated a large quantity of the gel being applied to the contact surface. The calibration of the device was checked after every sample measurement to check for any change in measurements that might result from this gel application.

For each of the 7 control samples, at least three end-to-end travel times were taken, with the location of the transmitter and receiver being switched between successive measurements. Measurements were taken in this manner until at least three of them came within 0.5 μs agreement with each other. The average of these three values were then taken as a representative travel time for the specimen. To determine the travel distance, a caliper with an accuracy of 0.01 mm was used to measure the end-to-end length of the cylinder. Surface

roughness at the ends was on the order of 1 mm, so there is slight uncertainty over the exact distance between the ends.

The ultrasonic pulse velocity used this average travel time and measured distance to compute the velocity as Equation 5.12

$$v = x/t$$

Equation 5.12- Pulse velocity calculation for UPV

where *v* is the ultrasonic pulse velocity in s, *x* is the measured distance in m, and *t* is the travel time in s. The average of these UPV values from each of the 7 specimens was taken so that a single UPV value at the same point during curing could be compared from each of the 6 mixtures. Subsequently, every individual test specimen was tested before PT testing to make sure that the UPV agreed with the 28 day cured specimens.

5.4. Results and Discussion

5.4.1. Nondestructive monitoring

5.4.1.1.Surface resistivity

All six of the mixtures exhibited a gradual increase in surface resistivity as a function of curing time as depicted in Figure 5.3. This increase in SR readings is most likely associated with the continuing production of cement hydrates filling in available pore spaces, which would decrease the number of pathways the SR measurement current can pass through and therefore increase the measured resistivity. The lower w/c mixtures showed a greater surface resistivity at earlier ages, and it also increased by a larger amount compared to those mixtures of higher w/c. These relationships were anticipated due to the greater proportion of cement in the lower w/c mixtures. The mixtures with air-entrainment exhibited very similar resistivity values when

compared to the regular mixtures of the same w/c, but on average, the air-entrained mixtures were measured to have a slightly greater average resistivity as compared with their regular mixtures.

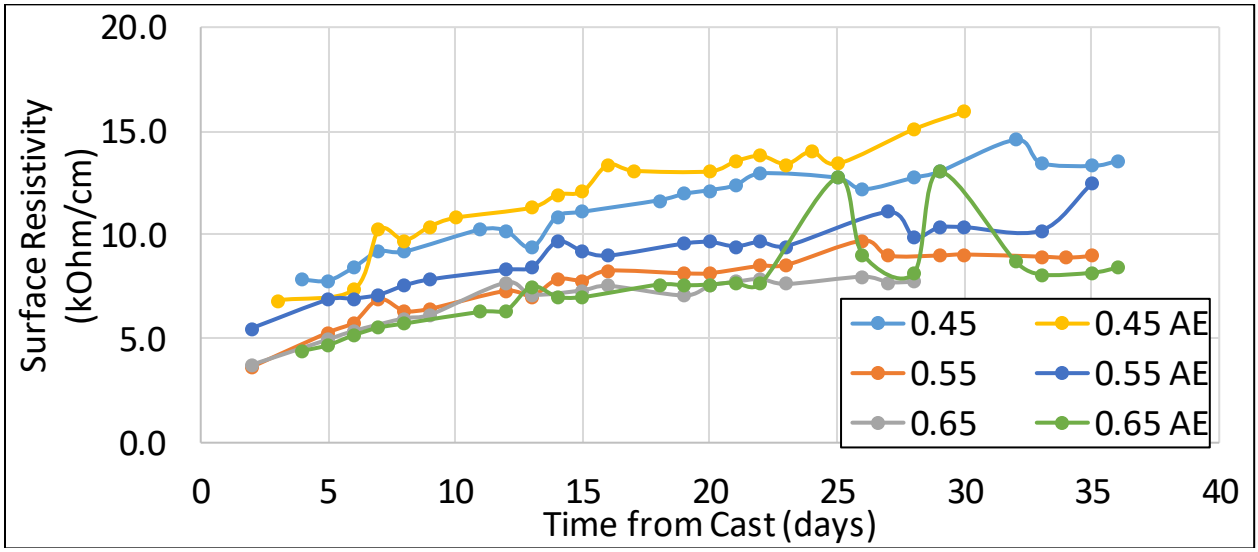

Figure 5.3- Relationship between curing time and measured surface resistivity on six mixtures

This dissimilar relationship between air-entrained and regular concrete of the same w/c was considered statistically significant per a 2-sample unequal variance test for 4 of the 6 mixtures. The only paired mixtures that were not considered significantly different from each other at all points during the curing monitoring with SR was the 0.65 and 0.65 AEA, which were much closer to each other in terms of SR readings, as can be seen in Figure 5.3.

However, even within this mix, there are some points at which the AEA mixture was tested to have a significantly higher reading when compared to the regular mixture, but this relationship does not hold throughout the curing process and is thus considered inconclusive. An explanation for air entrainment causing a higher measured surface resistivity could be that the air entraining bubbles are not connected to the void space due to the mechanism of their formation. These

voids would be an impermeable volume that could not allow current to pass and thus cause an increase in the measured resistivity of the whole volume.

The SR readings from the test specimens were not significantly different from those values that were measured after 28 days of curing, so any additional changes in the pore structure that occurred between 28 days of curing and the testing age after exposure were not detectable using SR.

5.4.1.2.Ultrasonic pulse velocity

Most the mixtures exhibited a gradual increase in UPV as a function of the curing time as seen in Figure 5.4. The exception to this general relationship was the 0.65 AEA mixture, which had a much greater degree of UPV variability compared to all of the other mixtures. This trend was not otherwise apparent from the collected data. This anomalous data may be attributable to the particular difficulties of UPV testing on the rougher surface of the 0.65 AEA specimens. For all the mixes, there were anomalous one-day changes in the average UPV data that did not persist over multiple testing intervals

This gradual increase in transmission velocities was expected since curing would produce additional cementitious hydrates to fill up available pore space, thus giving the stress waves a more cohesive material to pass through. In addition, the lower w/c mixtures with the greater proportion of cement per volume showed a greater pulse velocity as compared to the higher w/c mixtures. This trend was true for both the air entrained and regular mixtures. These two relationships can be seen in Figure 5.4.

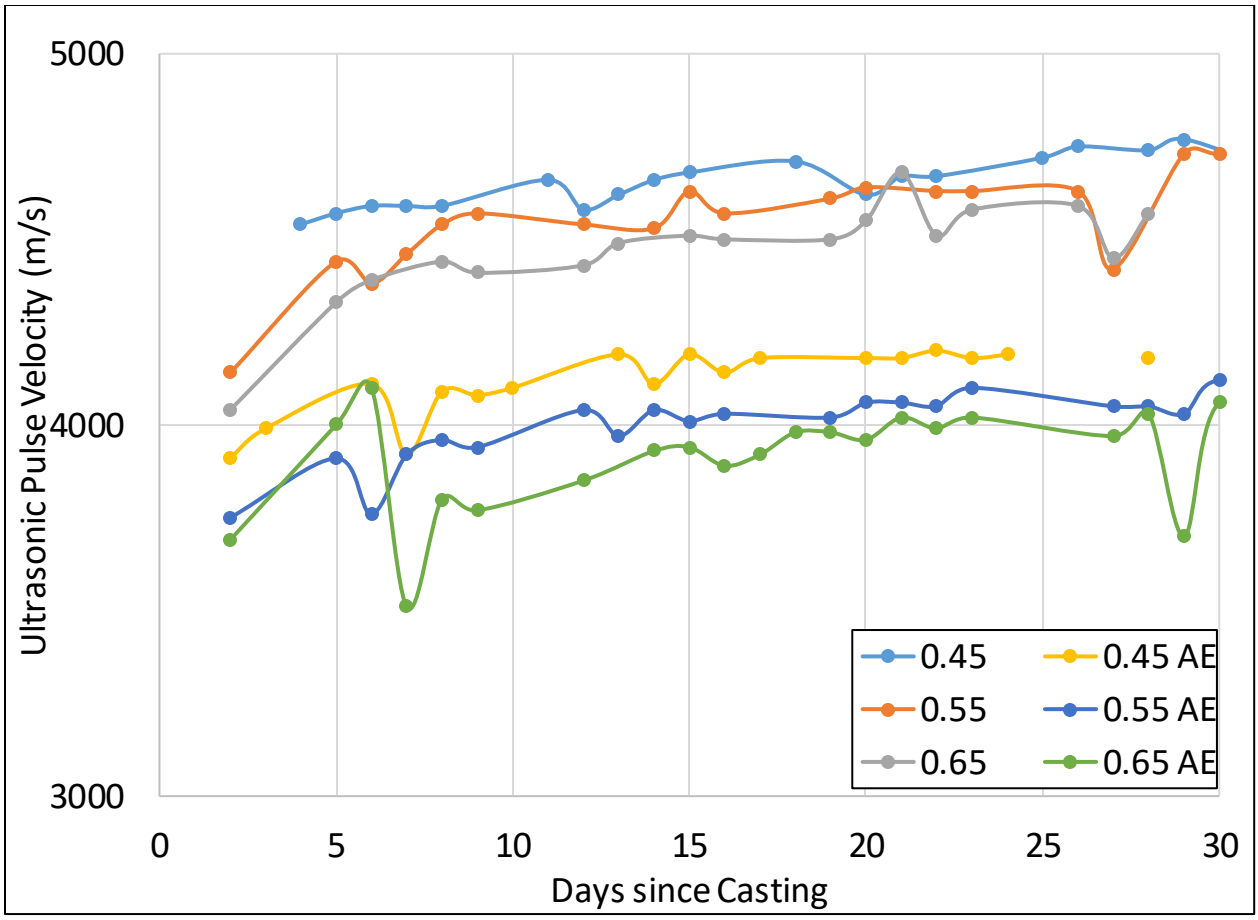

Figure 5.4- The effect of curing time on stress wave propagation

Another notable relationship is that all the air entrained mixtures produced a lower transmission velocity when compared to the normal mixtures. The significant increase in travel time of the stress waves resulting in a lower pulse velocity was most likely due to the additional voids that were created due to the inclusion of the air entrainment in the mixtures. This effect was much greater in magnitude than the effect of differing w/c on the pulse velocity.

5.4.2. Destructive testing

5.4.2.1.Compressive strength

The results of the compressive strength testing for all six mixtures can be found in Table 5.3. Lower W/C mixtures exhibited higher average compressive strength, as was expected based on

the greater cementitious content. The air entrainment significantly lowered the compressive strength by almost 50% in all three cases. The extra void space created by the air entrainment bubbles had a significant effect on the ability for the material to resist applied stresses.

Table 5.3- Compressive strength results

Mixture	Average Failure (MPa)
0.45	50.48
0.45 AEA	26.51
0.55	30.77
0.55 AEA	16.06
0.65	25.82
0.65 AEA	11.66

5.4.2.2.Absorption and void space

An estimate of the permeable void space and absorption potential of each of the mixtures was conducted based on the outlined procedure using gravimetric drying measurements. Due to the large variability in fragment mass loss due to PT testing, the estimates of the total amount of evaporable water within the same mixture were highly variable. These averages represent connected void space with evaporable water. The average values and their standard deviations can be found in Table 5.4. The proportion of void space containing evaporable water increases as a function of increasing w/c, and the higher w/c mixtures have a greater capacity for absorbing water. Furthermore, the air-entrainment had the effect of increasing the net volume of measured permeable spaces when compared to the normal concrete, suggesting that at least some part of the air entraining bubbles were connected to the rest of the void network through which evaporable water could flow. However, this increase is not considered statistically significant per the 2-sample unequal variance student T test. Otherwise, these measured relationships are well

within the established understanding of the relationship between pore space and w/c despite the high variability in the data.

Table 5.4- Permeable void space for mixtures

Mixture	Volume of Permeable Voids (% Volume)	Standard Deviation (% Volume)
0.45	13.11	0.49
0.45 AEA	13.35	2.21
0.55	14.52	0.62
0.55 AEA	15.71	1.00
0.65	15.07	1.29
0.65 AEA	15.44	1.54

5.4.2.3. Variable moisture content and pressure tension

The estimates of moisture content at the time of testing were significantly complicated by the large mass losses due to pressure tension testing creating fragments. In some cases, the exact moisture content could not be reliably calculated from this gravimetric data due to these complications. For those samples, the moisture content was assumed to be 100%. Figure 5.5 shows the data from each test from all of the different mixtures. For all the mixtures, the pressure tension values were significantly lower at low or no moisture content then when compared to a higher saturation. Figure 5.5 shows that the vacuum saturated samples (with θ >100 %) for each mixture are at the high end of the saturated values for each mixture. None of the vacuum saturation specimens exceeded 2% additional absorption over the regular saturation values.

The lower w/c mixtures were consistently found to have a higher net tensile strength. However, there was no clear pattern in terms of tensile strength between the same mixtures with and without air entrainment. A downward trend from the saturated condition toward the oven dry condition can be observed for all of the mixtures despite the high variability within the moisture

content data. It is also apparent from Figure 5.5 is that the majority of the moisture content values measured were in the 75-100% range. Regardless of their exposure conditions other than oven dried, all the different mixtures retained most their water.

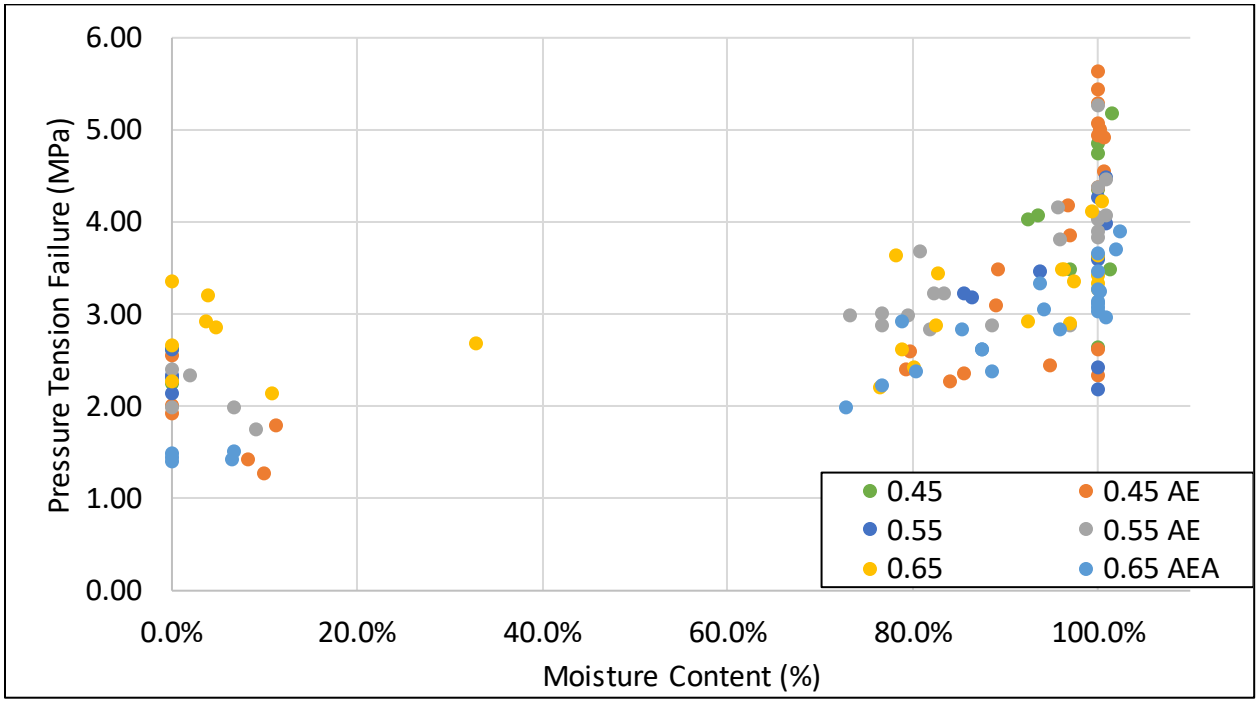

Figure 5.5- Relationship between moisture content and pressure tension failure level for six mixtures

5.4.2.4. Exposure conditions and pressure tension

Given the difficulty in accurately determining the moisture content of the PT specimens, the data were also analysed with respect to the exposure conditioning of the specimens as opposed to their bulk water content. The average pressure tension failures for each of the six mixtures and the four different exposure conditions can be found in Figure 5.6. All mixtures showed a clear decrease in measured tensile strength between the saturated and oven dried conditions, which was statistically significant per a 2-sample unequal variance student T test. There was also a slight observed increase in the average pressure tension failure level for the specimens that had undergone vacuum saturation versus those that were just saturated by regular means. This effect

was not large enough to be considered statistically significant, although the same trend appears for all six mixtures.

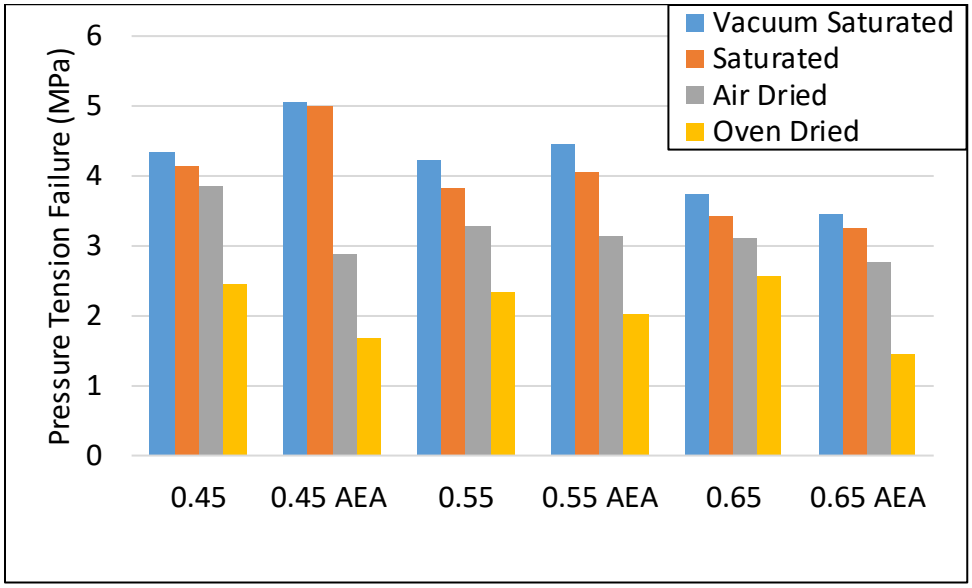

Figure 5.6- The effect of different exposure conditions on the pressure tension failure level for six mixtures

Figure 5.6 shows all the air-dried specimens with pressure tension failure stresses falling in between the saturated and oven dried average values. This effect was considered statistically significant for all the mixtures per the 2-sample unequal variance student T test. The air-entrained concretes exhibited a higher average failure stress in the saturated condition, which was not expected, considering that the same compressive strengths were consistently lower for these same mixtures. However, after oven drying, all of their measured failure stresses were consistently lower than the non-entrained counterparts of the same w/c. Table 5.5 shows the average failure stress levels of the specimens from the different exposure conditions when normalized with respect to the average saturated failure stress from each mixture. The oven dried specimens of the air entrained mixtures failed at a consistently lower normalized stress

level for the same w/c, which suggests that the higher porosities of these mixtures caused both a lower failure at a lower moisture content as well as a higher failure at a higher moisture content.

Table 5.5-Normalized pressure tension stress failure values for different exposure conditions

Mixture	Vacuum Saturated	Saturated	Air Dried	Oven Dried
0.45	104.6%	100.0%	93.2%	58.8%
0.45 AEA	100.8%	100.0%	57.7%	33.8%
0.55	110.6%	100.0%	86.0%	61.4%
0.55 AEA	110.3%	100.0%	77.8%	50.2%
0.65	109.4%	100.0%	90.8%	74.8%
0.65 AEA	106.2%	100.0%	85.1%	44.7%

This downward trend in pressure tension stress failure is also apparent when the air-drying condition is considered in greater detail, as seen in Figure 5.7. Figure 5.7 shows the normalized pressure tension failure stresses for the six mixtures relative to the different durations of air drying. There is a large amount of variability within the data, but there is the same gradual trend towards a lower tensile failure stress, which is clear from Figure 5.7.

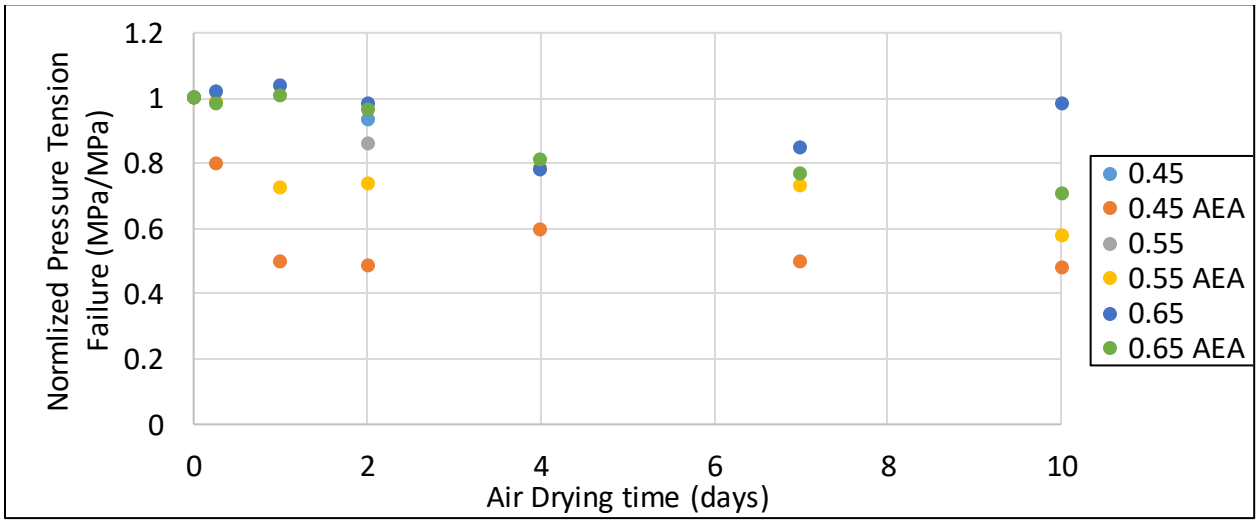

Figure 5.7- Normalized pressure tension failure stresses after different durations of air drying

5.4.3. Visual observations

One visual observation made during the testing is that the failure mode of the specimens was different between the saturated and dried specimens. For the specimens that were tested with a high moisture content, a single tensile crack perpendicular to the loading direction was generally the mode of failure, as can be seen in Figure 5.8. The crack surface propagated through the ITZ around aggregates, and sometimes caused a fracturing of the aggregate as well. There was generally a higher proportion of failure in the ITZ for the higher w/c mixtures, whereas there was a greater amount of failure through the aggregates where the w/c was lower. This mode of failure has been previously noted by others performing PT testing.

Figure 5.8 - Typical tensile crack for high moisture content specimens

However, for the specimens with a very low moisture content, a new mode of failure was observed. Instead of the typical crack developing perpendicular to the loading direction, the specimens seemed to exhibit a net paste failure through a large portion of the specimen volume. Instead of two distinct portions of the specimen separated by the tensile crack, the volume would

essentially disintegrate, leaving a large mass of rubble, as seen in Figure 5.9. This effect was generally more prominent for the higher w/c mixtures, but this mode of failure was observed for all six mixtures on the oven-dried specimens.

Figure 5.9- Volumetric paste failure of typical low moisture content specimens

For those specimens that were neither fully saturated nor oven dried, the failure mode was generally of the net tensile crack perpendicular to the crack face. One notable observation was from the partially dried specimens, where a distinctive core of higher moisture content could be observed on the crack face, with a ring of drier concrete at the exterior as seen in Figure 5.10.

Figure 5.10- Distinctive partially saturated crack surface face

The specific kinematics of the 3-dimensional transport properties of coupled water-vapor system through partially saturated porous concrete during drying in a variable relative-humidity environment were not investigated during this study. However, Figure 5.10 demonstrates that the specimens appear to dry from the outside of the diameter radially inward, as opposed to uniformly decreasing the volume fraction of water occupying the pore space.

5.5. Conclusions

Surface resistivity testing during the curing period showed that all of the mixes gradually developed an increased resistivity as a function of curing time. This detected signal would be associated with a densification of the cementitious matrix as a function of continuing hydration. Similarly, the UPV testing showed that the mixtures gradually increased the transmission velocity of stress waves as a function of curing time. This change is also associated with the densification of the cementitious matrix due to the additional cement hydrates being deposited within the pore structure. Subsequent UPV and SR testing showed that the samples used in a variety of moisture conditions were not detectably different from these control samples used for the NDT. Pressure tension failure stresses were highly dependant on the moisture content of the samples, which was detectable using pressure tension testing, despite the high variability, from measuring the moisture content and pore space of the samples. Furthermore, the effect of different pore volumes had a detectable effect on the measured tensile failure stress for a variety of moisture contents. For those mixtures with a higher overall pore volume induced by air entrainment, they exhibited a higher tensile stress when those pores were saturated, but for the same mixtures, failed at a lower tensile stress when those pores were emptied of their water due to drying. There was an increase noted in the pressure tension failure stress when comparing vacuum saturated

specimens with regular saturation specimens, suggesting that the slight amount of additional water forced into the void space by vacuum may be causing additional resistive forces to develop internally. This effect was not large enough to be statistically significant within the context of the study, however it was certainly intriguing.

The effect on tensile failure stresses of moisture contents between 1 and 0 was more conclusive, showing that all mixtures lost strength as a function of decreasing moisture content, and all mixtures were significantly weaker when there was no water within the pore structure. There were experimental difficulties in conditioning specimens to have moisture contents between 10%-75%, which may be due to the complex way that the specimen dries out and the limited timeframe allotted for drying. Those mixtures with air entrainment also lost a greater proportion of their strength due to drying when compared to a regular mixture. The failure mode observed on the oven-dried specimens suggests that water within the pore volume is somehow moderating the application of stresses to the solid phase. As the visual observations note, in the absence of water within the pores, it appears that instead of a single tensile crack at failure, a large volume of the solid material fails at a substantially lower stress level that would be found in saturated testing conditions associated with the more commonly observed tensile cracking.

More studies to investigate this moisture content dependency of pressure tension failure stresses are certainly in order. Such investigation could include a more rigorous characterization of the geometry of the pore spaces and the behavior of water within these voids under partially saturated conditions with mercury intrusion porosimetry or computer modelling. Another study could investigate the effect on pressure tension failure stress by replacing the pore water in concrete samples with another liquid that has a radically different viscosity compared to air or

water to determine the magnitude of the effect that viscosity has on the level and mode of failure. Different drying techniques other than with an oven should be used for this kind of partial saturation study, given that oven drying may be causing destructive stresses on the cementitious matrix that would lower the tensile stress resistance, which would be detectable using pressure tension. Finally, water with dissolved surfactant could be used to characterize the specific effect that the surface tension of the water within the capillary pores is having on pressure tension failure stress levels.

Pressure tension is a very reliable method of determining the resistance of a sample to indirect tensile stresses. The test is very sensitive to small changes in the state of the solid phase of concrete, such as those induced by various deterioration processes, and particularly by expansive mechanisms. The variable effect of moisture content on the pressure tension results is therefore an important relationship to understand, since the type of concrete in real-world conditions will often be in a partially saturated state. This study showed that the extent of this variability can be accurately characterized with pressure tension testing.

5.6. Acknowledgements

The authors of the study acknowledge the donation of the coarse and fine aggregates used for the entirety of the study by Bauval LLC. They also acknowledge the donation of the Surface Resistivity meter by Proceq, which was used for the entire duration of the study.

5.7. References

[1] Clayton, N. and Grimer, F. (1979): The Diphase Concept, with Particular Reference to Concrete. In: *Developments in Concrete Technology*, Elsevier Science & Technology, Waterford, UK, pp. 283-317

[2] Terzaghi, K., and Peck, R. (1967)*: Soil Mechanics in Engineering Practice*. Wiley, New York,

[3] Uno, T., Fujikake, K., Mindess, S. and Xu, H. (2010): The Nitrogen Gas Tension Test of Concrete, Part 1: Effect of Boundary Conditions and Axial Strain Response. In: *Materials and Structures*. 44 No.4, pp. 857-864

[4] Fujikake, K., S. Mindess, T. Uno, and H. Xu. "The Nitrogen Gas Tension Test. Part 2: Failure Mechanism." Materials and Structures 44, no. 4 (2011): 865-77.

[5] Nokken, M., Hooten, D. (2008): Using pore parameters to estimate permeability or conductivity of concrete. In: *Materials and Structures* 41 No.1, pp. 1-16

[6] Hughes, D.C. (1985): Pore structure and permeability of hardened cement paste. In: *Magazine of Concrete Research* 37:133, pp. 227-233

[7] Benboudjema, F., Meftah, F., Torrenti, J.M. (2005): Interaction between drying, shrinkage, creep and cracking phenomena in concrete. In: *Engineering Structures* 27, No. 2, pp 239-250

[8] Bu, Y., Spragg, R., Weiss, W.J. (2014): Comparison of the pore volume in concrete as determined using ASTM C642 and Vacuum Saturation. In: *Advances in Civil Engineering Materials* (3) No.1. pp 308-315

[9] Safiuddin, Md., Hearm, N. (2005): Comparison of ASTM saturation techniques for measuring the permeable porosity of concrete. In: *Cement and Concrete Research* (35) pp 1008-1013

[10] Safiuddin, Md., Mahmud, H.B., Jumaat, M.Z. (2011): Efficacy of ASTM saturation techniques for the water absorption of concrete. In: *Arab J Sci Eng* (36) pp 761-768

[11] Komar, A., J. Hartell and A. J. Boyd. (2013) Pressure tension: reliability for assessing concrete deterioration. In: *Proceedings of The Seventh International Conference on Concrete under Severe Conditions*, Nanjing, China, No.1, pp. 337-344

[12] Komar, A.J.K.; Boyd, A.J. (2014); Pressure-tension testing in the evaluation of freeze-thaw deterioration. In *Proceedings of 10th Fib International PhD Symposium in Civil Engineering*, Université Laval, Québec. p. 143-148

[13] Hartell, J., Boyd, A. J., and Ferraro, C.C. (2011): Sulfate attack on concrete: effect of partial immersion. In: *Journal of Materials in Civil Engineering*. 23 No.5, pp. 572-579

[14] Boyd, A., and Mindess, S. (2001): The effect of sulfate attack on the tensile to compressive strength ratio of concrete. In: *Proceedings of The Third International Conference on Concrete under Severe Conditions*, Vancouver, Canada, pp. 789-796

ASTM. "Standard Test Method for Air Content of Freshly Mixed Concrete by the Pressure Method." West Conshohocken, PA: ASTM International, 2014.

ASTM. "Standard Test Method for Compressive Strength of Cylindrical Concrete Specimens." West Conshohocken, PA: ASTM International, 2017.

ASTM. "Standard Test Method for Density, Absorption, and Voids in Hardened Concrete." West Conshohocken, PA: ASTM International, 2013.

ASTM. "Standard Test Method for Slump of Hydraulic-Cement Concrete." West Conshohocken, PA: ASTM International, 2015.

ASTM. "Standard Test Method for Splitting Tensile Strength of Cylindrical Concrete Specimens." West Conshohocken, PA, ASTM International, 2004.

Foreword to Chapter 6

Chronologically, the research detailed in Chapter 6 was the first experimental work performed with the pressure tension system by the researcher. The observations concerning the reliability of the control system implemented by the researcher were included for reference. The durability mechanism of external sulphate attack in a slab exposed to evaporative flow of a sulphate ion solution is relevant to the overall research goals of this thesis, as it touches on both the transport properties of concrete in a durability context as well as the effect of the expansive sulphate attack on the tensile resistance of concrete. The slabs were undergoing a more complex two-dimensional evaporative transport condition and the overall length of mass transport was longer than the type investigated with the MRI studies in Chapter 3 and the evaporative transport paper. However, in some regions far from the edges of the slab, the conditions would more closely resemble a uniform one-dimensional flow, and thus the broader conclusions of Chapter 3 and the related evaporative transport paper studies would be relevant.

The pressure tension test detected a damage gradient in the slab, with the most severe damage occurring in regions with a saturated condition filled with sulphated ions. Less severe damage was detected in the region where there was evaporative flow occurring. In the region far removed from the evaporative mass transport at the extreme dry face, there was no detectible evidence of sulphate damage. The results from Chapter 6 also demonstrated the effect of moisture content on hydration in evaporative transport conditions. The greatest magnitude of tensile resistance was found for both sulphate immersed and control specimens (without deleterious ions) to be in the saturated regions. A gradient of strength ranging from the

evaporative transport regions to the weaker areas that were dried. All specimens were conditioned to be in a saturated condition before the pressure tension test, so this moisture content effect of hydration on the tensile strength is independent of the moisture content pressure tension relationship detailed in Chapter 5. The paper was prepared and presented for a conference:

Komar, A.J.K., J.A. Hartell, and A.J. Boyd. "Pressure Tension: Reliability for Assessing Concrete Deterioration." In Proceedings of The Seventh International Conference on Concrete under Severe Conditions, edited by Z.J. Li, W. Sun, C.W. Miao, K. Sakai, O.E. Gjørv and N. Banthia, 337-44. Nanjing, China: RILEM Publications, 2013.

Chapter 6: Pressure Tension Test: Reliability for Assessing Concrete Deterioration

Komar, A.J.K, Hartell, J.A., Boyd, A.J.

McGill University, Montreal, Quebec, Canada

6.1. Abstract

In previous research, the pressure tension test was shown to be effective in assessing the loss in tensile strength of concretes subjected to various degradation mechanisms. It was found to be particularly suitable for detecting damage at early stages of deterioration due to the failure mechanism's explicit sensitivity to the weakest microstructural features of the degraded concrete, as opposed to the traditional cylinder splitting tension test wherein tensile failure is forced to develop along the longitudinal axis of the cylinder, often giving results that do not accurately reflect damage variations or gradations within the sample. Compression testing is also often used to determine changes in structural properties, though it was found that it may not be appropriate for evaluating degradation caused by expansive reactions and softening of the cementitious material. In this study, a series of 70 loading trials was conducted to calibrate the rate response of the control system for the pressure tension test. Once calibrated, a second series of trials was conducted to examine the ultimate tensile strengths of sulfate degraded concrete cores. The controller was able to maintain the specified rate of loading to a high degree of accuracy, further increasing the consistency of the test method. The results illustrate the high

repeatability of the pressure tension test for deteriorated concrete, permitting a conclusive analysis on the effects of sulfate exposure and related degradation mechanisms.

6.2. Introduction

The pressure tension test, also known as the indirect tension test or nitrogen gas pressure test, was first developed by The Building Research Council of Waterford, UK as a means of investigating anisotropic behavior in materials [1,2]. The pressure tension test uses compressed gas to apply a uniformly distributed pressure to the curved surface of standard 100 mm by 200 mm concrete test cylinders or cores. The apparatus consists of a hollow cylindrical test chamber which envelops the curved surface of the test cylinder. At either end of the testing chamber, rubber "O-rings" are used to seal the compressed gas so that it only acts upon the curved surface of the specimen, as seen in Figure 6.1. Both ends are left open to atmospheric pressure, resulting in a biaxial loading configuration. Gas pressure is monotonically increased until the test cylinder fails in a plane transverse to the axis of the testing chamber.

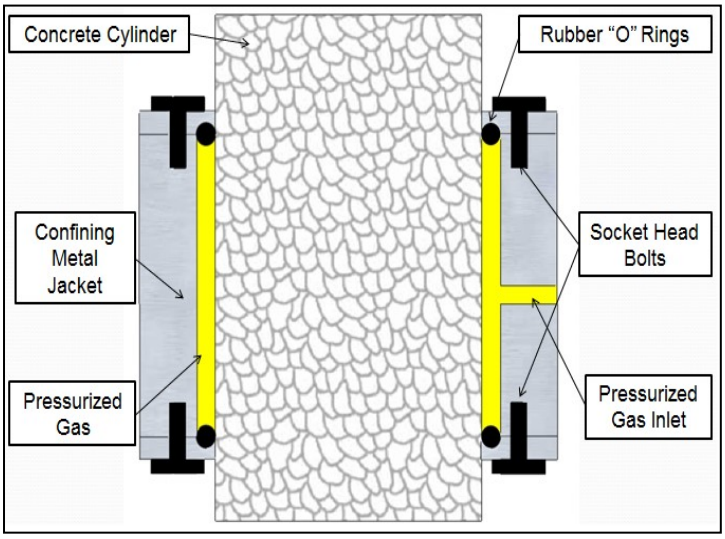

Figure 6.1- Cross section of pressure chamber

The perpendicular failure plane is indicative of a tension failure although there is no direct tension being applied. This counter-intuitive result can be understood by applying the effective stress theory originally developed for soil mechanics, in which concrete is modeled as a diphase material consisting of a solid and liquid phase [3]. The gas pressure applied to the curved surface is a biaxial loading condition but the reaction forces within the diphase model differ. In particular, the pore water reacts hydrostatically whereas the solid phase reacts biaxially, resulting in a net internal tensile force driven by the pore fluid.

The resultant internal tension force is the primary reason why the pressure tension method is well suited for detecting durability issues which affect the integrity of the cementitious microstructure. Previous work has shown that pressure tension testing can detect damage associated with expansive processes such as external sulfate attack earlier than standard methods of testing [4]. This type of damage detection is not possible using the standard tension test ASTM C 496 (splitting tension), since the failure plane is a direct result of the loading boundary conditions of the test [5].

The specific moisture content of the concrete at the time of pressure tension testing has previously been shown to have a measurable effect on the ultimate strength of the specimen in failure. Specimens that were tested at moisture contents closer to saturation failed at levels three times higher than values obtained via splitting tension at the same moisture content [6].

For this reason, gas pressure tension was the chosen test method for assessing the change in engineering properties of concrete exposed to an evaporative transport mechanism in a sulfate environment. Herein, the reliability of the test method is investigated.

6.3. Materials and Methods

6.3.1. Control system calibration

A set of 70 calibration trials was conducted to characterize the accuracy of the actuated controller valve in maintaining a specified rate of loading. An aluminum cylinder 100 mm in diameter by 200 mm long was used in lieu of concrete test specimens to ensure consistent sealing condition across all trials and to provide adequate sealing with the O-rings. Each trial consisted of the application of a linear loading from 0.00 to 7.00 ±.05 MPa at a specified load rate. A constant loading rate between 0.005 MPa/s and 0.100 MPa/s was fed into the control system. The pressure within the cell was monitored with a pressure transducer attached to the testing chamber. 10 pressure readings per second were recorded. Trials were performed at supply pressure heads of 6.89, 8.62, 10.34 and 13.79 MPa.

The measured rate of loading and the coefficient of determination were obtained from a least-squares linear regression analysis of the time-dependant rate response measured by the pressure transducer. This data was used as a quantitative measure of the control system's accuracy.

6.3.2. Sample preparation

The first set of trials was conducted on standard 100x200 mm concrete cylinders cast with Mixture Design A, shown in Table 6.1. After 24 hours of curing in their moulds, the cylinders were removed and stored in ambient laboratory conditions for over 2 years.

Table 6.1- Concrete mixture designs

Mixtures		A	B
		0.48 w/c	0.45 w/c
Cement – ASTM Type I/II	[kg/m3]	448.18	507.70

Water	[kg/m3]	217.45	228.60
Fine Aggregate (0-5 mm)	[kg/m3]	838.00	855.10
Coarse Aggregate (5-14 mm)	[kg/m3]	848.00	733.40

The second set of trials was conducted on cores taken from two large scale concrete blocks partially immersed in 5% Na2SO4 solution and saturated limewater, respectively, for a period of two years, as seen in Figure 6.2. In order to recreate a realistic field exposure mimicking that of foundation structures in sulfate laden soils, concrete blocks measuring 900 mm long x 240 mm thick x 485mm high were cast and immersed to a depth of 150 mm in the solutions. The blocks were prepared with mixture proportions representing the prescribed value in the Canadian standard to resist a severe sulfate exposure [5] (0.45 w/c). These blocks were cast from concrete batched in accordance with Mixture Design B in Table 6.1. After two years of evaporative exposure, the blocks were removed from the solutions and sealed with paraffin wax in order to minimize further interactions with the ambient surroundings and to prevent the washout of sulfates and other compounds during coring. A total of 18 cores were taken per block: six samples were cored from the immersed portion of the block (immersed), six samples were taken from directly above the immersion plane (evaporative), and six samples were cored from the unaffected top portion of the block (ambient) well above the immersion plane, as seen in Figure 6.3. Subsequently, the cores were stored in ambient laboratory conditions for over 2 years. Because of coring difficulties, only four or five samples out of the six were used for testing at each level.

Figure 6.2- Partial immersion of concrete blocks [8]

Figure 6.3- Location of cores taken from concrete blocks [8]

After calibration of the control system, the apparatus was ready for the trials on the concrete materials. Prior to testing, to ensure complete saturation of the concrete matrix, all samples were submerged in saturated limewater for a period of seven days.

6.3.3. Experimental setup

The pressure tension machine used compressed air as the loading medium in all of the experiments. The air was pressurized using a portable air compressor with a maximum available pressure of 17.23 MPa, which was stored in a pressurized gas canister attached to the compressor

and the testing machine. A variable check valve was used to keep the pressure head constant in order to minimize testing variance caused by variable storage tank pressure.

A needle valve was used as the controller for the flow rate of the compressed gas into the testing chamber. The valve was operated by a mechanical actuator which was controlled using custom software and monitored using a digital acquisition device (DAQ). Measurement of pressure within the test chamber was obtained using a digital pressure transducer directly adjacent to the chamber, which was used as a control input in the software. The pressure transducer had a measured error of ± 0.05 MPa. The DAQ had a sensing resolution of approximately 0.1 s. All pressure-time plots were recorded and stored, and the data point immediately preceding failure was used as the failure load for it.

The control algorithm which was implemented was a modified proportional integral derivative function which automatically varies the valve position based on the detected error between the measured pressure and the set point. The set point is an arbitrary time dependant function, and all trials using concrete within this study used a monotonically increasing pressure-time signal with a rate of 0.02 MPa/second, comparable to loading rates in both ASTM C 496 and ASTM C 33.

Finally, each test cylinder was prepared for testing. Rubber O-rings with a diameter of 10 mm were used to seal the interface between the test chamber and the concrete sample. A layer or two of polyvinylchloride tape was applied on both ends of the cylinder to provide a better seal between the O-rings and the cylinder, which occasionally had voids or deterioration defects that could cause leakage around the O-rings. The latter were torqued with a series of six lug nuts

bearing on a steel plate in a manner that applied equal pressure on the O-ring and a positive seal for the loading gas.

6.4. Results and Discussion

6.4.1. Pressure tension test reliability

Based on the results of the calibration trials, it was found that the controller could maintain a high degree of linearity (R^2 greater than .9975) between the ranges of 0.005 MPa/s and 0.060 MPa/s as shown in Figure 6.4. The error within this range between input and output load rate was never greater than 0.008 MPa/s, and for most trials the error between input and output was less than 0.001 MPa/s.

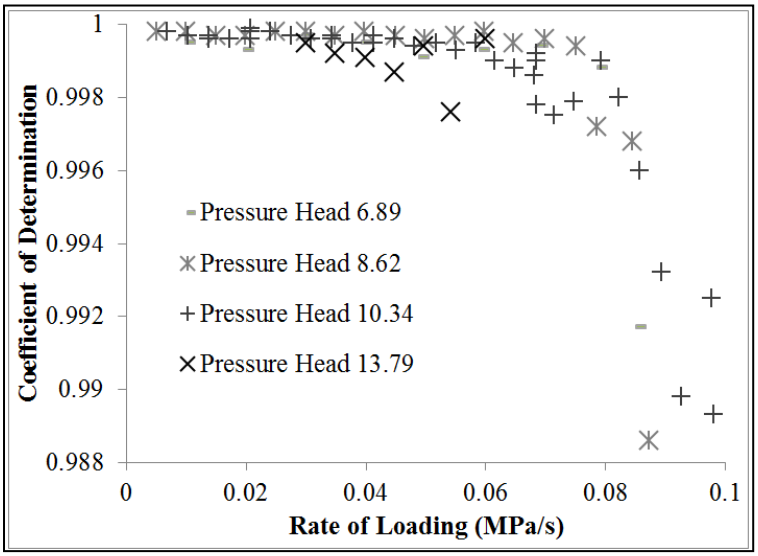

Figure 6.4- Coefficient of determination versus load rate

For loading rates higher than this limit, the system response time was inadequate to properly adjust the flow rate, and the ability of the system to maintain a linear loading rate rapidly diminished. Trials at these higher load rates more closely resembled a step function. The pressure head was not found to have a significant effect on the load repeatability, although the trials

performed at lower pressure heads had a greater degree of linearity based on the R^2 values. All subsequent concrete samples were tested within this range to ensure high repeatability of loading. These stress application values are also within ranges used in the splitting tension (ASTM C496) and compressive strength standards (ASTM C39), so they were not considered to be unusual rates of loading

6.4.2. Destructive testing

The first trial of samples consisted of six standard concrete cylinders. The results of each individual test are presented in Table 6.2. The statistical analysis in Table 6.2 demonstrates that the coefficient of variation, 9.30% of the average tensile strength, was better than that prescribed in the ASTM C 496 standard (i.e. 14%). Based on that value, the test procedure was considered to be acceptable and reliable. For deteriorated concrete, the results continued on the same trend.

Table 6.2- Tensile strength of concrete exposed to ambient conditions for two years

Samples	Ultimate Tensile Strength (MPa)
1	2.81
2	3.50
3	2.96
4	2.81
5	3.17
6	2.80
Statistical Analysis	
Average (MPa)	3.01
Standard Deviation (MPa)	0.28
Coefficient of Variation	9.30%

These results obtained for the trials on cores were considered reliable. As seen in Table 6.3, the coefficients of variation calculated were all below 14%. Because of the repeatability of the test, a comparison analysis between sample means was possible for each. Here, the F-Test was used to determine whether there was a significant difference between the samples variances. With p-values above the selected level of significance (α=0.05), the results of the F-Test demonstrated that all of the sample's variances were the same; therefore, a pooled-variance student's t-test with the following parameters was chosen to compare the means of each exposure type: equal variance, two-tailed normal distribution, level of significance (α) equal to 0.05.

Table 6.3- Tensile strength of cores taken from exposure blocks

Plane	Immersed		Evaporative		Ambient	
Solutions	5% SO4	Limewater	5% SO4	Limewater	5% SO4	Limewater
Samples	Ultimate Tensile Strength (MPa)					
1	5.66	6.63	3.80	4.94	3.38	3.52
2	5.98	7.21	4.42	6.23	2.65	3.83
3	5.90	6.84	4.58	4.92	2.93	3.13
4	6.02	7.04	4.25	5.73	3.53	3.54
5	-	7.12	4.55	-	2.85	3.57
Statistical Analysis						
Average (MPa)	5.89	6.97	4.32	5.45	3.07	3.52
Standard Deviation (MPa)	0.16	0.23	0.32	0.64	0.37	0.25
Coefficient of Variation	2.72%	3.30%	7.41%	11.74%	12.05%	7.10%
F-Test p-value	0.59		0.21		0.47	
t-Test p-value	1.03E-04		0.01		0.05	

The results of the comparison analysis, shown in Table 6.3, were used to evaluate whether the tensile properties of the concrete material were affected by sulphate solution exposure. The average tensile strengths obtained for each type of sulphate exposure (immersed, evaporative and ambient) were compared with their respective control (limewater) exposure. Starting with the immersed portion of the concrete block, the probability that the means are equal was 1 in 10,000. Therefore, it was concluded with high confidence that the sulphate solution exposure had an effect on the material properties. In this case, there was a 15% loss in tensile strength due to the chemical degradation mechanism associated with external sulphate attack [9]. In the case of evaporative exposure, the physical type of degradation noticed on the surface of the block (i.e. salt weathering) indicated that it was sufficiently significant to cause damage to the microstructure of the cementitious matrix [9]. The results of the t-test returned a probability (1%) lower than the level of significance (5%), indicating that there was a significant (21%) drop in tensile properties directly above the immersion line.

Finally, the lowest tensile strength recorded was for the upper part of the block which was not exposed to sulphate or limewater solution. However, though there was a difference of 13% between the means, the results of the t-test demonstrated that the two-sample means were not significantly different. Therefore, under the same ambient laboratory conditions, the concrete matrices in the upper portion of the blocks were not affected by sulphates, nor limewater for that matter. The difference in strengths between the submerged part and the upper part of the control blocks is almost double. This may be attributed to the difference in hydration conditions; the lower portion was continuously submerged in solution promoting continuous cement hydration while the upper portion was allowed to dry and thus received much less curing.

6.5. Conclusions

When evaluating concrete material properties under severe exposure conditions, it is important to have reliable test equipment. The test procedure and equipment used may influence the results obtained. In this case, a gas pressure test apparatus was built and trialed to measure the tensile strength of concrete cylinders and cores. Knowing the actual tensile strength of a concrete material is imperative toward understanding concrete durability issues. For this study, the effects of external sulphate attack on the tensile properties of a concrete mixture were evaluated. From the results obtained, it can be concluded that the presence of sulphates migrating into the concrete matrix and interacting with the cementitious phase for a period of two years contributed to the recorded loss in tensile properties of a 0.45 w/c concrete mixture. The gas pressure tension test is therefore considered to be sensitive in assessing the presence and degree of such degradation. For this reason, the test procedure is currently being further refined and an extensive test program is being carried out to standardize the equipment and procedure in the near future.

6.6. References

[1] Clayton, N., and F. Grimer. "The Diphase Concept, with Particular Reference to Concrete." Chap. 7 In Developments in Concrete Technology, 283-317. Waterford, UK: Elsevier Science & Technology, 1979.

[2] Clayton, N. "Fluid-Pressure Testing of Concrete Cylinders." Magazine of Concrete Research 30, no. 102 (1978): 26-30.

[3] Terzaghi, K., R.B. Peck, and G. Mesri. Soil Mechanics in Engineering Practice. 3rd ed. New York: Wiley, 1996.

[4] Boyd, A.J., and S. Mindess. "The Effect of Sulfate Attack on the Tensile to Compressive Strength Ratio of Concrete." In Proceedings of Third International Conference on Concrete Under Severe Conditions, 789-96. Vancouver, Canada: ACI/CSCE, 2001.

[5] Hartell, J.A., A.J. Boyd, and C.C. Ferraro. "Sulfate Attack on Concrete: Effect of Partial Immersion." Journal of Materials in Civil Engineering 23, no. 5 (2011): 572-79.

[6] Uno, T., K. Fujikake, S. Mindess, and H. Xu. "The Nitrogen Gas Tension Test of Concrete. Part 1: Effect of Boundary Conditions and Axial Strain Response." Materials and Structures 44, no. 4 (2011): 857-64.

[7] Hartell, J.A., and A.J. Boyd. "Determining Sulphate Movement in Concrete Exposed to Evaporative Transport." In Proceedings from 9th fib International PhD Symposium in Civil Engineering, 511-16. Karlsruhe, Germany: KIT Scientific Publishing, 2012.

[8] Cumming, S. "Nondestructive Testing to Monitor Concrete Deterioration Caused by Sulfate Attack'." University of Florida, 2004.

[9] Marchand, J., I. Odler, and J.P. Skalny. Sulfate Attack on Concrete. CRC Press, 2003.

ASTM. "Standard Test Method for Splitting Tensile Strength of Cylindrical Concrete Specimens." West Conshohocken, PA,: ASTM International, 2004.

ASTM. "Standard Test Method for Compressive Strength of Cylindrical Concrete Specimens." West Conshohocken, PA: ASTM International, 2017.

Foreword to Chapter 7

Chapter 7 was a preliminary demonstration of the pressure tension machine in detecting freeze-thaw damage in concrete. The expansion of water in a saturated pore system caused damage which created cracks due to the expansive stresses in this microstructure. Chapter 7 was prepared as a conference paper which was then presented and published:

Komar, A.J.K., and A.J. Boyd. "Pressure-Tension Testing in the Evaluation of Freeze-Thaw Deterioration." In Proceedings of the 10th fib International PhD Symposium in Civil Engineering, edited by J. Bastien, N. Rouleau, M. Fiset and M Thomassin. Université Laval, Québec, Canada: International Federation for Structural Concrete, 2014.

The effectiveness of the pressure tension test in detecting the expansive damage causing changes to the pore system associated with mass transport was clearly demonstrated here, as well as the relative effect of different w/c on the tensile strength. Splitting tension and compressive strength tests were also performed to compare the magnitude of the deterioration as detected by these other, standard destructive tests. The chapter clearly demonstrates that pressure tension tests detected the greatest magnitude of tensile deterioration, which is directly related to the mode of loading through the connected pore structure. Another important conclusion reached during the testing for Chapter 7 was the high sensitivity of SR measurements to small temperature variations. Chapter 8 shows a similar study, but with the SR temperature correction method detailed in Chapter 4 applied to the data. The temperature correction method was developed after the testing for Chapter 7.

Chapter 7: Pressure-Tension Testing in the Evaluation of Freeze-Thaw Deterioration

Andrew J.K. Komar, Andrew Boyd

7.1. Abstract

The use of the pressure tension test to evaluate the effects of durability issues in concrete is a relatively new area of research which shows great promise in detecting a wide variety of expansive deleterious effects in concrete, particularly when compared with existing methods of evaluation. The primary research goal is to demonstrate the applicability of the pressure tension machine for such durability concerns. The results of using the pressure tension testing method to evaluate deterioration associated with freeze-thaw damage as compared to existing standards are presented in this paper. A series of 100 mm x 200 mm standard concrete cylinders were prepared at a variety of water to cement ratios (w/c) and cured for 28 days. After compressive and tension testing was carried out to evaluate undamaged strength characteristics, samples were subjected to sub-merged cyclic freeze-thaw damage per ASTM C 666. After every cycle, nondestructive testing using ultrasonic pulse velocity and surface resistivity were carried out to detect any changes associated with ongoing deterioration. Pressure tension testing as well as splitting tension strength per ASTM C 496 for comparison was performed on the deteriorated cylinders after every 5 cycles and the results compared to the undamaged resistance characteristics. Testing has demonstrated the pressure tension test is capable of detecting freeze-thaw damage in concrete even when the NDT monitoring is inconclusive. The goal is to

demonstrate the applicability of using the pressure tension test method for evaluating expansive damage associated with freeze-thaw damage, and to compare these results with existing standard testing methods to determine whether there is any advantage in using the pressure tension method.

Key words: Concrete, Durability, Freeze-Thaw, Tension, Monitoring, Nondestructive Testing

7.2. Background

The pressure tension (PT) testing method, also known as the indirect tension or gas tension test, is a test method originally developed by the Building Research Council as a new means of investigating anisotropic loading conditions on materials [1]. The PT method uses standard 100 mm x 200 mm concrete cylinders as samples, which allows it to be adapted to already common concrete testing procedures. The test consists of using a pressurized gas equally applied along curved surface of the cylinder, with rubber O-rings at either end of the specimen to contain the gas between the testing chamber and the sample surface as seen in Figure 7.1. The cylinder's flat ends are left open to atmosphere, which causes a net induced tension field to arise within the concrete sample parallel to axis of the cylinder.

The loading behaviour may appear paradoxical given that a tension field is being produced from a compressive load, but it can be understood as a net effective stress which is consistent with principles first developed for soil mechanics [2]. Concrete can be considered as a 'diphase' material with a solid phase consisting of the hydrated cementitious matrix and the aggregates, and a liquid phase consisting of the pore water. The different reaction of the two phases to a biaxial stress gives rise to the pressure tension effect: the liquid phase reacts hydrostatically

whereas the solid phase reacts in the directions of the applied load. The net effect is that all of the stresses in the plane of gas loading cancel out, with a net tension field arising along the axis of the cylinder [3]. A PT test consists of monotonically increasing the gas pressure applied until the point where the solid phase can no longer remain together, at which point the specimen breaks at the weakest point along the length. The gas pressure at the moment of failure is taken to be the ultimate tensile strength of the concrete.

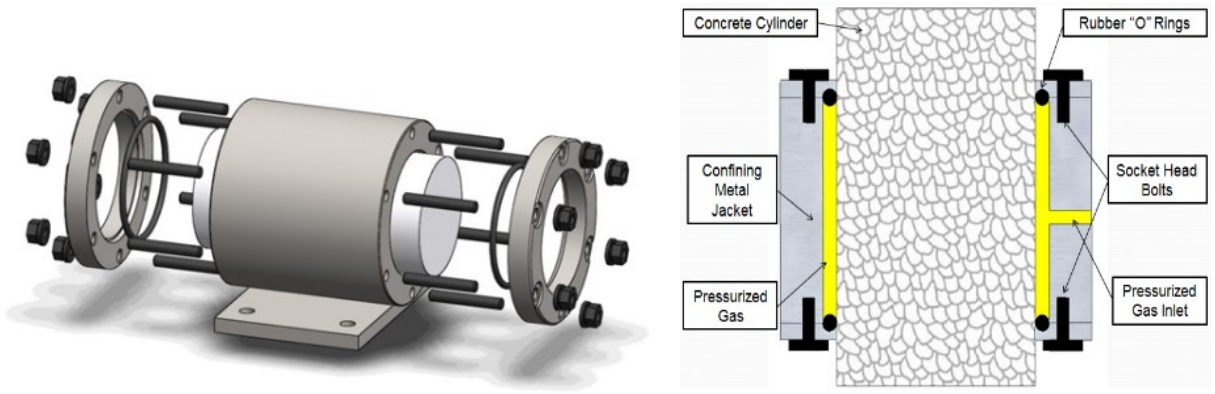

Figure 7.1- (Left) Exploded view of the PT apparatus with concrete cylinder in machine. (Right) Cross section of PT apparatus and concrete cylinder.

Since the tension is the result of an internal stress as opposed to an externally applied stress, the PT test is naturally more sensitive to detecting changes in material properties associated with expansive processes. Many durability issues common to concrete infrastructure are ultimately driven by these expansive processes, including sulphate attack, alkali-silicate reaction (ASR) and freeze-thaw damage, making PT a well-suited candidate for detecting changes in material properties. Previous work using PT has shown its sensitivity to ASR [4] and sulphate attack damage detection [5, 6, 7].

The potential applicability of PT in detecting expansive damage associated with ongoing freeze-thaw damage was the primary focus of this study. Of particular interest is comparing the evaluation of tensile strength in PT as well as standard tension test methods such as ASTM C 496 (splitting tension, or ST). In addition, nondestructive testing (NDT) was performed to determine whether ongoing expansive damage could be detected using Ultrasonic Pulse Velocity (UPV) or Surface Resistivity (SR).

7.3. Materials and Methods

7.3.1. Concrete mix design

Two similar concretes with different w/c (Table 7.1) were mixed and cured for 28 days in saturated limewater solution. For each mix design, approximately 45 100 mm x 200 mm concrete cylinders were prepared, for a total sample size of 90. Two different w/c were chosen to provide relatively stronger and weaker samples for comparison under the same exposure. Neither mixes were dosed with air-entraining admixtures, because the intent was to produce the severest possible exposure conditions for accelerated testing. One thermocouple was embedded in the centre of one cylinder from both mixes, so a measure of the in-situ internal temperature of the concrete samples could be taken.

Table 7.1- Mixture designs for freeze-thaw study

Component	0.45 W/C	0.65 W/C
Water (kg)	15.866	15.973
Cement (kg)	29.282	22.525
Coarse Aggregates (kg)	72.872	72.872
Fine Aggregates (kg)	79.093	85.266
Super Plasticizer (L)	0.146	0.113

7.3.2. Exposure conditions

In order to produce a cyclical freeze-thaw exposure condition consistent with ASTM C 666 with our non-standard sample dimensions, suitable containers were procured so that an individual concrete cylinder could be fully submerged in water during the freeze-thaw process while keeping the excess water to a minimum. Commercially available water jugs including a handle and lid were used, which made the subsequent handling of the samples throughout the testing procedure much simpler.

Two commercially available stand-up deep freezes were used in order to bring the temperature of the samples below freezing, down to measured minimum of approximately -20°C ± 5°C. Thawing was accomplished by re-moving the samples in their containers from the freezer and exposing the containers to ambient laboratory air, about 25°C ±10°C. The water was left in the containers to preserve the saturation condition. The freezing process took approximate 18 hours; the thaw portion, approximately 6 hours. The maximum temperature measured by the embedded thermocouples during the thaw portion of a cycle was 5°C ±5°C. This allowed for one full freeze-thaw cycle to be completed in a 24-hour period.

7.3.3. Test methods

7.3.3.1.Nondestructive test methods

Three concrete samples from each mix were randomly selected at the beginning of the trial for NDT testing after every freeze-thaw cycle. This control group was selected to monitor the ongoing damage as a function of freeze-thaw cycle. Two NDT methods were selected to be performed on these controls: UPV and SR. The controls were marked up to ensure that the NDT was conducted in the exact same position to minimize variability between cycles.

Surface resistivity readings were taken with a commercially available model which was used for the entire duration of the study. Each concrete cylinder was tested four times on the curved surface along the axis of the cylinder, with a quarter turn in between to cover the whole surface area. The average of these four readings was then taken to provide a single SR measurement (in kΩ·cm) for that sample. These four readings were taken on the control samples after the thaw on every cycle, whereas the remainder of the population was tested before their destructive testing.

Ultrasonic pulse velocity measurements were taken with a commercially available model of automatic UPV, which was used for the entire duration of the study. Three measurements of the transit times along the axis of the cylinder were recorded, and the average of these three values was recorded. Length measurements from the cylinders were used to convert the travel times into the UPV values reported. A commercially available water-based lubricant was used to ensure a good connection between the transmitter/receiver and the highly variable surface of the concrete samples. The controls were tested after every freeze-thaw cycle, whereas the remainder of the population was tested before their destructive testing.

7.3.3.2. Destructive test methods

Three different destructive test methods were performed to evaluate the ultimate mechanical properties of the cylinders in tension and compression. All compressive tests were performed in accordance with ASTM C 39 on ground cylinders. Three cylinders from both mixes were tested in compression before any cycles were completed to provide an estimate for the mixes' undamaged strength. After 20 freeze-thaw cycles and the conclusion of the study, a further six cylinders from both mixes were tested to provide a comparison.

The Splitting Brazilian test (ASTM C 496) was used on seven samples from each mix at the end of the study to provide a standardized comparison of measured tensile capacity as compared to PT.

PT was used to test cylinders from both mixes throughout the study. The gas used to provide the loading was compressed air, and the gas was loaded into the testing chamber at a controlled rate of 0.034 MPa/s, a loading rate consistent with ASTM C 496. Three specimens from both mixes were tested at cycles 0, 10, and 15, and remainder of the samples were tested after the 20th cycle. The maximum gas pressure at failure was recorded and this result taken as the tensile capacity of the cylinder.

7.4. Results and Discussion

7.4.1. Nondestructive testing

7.4.1.1.Surface resistivity

For both the high and low w/c mixes, a slight but statistically significant downward trend can be seen with respect to measured SR, as can be seen in Figure 7.2. A 44% and 57% reduction in SR measurements was observed in the 0.45 and 0.65 respectively. This drop is indicative of internal changes to resistance of current, since a lower resistance suggestive of increased pathways available for the induced current to travel through. Figure 7.2 also shows that the less dense 0.65 mix offers less impedance, and is therefore consistently lower.

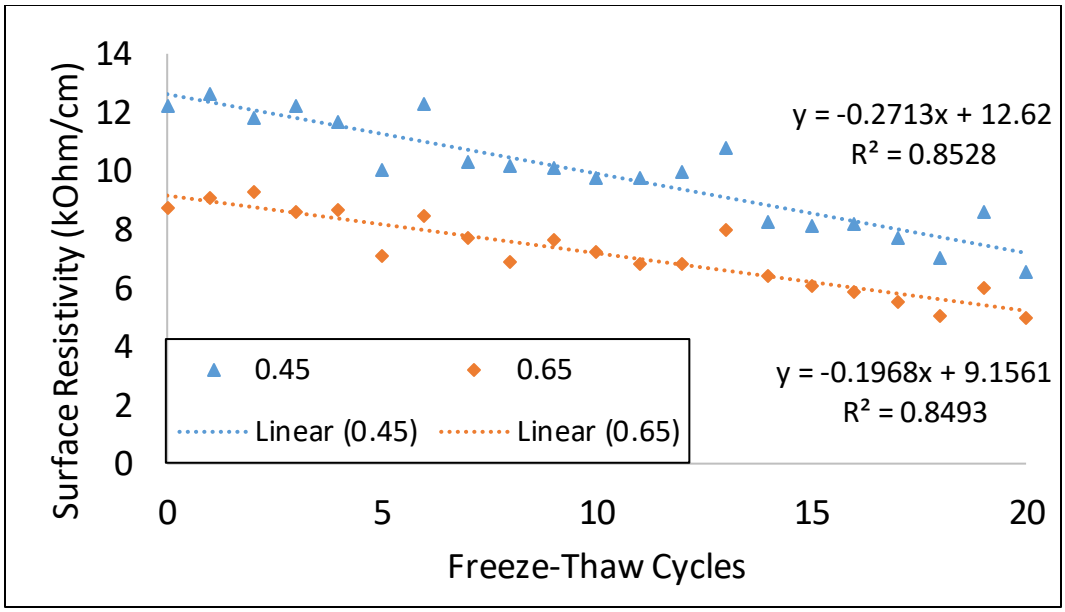

Figure 7.2- Average surface resistivity measurements as a function of freeze thaw cycles

Of note is the relative resistivity between the two mixes. Although there is much variability between testing cycles, the SR averages are remarkably consistent with respect to each other, as seen in Figure 7.3. Since both mixes were subject to the same temperature changes, this data suggests that the specific temperature at which the samples are tested at is extremely important for the measured resistance.

This temperature-dependant behaviour of the SR measurements is more apparent when a single sample is considered. Figure 7.3 depicts the four separate SR measurement data from a control sample. Although there is a range between the highest and lowest values on the order of 5 kOhm·cm, and single day changes on the same order, the range is relatively consistent across the entire cyclic testing.

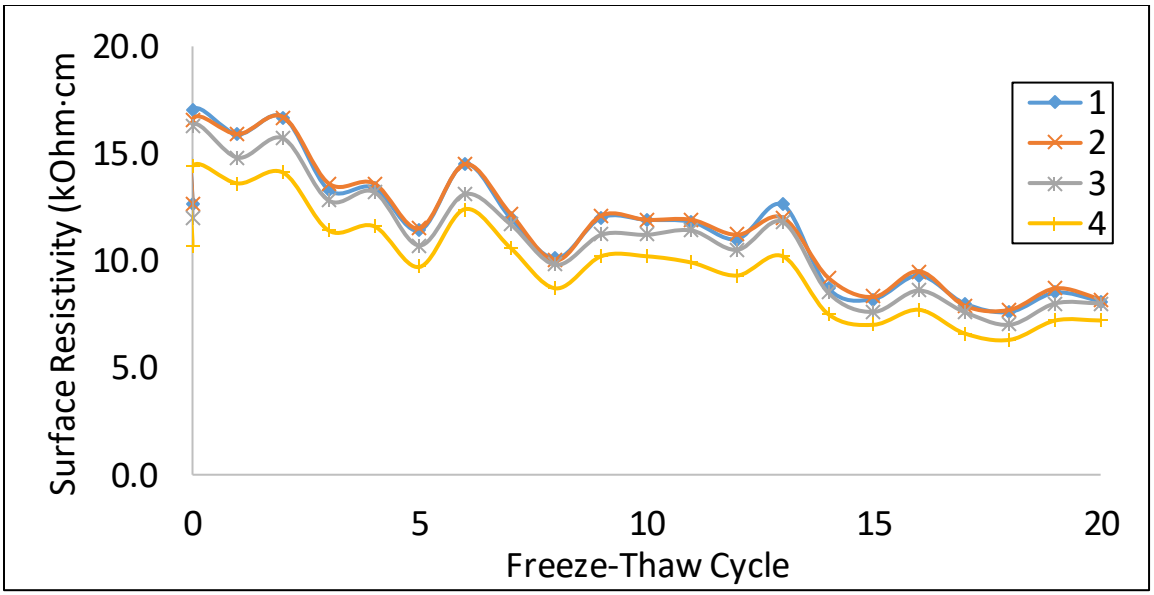

Figure 7.3- Surface resistivity measurements from 0.45 w/c control sample #3 from four separate locations on the surface

7.4.1.2.Ultrasonic pulse velocity

The average UPV measurements for both mixes can be found in Figure 7.4. A slight downward trend is apparent from the data, indicating decreased pulse velocities associated with ongoing freeze-thaw cycles. The 0.45 drops approximately 8%, while the 0.65 drops 37%. Higher UPV measurements are indicative an internal structure which is denser, allowing faster transmission of the pulse. The downward trend as seen in Figure 7.4 shows that the ongoing freeze thaw deterioration is affecting the internal structure so as to cause increased travel times and a lower UPV measurement.

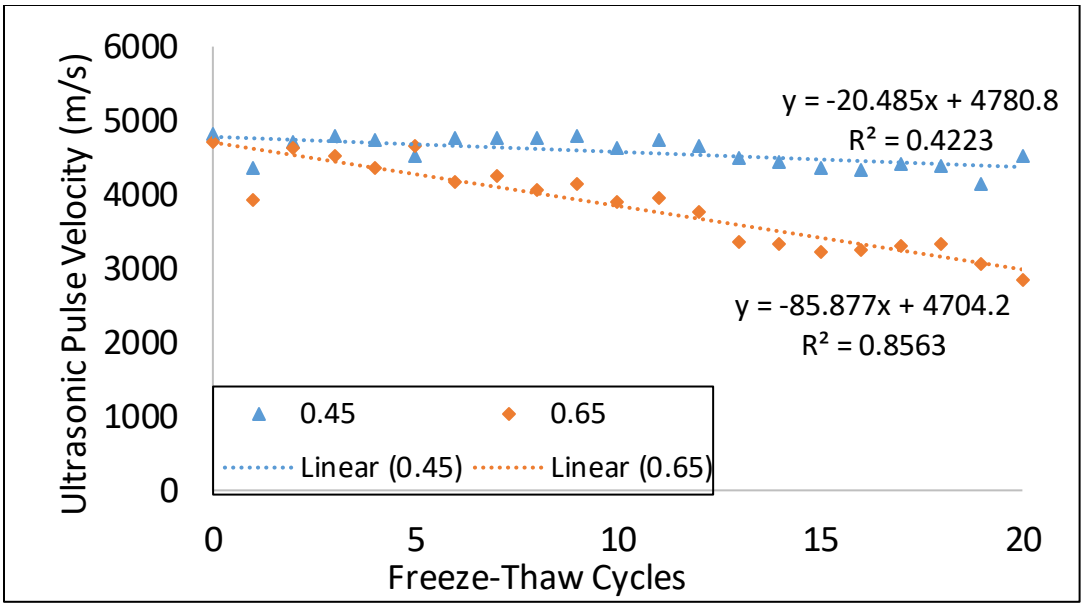

Figure 7.4- Average ultrasonic pulse velocity measurement as function of freeze-thaw cycle for two mixtures

Based on the slope of the average linear regression lines, the damage to the internal structure of the 0.65 mix is much more severe than the 0.45 mixture. This result is consistent with a higher volume of water present in a saturated 0.65 mixture causing expansive damage within the internal pore structure of the samples.

7.4.2. Destructive test results

7.4.2.1.Compressive strength

Average compressive strength results can be found in Figure 7.5. They show that for both mixes there is a slight but significant loss of compressive strength which is associated with ongoing freeze thaw deterioration. Furthermore, the magnitude of this strength loss is greater for the higher W/C ratio, since the 0.65 mix loses 41% of its undamaged strength whereas the 0.45 mix only loses 28%.

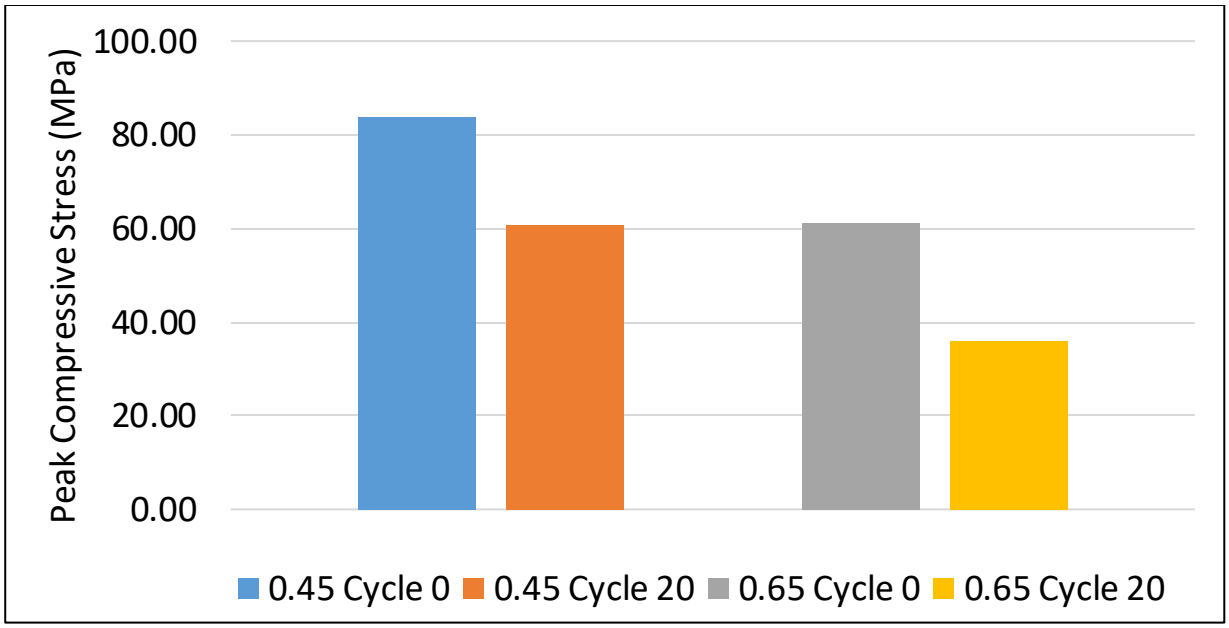

Figure 7.5- ASTM C 39 average compressive strength results from 0 and 20 freeze-thaw cycles for the two mixtures

7.4.2.2.Pressure tension strength

PT shows the same ongoing internal damage pattern consistent with the exposure, characterized by a decrease in material strength, as depicted in Figure 7.6. Most notable from Figure 7.6 is the magnitude of the effect. For the weaker 0.65 mix, PT measured a remarkable 92% strength loss associated with the freeze thaw damage. For the stronger 0.45 mix, a similar 78% tensile strength drop was measured.

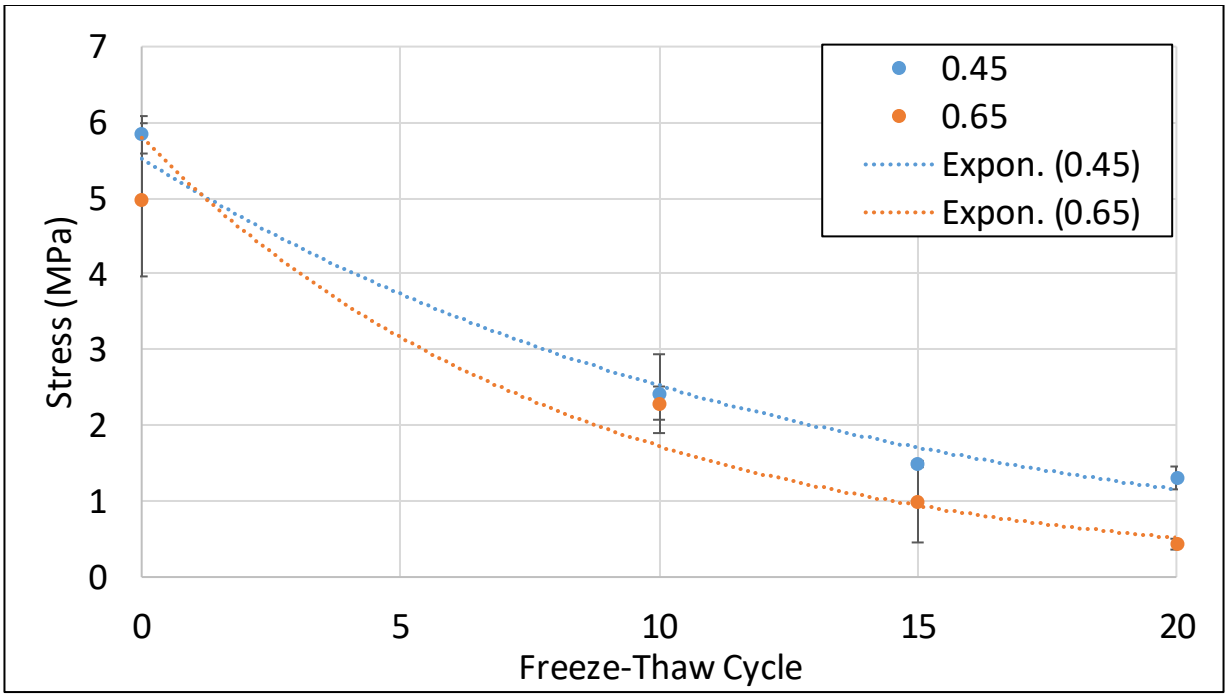

Figure 7.6- PT average failure levels as function of freeze thaw cycle for both mixes

A note on the failure mechanism: samples from both mix designs were similar in their mode of failure during PT testing. For the stronger 0.45 mix, the failure surface ran in a plane perpendicular to the loading direction, but failing through the aggregates, showing the aggregate-paste strength was greater than the local tensile capacity. For the weaker 0.65 mix, although there was a perpendicular failure plane, there was no corresponding failure of the aggregates, instead failing in a manner which suggests the aggregate-paste bond was weaker than bulk concrete.

The relative effectiveness of PT testing in detecting freeze-thaw damage as compared to the standardized ST test can be seen in Figure 7.7. For both mixes, the ST test measured tension strength which was significantly stronger than the corresponding PT measurement. For the 0.45

mix, the ST value was 6.02 MPa higher than the PT value of 1.31 MPa, and for the 0.65 mix the ST was 3.70 MPa higher than the PT value of 0.43 MPa.

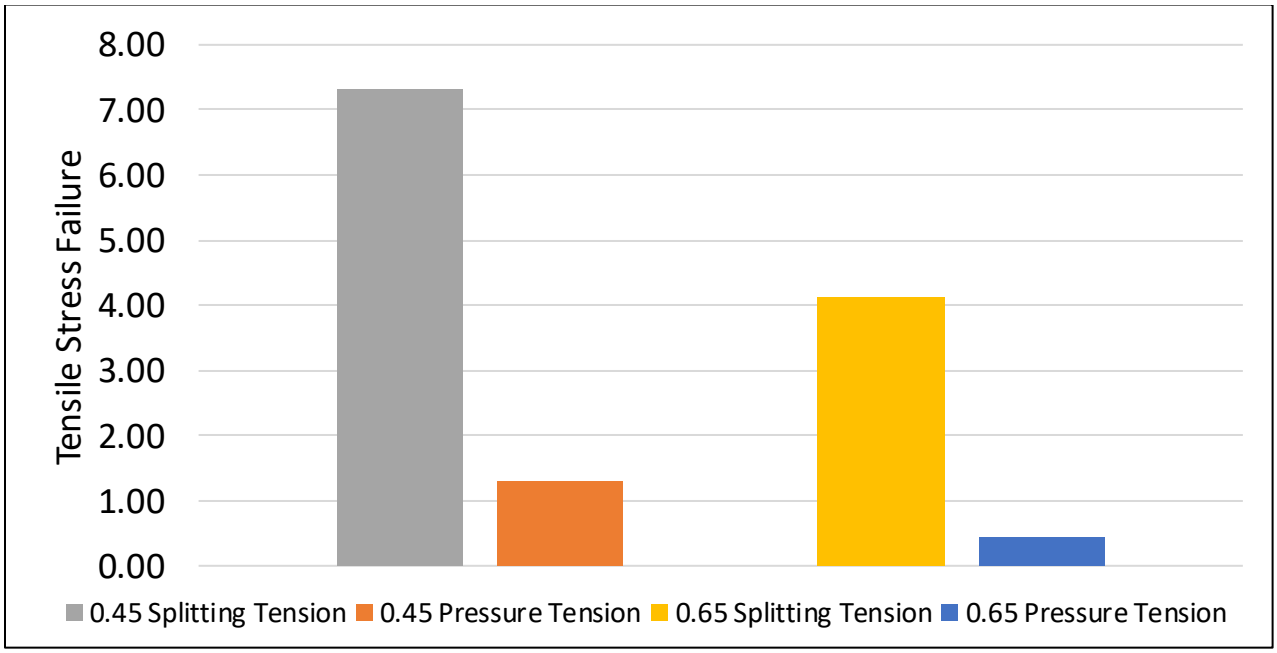

Figure 7.7- Tensile failure comparison between splitting tension (ST) and pressure tension (PT) for two mixes after 20 cycles of freeze-thaw damage

7.5. Conclusions

Of the three destructive test methods investigated in detecting the microstructural damage associated with ongoing freeze-thaw deterioration, the PT method was the most effective at its evaluation. Given that PT is the only method which loads a specimen indirectly, it is free from mechanically induced complications such as eccentricities which could lead to an overestimation of the material strength. The failure mode of PT specimens supports this conclusion, since the plane of failure in damaged concrete goes around the harder aggregates and through the weaker cementitious paste in its immediate vicinity. In all cases, the more damaged the concrete, the weaker the failure.

The two different methods of nondestructive testing used in the study both independently confirmed measurable changes within the internal structure of the concrete, both of which were consistent with the expansive failure mechanism. However, the magnitude of both of these effects was much smaller than the difference suggested by the PT results.

Surface resistivity is quite sensitive to small changes in the temperature of the specimen, leading to variability in the data. Nevertheless, SR was shown to detect expansive damage in as little to 20 cycles, so it can be useful as part of a nondestructive monitoring regime. To obtain results with less variability, efforts should be made to test the samples at an identical temperature every cycle.

Freeze-thaw damage is an expansive process and the damage it creates will induce tensile failures within the paste on the microstructural level. The PT test could detect this damage with greater success than either of the other test methods, both destructive and nondestructive, so it can be concluded that it is effective at evaluating freeze thaw damage. Further testing will include mixes with air entrainment in order to determine the effectiveness of PT testing at detecting ongoing freeze-thaw damage in types of concrete more closely approximating real world conditions.

7.6. References

[1] Clayton, N., and F. Grimer. "The Diphase Concept, with Particular Reference to Concrete." Chap. 7 In Developments in Concrete Technology, 283-317. Waterford, UK: Elsevier Science & Technology, 1979.

[2] Terzaghi, K., R.B. Peck, and G. Mesri. Soil Mechanics in Engineering Practice. 3rd ed. New York: Wiley, 1996.

[3] Uno, T., K. Fujikake, S. Mindess, and H. Xu. "The Nitrogen Gas Tension Test of Concrete. Part 1: Effect of Boundary Conditions and Axial Strain Response." Materials and Structures 44, no. 4 (2011): 857-64.

[4] Bremner, T.W., A.J. Boyd, T.A. Holm, and S.R. Boyd. "Tensile Testing to Evaluate the Effect of Alkali-Aggregate Reaction in Concrete." In Proceedings, International Workshop on Alkali-Aggregate Reactions in Concrete, 311-26. Dartmouth, Canada: CANMET/ACI, 1995.

[5] Boyd, A. J., and S. Mindess. "The Effect of Sulfate Attack on the Tensile to Compressive Strength Ratio of Concrete." In Proceedings of Third International Conference on Concrete Under Severe Conditions, 789-96. Vancouver, Canada: ACI/CSCE, 2001.

[6] Hartell, J.A., A. J. Boyd, and C.C. Ferraro. "Sulfate Attack on Concrete: Effect of Partial Immersion." Journal of Materials in Civil Engineering 23, no. 5 (2011): 572-79.

[7] Komar, A.J.K., J.A. Hartell, and A.J. Boyd. "Pressure Tension: Reliability for Assessing Concrete Deterioration." In Proceedings of The Seventh International Conference on Concrete under Severe Conditions, edited by Z.J. Li, W. Sun, C.W. Miao, K. Sakai, O.E. Gjørv and N. Banthia, 337-44. Nanjing, China: RILEM Publications, 2013.

Foreword to Chapter 8

The study performed in Chapter 8 is a direct continuation of the preliminary study that is detailed in Chapter 7. Both Chapters 7 and 8 concern the evaluation of freeze-thaw deterioration on the tensile capacity of concrete and the monitoring of this damage with a variety of non-destructive techniques. These studies relate to the broader theme of the research program of transport properties in concrete because the primary effect of the freeze-thaw damage causes changes in the properties of the pore structure. These changes were evaluated directly by the pressure tension test, but also indirectly using NDT techniques of SR, UPV, and expansion prisms. The selection of the destructive tests and testing intervals was influenced directly by the study performed in Chapter 7, since there were not as many destructive tests performed at earlier cycles. A direct evaluation of compressive strength at the same time as the tensile strength was performed to evaluate tensile to compressive strength ratio. Splitting tension tests were omitted due to their demonstrated insensitivity to the deterioration, as demonstrated in Chapter 7. Chapter 8 put a greater emphasis on earlier cycles, so that the effectiveness of the pressure tension test could be shown in more detail. Based on the high variability of the SR readings found in Chapter 7, the SR-T correction factor method detailed in Chapter 4 was applied to the samples so that a temperature independent evaluation of the SR signals would be possible. With SR correction factor applied, results from the SR accurately agreed with evaluations from the destructive testing (i.e. that the pore structure in the concrete was being altered as a function of freeze-thaw cycles). The effect on the pore structure involved in transport properties was clear;

SR detected a significant change in the pore structure after a single freeze-thaw cycle, and the pressure tension test could detect freeze-thaw damage evident after 5 cycles.

Chapter 8: The Influence of Freeze-Thaw Damage in Pressure Tension Testing

Komar, A.J.K., Boyd, A.J.

8.1. Abstract

Freeze-thaw damage is one of the leading causes of infrastructure deterioration in northern climates. This work presents the detection of ongoing freeze-thaw (F/T) damage in plain concrete cylinders with a tensile strength test, as it compares to compressive strength evaluations according to ASTM C39. Non-destructive (NDT) test methods including surface resistivity, ultrasonic pulse velocity and expansion prisms were also used in order to detect the initiation and progression of damage. Though all of the NDT methods were able to detect F/T damage, surface resistivity proved to be the most sensitive. A method for correcting surface resistivity measurements as a function of temperature and deterioration is presented. Pressure tension tests indicated significantly higher levels of deterioration compared to compression testing, with the samples losing up to 90% of their undamaged tensile capacity, and the tensile to compressive strength ratio dropping below 5%.

8.2. Background

Ordinary portland cement concrete (OPC) is among the most commonly used construction materials in the world, and is incorporated into many different kinds of structures and pavements. As such, it is widely subjected to inclement weather conditions that may adversely affect the material strength. In particular, temperate climates such as those found in North

America and Northern Europe go through months of weather that will be below 0°C, which will cause water to freeze and expand in volume by 9%.

This issue is particularly important when considering that concrete is a porous material. The solid material comprising the porous environment will act to constrain the volumetric expansion of water undergoing freezing, thus causing internal stresses to develop to resist this change. Additionally, movement of water through the concrete microstructure under pressure, due to differential freezing, can induce very large hydrostatic pressures. These stresses can cause internal damage on the microstructural level such as cracking, spalling, delamination, aggregate pop outs and other such flaws that can lead to dramatically increased porosity. [1,2,3,4]

This increase in porosity due to freeze/thaw (F/T) damage in OPC can lead to increases in the severity of many different durability issues. One such increase is the rate of corrosion in the steel reinforcement from direct water contact or from chlorides deliberately applied to OPC in the form of de-icing salts or marine exposure. Other durability issues such as ASR or sulphate attack may also become more severe due to the associated increases in transport properties brought on by F/T damage.

In modern engineering practice, concrete construction that is expected to undergo freeze-thaw cycling is treated with an air-entraining admixture, which provides dedicated voids that the pressurized water can enter without adversely affecting the rest of the pore structure. However, there are situations where air entrainment may not have been implemented, such as older construction built before air entrainment was widely available, or in the case of climates where freezing is not a common occurrence. Even small numbers of F/T cycles, especially on OPC

without air entrainment, can lead to serious material damage that would decrease the service life of infrastructure.

An important question for engineers is how one assesses the nature and severity of the material damage caused by F/T cycles in concrete. For evaluating the soundness of concrete in the field (a proxy measurement for material damage), NDT methods are preferable since they do not cause further damage to existing structures or require the removal of samples, and are thus highly repeatable [4].

8.2.1. Nondestructive testing

8.2.1.1. Ultrasonic pulse velocity

One nondestructive testing (NDT) method used in the field due to its relative ease of operation is the Ultrasonic Pulse Velocity (UPV) test method (ASTM C 215). This method determines the transit time of low-amplitude stress pulses through a material from an emitter to a detector. The soundness of the material between these two points will determine the speed of the transit time, since a more cohesive material will generally transmit stress waves at a faster velocity. When a stress wave must propagate around cracks such as those caused by F/T damage, the calculated velocity will decrease since the travel time will increase while the straight-line distance between the emitter and detector remains constant. Thus, by repeating UPV measurements in the same location after F/T damage has accrued we can obtain a proxy measurement of the extent of the damage via the pulse velocity. This deterioration has been shown to correlate well with strength loss in compression [4].

8.2.1.2.Surface resistivity

An NDT method that shows great potential in assessing the state of the pore structure is the Surface Resistivity (SR) method, which does not yet have an ASTM designation. The test uses four electrodes which contact the saturated concrete surface along a straight line. An alternating current passes between the outer electrodes under a known voltage, and the voltage drop between the inner electrodes is measured, from which a resistance to flow (or resistivity) is calculated. The resistance to this applied current will be proportional to the connectivity of the pore spaces that the current passes through, with higher porosity being correlated with a lower resistance due to the greater number of pathways through which the current can pass. This method is also appropriate for F/T damage evaluation because the expansive process will increase this connectivity through cracking and by increasing the overall pore space due to ongoing microstructural damage.

8.2.1.3.Expansion prisms

Another method commonly used to assess the effectiveness of a given mix at resisting F/T cycles is the one-dimensional length change associated with expansive damage (ASTM C 490). If the expansion after a certain number of cycles is below a specified threshold, the mix is considered to be adequate at resisting F/T cycles. This method requires specialized prisms to be cast and thus may not be applicable to samples drilled from in situ structures.

8.2.2. Destructive testing

8.2.2.1.Compressive strength

By far the most common method for evaluating the strength of a component in the field is by drilling test cores and subjecting them to ASTM C39 compressive strength tests. This method of

uniaxial compression puts the cylinder under a loading piston and applies a mechanical force to the ground flat surfaces until the point where it fails in crushing. Compressive strength may in fact be overestimating the true material resistance to crack propagation given that the direction of loading will act to close active cracks that are present in the material. Although compressive strength is the commonly accepted method for determining the strength of concrete cylinders and cores alike, other destructive test methods are more sensitive to the expansive damage associated with F/T cycles.

8.2.2.2. Pressure tension

The final method used for the study was the Pressure Tension (PT) test. This method applies compressed gas over the curved surface of a cylinder, where the flat ends of the cylinder are left exposed to regular atmospheric pressure [5]. The configuration of the test apparatus without a specimen can be found in Figure 8.1. The pore water contained within the sample comes to a hydrostatic equilibrium with the applied gas pressure [6]. However, since the applied gas pressure is a biaxial mode applied along the curved surface, there is no application of stress along the axis of the cylinder, thus a net tensile stress field develops parallel to the axis of the cylinder through the whole cross section of the cylinder [7]. This indirect tensile effect will act to apply tension at every point within the cylinder at a magnitude equal to the applied stress. This loading results in a tension failure crack that propagates across the specimen and pushes the specimen apart from the inside.

Figure 8.1- Pressure tension apparatus

The PT method, because its mode of action applies stress from within the sample as opposed to an external application, as shown in Figure 8.2, will be more sensitive to expansive damage such as the kind associated with F/T damage [7,8,9,10,11]. Any microstructural cracks that are present in a test specimen will be 'pushed apart' at the stress that is required to propagate them. Thus, this test will show a deterioration signal as a loss of tensile strength which would not otherwise be detectable using more common methods [12].

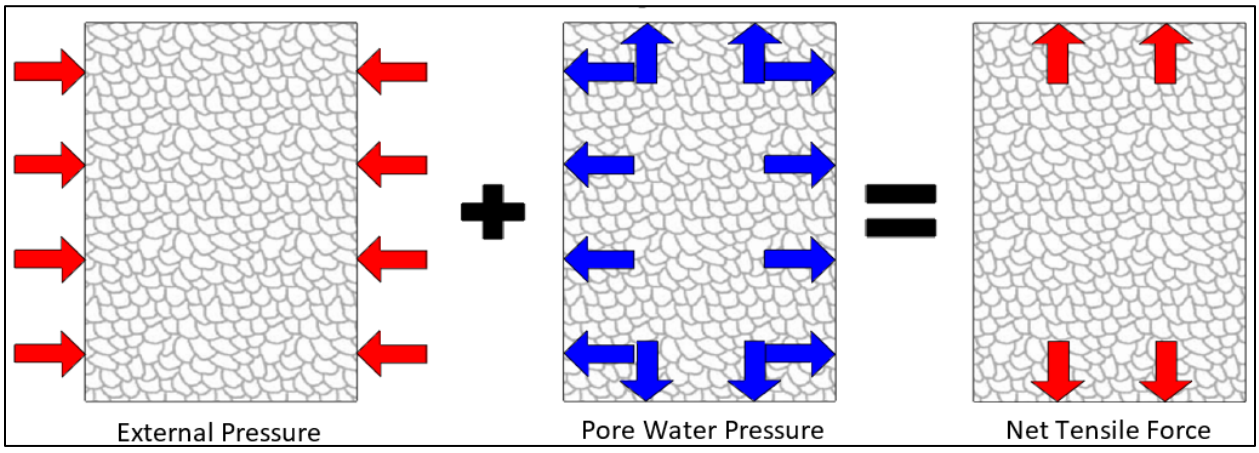

Figure 8.2- Pressure tension effect [5,6,7]

8.3. Materials and Methods

8.3.1. Mix design

Two OPC mixtures were prepared with different water to cement ratios (w/c). Both 0.45 and 0.65 W/C mixes were prepared to ascertain the effect of different porosities, with the 0.65 mix being expected to produce a higher porosity. The aggregate was selected for its low porosity (<0.5%), nonreactivity in ASR, dimensional stability as well as high strength. Granite was used for the study, obtained from a local quarry that met these specifications. Both the course and fine aggregates were graded conforming to standard specifications, with the maximum aggregate size being <14 mm. The mixture designs can be found in Table 8.1

Table 8.1- Mixture designs

Mixture	Cement (kg)	Fine Aggregate (kg)	Coarse Aggregate (kg)	Water (kg)
0.45	32.60	56.39	70.70	15.69
0.65	21.84	62.47	68.42	15.28

Air entrainment was not used for the study to simulate the most severe cyclic conditions. The purpose of this study was to demonstrate the effectiveness of a variety of test methods in detecting ongoing F/T damage, so this condition was selected to ensure adequate damage within a reasonable time frame.

Each mix resulted in one batch of 30 - 100 mm x 200 mm cylinders of standard dimension, as well as three expansion cylinders and an adequate amount of extra material to perform slump and air content tests. The total yield of specimens is shown in Figure 8.3. The results of these tests are shown in Table 8.2.

Figure 8.3- 0.45 W/C specimens as cast

Table 8.2- Fresh concrete properties

Mixture	Slump (mm)	Air Content (%)	Density (kg/m^3)
0.45	36	2.0	2436
0.65	56	2.4	2382

After demolding, the flat ends of the samples were ground to for easier coupling of the detectors required for the UPV tests. These samples were then cured in saturated limewater for 28 days at a temperature of 24 °C ± 2 °C prior to the beginning of freeze thaw cycling.

8.3.2. Exposure conditions

Each concrete cylinder was placed into an individual container conforming to the dimensional specifications laid out in ASTM C 666, specifically the maximum clearance between the edge of the container and the sample being <3 mm. These containers were filled with water so that the samples were completely submerged to a depth of <3 mm. Lids were fitted overtop of this configuration to minimize water lost during movement of the containers throughout the study.

The containers used were commercially available water containers which fit the specifications. The water used to surround the samples was tap water obtained from the local municipal supply, and this water was switched out during the thawing portion of every cycle for all the samples.

Figure 8.4-Samples and containers inside refrigerator

For the three expansion prisms, suitable containers conforming to the proper dimensional specifications were obtained from a freeze-thaw cycling apparatus conforming to the standard ASTM C 666 procedure.

For the freezing phase of the cycle the containers with the samples within were placed in a commercially available freezer with a minimum operating temperature measured to be -25 °C ± 3 °C. Approximately thirty samples could be placed within each freezer so two identical freezers were used for the freezing part of the cycle, as seen in Figure 8.4. Thermocouples were embedded in two samples and measurements taken during the cycling indicated that a uniform temperature of -25°C was reached at the centre of the specimens after approximately 18 hours

of exposure in the freezer. An infrared thermometer was used to measure the surface temperature of the samples and containers throughout the duration of the study.

Figure 8.5- Heating element on circulating water bath

For the thawing portion of the cycle, the entire population of samples (in their containers) was transferred in their frozen state from the freezers into a large water bath equipped with a heating element and a circulating pump. The bath was large enough to completely submerge the entire population of samples. The circulating action of the pump and heater shown in Figure 8.5 ensured that no thermal gradient could develop within the heat transfer medium of the water bath. From their frozen condition, it took on average 4 hours for the temperature of the water bath and the samples to reach a minimum surface temperature of 15 °C.

After this minimum temperature was measured on the samples via infrared thermometer, NDT was performed on representative samples and the whole population was replaced in the freezers

to begin another freezing cycle. In total, the thawing portion of a single cycle was under six hours, meaning an entire freeze-thaw cycle with this large temperature range was completed in 24 hours.

The extremes of the temperature range were beyond the standards as prescribed in ASTM C 666 but this was selected as a more severe environment to be more representative of extreme conditions which may occur on infrastructure in the field.

8.3.3. Destructive testing

A baseline for destructive test specimens was established by testing samples after the curing period. Pressure tension and compressive strength samples were randomly selected from the population and tested after the NDT census was completed.

Subsequent testing intervals were established to track ongoing changes to the material strength as detected by the destructive testing methods. Destructive tests were performed after 1, 5, 10, 20 and 30 F/T cycles.

8.3.3.1. Compressive strength

Standard compressive strength tests as prescribed in ASTM C 39 were performed on all specimens selected for compressive strength testing. At every testing interval, two samples were tested in this manner

8.3.3.2. Pressure tension

Pressure tension tests were conducted at every destructive testing interval on two samples. The load rate was set at 2 MPa/minute and there were minimal deviations from this load rate. In the cases where a gas leak developed due to imperfections in the specimens, a low-friction PVC tape

was applied on the specimen surface to interface with the O-rings that confined the pressurized gas.

8.3.4. Nondestructive testing

8.3.4.1.Surface resistivity

This study used a commercially available Resipod surface resistivity meter from Proceq with 50 mm spacing in the surface resistivity configuration for all the SR tests. To establish a baseline, SR readings of every sample were taken before the start of F/T cycling. For each sample, four SR measurements were taken on the curved surface of each cylinder. The spacing between the measurements was such that each successive reading was a quarter turn (90^o) from the previous one, so that the whole sample surface was evaluated. To minimize potential edge effects from the geometry of the specimens, the SR probe was aligned so that the midpoint of the probe coincided with the midpoint of the sample, ensuring that there was a minimum distance of 25 mm between the probe and the end of the sample. An average of these four readings was taken so that the samples could be compared with one another.

In addition to the SR readings, a temperature reading via IR thermometer was performed after each SR test. This surface temperature was then used to normalize the SR readings with respect to temperature so that the whole population could be compared, independent of any SR-Temperature effect

After the census, control specimens were selected and annotated with lines drawn on the surface so that the SR probe contacts could be placed in the exact same location for every subsequent test interval. The control specimens were then tested after every single F/T cycle to detect

ongoing changes in the SR signals. The temperatures of these specimens were also measured with an infrared thermometer

At each destructive test interval (1, 5, 10, 20, 30 cycles) all specimens that were to be destroyed were tested to detect any changes from the baseline established by the census at cycle 0.

8.3.4.2.SR-temperature curves

To adjust for the temperature dependent effects of SR, it was necessary to determine the relationship between measured SR readings and temperature. Specimens from each of the destructive test intervals were selected and marked so that there were eight spots equidistant from each other on the curved surface of the cylinder where the SR probe contacts could be placed in a repeatable manner.

The specimens were then submerged in a water bath equipped with a heating element and water circulator which was cooled with ice water. The temperature of the water bath and specimen came to a thermal equilibrium around 5°C ± 2°C as measured with a thermometer, thermocouple and IR thermometer. Eight SR readings were then taken and the surface temperature was determined using the IR thermometer.

The sample was then replaced into the water bath, with the heater and circulator switched on to raise the temperature of the water bath and sample at the same rate. After short intervals of about 90 seconds, the previous testing procedure was repeated on the warmer specimens, so that a representative range of SR readings from 5 °C to 30 °C was acquired for each of the destructive F/T intervals.

8.3.4.3. Ultrasonic pulse velocity

End-to-end UPV measurements were performed as part of the census on all cured samples at cycle zero. For each sample, a minimum of three measurements with a properly calibrated transmitter and receiver were made between the ground ends of the cylinder. The maximum variation between the three successive measurements was ≤ 0.5 µs. If this variation was exceeded, successive tests were performed until the measurements could come to this agreement. An average of these three values was then taken to represent the transit time for the sample.

To facilitate a sound connection between the transducers and the surface of the concrete, a commercially available water based lubricant was used. Between subsequent measurements, the position of the transmitter and receiver were reversed.

To determine the path length of the specimens, the distance between the flat ends was determined using a digital caliper accurate to 0.01 mm. This distance value was measured at every UPV test to ensure that any expansion of the cylinders was considered and the pulse velocity could be accurately calculated. The formula for calculating the pulse velocity is shown in Equation 8.1.

$$V = x/t$$

Equation 8.1: Ultrasonic pulse velocity

Where V is the pulse velocity, x is the distance in m between the flat ends and t is the transit time in seconds as measured by the UPV apparatus.

Control specimens were tested for UPV after every F/T cycle to establish cycle-to-cycle variations. In addition to the control specimens, the samples to be destroyed were tested in UPV at every destructive test interval (0, 1, 5, 10, 20, 30 cycles) to detect any changes from the baseline.

8.3.4.4. Expansion prisms

Three expansion prisms conforming to the standards outlined in ASTM C 490 were cast for each mix. These rectangular prisms were cast with embedded studs to interface with the extensometer apparatus. A baseline length measurement for each prism was taken immediately following the curing period. After every freeze thaw cycle, extensometer readings were again taken on every prism with an accuracy of 0.001 mm. Following each measurement, the calibration of the machine was checked to ensure the accuracy of the measurements.

8.4. Results and Discussion

8.4.1. Visual observations

After the testing, visual physical damage was observed on both the 0.45 and 0.65 samples. The extent of the deterioration was much more severe for the samples which had undergone more F/T cycles. As expected, the extent of surface scaling and deterioration was much more severe on the higher w/c specimens. The paste was particularly weakened, with some mass loss being observed through simple handling of the specimens, especially around the aggregates. In the case of the 0.65 w/c mixture, the extent of the surface deterioration led to some difficulties producing a solid seal during pressure tension testing, since 100% of the specimen exhibited surface scaling.

Figure 8.6- Undamaged failure plane from pressure tension test

Figure 8.7- Damaged failure plane from pressure tension test

Compressive tests failed in the usual manner, i.e. conical failure planes with paste crumbling. Pressure tension failure specimens showed a more disparate pattern across the levels of deterioration. Samples tested after few cycles showed a break perpendicular to the tensile stress, with the fracture surface passing through the aggregates, as shown in Figure 8.6. As damage levels increased, a greater area of the fracture surface was found to have passed around the surface of the aggregates. This failure resulted in an intact aggregate on one side of the

fracture surface with a corresponding area of discolored concrete on the other surface, which is shown in Figure 8.7. This apparent failure through the interfacial transition zone (ITZ) was found to be more prominent in the higher porosity w/c mix, as well as specimens exposed to more F/T cycles.

8.4.2. Destructive testing

8.4.2.1.Compressive strength

The results of the compression testing at the destructive intervals can be found in Figure 8.8. The compressive strength decreased as a function of cyclic deterioration for both mixtures, with the 0.45 w/c dropping from 48 MPa to 35 MPa over 30 cycles, and the 0.65 w/c dropping from 25 MPa down to 15 MPa over the same period. This represents a compressive strength loss of 27% and 40%, respectively.

The compressive strength results significantly differed between the undamaged and damaged state per a 2-sample unequal variance T-test after the 20^{th} cycle for the 0.45 w/c, and the 10^{th} cycle for the 0.65 w/c.

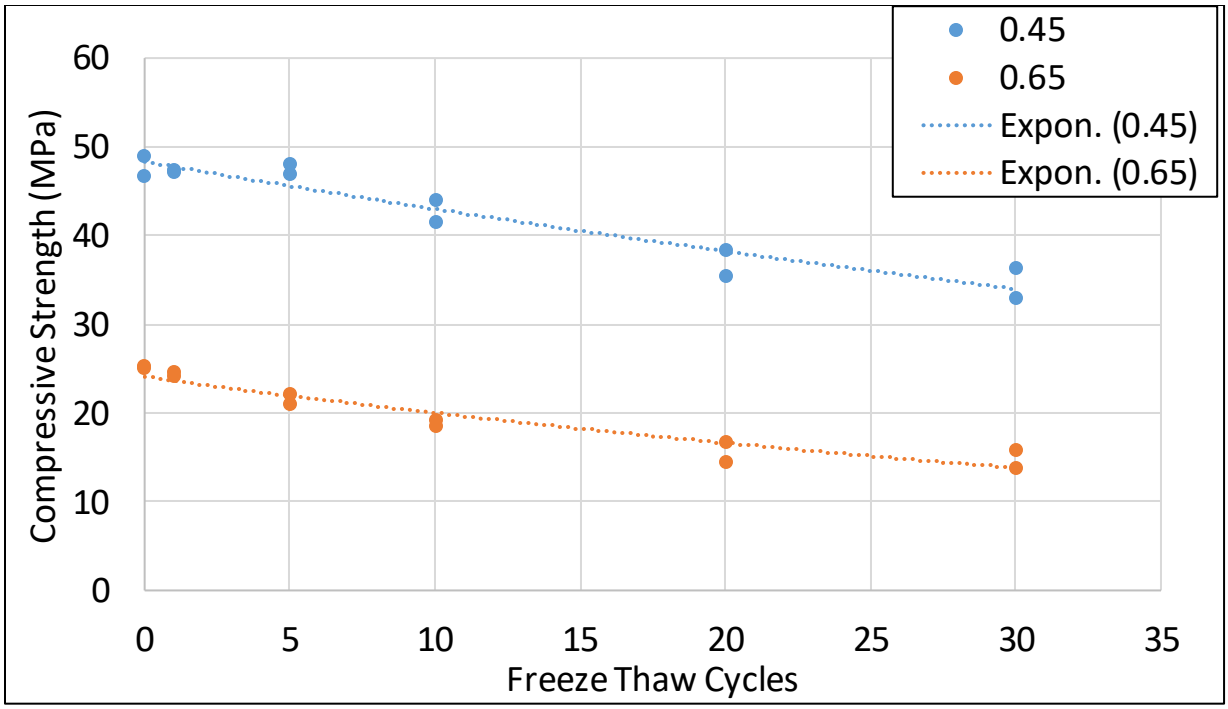

Figure 8.8- Compressive strength deterioration as function of freeze thaw cycle

8.4.2.2.Pressure tension

The results of the pressure tension testing can be found in Figure 8.9. For both mixes, deterioration in the tensile capacity was observed, with the 0.45 w/c dropping from 6.4 MPa to 1.4 MPa, and the 0.65 w/c dropping from 4.2 MPa to 0.4 MPa. This represents a tensile strength loss of 78% and 90%, respectively.

Of particular note was the dramatic reduction in tensile capacity for both mixes. After a single F/T cycle, the 0.65 w/c concrete lost 49% of its original strength. This falloff was statistically significant per a 2-sample unequal variance test. There appeared to be a slight increase in the tensile capacity of the 0.45 w/c for the first F/T cycle, but this behavior was not considered statistically significant. By the 10^{th} cycle the 0.45 w/c had lost 42% of its original tensile capacity, and this value was deemed significant per the 2-sample unequal variance t-test.

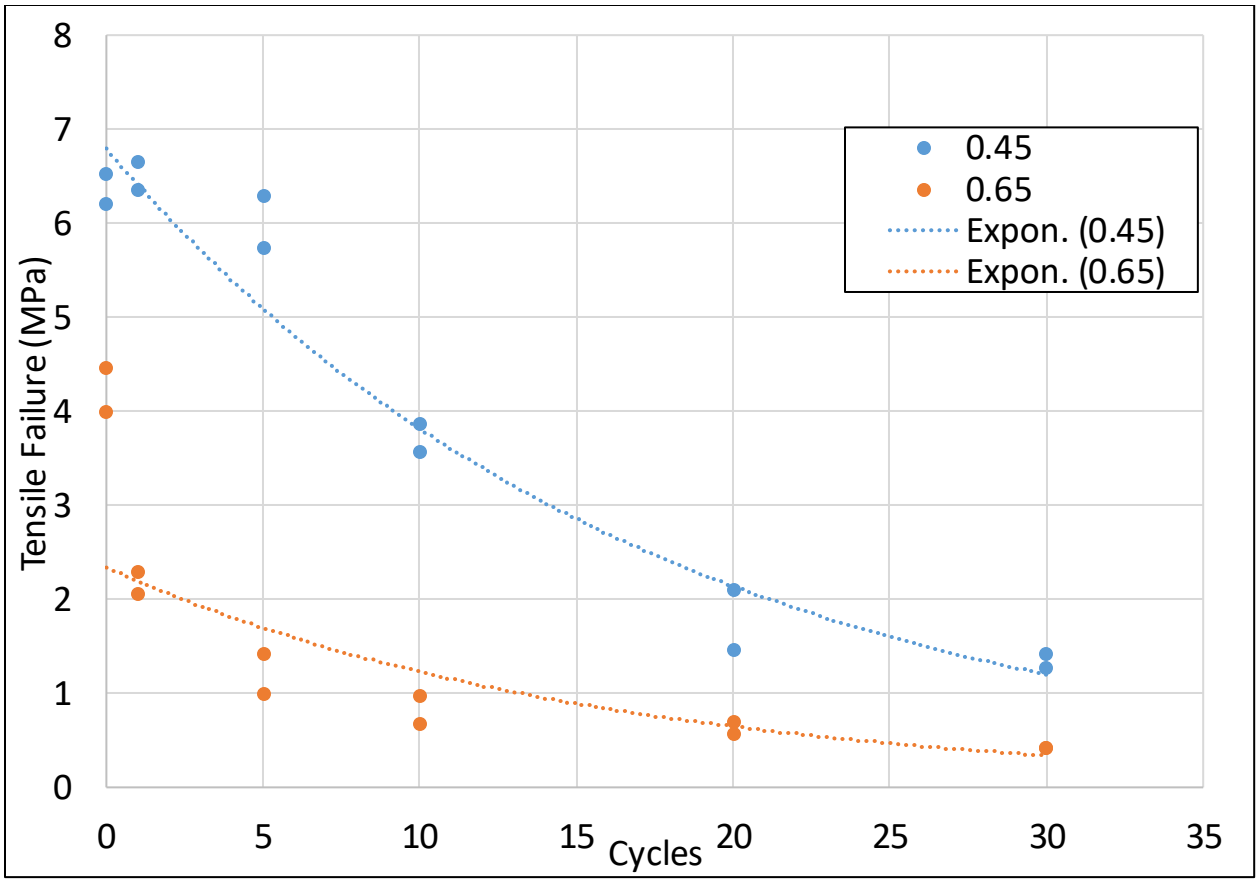

Figure 8.9- Pressure tension strength deterioration versus freeze thaw cycle for two mixtures

In both cases, the resulting tensile capacity resembled a negative exponential curve, with the damage converging on some minimal number for both mixtures, as seen in Figure 8.9. It is important to note that the assumption of tensile capacity of concrete being roughly 10-15% of the compressive strength does not hold true for this study. This behavior can be seen in Figure 8.10 by comparing the average tensile to compressive ratio for the two mixes.

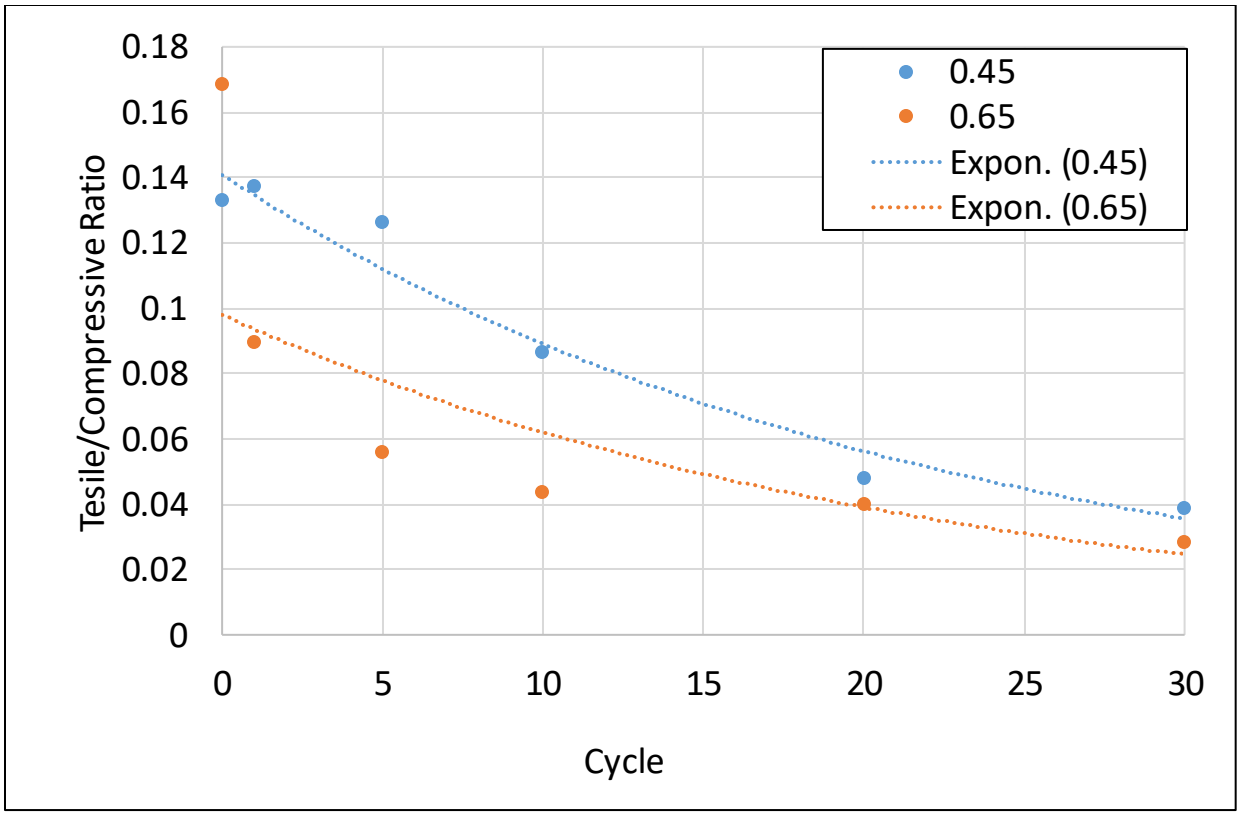

Figure 8.10- Average tensile to compressive ratio as a function of F/T cycling

As Figure 8.10 shows, the undamaged concrete at cycle zero reflected this initial assumption of a tensile compressive ratio of around 15%. However, Figure 8.10 clearly shows this assumption is invalid, since if it were true, Figure 8.10 would show a constant tensile to compressive ratio for both mixes and all cycles. However, by Cycle 20, for both mixes, the ratio had dropped below 5%, where it bottomed out at 4% for the 0.45 w/c and 3% for the 0.65 w/c mix.

This data demonstrates that the tensile capacity of concrete is more severely affected by F/T deterioration than compressive strength, which is understandable given that the mode of damage tends to be cracks in the concrete paste. Only a tensile mode of loading will open these existing cracks, thus resulting in failure at a lower applied stress when compared to compression.

A further observation was that the PT test detected a significant deterioration signal much earlier (i.e. at much fewer F/T cycles) than the compressive strength test.

8.4.3. Nondestructive testing

8.4.3.1.Surface resistivity

A decrease in the surface resistivity measurements was observed for both mixes as a function of F/T damage, as seen in Figure 8.11. The measured resistivity for the 0.45 w/c was greater than for the 0.65 w/c mixture, and this trend held for the entire study. The 0.45 w/c fell from 12 kΩ·cm to 6 kΩ·cm and the 0.65 w/c fell from 8 kΩ·cm to 3.5 kΩ·cm.

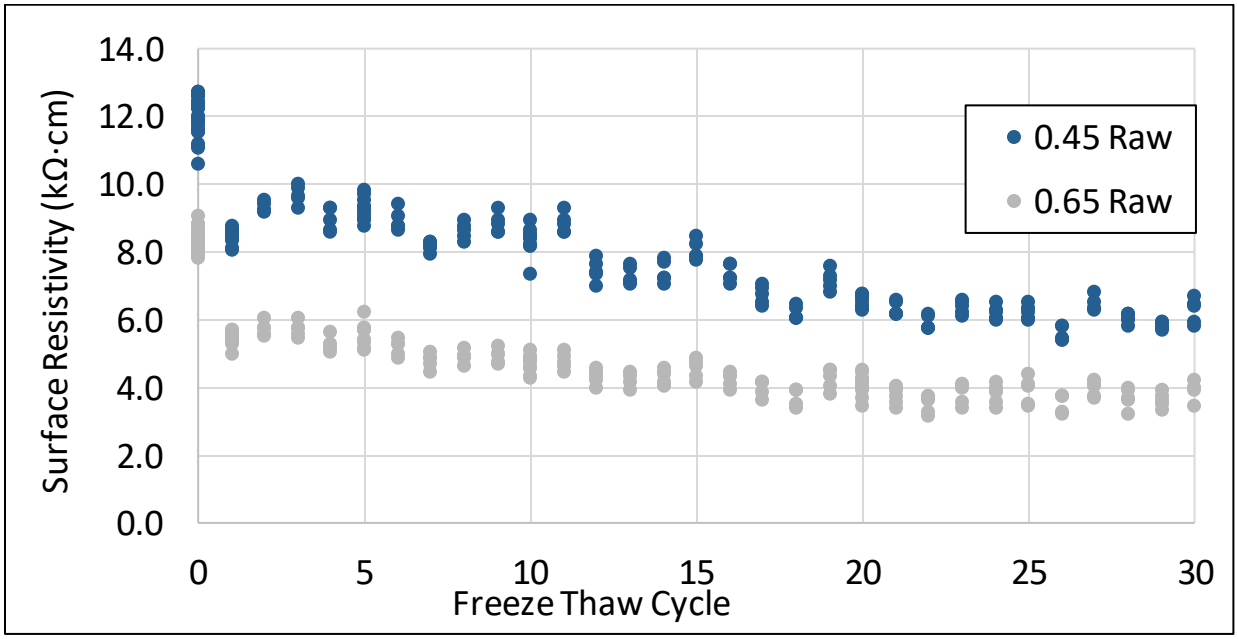

Figure 8.11- Surface resistivity versus freeze thaw cycle for two mixtures and 3 samples per mixture.

For both mixes, there was a large, significant drop in the measured SR after a single FT cycle, indicating that a change in the pore structure was detectable very early into the damage. The decrease in the resistivity was never as severe as it was observed to be in the first cycle. One characteristic evident in Figure 8.11 is a large day-to-day variation within the data, though the

raw measurements were very close together. Considering that the SR measurements were performed at temperatures ranging between 15-25 °C, this variation was expected.

8.4.3.2.SR-temperature correction

The large variation due to differences in the surface temperature of the specimen at the moment it was being measured required a method to correct for these differences. A series of SR-temperature curves were derived at the destructive test intervals so that a more general relationship between SR, temperature and level of deterioration could be determined. The resulting SR-T curves can be found in Figure 8.12.

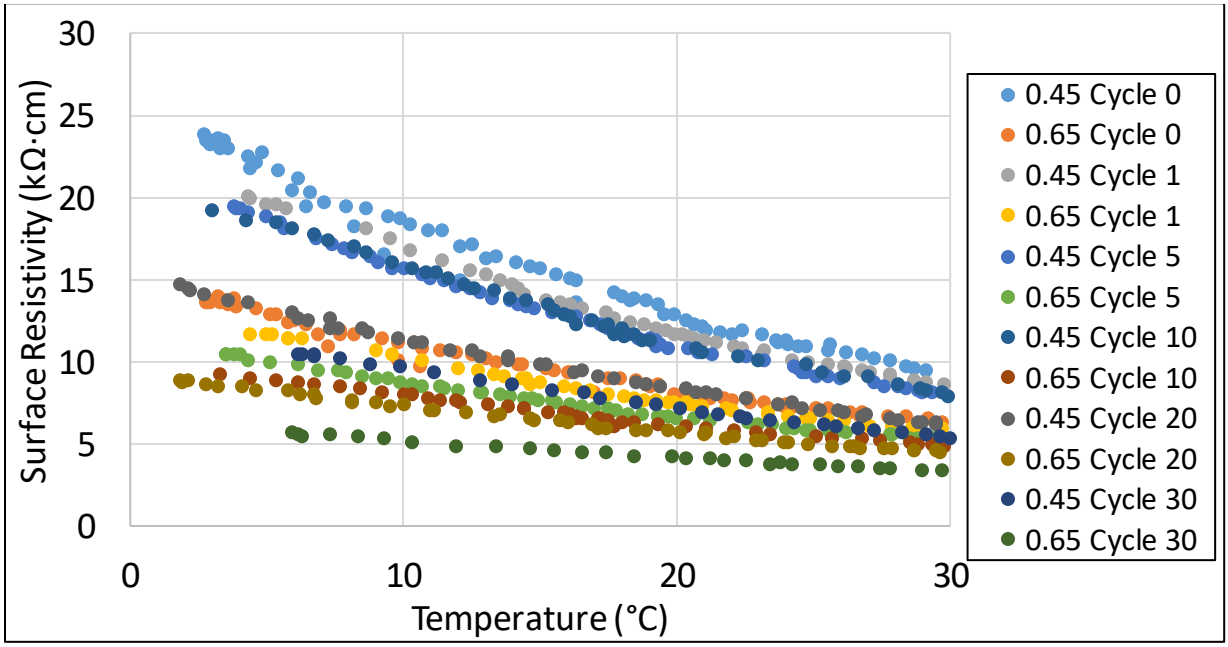

Figure 8.12- Surface resistivity versus temperature from different freeze-thaw cycles

A very highly correlated negative exponential relationship was found for all the SR-T curves (R^2 > 0.99) for both mixes between 5°C and 30 °C, shown in Figure 8.12. The slope of the curves also became less steep as a function of ongoing F/T damage. From this data, the relationship between

SR, temperature and F/T cycles could be derived so that all the raw SR data could be compared at the same temperature. To do so, a function of the form f(T, cycle) = SR was required.

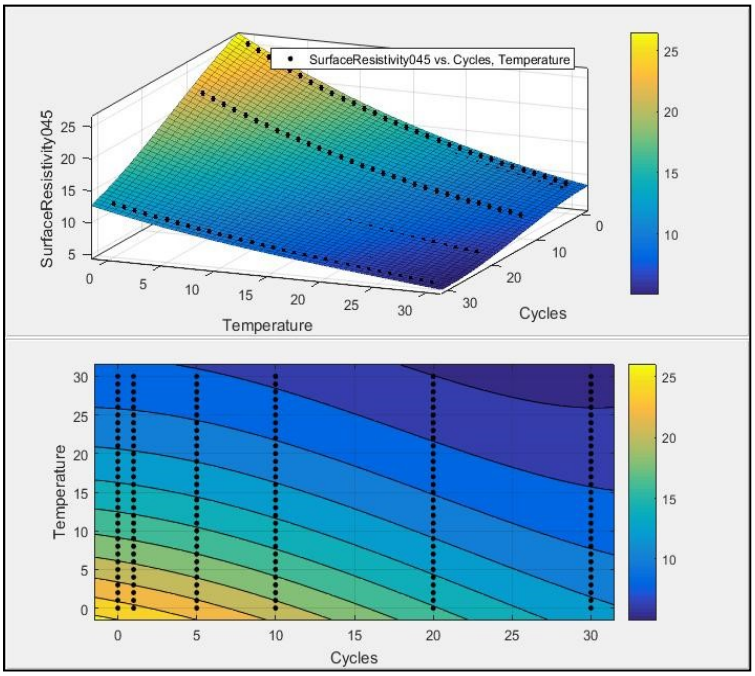

Figure 8.13- Surface resistivity as function of temperature and cycles, 0.45 w/c

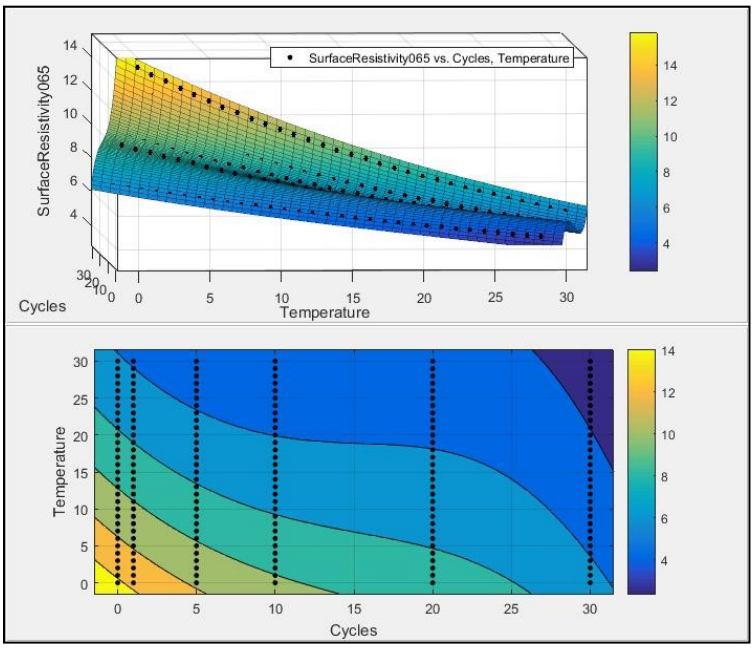

Figure 8.14- Surface resistivity as function of temperature and cycles, 0.65 w/c

Using the curve fitting software of MATlab, a 3rd order polynomial of this form was interpolated for both sets of data. The resulting contour maps of these functions can be found in Figures 8.13 and 8.14. Using these polynomial equations, a SR correction factor was derived for each raw data point so that all the SR data could be compared at the same temperature. The equations to determine this correction factor for each data point can be found in Equations 8.2 and 8.3 below

$$SR_{corrected} = SR_{raw} + \Delta SR$$

Equation 8.2- Surface resistivity correction factor

Where SR_{raw} was the measured SR reading at the measured temperature, and

$$\Delta SR = f(T_{corrected}, Cycle) - f(T_{raw}, Cycle)$$

Equation 8.3- Correction factor calculation

Where *f* is the 3rd order best fit polynomial for each mix, T_{raw} is the measured surface temperature of the sample, $T_{corrected}$ is the reference temperature and *Cycle* is the freeze-thaw cycle number of the data. For samples which were measured at a temperature below the reference temperature, ΔSR would be positive. Note that temperature is a continuous variable but cycle is an integral variable.

By applying this procedure, all SR data was corrected to an equivalent reading at 20 °C. The results of this procedure can be found in Figure 8.15.

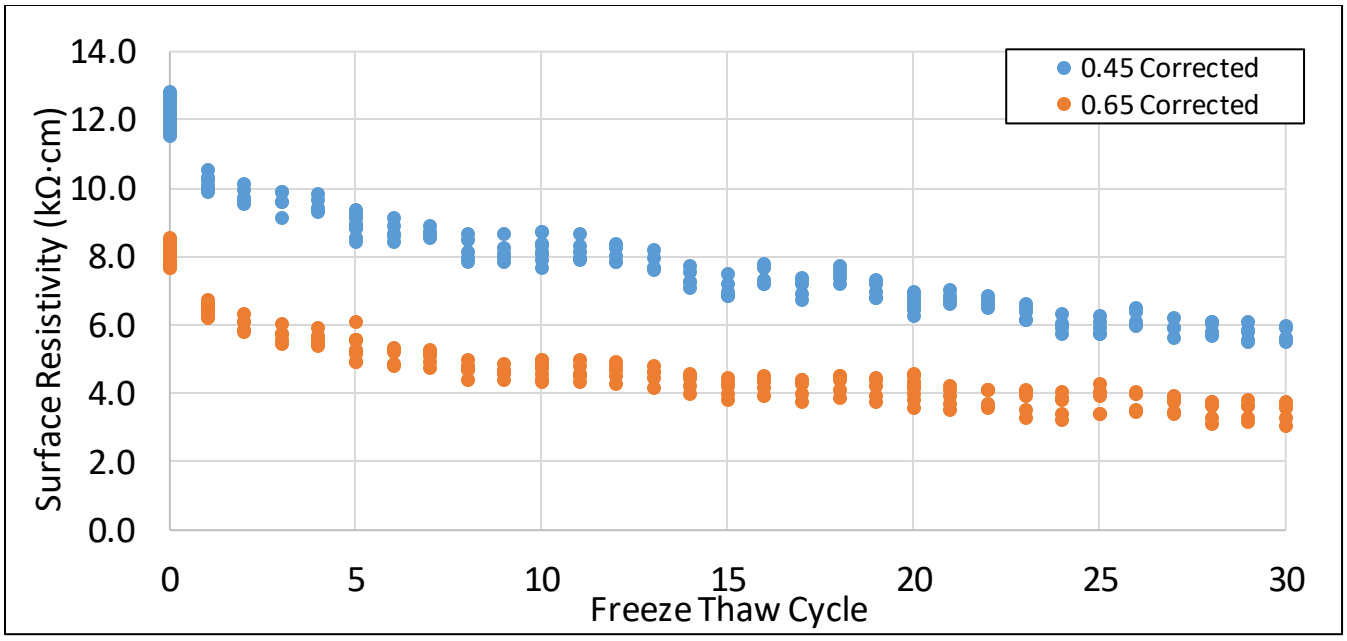

Figure 8.15- Corrected surface resistivity versus freeze thaw cycle for two mixtures for three samples per mixture

Figure 8.15 shows much less cycle to cycle variation among data points, and the spread of SR values is much smaller as compared to the uncorrected Figure 8.11. However, the general relationship of the most severe damage happening after the first F/T cycle and the subsequent deterioration becoming less severe continues to hold for the corrected data set, though the severity of the drop-off is less than the uncorrected data set would otherwise indicate. This suggests that severe damage altering the nature of the pore structure occurs after as little as a single F/T cycle, and subsequent continued deterioration due to additional F/T cycles has a progressively less incremental effect on the overall connectivity of the pore structure.

The data shows that surface resistivity measurements exhibit extreme sensitivity to temperature variation on the surface of the samples, but that this effect can be adjusted for with appropriate measures, making interpretation of the results easier, as seen in Figure 8.16.

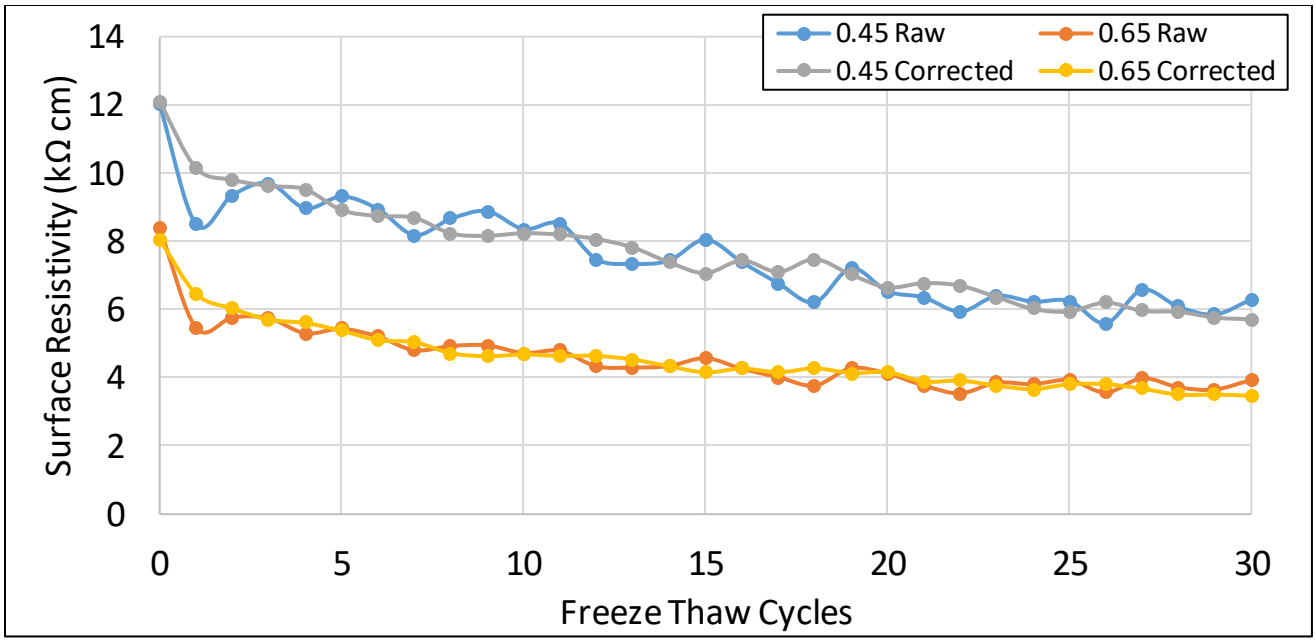

Figure 8.16- Comparison between calibrated and uncalibrated surface resistivity measurements as a function of freeze-thaw cycles

8.4.3.3. Ultrasonic pulse velocity

For both mixes, there was a steady decrease evident in the pulse velocity as a function of freeze-thaw damage, as depicted in Figure 8.17. The slope of the deterioration was more severe for the 0.65 w/c mix, losing 2420 m/s in velocity over the course of the 30 cycles, whereas the 0.45 w/c lost 550 m/s over the same period. As the number of cycles increased, there was also an increase in the variation in the velocities measured, as depicted in Figure 8.18.

At the beginning, the standard deviation for the measurement was 50 m/s for the 0.45 w/c and 60 m/s for the 0.65 w/c, but at Cycle 30 the standard deviations had increased to 108 m/s and 182 m/s, respectively. This increase in variability can be seen in Figure 8.18 as an increase between the maximum and minimum measured values for any given cycle.

The damage did not become significant, per a 2-sample unequal variance T-test, until the 7th cycle for the 0.45 w/c mix and the 5th cycle for the 0.65 w/c mix. There was no significant difference between the control samples tested and the destructive test samples.

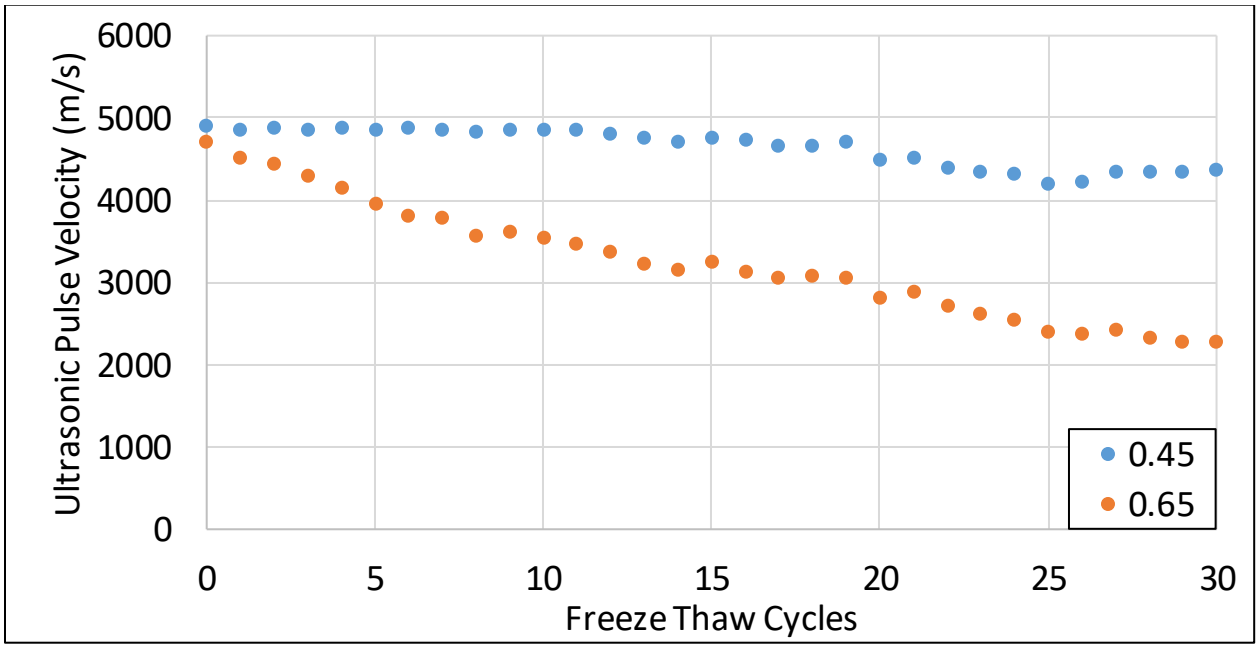

Figure 8.17- Average ultrasonic pulse velocity measurements as a function of freeze thaw cycles for two mixtures.

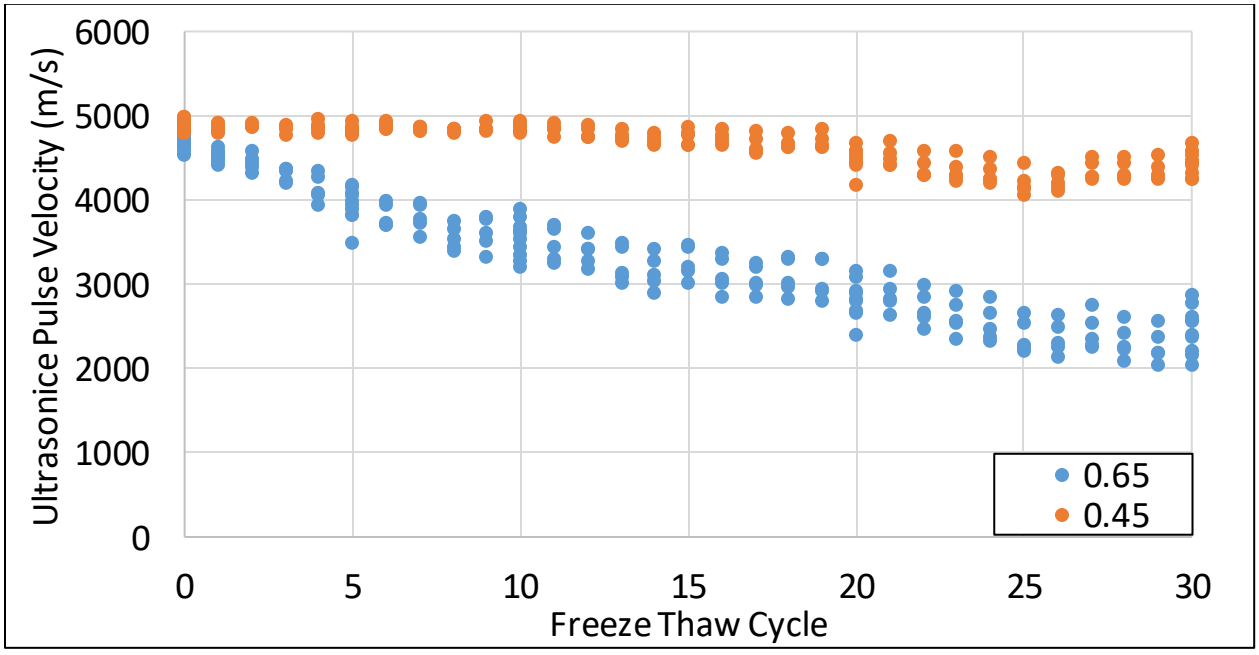

Figure 8.18- Ultrasonic pulse velocity versus freeze thaw cycles from three samples per mixture

8.4.3.4.Expansion prisms

Both mixtures exhibited expansive behavior as a function of F/T cycle, as depicted in Figure 8.19. The extent of the expansion was found to be more severe for the 0.65 w/c mix. Based on the figure, it appears that the rate of expansion increased at around the 12th cycle, with a change in the slope of both lines occurring after this point. The expansion became statistically significant based on a 2-sample unequal variance T-test at the 15th cycle for the 0.45 w/c and the 4th cycle for the 0.65 w/c.

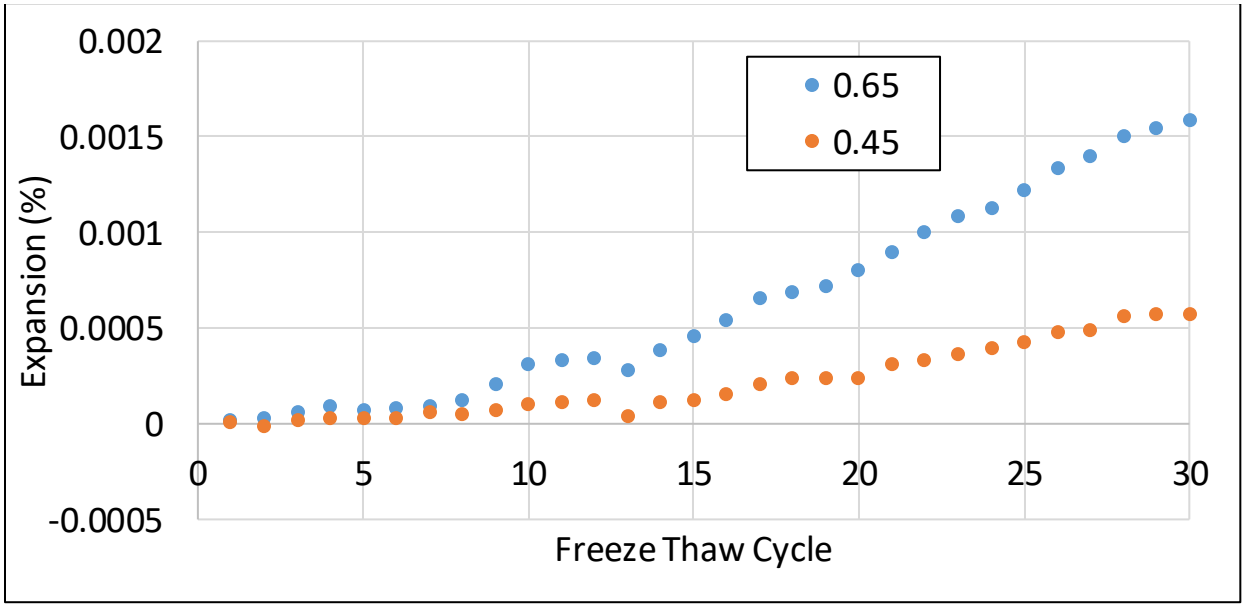

Figure 8.19- Linear expansive behavior during F/T cycles

All the NDT methods that were used to observe F/T damage were successful at detecting an associated signal. The SR method, particularly with a temperature correction, showed the earliest successful NDT detection of damage that was statistically significant. Both UPV and expansion measurements took longer to detect the associated change, suggesting that the SR method may be the most sensitive to early freeze-thaw damage.

A possible explanation for this discrepancy is the difference between testing locations for both UPV and SR. The ultrasonic pulses will generally pass through the least damaged path (which would be the interior of the samples in this case), whereas the SR test evaluates the outer surface on the sides of the cylinder. The expansive freeze-thaw damage could be progressing from the exterior of the sample towards the interior, so more severe expansive damage accrues on the surface of the sample resulting in a more significant decrease in resistivity at an earlier time. The relatively protected interior of the specimen would remain more intact resulting in a more cohesive material for the stress pulses to travel through.

The results from the expansion prisms agree with the UPV results in this sense, whereas accumulating damage takes some time to significantly affect the measurements since the damage must occur throughout the sample to be detected by this method.

8.5. Conclusions

As for the destructive test results, pressure tension testing detected F/T damage much earlier than compression testing. This result was particularly true for the higher porosity mix, where a significant loss in material strength was detected after a single F/T cycle. Considering that cracking has such a strong effect on tensile capacity, more research into this significant drop-off in tensile strength as a function of deterioration is clearly in order. The basic engineering assumption of a constant ratio between tension and compression was shown to be invalid in this case due to the greater effect of cracking on tensile capacity, which could lead to an overestimation in the true material capacity to resist cracking or other tensile modes of loading such as flexure.

In addition, the fracture surfaces associated with the pressure tension failure specimens showed a systematic change in the material behavior due to the ongoing F/T cycles. The fracture surfaces first showed a cohesive bond between the aggregates and the surrounding paste in the undamaged state resulting in aggregate failure. Samples from increased F/T cycles, however, exhibited more intact aggregate particles while the paste appeared to fail around them within the ITZ.

Since the ITZ is a zone of higher porosity, it follows that more severe damage from expansive processes would occur there, yet 'aggregate pullout' phenomenon was not observed on the compressive strength failure specimens which also displayed a less significant deterioration trend. This aggregate pullout was only detected using the pressure tension method. This is expected, since that is the only method that will act to open existing cracks as opposed to compressing the existing fracture surfaces together. Considering that many structural loading modalities such as flexure incorporate tension, it is of integral importance to understand the true material behavior.

8.6. Acknowledgements

The authors wish to thank Proceq North America for their donation of the Resipod surface resistivity meter. The authors also thank Bauval CMM for the donation of the aggregates used in the study.

8.7. References

[1] Kosmatka, S.H.; Kerkhoff, B.; Panarese, W.C.; MacLeod, N.F.; McGrath, R.J., *Design and Control of Concrete Mixtures,* EB 101, 7th edition, Cement Association of Canada, Ottawa, Ontario, Canada, 2002

[2] Prado, P.J.; Balcom; B.J.; Beyea; S.D., Bremner; T.W., Armstrong; R.L., and Grattan-Bellew, P.E.: Concrete Freeze/Thaw as Studied by Magnetic Resonance Imaging. Cement and Concrete Research, Vol. 28, No. 2, pp. 261–270, 1998

[3] Shang, H.S., Y.P. Song, and L.K. Qin. "Experimental Study on Strength and Deformation of Plain Concrete under Triaxial Compression after Freeze-Thaw Cycles." Building and Environment 43, no. 7 (2008): 1197-204.

[4] Shang, H.S., T.H. Yi, and X.X. Guo. "Study on Strength and Ultrasonic Velocity of Air-Entrained Concrete and Plain Concrete in Cold Environment." Advances in Materials Science and Engineering (2014).

[5] Clayton, N. and Grimer, F.: The Diphase Concept, with Particular Reference to Concrete. In: *Developments in Concrete Technology*, Elsevier Science & Technology, Waterford, UK (1979), pp. 283-317

[6] Terzaghi, K., and Peck, R.*: Soil Mechanics in Engineering Practice*. Wiley, New York, (1967)

[7] Uno, T., Fujikake, K., Mindess, S. and Xu, H.: The Nitrogen Gas Tension Test of Concrete, Part 1: Effect of Boundary Conditions and Axial Strain Response. In: *Materials and Structures*. 44 (2010) No.4, pp. 857-864

[8] Boyd, A. J., Bremner, T. W., Holm, T. A., & Boyd, S. R.: Tensile Testing to Evaluate the Effect of Alkali-Aggregate Reaction in Concrete. (1998) T192-2, Ottawa, Canada: IRC National Research Council.

[9] Boyd, A., and Mindess, S.: The Effect of Sulfate Attack on the Tensile to Compressive Strength Ratio of Concrete. In*: Third Int. Conf. on Concrete under Severe Conditions*, Vancouver, (2001) pp. 789-796

[10] Hartell, J., Boyd, A. J., and Ferraro, C.C.: Sulfate Attack on Concrete: Effect of Partial Immersion. In: *Journal of Materials in Civil Engineering.* 23 No.5, (2011) pp. 572-579

[11] Komar, A., J. Hartell and A. J. Boyd. In: *Proceedings of The Seventh International Conference on Concrete under Severe Conditions*, No.1, pp. 337-344

[12] Komar, A.J.K.; Boyd, A.J.; Pressure-tension testing in the evaluation of freeze-thaw deterioration. In *Proceedings of 10th Fib International PhD Symposium in Civil Engineering*, Université Laval, Québec. p. 143-148

ASTM. "Standard Test Method for Compressive Strength of Cylindrical Concrete Specimens." West Conshohocken, PA: ASTM International, 2017.

ASTM. "Standard Test Method for Resistance of Concrete to Rapid Freezing and Thawing." West Conshohocken, PA: ASTM International, 2015.

ASTM. "Standard Test Method for Splitting Tensile Strength of Cylindrical Concrete Specimens." West Conshohocken, PA, ASTM International, 2004.

Foreword to Chapter 9

Chapter 9 is a paper focused on the pressure tension test in evaluating tensile deterioration due to a transport related durability issue, in this case, creep. Long term uniaxial tension stress was applied to concrete specimens at different percentages of their ultimate tension capacity. This chapter is relevant to the theme of evaporative transport based deterioration because creep deterioration is associated with the long-term migration of water from within the smallest nanopores of the concrete. As water moves from these smaller pores into the larger capillary pore structure due to the stress, there is change in the volume of the material as well as a decrease in the ultimate tensile capacity, which was measured as a time dependant relationship dependant on the duration of the applied stress at a constant magnitude. Both saturated and oven-dried specimens were evaluated and similar creep behavior was identified, with the dried specimens failing at a lower stress as compared to the saturated specimens. This finding was in line with the relationship outlined in Chapter 5. The mechanism of pressure tension loading as a uniform tension field was particularly relevant for the transport properties, since the differential pressure between the interior and exterior of the pore system would accelerate the movement of water from the high-pressure to the low-pressure regions (i.e. permeation). Evidence of mass transport through the exposed end of the specimen was observed for both the saturated and dry specimens. This study was important in demonstrating that the pressure tension test could be used to evaluate the creep behavior of concrete in tension, as it allowed for creep studies to be performed without any of the issues involved in the direct tension testing more commonly used for tensile creep studies.

Chapter 9: Tensile Strength of Plain Concrete under Sustained Load by Pressure Tension

Andrew Komar, Gaowei Xu, Andrew J. Boyd

9.1. Abstract

This article illustrates new research regarding long-term deterioration in the tensile strength of plain concrete samples due to sustained stress loading. Two different water-cement ratio mixtures were subjected to sustained load using a Pressure Tension (PT) apparatus. Both saturated and oven dry samples were tested. Long-term PT strength under different load levels was found to decrease linearly as a function of the logarithm of time, corroborating existing creep studies. Pressure tension testing was used to determine the original strength of samples, and the effects of sustained load on tensile strength were analyzed. These results were compared with previous data obtained by direct tension tests to demonstrate efficacy of pressure tension testing for long-term creep studies. In addition, based on the analysis of failed samples, an assumption for the mechanism of the damage process is proposed.

Keywords: Long-Term Strength of Concrete, Creep, Pressure Tension Test, Linear Attenuation

9.2. Background

9.2.1. Creep testing

The strength of concrete under sustained loading is a significant material property. Its long-term loading capacity can be significantly lower than its original capacity. This will influence the

structural capacity of concrete structures over long time scales. One of the mechanisms of such strength loss is crack propagation in concrete. When concrete undergoes loading, particularly in a tensile mode, existing cracks or flaws in the concrete will be subject to stresses that will act to open or propagate them. This is particularly evident in the interfacial transition zone (ITZ), which is the weakest phase of concrete due to the locally higher water to cement ratio caused by the wall effect between bulk cement paste and aggregates. Thus, initial cracking may begin in these areas and expand out into the bulk cement paste over time [1,2]. Though this phenomenon of crack propagation can take place under both compressive and tensile loads, it is particularly severe under tension loading since compressive stresses will generally act to compress the fracture faces together instead of pulling them apart, thus inhibiting crack propagation. If the applied load increases over a critical stress level, however, the crack will continue to propagate due to the indirect tensile stresses that are generated. These microcracks may be bridged by autogenously healing due to continuing hydration, in which case a bulk failure will not occur [3]. Long-term strength behavior under sustained loading is like cyclic loading, which produces a linear relationship between the residual strength and the logarithm of elapsed time [4]. Concrete is not the only material that undergoes this creep behavior, as it has also been observed in some composites [5].

There has been more research on the deflection caused by ongoing creep than on the decrease in load-carry capacity. Bissonnette [6] and Kovler [7] used a uniaxial restriction test machine to find early age tensile creep characteristics by qualitative analysis. Østergaard [8] established a mathematical tensile creep model for early-age concrete. Bažant investigated the creep behavior of concrete at variable humidities and formulated a mechanical model [9]. Other research was

based on results from a uniaxial restriction test machine to explore the relationship between tensile creep and shrinkage at early ages. Altoubat reported that the tensile creep is about 50% of overall shrinkage, and this creep can act to decrease stress from the restricted status and slow down other cracking [10].

For undamaged concrete, ultimate tensile strength is only about 10% of ultimate compression strength. Consequently, in any concrete tensile creep test, the applied load must be significantly smaller than that in a compression creep test on the same material, so that the corresponding tensile strain will be much smaller as well. This can cause complications for testing due to the relatively low measurement accuracy of strain gauges and material variability relative to their resistance at these lower stress levels. As a result of these complications, there is very little research into long term loading of plain concrete in tension.

Strength is proportional to the logarithm of time, so short-term sustained loading (from several minutes to several days) and long-term sustained load over longer time periods must be investigated separately. The difficulty is that the critical stress level which will cause a crack to propagate into a bulk failure is unknown, so some researchers embarked on searching for reasonable stress levels below the critical stress as a starting point. For short-term sustained compression load, Shank tested the plastic flow of 8 cylinders with an average strength of 5024 psi (34.6 MPa) under various stresses and suggested 85% of ultimate strength [11]. Price suggested the critical stress should be considered as low as 70% of ultimate strength [12]. Surendra *et al.* studied a 4-hour sustained load on normal-strength concrete and found that the

sustained load strength should be within 70% to 80% of ultimate strength [4]. Thus, all indicated that the minimum stress level should be around 70% of strength.

Rusch found that prism specimens failed within 7 days under a load representing 80% of ultimate strength, and wouldn't fail under 75% of ultimate strength [13]. Stockl did a 15-year study with a similar methodology and concluded that the critical stress should be around 80% of ultimate, if eccentricities are ignored [3]. Ngab *et al.* tested specimens with an ultimate strength of 62 MPa and they did not fail below a stress level of 85% over 60 days [14]. Smadi *et al.* tested concrete samples for 60 days, and concluded that the long-term strength should be no more than 75% of ultimate strength [15]. Thus, the critical stress level for long-term strength is around 75%. According to tests by Said *et al.*, the critical stress level for concrete cylinders under high, sustained compressive load for three months was higher if the compressive strength was higher. A small eccentricity slightly improved this critical stress level [16].

There are few studies of short or long-term concrete strength under sustained tensile loading. AI-Kubaisy *et al.* investigated concrete cracking under sustained axial tensile loading [17]. They made concrete specimens with a 0.5 w/c. The diameter of each specimen was 100 mm, and the length was 200mm, as seen in Figure 9.1. Two sets of specimens were cast and cured for 21 days in a water tank at 20 ºC. High alumina cement (HAC) concrete was applied to the concrete at the two ends of the specimens to interface with the mechanical grips. All specimens were loaded in direct tension applied by mechanical grips on either end. The loading rate was 0.9 MPa per minute. The sustained load tests were carried out at stress levels varying from 65% to 95% of

ultimate strength, which was determined via rapid strength tests in direct tension. The results of the long-term strength tests are depicted in Figure 9.1.

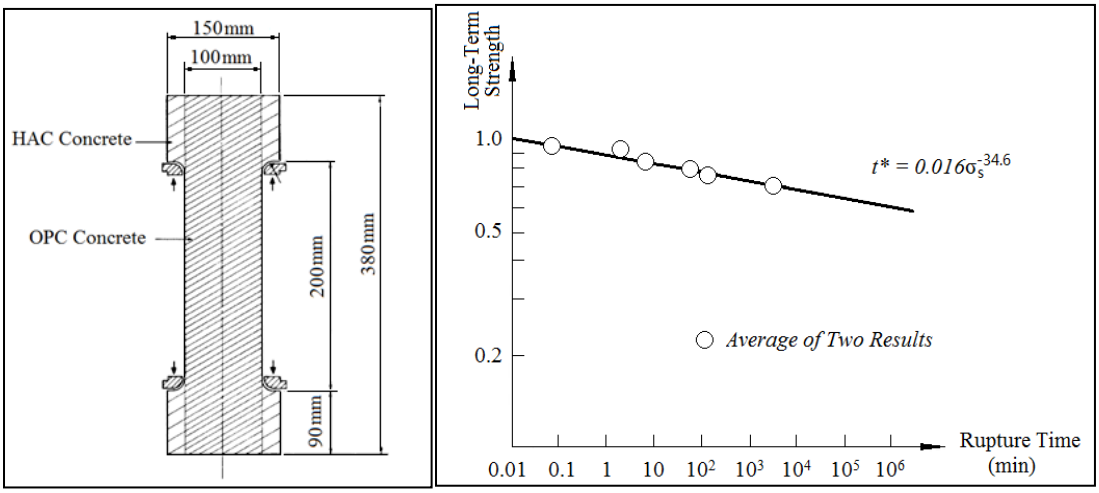

Figure 9.1-Tension testing specimen configuration and results from Al-Kubaisy et al. [17]

Shkoukani *et al.* tested two sets of specimens – one with a concentric tension load, the other with eccentric tension loading [18]. The diameter and the length of these samples was 150 mm and 300 mm, respectively. The specimens were sealed before and during the test with plastic sheets to prevent moisture loss, which is associated with creep behavior. When adding sustained load, the loading rate was lower as compared to when they were loaded to determine the ultimate strength via rapid strength tests. The results showed that the critical stress level should be around 70% for concentric tension, but was inconclusive for eccentric tension tests, as can be seen from Figure 9.2.

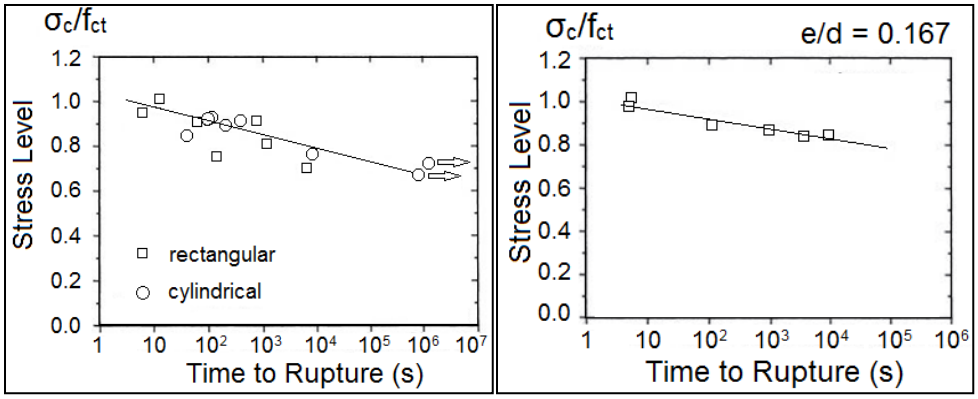

a) b)

Figure 9.2- Relationship between relative sustained stress level and time to failure for concentric tensile tests (a) and eccentricity of .167 (b). From Shkoukani et al. [18]

Shkoukani *et al.* found that the tensile deterioration in creep dramatically decreased with an increase in eccentricity. Figure 9.2a shows the typical deterioration without an eccentricity. In Figure 9.2b, however, they found that no failure occurred with loading below 75% of the undamaged stress. They also tested specimens with an eccentricity of 0.50, and found that there was virtually no tensile deterioration, with no specimens failing below 90% of the undamaged stress. They also found that the eccentrically loaded specimens which did not fail showed an increase in tensile stress when tested in short term loading.

Carpinteri *et al.* performed two sets of creep tests, looking at both tensile creep and flexural creep behavior [19]. All specimens were stored at 20 ºC and either 95% or 50% relative humidity. For tensile creep tests, they tested 13 specimens in total under sustained loads varying from 70% to 95% of the ultimate strength. The results are shown in Figure 9.3, for which they derived the best-fit equation seen in Equation 9.1.

$$t_{cr} = 104\left(\frac{\sigma_s}{\sigma_p}\right)^{-27}$$

Equation 9.1- Empirical best-fit relationship for variable sustained loading. From Carpinteri et al. [19]

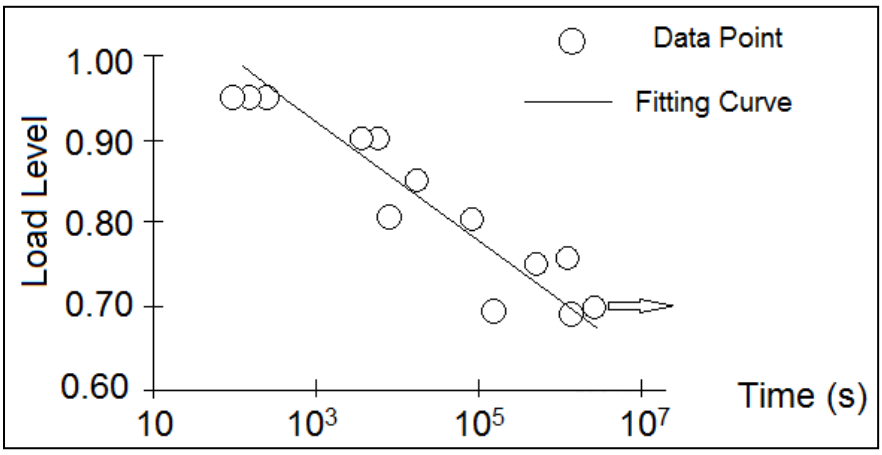

Figure 9.3- Sustained load levels versus failure in lifetime creep testing. Arrow indicates that failure did not occur during testing. From Carpinteri et al. [19]

9.2.2. Tension testing

The tensile strength of concrete is generally determined by either a direct uniaxial strength test performed with mechanical clamps, or the splitting tension test (ASTM C496). In direct tension testing, the specimen is subjected to a uniformly distributed monotonic increasing axial tension load applied via mechanical grips along the ends of the tension coupon until the sample breaks into two parts. It provides generally accurate results, but complications arise from uncertainties related to the stress concentrations that develop in the proximity of the mechanical grips. The grips work via frictional contact, which will result in a confinement pressure that may act to close existing microcracks and possibly overestimate the tensile strength, especially if the critical flaw happens to exist within these areas. These may happen at either end near the grips. Furthermore, the exerted load may be eccentric due to the specific placement of the tensile coupon within the machine, since any offset from the applied loading direction would affect the measured results.

Compared with direct tension test, the splitting tensile test is a more indirect way to measure concrete tensile strength. The splitting tension test applies a compression load in a plane parallel to the axis of the cylinder. Due to the equilibrium of forces resultant from this loading situation, a net tensile stress perpendicular to the applied stress develops over approximately 90% of the cross-sectional area. Based on solid mechanics calculations, the magnitude of this stress is inversely proportional to the product of the length and diameter of the cylinder and is directly proportional to the applied load [20,21]. However, Popovics reported that the result was lower due to the assumption of plastic behavior being underestimated [22], and other reports claimed that aggregate size and aggregate interlock have a large effect on the results [23]. Furthermore, the maximum tensile stress only develops along the plane of loading concomitant with the compressive force application, so any critical flaws not coinciding with this loading plane will be rendered less effective and the peak tensile resistance may be overestimated relative to a more sensitive test method [23]. Therefore, a new tensile testing method without eccentric or stress concentration effects is advisable.

The basic version of the pressure tension machine for testing tensile strength of materials was developed by the BRC in the 1970s. The prototype used a cylindrical specimen inserted into a special chamber, and used water pressure applied to its curved surface as the loading medium. The only area not exposed to the applied water pressure was the two ends [24]. Thus, the applied pressure around the sample was uniformly distributed on the curved surface. This application of symmetric uniform pressure to a cylindrical specimen's surface causes a unique stress state to develop as long as the material being tested is considered 'diphase', i.e. having a continuous solid phase and a liquid phase distributed throughout the volume. This condition is satisfied by

concrete since it is porous throughout. When using principles first developed for soil mechanics, it can be shown that this load application causes the equivalent of a hydrostatic pressure to develop throughout the interior of the specimen, which acts to cancel the biaxial application of stress along the curved surface. The resultant stress state is equivalent to a uniform tension field perpendicular to the applied load [25,31,32]. This pressure tension effect is illustrated in Figure 9.4.

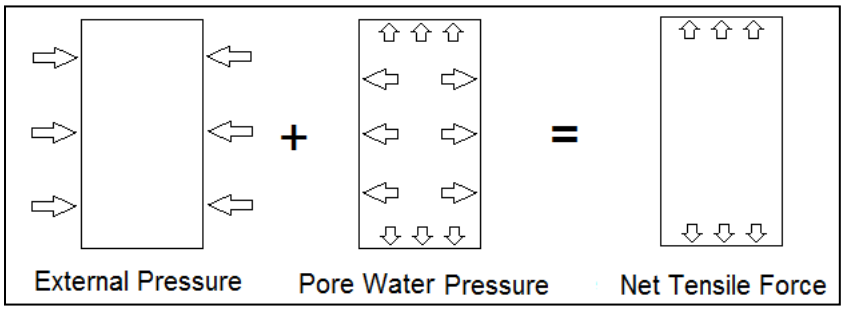

Figure 9.4- Pressure tension effect

Specimens that have been failed in pressure tension appear as if they have been pulled apart by the two ends, as if they were subjected to applied tension rather than compression. Some research that uses a similar fluid-pressure test to measure tensile strength of concrete are ongoing. Victor *et al.* tested the tensile strength of concrete cylinders with centered internal holes by applying radial internal fluid pressure, as seen in Figure 9.5. They reported that the tensile strength was about 17% greater than the tensile strength obtained from splitting tensile tests or equivalent to around 11% of compressive strength. However, since the fluid pressure affects the moisture content of the test sample, the machine cannot be used to test dry or unsaturated samples. Significant testing difficulties also arose from creating test specimens of the proper geometry that could be properly sealed.

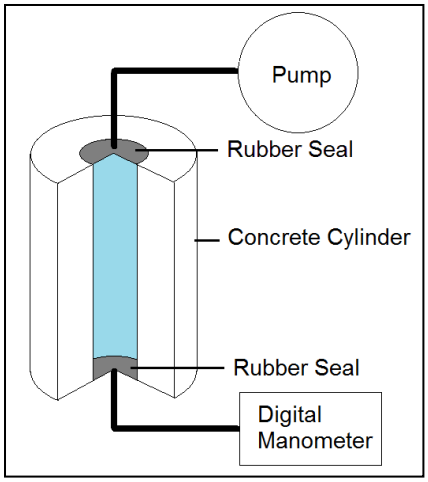

Figure 9.5- Schematic view of a fluid-pressurized tensile test system for concrete. From Cantillo and Andrés [17]

This pressure tension principle is not exclusive to a load application by water. This work presents a gas-based pressure tensile machine that uses compressed air as the loading medium. Figure 9.6 shows the configuration of the system. A concrete cylinder is sealed within the cylindrical chamber via O-rings so that only the flat surfaces at the top and bottom of the cylinder are exposed to ambient atmospheric pressure. A series of computer-controlled valves precisely control the rate of flow of pressurized gas into the chamber, and the resulting pressure development within is measured using a digital pressure transducer. In this manner, the application of stresses can be controlled or maintained, which allows for a variety of tests including a fast-uniaxial tensile failure test or a sustained loading mode as found in creep.

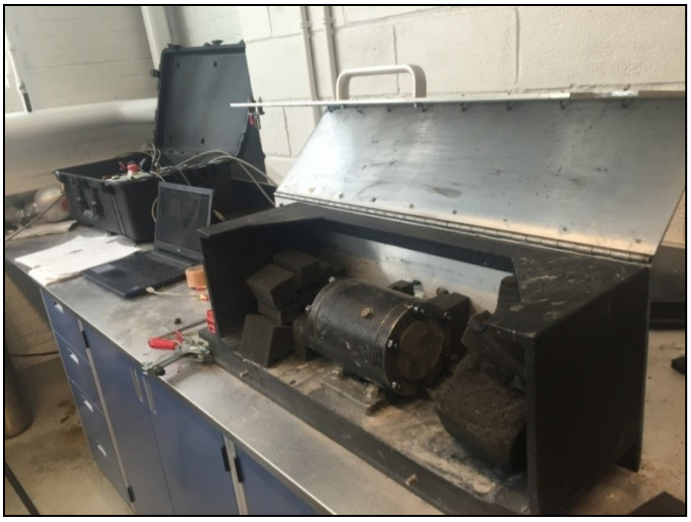

Figure 9.6- Photograph of pressure tension testing machine

Pressure tension tests are much more sensitive to pre-existing internal damage, especially that caused by expansive pressures often associated with durability damage since the porous space being pressurized via hydrostatic or gas pressure will act to open existing cracks. Boyd and Komar used the PT machine to test concrete samples immersed in a sulfate solution for up to one year, and the results showed that pressure tension was more sensitive to durability related damage than other tension testing methods [28,29,30,33]. Li tested 56 cylinders of two different w/c with the gas-based PT machine to investigate the effect of moisture content on the mechanical properties of plain concrete [30]. The mixes had a 0.45 and 0.65 w/c. In addition, both oven dried and immersed samples of both mixes were investigated. Li reported that the concrete with the lower water to cement ratio was more sensitive to moisture content in terms of measured PT strength. The strength showed reductions of 21.58% and 8.33%, respectively, as a function of increasing immersion time. Uno *et al.* embedded strain gauges in concrete cylinders or on the surface of concrete cylinders and obtained strain-stress curves which reflected the common understanding of concrete tension stress-strain mechanics [31,32]. They found a different

relationship to Li in terms of moisture content and pressure tension failure. They found the highest measured pressure tension failure was associated with a higher moisture content, and that there was a significant decrease in measured tensile strength as a function of continued drying. They also developed a model based on linear elastic fracture mechanics (LEFM) to investigate its failure criterion [32]. However, the long-term loading of plain concrete with pressure tension has never been attempted, so feasibility and reliability of the long-term gas pressure tensile test will be investigated.

9.3. Materials and Methods

9.3.1. Mix design

Sixty specimens of two w/c ratios were cast, thirty at a w/c = 0.45 and thirty with a w/c = 0.65, respectively. The two mixture designs are described in Table 9.1. An air entraining admixture was added to both mixtures at the manufacturer's recommended dosage. The aggregate used was a granitic aggregate with a specific gravity of 2.65 and an absorption of less than 0.5%.

The samples were divided into three groups: Group 1 was for saturated samples with w/c = 0.45, group 2 was for saturated samples with w/c = 0.65 and group 3 was for oven-dry samples with w/c = 0.65.

Table 9.1- Mixture design of concrete samples

w/c / Term	**0.45**	**0.65**
Cement	34.63 kg	21.16 kg
Coarse	77.55 kg	68.42 kg
Fine	56.82 kg	57.78 kg

H_2O	16.59 kg	14.74 kg
AEA	0.18 kg	0.11 kg
Slump	81 mm	120 mm
Air Content	8%	9.5%

9.3.2. Exposure conditions

The study was formulated to determine the long-term tensile strength variation under different stress levels, moisture content, and water to cement ratios. In particular, it was designed to investigate whether the rule of long-term linear strength decrease as a function of logarithmic time would be detectable using the pressure tension test.

A key experimental variable was to control for the maturity of the specimens from each mixture so that they would all achieve the same strength development. A significant difficulty arose considering that there was only one PT machine available to perform tests, some of which could last hundreds of hours. Thus, ascertaining the time dependent strength gain due to continuing hydration presented a difficulty in the analysis of results. To mitigate this uncertainty, two different methods of halting hydration were used and the results compared. The first method was to force some specimens to dry, as lower relative humidity within the concrete would slow the rate of continuing hydration. The second method used was to place saturated specimens in a freezer, bringing the internal temperatures below -15°C and halting the hydration reactions.

All samples were cured in saturated limewater solution for 45 days at a temperature of 24 ± 2 °C. After the curing period, the samples were divided into the three groups as previously described. The saturated sample set was then frozen to a temperature below -15°C. When they were to be

tested, the samples were individually removed from the freezer and thawed through immersion in room temperature tap water for 24 hours before the pressure tension test would commence.

For the subset of dried specimens, cured cylinders were placed in an oven at 105 ± 5 °C. Gravimetric mass measurements were performed until the measured mass did not change by 0.5 g over a 24-hour period. After this condition was satisfied, the cylinders were considered to be dry. Examples of both conditions can be seen in Figure 9.7.

Figure 9.7- Frozen and oven-dried sample conditions

9.3.3. Destructive testing methodology

It was necessary to determine the ultimate tensile strength for each exposure condition so that an appropriate load level could be set for the long-term tests. Three samples from each of the exposure conditions were tested in the pressure tension machine at a monotonously increasing loading rate of 10 psi/second (4 MPa /min) until failure. The maximum pressure at failure was taken as the maximum tensile capacity, and an average of the three samples was used to determine the control point of the undamaged concrete.

For the sustained loading portion, this control point was used to determine the pressure level that the pressure tension machine would maintain until the specimens failed in tension. The

ramp-up to this pressure proceeded at a stress rate of 5 psi/second (2 MPa/min), and the pressure level was thereafter maintained automatically via computer controlled servo-valves. To choose a set of appropriate stress levels for each exposure condition, a minimum pressure of 70% of the undamaged tensile stress was used. Other stress levels were also tested, as found in Table 9.2.

Table 9.2- Classification of the long-term testing samples

Exposure Condition Group	#	Stress Level	Quantity
1 Saturated w/c = 0.45	1	90%	3
	2	85%	3
	3	80%	3
	4	70%	3
2 Saturated w/c= 0.65	1	80%	3
	2	70%	3
	3	60%	3
	4	50%	3
3 Oven Dry w/c = 0.65	1	80%	3
	2	75%	3
	3	70%	3
	4	65%	3
Total			36

9.4. Results and Discussion

9.4.1. Destructive testing for set point

The results of the destructive testing to determine the control points for the long-term strength study can be found in Table 9.3.

Table 9.3- 'Instantaneous' strength testing results for 4 MPa per minute strain rate

Group	w/c	Exposure Condition	Average PT Strength (MPa)	Standard Deviation (MPa)

1	0.45	Saturated	4.768	0.256
2	0.65	Saturated	3.015	0.302
3	0.65	Oven Dry	1.923	0.392

9.4.2. Decrease of long-term pressure tension strength

For most of the samples tested, there was a significant loss of tensile strength after exposure to long term loading. To derive an empirical relationship between loading duration and strength deterioration, the test results were plotted on a logarithmic scale, and a logarithmic Root Mean Square (RMS) best fit line of the form in Equation 9.2.

$$\sigma_t = \alpha \cdot \ln(t) + \beta$$

Equation 9.2- Logarithmic best fit curve form

Where σ_t is the stress at time t, and α and β are the experimental curve fitting parameters. Parameters α and β were derived using curve-fitting software. The nine control point strength tests at the strain rate of 4 MPa per minute were regarded as 'instantaneous' tests, so the load duration was taken to be one second. Thus, the y-intercept of the best fit line is concomitant with these instantaneous strength values. These results were also normalized with respect to the strength determined from the undamaged strength tests. The linear regression results and the formulas derived, as well as normalized best-fit data can be found in Figures 9.8 through 9.11.

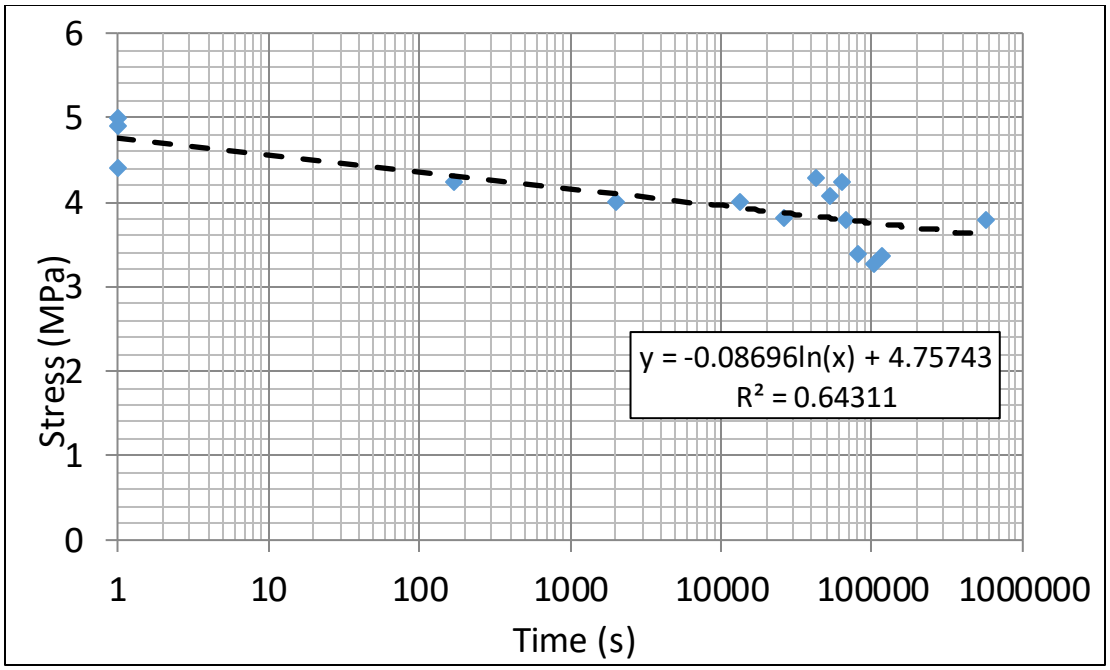

Figure 9.8- Creep test results for group 1 (saturated specimens of W/C 0.45)

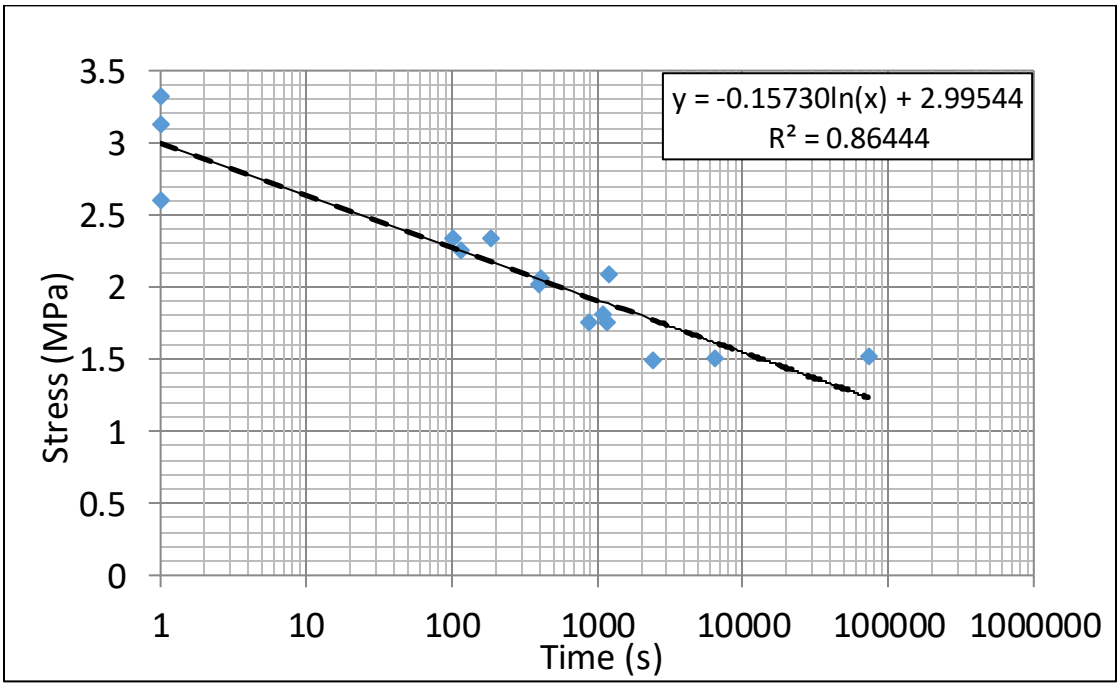

Figure 9.9- Creep test results for group 2 (saturated specimens of W/C 0.65)

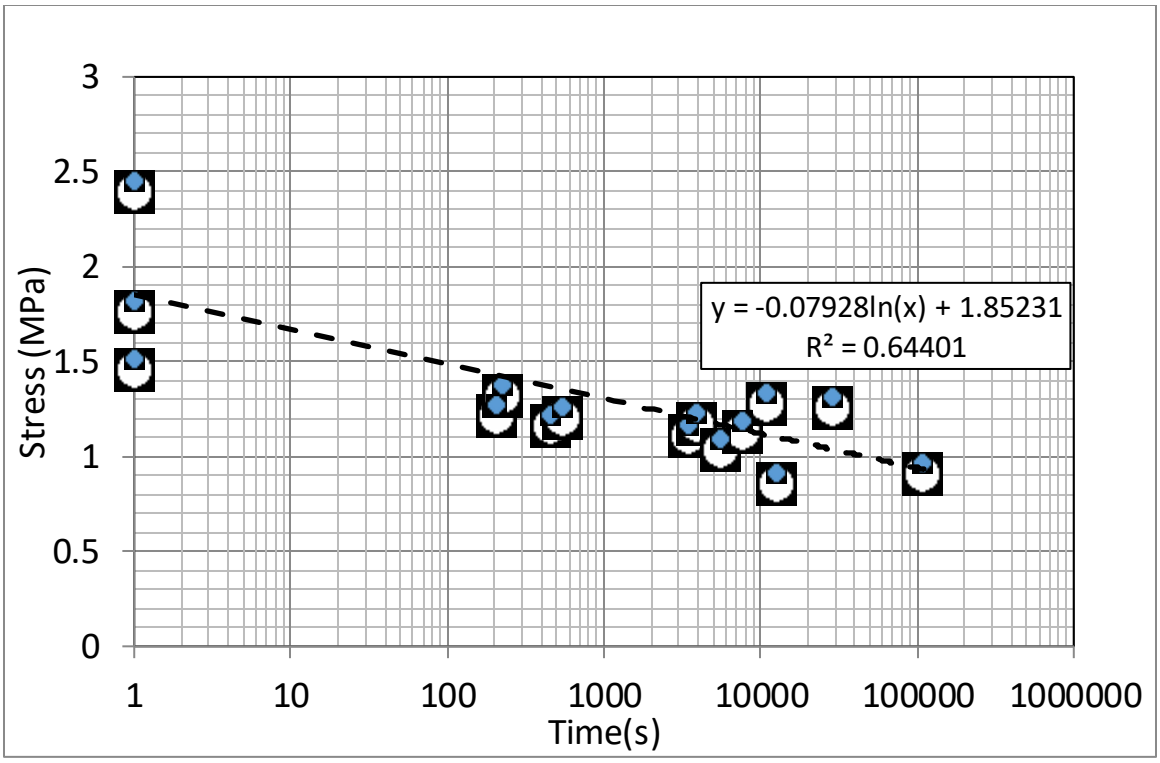

Figure 9.10- Creep test results for group 3 (oven dried specimens of W/C 0.65)

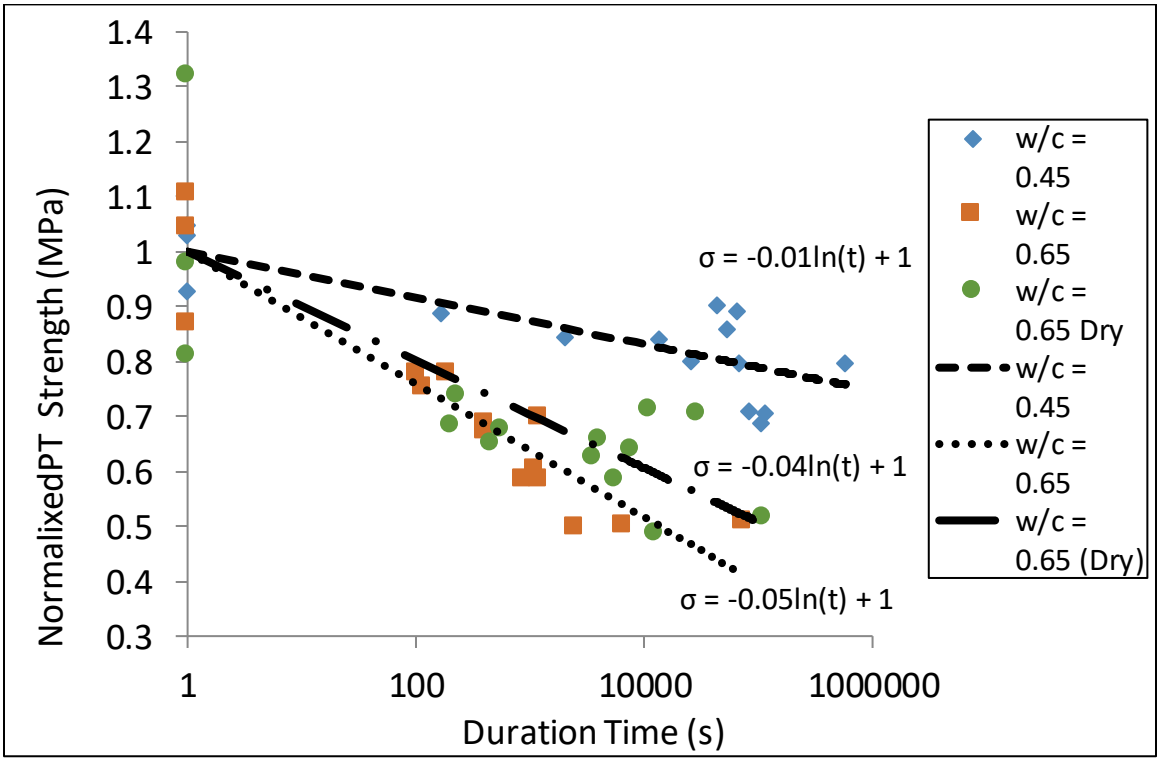

Figure 9.11- Comparison of the three exposure conditions, normalized with respect to instantaneous failure level

9.4.3. Prediction of original strength

A procedure for estimating an 'undamaged' material strength was developed. As can be seen in Figure 9.11, there was some variation in the measured concrete strength at similar stress exposure durations. The signal associated with the long-term deterioration was on the same order as this statistical variation, and since the original, undamaged strength of the samples that failed during sustained loading cannot be obtained directly by testing instantaneous strength, a method to estimate the original PT strength from the creep failure specimens was developed as follows.

It was assumed that the fluctuation in long-term strength observed in the damaged specimens was a consequence of statistical variations in the original strength of samples (i.e. the strength of concrete samples had a normal distribution with respect to their average). Thus, the long-term strength deterioration would also yield the same normal distribution with respect to the regression line. Since the relationship between the stress level and logarithm of time was found to be linear, the original strength of each sample can be back-estimated from these regression lines by extrapolating each of the damaged datum back to the y-intercept, as seen in Figure 9.12.

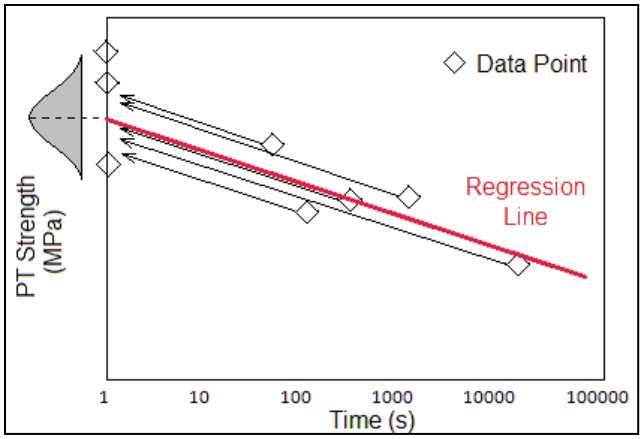

Figure 9.12- Explanation of predicting original strength

The y-intercept of these projected lines represents an estimated value of the undamaged strength of all the specimens, which, if this predictive theory is valid, will be around the same magnitude as the 'instantaneous' specimens. In addition, if the assumption of a normal distribution is true, the projected data points on the y-axis will also yield a normal distribution, as seen in Figure 9.12. This procedure was implemented and the comparison between the instantaneous failure levels and the predicted strength can be found in Table 9.4.

Table 9.4- Comparison between predicted strength and instantaneous failure levels

Group	Instantaneous failure (MPa)	Standard Deviation (MPa)	Predicted Strength (MPa)	Standard Deviation (MPa)	Error (MPa)
1 W/C 0.45, Saturated	4.768	0.256	4.757	0.292	0.010
2 W/C 0.65, Saturated	3.015	0.302	2.995	0.197	0.020
3 W/C 0.65, Oven-dry	1.923	0.392	1.852	0.217	0.071

Table 9.4 shows that the predicted PT strengths of all three exposure groups from the creep study were extremely close to the actual instantaneous failure levels for the exposure groups. For all

three groups, the prediction and the actual values were statistically indistinguishable per a two-sample unequal variance student-t test. The concrete samples with higher w/c consistently failed at a lower stress level than those with a lower w/c, which was expected given that the higher w/c has more pore space and less binder content. In addition, when comparing Groups 2 and 3, the oven-dried samples exhibited lower strengths relative to the saturated specimens while w/c remained the same. The largest variance sample group was found to be the 0.45 w/c (Group 1).

9.4.4. Comparison with previous studies

Linear regression curves from this study were plotted alongside fitting curves from previous research are shown and compared in Figure 9.13. The performance of concrete under sustained load by gas based pressure tension tests produces results comparable to those found by other existing methods [17,18,19].

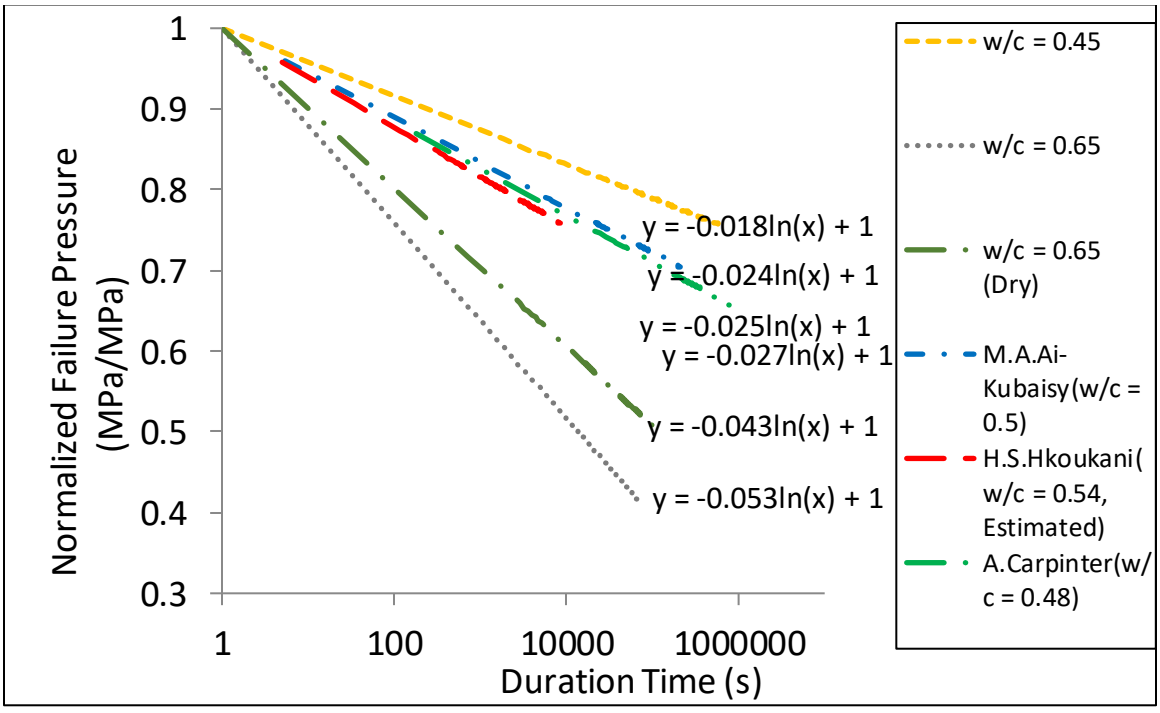

Figure 9.13- Comparison of groups 1 through 3 with previous studies [17, 18, 19]

The most remarkable effect observed from this study that was also found in other studies was the effect on the slope of these regression curves as a function of w/c. This observation was expected, as a higher w/c is associated with higher permeable void contents, therefore these samples would be more susceptible to crack propagation due to the greater volume of pressurized air or water within these pore spaces. This greater magnitude of pressure on a smaller volume of binder would have the net result of causing failure at a lower applied stress level. Conversely, specimens comprised of a lower w/c concrete will have a corresponding decrease in permeable voids. Thus, pressurized fluids such as air will have a smaller volume to occupy, leading to a higher stress resistance because of more continuous solid material resisting this stress. By comparing the curves of saturated and oven-dry samples of w/c = 0.65, it became clear that the moisture content of concrete also affects the slope of this creep damage curve.

9.4.5. Analysis of failure patterns

Figures 9.14 shows the general failure patterns observed on the saturated samples. Different failure modes occurred between the saturated and unsaturated samples, although the failure mode of the saturated samples was consistent across different w/c in Groups 1 and 2.

Figure 9.14- Typical failure pattern of saturated samples

These saturated samples consistently failed with a single tensile crack perpendicular to the applied stress field, resulting in two sample fragments of roughly equal size. This failure mode is consistent with previous research using similar test methods [24,28,29,31,32].

The fracture surface was observed to pass through the aggregate in some cases, resulting in a 'mirror image' of the fractured aggregates on either one of the two fragments. In other cases, the crack passed around the aggregate through the ITZ, resulting in an intact aggregate on one side of the crack, and a different colored region of the cement paste in the same shape as the intact aggregate on the other face. The fractures that passed through aggregates instead of around them were more commonly observed in the lower w/c sample set, suggesting that this disparate behavior is correlated with the higher binder content found in lower w/c samples. In some cases, there were a couple of additional fragments near this single crack, but these additional fragments might have resulted from impact damage at failure. Virtually all the specimens failed in the region of compressed gas application between the two sealing O-rings, though there were a few samples that failed due to a crack in the O-ring sealing area, as seen in Figure 9.15

Figure 9.15- Failure adjacent to sealing O-ring

The failure mode for the oven-dried samples was markedly different from this first mode of failure. As Figure 9.16 shows, the typical failure resulted in a large volume of the samples being completely fragmented into small pieces. The fragments observed seemed to closely coincide with the aggregates within the concrete, and there were no fractures observed that passed through the aggregates themselves. This observation strongly suggests that this failure mode is resultant from a paste failure near the ITZ.

Figure 9.16- Typical failure pattern of dry samples

In addition, the dry samples failed at a significantly lower stress level when compared to the same samples that were saturated. Various mechanisms have been proposed by others to explain this disparate phenomenon. Uno *et al.* [31,32] hypothesized that the lower failure level was due to the differences in viscosity between water and air. The more viscous water essentially prevents the rapid intrusion of additional gas near the growing crack face; thus, a higher net gas pressure is necessary to propagate the tensile crack through this water viscosity.

The authors have proposed two other possible explanation mechanisms elsewhere, in Chapter 6 of this document [34]. The second explanation is that water and gas store different amounts of energy relative to each other in the same respective volume. The difference is that gas is compressible, whereas water is essentially not, over this temperature and pressure range. Thus,

a larger mass of compressed air can occupy the same permeable void space as water, 'pushing' with a greater impulse on the crack faces relative to the same volume of pressurized water.

The third possible explanation for this disparate failure behavior between saturated and dried specimens is related to the additional adhesive forces imparted by water due to surface tension. In saturated specimens, the net failure stress must overcome the cohesive surface tensile forces from menisci within the permeable void space, in addition to the regular tensile resistance from the solid phase. Thus, in saturated specimens the net failure stress would be expected to be larger, since a larger magnitude of stress would be required to overcome this additional resistive force. This may also explain why the failures of saturated specimens result in fragments that are more intact; there is still additional cohesive force within the fragments that are not otherwise present in the dried specimens.

An important observation is that, for all the specimens, there was some definite permeation of compressed gas through the unsealed faces of the cylinders outside of the pressure chamber. A gel was applied to the surface of the flat ends, and over the course of the creep testing, air bubbles were observed to form in this gel driven from the inside of the pressurized chamber, as seen in Figure 9.17. This was observed for both the saturated and dry samples, although the magnitude of the apparent air migration was larger for the dry specimens.

Figure 9.17- Air bubbles observed on outer surface of sample

This observation suggests that there was some definite mass transport through the ends of the cylinders, which may be associated with drying due to this permeation. Since this possible drying phenomenon in the immediate vicinity of the ends of the cylinders may be correlated with changes in the net specimen failure stress level, more research into this phenomenon is warranted to determine the exact causes of this phenomenon.

9.5. Conclusions

The experimental data clearly indicated that there was a significant relationship between long-term strength deterioration and exposure to a constant load over time. A linear regression of this data yielded a logarithmic function, which is comparable to results obtained from direct tension testing. Oven-dry concrete had significantly lower PT strength as compared to partially saturated concretes. By comparing with other test results, the PT test is a suitable testing method for evaluating concrete behavior under sustained load. By analyzing the failure modes of test results, three possible explanations for the different failure modes between saturated samples and oven-dry samples were offered, which depended on various proposed mechanisms. More research to

determine the exact nature of this behavior is certainly warranted based on the observations presented here.

There are a few issues that should be addressed in future research using pressure tension, particularly for further creep testing. Unlike direct tension testing, one shortcoming of pressure tension is that it is difficult to measure the strain behavior of the specimen during testing. If this can be addressed, more relevant data could be collected that would be very useful for long term creep studies. In addition, if some sort of acoustic emission monitoring system could be implemented on the flat faces of the cylinder, it would be possible to observe the exact progression of crack initiation and propagation in greater detail. Another issue that was difficult to control was changing moisture content during long term testing. For saturated specimens, the timescales would allow for some partial drying from the exposed ends of the specimen, driven by the pressure gradient between the chamber and the rest of the environment, which would gradually change the moisture content and thus affect the strength over time. As well, for the oven dry specimens, some re-absorption of atmospheric humidity would occur as a result of prolonged exposure to the atmosphere even with the pressure gradient. Furthermore, oven drying above 100 °C can cause micro-structural damage to the specimen due to evaporative pressures that could cause a direct decrease in tensile capacity due to a weakening of the binder phase, so other methods of drying which are not subject to this complication should be investigated.

9.6. Acknowledgements

This work was financially supported by the Natural Sciences & Engineering Research Council of Canada. Bauval CMM is thanked for their generous donation of the aggregate used in this study.

9.7. References

1] Ollivier, J. P., J. C. Maso, and B. Bourdette. "Interfacial Transition Zone in Concrete." *Advanced Cement Based Materials* 2, no. 1 (1995): 30-38.

[2] Scrivener, K.L., A.K. Crumbie, and P. Laugesen. "The Interfacial Transition Zone (ITZ) between Cement Paste and Aggregate in Concrete." *Interface Science* 12, no. 4 (2004): 411-21.

[3] Stockl, S. "Strength of Concrete under Uniaxial Sustained Loading." *Special Publication* 34 (1972): 313-26.

[4] Surendra, P.S., and C. Sushil. "Fracture of Concrete Subjected to Cyclic and Sustained Loading." *Journal Proceedings* 67, no. 10 (1970): 816-27.

[5] Abdel-Magid, B., R. Lopez-Anido, G. Smith, and S. Trofka. "Flexure Creep Properties of E-Glass Reinforced Polymers." *Composite Structures* 62, no. 3–4 (2003): 247-53.

[6] Bissonnette, B., and M. Pigeon. "Tensile Creep at Early Ages of Ordinary, Silica Fume and Fiber Reinforced Concretes." *Cement and Concrete Research* 25, no. 5 (1995): 1075-85.

[7] Kovler, K. "Testing System for Determining the Mechanical Behavior of Early Age Concrete under Restrained and Free Uniaxial Shrinkage." *Materials and Structures* 27, no. 6 (1994): 324.

[8] Østergaard, L., D.A. Lange, S.A. Altoubat, and H. Stang. "Tensile Basic Creep of Early-Age Concrete under Constant Load." *Cement and Concrete Research* 31, no. 12 (2001): 1895-99.

[9] Bažant, Z.P., and J.C. Chern. "Concrete Creep at Variable Humidity: Constitutive Law and Mechanism." *Materials and Structures* 18, no. 1 (1985): 1.

[10] Altoubat, S.A., and D.A. Lange. "Creep, Shrinkage, and Cracking of Restrained Concrete at Early Age." *ACI Materials Journal* 98, no. 4 (2001): 323-31.

[11] Shank, J.R. "Plastic Flow of Concrete at High Overload." *Journal Proceedings* 45, no. 2 (1949): 493-98.

[12] Walter, H. Price. "Factors Influencing Concrete Strength." *Journal Proceedings* 47, no. 2 (1951).

[13] Rusch, H. "Researches toward a General Flexural Theory for Structural Concrete." *Journal of the American Concrete Institute* 57, no. 1 (1960): 1-28.

[14] Ngab, A.S., A.H. Nilson, and F.O. Slate. "Shrinkage and Creep of High Strength Concrete." *Journal Proceedings* 78, no. 4 (1981): 255-61.

[15] Smadi, M.M., F.O. Slate, and A.H. Nilson. "Shrinkage and Creep of High-, Medium-, and Low-Strength Concretes, Including Overloads." *Materials Journal* 84, no. 3 (1987): 224-34.

[16] Said, I., and J.G. MacGregor. "Sustained Load Strength and Short-Term Strain Behavior of High-Strength Concrete." *Materials Journal* 95, no. 5 (1998): 636-47.

[17] Al-Kubaisy, M.A., and A.G. Young. "Failure of Concrete under Sustained Tension." *Magazine of Concrete Research* 27, no. 92 (1975): 171-78.

[18] Shkoukani, H., and J. Walraven. "Sustained Tensile Strength of Concrete." Zurich, Switzerland: Swiss Federal Institute of Technology, 1991.

[19] Carpinteri, A., S. Valente, F. P. Zhou, G. Ferrara, and G. Melchiorri. "Tensile and Flexural Creep Rupture Tests on Partially-Damaged Concrete Specimens." *Materials and Structures* 30, no. 5 (1997): 269-76.

[20] Mindess, S., J.F. Young, and D. Darwin. *Concrete*. 2 ed.: Pearson, 2002.

[21] Petroski, H.J., and R.P. Ojdrovic. "The Concrete Cylinder: Stress Analysis and Failure Modes." *International Journal of Fracture* 34, no. 4 (1987): 263-79.

[22] Popovics, S. *Strength and Related Properties of Concrete: A Quantitative Approach*. Wiley, 1998.

[23] Hannant, D.J., K.J. Buckley, and J. Croft. "The Effect of Aggregate Size on the Use of the Cylinder Splitting Test as a Measure of Tensile Strength." *Matériaux et Construction* 6, no. 1 (1973): 15-21.

[24] Clayton, N. "Fluid-Pressure Testing of Concrete Cylinders." *Magazine of Concrete Research* 30, no. 102 (1978): 26-30.

[25] Terzaghi, K., R.B. Peck, and G. Mesri. *Soil Mechanics in Engineering Practice*. 3rd ed. New York: Wiley, 1996.

[26] Bridgman, P.W. *The Physics of High Pressure*. Dover Publications, 1931.

[27] Cantillo, V., and Andrés G. "Fluid-Pressured Test to Measure Tensile Strength of Concrete." Journal of Materials in Civil Engineering 26, no. 4 (2014): 776-80.

[28] Boyd, A.J., and S. Mindess. "The Use of Tension Testing to Investigate the Effect of W/C Ratio and Cement Type on the Resistance of Concrete to Sulfate Attack." *Cement and Concrete Research* 34, no. 3 (2004): 373-77.

[29] Komar, A.J.K., J.A. Hartell, and A.J. Boyd. "Pressure Tension: Reliability for Assessing Concrete Deterioration." In *Proceedings of The Seventh International Conference on Concrete under Severe Conditions*, edited by Z.J. Li, W. Sun, C.W. Miao, K. Sakai, O.E. Gjørv and N. Banthia, 337-44. Nanjing, China: RILEM Publications, 2013.

[30] Li, G. "The Effect of Moisture Content on the Tensile Strength Properties of Concrete." University of Florida, 2003.

[31] Uno, T., K. Fujikake, S. Mindess, and H. Xu. "The Nitrogen Gas Tension Test of Concrete. Part 1: Effect of Boundary Conditions and Axial Strain Response." *Materials and Structures* 44, no. 4 (2011): 857-64.

[32] Fujikake, K., S. Mindess, T. Uno, and H. Xu. "The Nitrogen Gas Tension Test. Part 2: Failure Mechanism." *Materials and Structures* 44, no. 4 (2011): 865-77.

[33] Hartell, J.A., A. J. Boyd, and C.C. Ferraro. "Sulfate Attack on Concrete: Effect of Partial Immersion." *Journal of Materials in Civil Engineering* 23, no. 5 (2011): 572-79.

[34] Komar, A.J.K. " Development of Evaluation Procedures for Evaporative Transport Based Deterioration." McGill University, 2017.

Chapter 10: Conclusions & Recommendations

The primary focus of the research program was using novel experimental techniques to characterize the transport properties of cement systems and their effect on deterioration processes. A large variety of experimentation was performed to characterize these transport properties as well as more directly evaluating the consequences of deterioration using both destructive and nondestructive testing techniques. The program was successful in this pursuit, both with the development and subsequent proof testing of the pressure tension machine for durability issues, as well as the use of magnetic resonance imaging techniques to directly image the flow of water under transport conditions associated with severe deterioration of concrete. The implications of the program results will be described herein.

10.1. Magnetic resonance imaging

10.1.1. Contributions

The moisture content distribution imaging under both sorptivity and steady state conditions was very effective in illustrating the complexities of mass transport of water under commonly encountered boundary conditions. The MRI studies showed dramatic differences in the magnitude of transport properties over differing W/C, even for relatively small variations such as between 0.40 and 0.45. The SPRITE MRI technique could reliably distinguish between water present in large pores associated with mass transport properties, and water which was bound up within the nanopores associated with the intercrystalline layers of the hydration by-products.

10.1.1.1. Sorptivity

As hydration continued due to the renewed presence of water within the larger macropores, this technique could directly image the changes in the amount of water within the nanopores as additional cement hydrates were formed. Other techniques that examine mass transport in porous systems, particularly gravimetric approaches, are not able to distinguish this nuance of pore space evolution. The associated experimental techniques involved in this observation, namely the fiduciary markers, can allow these kinds of studies over a wider range of MRI facilities than those specialized ones for use in the research program. Using the fiduciary marker technique, it is possible to detect a gradient due to evaporation in samples undergoing sorptive flow in a non-steady state condition.

10.1.1.2. Steady-state evaporative flow

With the MRI studies and steady state flow conditions, a notable observation was the experimental detection of water in large pores in regions that were predicted by commonly used mass transport to be dry. Since water was detected at significant concentrations in these regions that would be considered dry using these models, this presents an experimental verification of a more severe durability risk than would be ordinarily expected for concrete. Where there is water, there is also the risk of deleterious ions being dissolved within the water, which can induce several durability risks. These risks could lead to premature deterioration of the concrete or the embedded reinforcing steel, which would necessitate repair or replacement of the system in a timeframe not anticipated by the designers. This would have significant economic and social implications depending on the severity of the deterioration.

An important contribution of this experimental work was demonstrating that simple power law or exponential models for mass transport are insufficient for capturing the actual behavior of mass transport under evaporative flow conditions. More complicated modelling systems, more commonly used for geotechnical applications, were required to accurately validate the experimental observations found within the study. The complex dynamics of evaporation from the 'dry' end of the sample were also very useful in understanding the results from the pressure tension moisture content study, since there were significant experimental difficulties associated with conditioning samples to low moisture contents.

The experimental imaging of 'dry' regions in the MRI study showed that there were significant amounts of water at low moisture contents for all w/c's tested. This higher than expected moisture content in these regions would explain another part of the research program. Specifically, in the pressure tension moisture content study, there was great difficulty in conditioning the samples to very low bulk moisture contents. As was found in this steady state study, even after an entire year of steady state conditions, the samples had not completely dried out. While the boundary conditions are not the same between the wicking action and the 2D drying of the cylinders for the pressure tension moisture content study, there were still wet and dry regions observed on the fracture surface which was analogous to the profiles obtained from the MRI studies.

10.1.2. Suggested future studies

This MRI portion of this research program represents some of the first steps down a promising avenue of experimental research. In the studies performed to date, it was only technically feasible to examine the behavior of ^{1}H nuclei in relatively simple pastes and mortars with a

limited range of gradation. However, one important future study would be to examine concretes with a wider range of aggregate gradations beyond simple mortars, since these systems would have a broader distribution of the interfacial transition zone, which would lead to more complicated mass transport behavior that would be ideally suited to MRI imaging.

Directly imaging the distribution of deleterious ions dissolved within the pore water of concrete undergoing 1D evaporative steady state flow would be another promising avenue of research within this subject area. It was assumed in these studies that there would be deleterious ion penetration associated with the mass transport of the water, even at low moisture contents, but an important next step would be to directly validate these assumptions experimentally. This coupled ion flow study was not performed directly due to the experimental complexities in detecting some of these nuclei in SPRITE, as many have MRI properties that are incompatible with the setup used for these studies. However, it is within the realm of possibility, and there would be great value in directly imaging the penetration of chlorides, sulphates or carbonates under these conditions.

Directly validating the distribution of these penetrating ions to the depth of the reinforcing steel over a length representative of commonly used slab depths in a nondestructive manner would be very illustrative of the actual complexities of coupled moisture-ion flow within concrete conditions. Examining the variations of coupled moisture-ion flow using different cement systems with a variety of W/C, aggregate gradations or admixtures would also be important in validating engineering best practice assumptions to improve the durability and sustainability of concrete.

A third possible future avenue of study using the SPRITE MRI imaging technique would be to look more directly at the mass transport of 1H nuclei in cement systems that have been deliberately cracked. Having cracks running perpendicular to the flow of moisture would allow for a characterization of mass transport across the faces of a crack, and inducing a crack running parallel to the flow direction would give conditions more representative of transport properties in cement systems already affected by ongoing durability issues in the field.

Related to this avenue of study would be examining the transport properties across an interface between two different types of concrete, such as an original deteriorated concrete and a 'patch' concrete that does not have cracks. Having an interface between two different W/C concretes, pastes, or mortars would be another way of looking at this behavior.

In any case, the MRI techniques used for this research program provided very useful information on the distribution of water during mass transport in cement systems that would not have been possible to directly detect using any other experimental technique.

10.2. Surface resistivity

10.2.1. Contributions

The experimental work undertaken to characterize the temperature dependant behavior of surface resistivity readings was very successful. A relatively simple procedure for determining the empirical form of these curves was implemented and carried out over a variety of different W/C and hydration times, which allowed temperature correction factors to be generated during the hydration process.

These types of temperature-dependant hydration curves are very useful for the ongoing evaluation of concrete in field conditions, since variation in temperatures encountered in fieldwork conditions will cause large changes in the surface resistivity readings. These SR-T curves are related but distinct from the commonly used temperature correction that depends upon the activation energy of conduction using the Arrhenius method. One of the issues demonstrated in this portion of the research program was that the assumption of a constant activation energy of conduction is not necessarily valid when considering the evolution of a pore system undergoing hydration. Using this method of correction could lead to large errors due to temperature correction that would not accurately account for the evolution of the true signal.

On the other hand, using SR-T-hydration curves, the temperature-independent surface resistivity measurements can be used to track the changes in the pore structure associated with ongoing hydration. This type of nondestructive testing could be used to monitor new concrete cast in the field, either as a part of new construction or patch repair. The method of generating the SR-T curves was quite simple to implement, and these empirical equations which allow for the temperature correction can be generated directly from the technique without a significant amount of analysis.

The effectiveness of normalizing the temperature dependant signal using the outlined technique was clear when examining the SR data from freeze thaw studies presented elsewhere in the research program. By normalizing the data with respect to temperature, the day-to-day variability in the ongoing freeze thaw deterioration was greatly minimized. Based on this ongoing temperature corrected monitoring with surface resistivity, it was clear that there was serious

deterioration to the connected pore structure occurring as a direct result of the ongoing freeze thaw cycles.

Remarkably, this damage was most prominently detected using surface resistivity, which showed a statistically significant change in the signal after a single freeze-thaw cycle. While the other testing methods also eventually detected this change in pore properties after further freeze thaw cycling, the surface resistivity technique could reliably detect the damage at much earlier stages of deterioration. This durability research demonstrated the power of the surface resistivity test method, especially when the temperature effects are accounted for using temperature correction techniques.

10.2.2. Suggested future studies

The relationship between the SR-T-hydration curves derived using the testing technique outlined in the research program should be further investigated to validate the applicability of using these curves to temperature correct values measured in field conditions, especially those associated with ongoing durability. For example, a study could be performed that casts both slabs and cylinders, with cores drilled from the slabs at a variety of hydration times to determine whether the SR-T-Hydration curves between the two different samples are identical for different casting conditions.

A wider variety of admixtures, aggregates, W/C and cementitious systems should also be validated, with a greater range of hydration times included so that the effect of these parameters on the SR-T-Hydration behavior can be accounted for beyond 90 days of curing. While most engineering practice assumes that most hydration occurs before 28 days of curing, it would be

useful to look at curing times greater than 90 days to experimentally verify that these SR-T-hydration tests could be valid for mature concrete encountered in field conditions and would therefore be applicable in terms of normalizing temperature readings using surface resistivity.

Examining a wider variety of deterioration processes using these SR-T hydration curves, particularly those processes that occur because of ionic species that are electrochemically active, would also be illustrative in terms of characterizing this variable SR-T behavior. Sulphate attack, carbonation, and chloride penetration would all be examples of these types of deleterious ions that would affect the surface resistivity measurement since they involve ionic species within pore water, and accounting for the effect of their presence on SR-T curves would be very useful in terms of normalizing results from concrete affected by these processes.

Finally, a third possible avenue of further study for the surface resistivity temperature corrections would be to examine the effect of variable saturation on this temperature effect. All the testing for the research program outlined were on saturated specimens; however, the environmental conditions present in field are not necessarily the same, so an effort should be made to characterize this behavior for variations in moisture content below full saturation.

10.3. Pressure tension

10.3.1. Contributions

The development and proof testing of the pressure tension device as a destructive test for concrete was a core part of this research program. The multiple innovative improvements made to the machine created testing opportunities that had not previously been possible using earlier iterations of the system. The operation of the machine was upgraded to full automation during

the testing protocol, which reduced a large source of loading rate error that had previously resulted from the manual opening of the pressure inlet valves. This innovation allowed for an operator to set an arbitrary load rate and have the system maintain this rate with a much smaller margin of error than was previously possible. As part of this automation, the system could also compensate for small leakages resulting from the variability of sample quality or damage, which created more opportunities for destructive testing of samples, particularly those that had deteriorated due to durability related issues. Sample conditioning techniques that could address small leaks were also explored and experimentally validated, including the use of low-friction tape that would seal small leaks near the O-rings.

Related to this automation was the novel addition of an automated unloading valve. The inclusion of the unloading valve allowed for a completely automated cyclical loading protocol, which created research opportunities such as a constant magnitude creep loading as well as cyclical loading of the kind involved in fatigue. This innovation was key to allowing the study presented within the research program which represents the first time that a pressure tension machine has been used to detect long term deterioration caused by creep. The possibilities of a short term automated creep testing protocol using an ordinary 100 mm x 200 mm cylinder represents an advancement in potential experimental capabilities for engineers.

The data acquisition for the new pressure tension machine was fully digitized, which made the analysis of the testing information much simpler and less error prone than the previous method of determining the maximum pressure at failure

A further contribution of the research program was the development of standard operating procedures for the test method, which allowed for more repeatability and a faster rate of testing by operators, allowing more tension tests in a smaller amount of time. Included in this standard operating procedure was the development of a standard training protocol that was subsequently used to train multiple operators in the safe and effective use of the machine for research purposes.

10.3.1.1. Creep

The pressure tension test was successfully used to demonstrate the applicability of the test method in the detection of several different durability issues. With the pressure tension test, a tensile creep test was used to demonstrate results that were in line with previously established tension tests. Unique among them was the simplicity and repeatability of the pressure tension tests relative to other existing test methods. Uniquely, the pressure tension creep test does not use a mechanical interface such as clamps to produce the stress in the test specimen, and thus, significant localized stresses found near these interfaces were not present. This demonstration of an accelerated creep test using tabletop laboratory equipment was a notable achievement for the goals of the research program

The pressure tension test produces a stress within the porous structure of concrete, either via direct pressurized gas as is the case with unsaturated specimens or via hydraulically pressurized water. This loading mechanism indirectly applies a stress internally on the solid phase instead of it being transferred mechanically as is the case with mechanical test methods such as compressive strength tests. The unique expansive method of indirect stress application was shown to be very effective at detecting the types of changes associated with expansive

deterioration processes that are associated with the pore structure and transport properties of the concrete.

10.3.1.2. Freeze-thaw

The effect of freeze-thaw damage in ordinary concrete on the pressure tension failure stresses was particularly notable. Firstly, there was a significant drop in the tensile resistance that was detected in the pressure tension test that was not observed in other standard test methods such as compressive strength and splitting tension. Thus, the pressure tension test was shown to have the most sensitivity to this ongoing freeze-thaw damage of all the test methods, even in test specimens which did not exhibit any visual signs of deterioration.

Unique among these destructive test methods was the nature of the failure mechanism in specimens undergoing expansive deterioration processes. In samples with low exposure to these deleterious conditions, the crack propagated through the aggregate, failing both the aggregates and the cement paste at the same time. However, with the more severely deteriorated conditions, a new failure mode was observed that passed through the ITZ, leaving intact aggregates on one side of the fracture with a clearly defined ITZ on the other side, showing that the paste in the ITZ had significantly weakened to the point where the fracture was passing through the ITZ rather than through the stronger aggregate. This observation demonstrated that the pressure tension test was sensitive to these microstructural strength variations caused by deterioration within the pore structure, which was not observed in any of the other destructive tests.

10.3.1.3. Sulphate attack

The pressure tension test could distinguish between the effects of different exposure conditions to sulphate ions undergoing evaporative transport through a slab. In regions of full saturation, the tension strength of the concrete was at its highest, but it was still found to be significantly weaker in the presence of sulphates when compared to the control. In the region of evaporative transport, there was a drop in the tensile strength as compared to the fully immersed specimens, but again, the specimens which were subject to sulphate attack were found to be significantly weaker than the control specimen. It was only for the regions of the slab far from the evaporative flow where no significant differences were detectible using the pressure tension machine. However, this study also demonstrated the significant differences in strength which develop due to differences in the hydration conditions in this type of slab subject to evaporative flow, with the fully saturated regions developing the most strength whereas the drier regions were significantly weaker.

10.3.1.4. Moisture content

The specific effect of different moisture contents within concrete specimens on pressure tension failure results was examined. It was demonstrated that the saturated specimens were significantly higher in tensile capacity than the partially saturated or dried specimens, with the dried specimens having the greatest loss of strength relative to the saturated specimens. There may have been some expansive damage in the oven-dried specimens related to the drying process itself, which would cause expansive stresses in the pore structure due to the phase change of water from a liquid to a gas. However, since this trend of decreasing strength was also

found in specimens which had not been subject to these high heat conditions, there was a significant moisture content effect independent of these additional drying processes.

In addition to this moisture content dependence of the stress failure level, a new failure mode in pressure tension was observed for low moisture content test specimens. Where the saturated and partially saturated specimens failed in a consistent manner with a single tensile crack perpendicular to the loading direction, resulting in two fragments divided by the crack, the dried specimens failed as if a whole portion of the volume failed simultaneously, resulting in many fragments. The existence of this failure mechanism was unexpected, but it offered possible explanations as to the nature of this pressure tension failure-moisture content phenomenon. Based on the results of this moisture content study, it was found that the failure level for the saturated specimens was, on average, the highest. Saturated specimens were used for the other parts of the research program given that this larger magnitude would more conservatively estimate the highest possible material capacity in tension.

10.3.2. Suggested future studies

The pressure tension test method was shown to be very effective at detecting the results of ongoing damage due to deterioration caused by expansive stresses within the connected pore structure of concrete related to its transport properties. A wide array of research opportunities using the pressure tension test are clearly possible based on this formative work.

The first that would look specifically at evaporative transport properties and pressure tension would be to set up destructive test specimens subject to 1D evaporative flow conditions, such as those used in the MRI studies. Then, once a steady-state moisture gradient was established, the

specimens could be tested in pressure tension. It would be very informative to examine the level and mode of failure in pressure tension specimens where there is a clear moisture gradient. The pressure tension specimens will fail at the weakest region, so this type of evaporative flow study would be very useful in characterising the nuances of the moisture content dependant behavior of the pressure tension test.

A study which uses methods other than oven drying to condition the moisture content should be carried out to more fully characterize the moisture content dependant stress behavior in pressure tension. These studies should ideally include tests using a saturating fluid other than water, particularly ones with different viscosity and surface tension properties that would be important to determine the exact mechanisms of this pressure tension-moisture content variable behavior.

Other durability studies should be performed, such as a freeze thaw study that also incorporates air entrainment in order to examine the effectiveness of air entraining at resisting the effects of freeze thaw damage. While this research program was successful at demonstrating the effect of damage on ordinary concrete, the current best practice for concrete in cold-weather conditions involves air entrainment, so evaluating air entrained specimens subject to freeze-thaw damage would be a natural next step.

Other expansive durability issues such as the alkali-silicate reaction would be ideal possibilities for testing in pressure tension. Early age ASR detection would represent a very important step forward in terms of durability research, since the current best practice for ASR testing requires two years to complete. Based on the detection of expansive stresses in freeze-thaw specimens

in this research program, the pressure tension test could possibly detect changes to the pore structure even at low damage levels. This would be very useful for evaluating potential ASR deterioration, especially if there was significant detection at shorter time scales.

The pressure tension test would also be very effective at evaluating the bond strength between different kinds of concrete, such as an original damaged concrete and a patch repair. Having a simple and reliable method of directly evaluating the effectiveness of the bond strength between concretes would be important for creating concrete mixtures that are both effective as a repair material and durable in the long term. This type of test would be applicable to the type of material used in rehabilitation including shotcrete or other fast-curing patch repair materials.

Examining the relationship between pressure tension failure levels on specimens cast into cylinders as well as those resulting from core drilling would be another possible future avenue of research. A study could be done that uses cores drilled from slabs as well as regularly cast cylinders. The cutting process involved in extracting cores might induce some microstructural damage that could be detectable using pressure tension, so it would be important to characterize this behavior for future studies, especially if pressure tension is to be more widely adopted to evaluate the tensile strength of concrete cored from structures in the field.

Finally, further modifications to increase the capabilities of the pressure tension test should be explored. One modification which would allow for real-time stress-strain behavior to be captured would be adding sensitive distance measuring sensors to either end of the pressure tension chamber. Sensors such as lasers that could detect micron-level changes in distance would be sufficient to detect the one-dimensional length changes in the concrete occurring because of the

applied tensile stress. Having two of these lasers focused on the ends of the open face of the test specimen would accurately measure the strain as a function of applied stress in real time, which would allow a direct measurement of a large variety of material properties including the modulus of elasticity. This real-time nondestructive detection of strain would be particularly useful when measuring properties such as fatigue damage under cyclic loading or dimensional changes resulting from creep. This type of modification was not feasible given the current focus of the research program, but it does represent a promising possibility for materials testing.

10.4. Conclusion

This research program was focused on the transport properties of concrete systems and the implications of these properties on the durability of concrete. The newly developed pressure tension test method was very effective in investigations of durability involving these transport properties, and this test has unique features that set it apart from existing standard test methods. The nondestructive test methods, in particular the magnetic resonance imaging studies, could directly image the subtle but important behavior of water in evaporative and sorptivity flow conditions. These observations were shown to have large implications for the durability of concrete in similar types of flow conditions.

Concrete is the most commonly used building material in the world, and this research program has demonstrated that the transport properties of this material have enormous implications for the long-term durability and use of this ubiquitous material. Understanding these properties with the best tools available is a key to the safe and sustainable use of this material into the future.

Master Reference List

Abdel-Magid, B., R. Lopez-Anido, G. Smith, and S. Trofka. "Flexure Creep Properties of E-Glass Reinforced Polymers." Composite Structures 62, no. 3–4 (2003): 247-53.

Al-Kubaisy, M.A., and A.G. Young. "Failure of Concrete under Sustained Tension." Magazine of Concrete Research 27, no. 92 (1975): 171-78.

Altoubat, S.A., and D.A. Lange. "Creep, Shrinkage, and Cracking of Restrained Concrete at Early Age." ACI Materials Journal 98, no. 4 (2001): 323-31.

ASTM. "Standard Test Method for Air Content of Freshly Mixed Concrete by the Pressure Method." West Conshohocken, PA: ASTM International, 2014.

ASTM. "Standard Test Method for Density, Absorption, and Voids in Hardened Concrete." West Conshohocken, PA: ASTM International, 2013.

ASTM. "Standard Test Method for Flexural Strength of Concrete (Using Simple Beam with Center-Point Loading)." West Conshohocken, PA: ASTM International, 2016.

ASTM. "Standard Test Method for Flexural Strength of Concrete (Using Simple Beam with Third-Point Loading)." West Conshohocken, PA: ASTM International, 2016.

ASTM. "Standard Test Method for Resistance of Concrete to Rapid Freezing and Thawing." West Conshohocken, PA: ASTM International, 2015.

ASTM. "Standard Test Method for Slump of Hydraulic-Cement Concrete." West Conshohocken, PA: ASTM International, 2015.

ASTM. "Standard Test Method for Splitting Tensile Strength of Cylindrical Concrete Specimens." West Conshohocken, PA,: ASTM International, 2004.

Balcom, B.J., J.C. Barrita, C. Choi, S.D. Beyea, D.J. Goodyear, and T.W. Bremner. "Single-Point Magnetic Resonance Imaging (MRI) of Cement Based Materials." Materials and Structures 36, no. 3 (2003): 166.

Banthia, N., M. Pigeon, and L. Lachance. "Calorimetric Study of Freezable Water in Cement Paste." Cement and Concrete Research 19, no. 6 (1989): 939-50.

Bažant, Z.P., "Size Effect in Blunt Fracture: Concrete, Rock, Metal." Journal of Engineering Mechanics 110, no. 4 (1984/04/01 1984): 518-35.

Bažant, Z.P., and J.C. Chern. "Concrete Creep at Variable Humidity: Constitutive Law and Mechanism." Materials and Structures 18, no. 1 (1985): 1.

Bažant, Z.P., and L.J. Najjar. "Nonlinear Water Diffusion in Nonsaturated Concrete." Matériaux et Construction 5, no. 1 (1972): 3-20.

Benboudjema, F., F. Meftah, and J.M. Torrenti. "Interaction between Drying, Shrinkage, Creep and Cracking Phenomena in Concrete." Engineering Structures 27, no. 2 (2005): 239-50.

Bentz, D.P., G. Sant, and J. Weiss. "Early-Age Properties of Cement-Based Materials. I: Influence of Cement Fineness." Journal of materials in civil engineering 20, no. 7 (2008): 502-08.

Beyea, S.D., B.J. Balcom, T.W. Bremner, R.L. Armstrong, and P.E. Grattan-Bellew. "Detection of Drying-Induced Microcracking in Cementitious Materials with Space-Resolved 1h Nuclear

Magnetic Resonance Relaxometry." Journal of the American Ceramic Society 86, no. 5 (2003): 800-05.

Beyea, S.D., B.J. Balcom, T.W. Bremner, P.J. Prado, A.R. Cross, R.L. Armstrong, and P.E. Grattan-Bellew. "The Influence of Shrinkage-Cracking on the Drying Behaviour of White Portland Cement Using Single-Point Imaging (SPI)." Solid State Nuclear Magnetic Resonance 13, no. 1–2 (1998): 93-100.

Beyea, S.D., B.J. Balcom, T.W. Bremner, P.J. Prado, D.P. Green, R.L. Armstrong, and P.E. Grattan-Bellew. "Magnetic Resonance Imaging and Moisture Content Profiles of Drying Concrete." Cement and Concrete Research 28, no. 3 (1998): 453-63.

Beyea, S.D., B.J. Balcom, P.J. Prado, A.R. Cross, C.B. Kennedy, R.L. Armstrong, and T.W. Bremner. "Relaxation Time Mapping of Short T*2 Nuclei with Single-Point Imaging (SPI) Methods." Journal of Magnetic Resonance 135, no. 1 (1998): 156-64.

Bissonnette, B., and M. Pigeon. "Tensile Creep at Early Ages of Ordinary, Silica Fume and Fiber Reinforced Concretes." Cement and Concrete Research 25, no. 5 (1995): 1075-85.

Bogdan, M., B.J. Balcom, T.W. Bremner, and R.L. Armstrong. "Single-Point Imaging of Partially Dried, Hydrated White Portland Cement." [In 1064-1858]. Journal of Magnetic Resonance 116, no. 2 (1995).

Bohris, A.J., U. Goerke, P.J. McDonald, M. Mulheron, B. Newling, and B. Le Page. "A Broad Line NMR and MRI Study of Water and Water Transport in Portland Cement Pastes." Magnetic Resonance Imaging 16, no. 5–6 (1998): 455-61.

Bolzan, P. E., and G.A. Huber. "Direct Tension Test Experiments." Strategic Highway Research Program, National Research Council Washington, DC, 1993.

Boyd, A.J., and S. Mindess. "The Effect of Sulfate Attack on the Tensile to Compressive Strength Ratio of Concrete." In Proceedings of Third International Conference on Concrete Under Severe Conditions, 789-96. Vancouver, Canada: ACI/CSCE, 2001.

Boyd, A.J., and S. Mindess. "The Use of Tension Testing to Investigate the Effect of W/C Ratio and Cement Type on the Resistance of Concrete to Sulfate Attack." Cement and Concrete Research 34, no. 3 (2004): 373-77.

Bremner, T.W., A.J. Boyd, T.A. Holm, and S.R. Boyd. "Tensile Testing to Evaluate the Effect of Alkali-Aggregate

Reaction in Concrete." In Proceedings, International Workshop on Alkali-Aggregate Reactions in Concrete, 311-26. Dartmouth, Canada: CANMET/ACI, 1995.

Bridgman, P.W. The Physics of High Pressure. Dover Publications, 1931.

Bu, Y., R. Spragg, and W. Weiss. "Comparison of the Pore Volume in Concrete as Determined Using ASTM C642 and Vacuum Saturation." Advances in Civil Engineering Materials 3, no. 1 (2014): 308-15.

Bürchler, D., B. Elsener, and H. Böhni. "Electrical Resistivity and Dielectric Properties of Hardened Cement Paste and Mortar." Paper presented at the MRS Proceedings, 1995.

Cai, H., and X. Liu. "Freeze-Thaw Durability of Concrete: Ice Formation Process in Pores." Cement and Concrete Research 28, no. 9 (1998): 1281-87.

Cano-Barrita, P.F. de J., B.J. Balcom, T.W. Bremner, M.B. MacMillan, and W.S. Langley. "Moisture Distribution in Drying Ordinary and High Performance Concrete Cured in a Simulated Hot Dry Climate." Materials and Structures 37, no. 8 (2004): 522.

Cantillo, V., and Andrés G. "Fluid-Pressured Test to Measure Tensile Strength of Concrete." Journal of Materials in Civil Engineering 26, no. 4 (2014): 776-80.

Carneiro, F.L.L.B. "A New Method to Determine the Tensile Strength of Concrete. In:" Paper presented at the Proceedings of the 5th meeting of the Brazilian Association for Technical Rules, 1943

Carpenter, T.A., E.S. Davies, C. Hall, L.D. Hall, W.D. Hoff, and M.A. Wilson. "Capillary Water Migration in Rock: Process and Material Properties Examined by NMR Imaging." Materials and Structures 26, no. 5 (1993): 286.

Carpinteri, A., S. Valente, F.P. Zhou, G. Ferrara, and G. Melchiorri. "Tensile and Flexural Creep Rupture Tests on Partially-Damaged Concrete Specimens." Materials and Structures 30, no. 5 (1997): 269-76.

Carrasquillo, P.M., and R.L. Carrasquillo. "Improved Concrete Quality Control Procedures Including Third Point Loading." Center for Transportation Research, The University of Texas at Austin, 1987.

Clayton, N. "Fluid-Pressure Testing of Concrete Cylinders." Magazine of Concrete Research 30, no. 102 (1978): 26-30.

Clayton, N., and F. Grimer. "The Diphase Concept, with Particular Reference to Concrete." Chap. 7 In Developments in Concrete Technology, 283-317. Waterford, UK: Elsevier Science & Technology, 1979.

Crammond, N. "The Occurrence of Thaumasite in Modern Construction – a Review." Cement and Concrete Composites 24, no. 3 (2002/06/01 2002): 393-402.

Cumming, S. "Nondestructive Testing to Monitor Concrete Deterioration Caused by Sulfate Attack'." University of Florida, 2004.

Cumming, S.R., A.J. Boyd, and C.C. Ferraro. "Tensile Strength Prediction in Concrete Using Nondestructive Testing Techniques." Research in Nondestructive Evaluation 17, no. 4 (2006/12/01 2006): 205-22.

Davies, J.D., and D.K. Bose. "Stress Distribution in Splitting Tests." J. Am. Concr. Inst. 65 (1968): 662.

Enjilela, R., P.F. de J. Cano-Barrita, A.J.K. Komar, A.J. Boyd, and B.J. Balcom. "Monitoring Steady State Moisture Distribution During Wick Action in Mortar by Magnetic Resonance Imaging (MRI)." Materials and Structures 50, no. 2 (2017): 151.

Fischer, N., R. Haerdtl, and P.J. McDonald. "Is Colour Change a Good Measure of a Water Penetration Front?". Magazine of Concrete Research 67, no. 19 (2015): 1048-53.

Fournier, B., and M.-A. Bérubé. "Alkali-Aggregate Reaction in Concrete: A Review of Basic Concepts and Engineering Implications." Canadian Journal of Civil Engineering 27, no. 2 (2000): 167-91.

Fraay, A.L.A., J.M. Bijen, and Y.M. de Haan. "The Reaction of Fly Ash in Concrete a Critical Examination." Cement and Concrete Research 19, no. 2 (1989): 235-46.

Fujikake, K., S. Mindess, T. Uno, and H. Xu. "The Nitrogen Gas Tension Test. Part 2: Failure Mechanism." Materials and Structures 44, no. 4 (2011): 865-77.

Gillott, J. E. "Alkali-Aggregate Reactions in Concrete." Engineering Geology 9, no. 4 (1975): 303-26.

Gonnerman, H., and E. Shuman. "Compression, Flexural and Tension Tests of Plain Concrete." ASTM Proceedings 28 (1928): 527-64.

Gowers, K.R., and S.G. Millard. "Measurement of Concrete Resistivity for Assessment of Corrosion." ACI Materials Journal 96, no. 5 (1999).

Grimer, F., and R.E. Hewitt. "The Form of the Stress-Strain Curve of Concrete Interpreted with a Diphase Concept of Material Behavior." 681-91. Building Research Station: Ministry of Public Building and Works, 1968.

Gummerson, R. J., C. Hall, and W. D. Hoff. "Water Movement in Porous Building Materials—Ii. Hydraulic Suction and Sorptivity of Brick and Other Masonry Materials." Building and Environment 15, no. 2 (1980/01/01 1980): 101-08.

Gummerson, R.J., C. Hall, W.D. Hoff, R. Hawkes, G.N. Holland, and W.S. Moore. "Unsaturated Water Flow within Porous Materials Observed by NMR Imaging." Nature 281, no. 5726 (1979): 56-57.

Hall, C. "Water Movement in Porous Building Materials—I. Unsaturated Flow Theory and Its Applications." Building and Environment 12, no. 2 (1977): 117-25.

Hall, C. "Water Sorptivity of Mortars and Concretes: A Review." Magazine of Concrete Research 41, no. 147 (1989): 51-61.

Hall, C., and W.D. Hoff. Water Transport in Brick, Stone and Concrete. Spon Press, London: Routledge, 2002. doi:10.4324/9780203301708.

Hall, C., and T.K.M. Tse. "Water Movement in Porous Building Materials—Vii. The Sorptivity of Mortars." Building and Environment 21, no. 2 (1986): 113-18.

Halperin, W. P., J-Y Jehng, and Y-Q Song. "Application of Spin-Spin Relaxation to Measurement of Surface Area and Pore Size Distributions in a Hydrating Cement Paste." Magnetic Resonance Imaging 12, no. 2 (1994): 169-73.

Hannant, D.J., K.J. Buckley, and J. Croft. "The Effect of Aggregate Size on the Use of the Cylinder Splitting Test as a Measure of Tensile Strength." Matériaux et Construction 6, no. 1 (1973): 15-21.

Hanzic, L., and R. Ilic. "Relationship between Liquid Sorptivity and Capillarity in Concrete." [In English]. Cement and Concrete Research 33, no. 9 (2003): 1385-88.

Hartell, J.A., and A.J. Boyd. "Determining Sulphate Movement in Concrete Exposed to Evaporative Transport." In Proceedings from 9th fib International PhD Symposium in Civil Engineering, 511-16. Karlsruhe, Germany: KIT Scientific Publishing, 2012.

Hartell, J.A., A.J. Boyd, and C.C. Ferraro. "Sulfate Attack on Concrete: Effect of Partial Immersion." Journal of Materials in Civil Engineering 23, no. 5 (2011): 572-79.

Hughes, D.C. "Pore Structure and Permeability of Hardened Cement Paste." Magazine of Concrete Research 37, no. 133 (1985): 227-33.

Julio-Betancourt, G.A., and R.D. Hooton. "Study of the Joule Effect on Rapid Chloride Permeability Values and Evaluation of Related Electrical Properties of Concretes." Cement and Concrete Research 34, no. 6 (2004): 1007-15.

King, D., H. Fict, M. Dip, and M.C.I.M. Chartered. "The Effect of Silica Fume on the Properties of Concrete as Defined in Concrete Society Report 74, Cementitious Materials." In 37th Conference on Our World in Concrete & Structures, 29-31. Singapore, 2012.

Komar, A.J.K. "Investigations into Tensile and Transport Properties of Concrete." McGill University, 2017.

Komar, A.J.K., and A.J. Boyd. "Pressure-Tension Testing in the Evaluation of Freeze-Thaw Deterioration." In Proceedings of the 10th fib International PhD Symposium in Civil Engineering, edited by J. Bastien, N. Rouleau, M. Fiset and M Thomassin. Université Laval, Québec, Canada: International Federation for Structural Concrete, 2014.

Komar, A.J.K., J.A. Hartell, and A.J. Boyd. "Pressure Tension: Reliability for Assessing Concrete Deterioration." In Proceedings of The Seventh International Conference on Concrete under Severe Conditions, edited by Z.J. Li, W. Sun, C.W. Miao, K. Sakai, O.E. Gjørv and N. Banthia, 337-44. Nanjing, China: RILEM Publications, 2013.

Koptyug, I.V. "MRI of Mass Transport in Porous Media: Drying and Sorption Processes." Progress in Nuclear Magnetic Resonance Spectroscopy 65 (2012): 1-65.

Kosmatka, S.H., B. Kerkhoff, W.C. Panarese, N.F. MacLeod, and R.J. McGrath. Design and Control of Concrete Mixtures. Vol. 5420, Ottawa, Ontario, Canada: Cement Association of Canada, 2002.

Kovler, K. "Testing System for Determining the Mechanical Behaviour of Early Age Concrete under Restrained and Free Uniaxial Shrinkage." Materials and Structures 27, no. 6 (1994): 324.

Kumar, Rakesh, and B. Bhattacharjee. "Porosity, Pore Size Distribution and in Situ Strength of Concrete." Cement and Concrete Research 33, no. 1 (2003): 155-64.

Langan, D., and F.K. Garas. "The Failure of Concrete under the Combined Action of High Shearing Forces and Biaxial Restraint." Paper presented at the International Conference of Structure, Solid Mechanics and Engineering Design in Civil Engineering, Southampton, 1969.

Larbi, J.A., A.L.A. Fraay, and J.M.J.M. Bijen. "The Chemistry of the Pore Fluid of Silica Fume-Blended Cement Systems." Cement and Concrete Research 20, no. 4 (1990): 506-16.

Leech, C., D. Lockington, and P. Dux. "Unsaturated Diffusivity Functions for Concrete Derived from NMR Images." Materials and Structures 36, no. 6 (2003): 413.

Li, G. "The Effect of Moisture Content on the Tensile Strength Properties of Concrete." University of Florida, 2003.

Lin, Z., and L. Wood. "Concrete Uniaxial Tensile Strength and Cylinder Splitting Test." Journal of Structural Engineering 129, no. 5 (2003): 692-98.

Lockington, D.A., J.-Y. Parlange, and P. Dux. "Sorptivity and the Estimation of Water Penetration into Unsaturated Concrete." Materials and Structures 32, no. 5 (1999): 342-47.

Lockington, D. A., J.-Y. Parlange, and M. Lenkopane. "Capillary Absorption in Porous Sheets and Surfaces Subject to Evaporation." Transport in Porous Media 68, no. 1 (2007): 29-36.

Lu, Aifei. "Preliminary Assessment of the Base Variables for Standardizing the Pressure Tension Test." McGill University, 2015.

Marchand, J., I. Odler, and J.P. Skalny. Sulfate Attack on Concrete. CRC Press, 2003.

McCarter, W.J., G. Starrs, and T.M. Chrisp. "Electrical Conductivity, Diffusion, and Permeability of Portland Cement-Based Mortars." Cement and Concrete Research 30, no. 9 (2000): 1395-400.

Milton, S. "Evaluation of Various Parameters Affecting the Surface Resistivity Test." edited by A.J. Boyd. Montreal, Quebec: McGill University, 2016.

Mindess, S., J.F. Young, and D. Darwin. Concrete. 2 ed.: Pearson, 2002.

Morris, W., E.I. Moreno, and A.A. Sagüés. "Practical Evaluation of Resistivity of Concrete in Test Cylinders Using a Wenner Array Probe." Cement and Concrete Research 26, no. 12 (1996): 1779-87.

Morsy, M.S. "Effect of Temperature on Electrical Conductivity of Blended Cement Pastes1." Cement and Concrete Research 29, no. 4 (1999): 603-06.

Neville, A.M. "The Confused World of Sulfate Attack on Concrete." Cement and Concrete Research 34, no. 8 (2004): 1275-96.

Neville, A.M. Properties of Concrete. 4 ed. Harlow Essex, England: Longman Group Limited, 1996.

Ngab, A.S., A.H. Nilson, and F.O. Slate. "Shrinkage and Creep of High Strength Concrete." Journal Proceedings 78, no. 4 (1981): 255-61.

Nokken, M.R., A. Boddy, X. Wu, and R.D. Hooton. "Effects of Temperature, Chemical, and Mineral Admixtures on the Electrical Conductivity of Concrete." Journal of ASTM International 5, no. 5 (2008): 1-9.

Nokken, M.R., and R.D. Hooton. "Using Pore Parameters to Estimate Permeability or Conductivity of Concrete." Materials and Structures 41, no. 1 (2007): 1-16.

Ollivier, J.P., J.C. Maso, and B. Bourdette. "Interfacial Transition Zone in Concrete." Advanced Cement Based Materials 2, no. 1 (1995): 30-38.

Østergaard, L., D.A. Lange, S.A. Altoubat, and H. Stang. "Tensile Basic Creep of Early-Age Concrete under Constant Load." Cement and Concrete Research 31, no. 12 (2001): 1895-99.

Petroski, H.J., and R.P. Ojdrovic. "The Concrete Cylinder: Stress Analysis and Failure Modes." International Journal of Fracture 34, no. 4 (1987): 263-79.

Petrov, O.V., G. Ersland, and B.J. Balcom. "T2 Distribution Mapping Profiles with Phase-Encode MRI." Journal of Magnetic Resonance 209, no. 1 (2011): 39-46.

Phillipson, M.C., P.H. Baker, M. Davies, Z. Ye, A. McNaughtan, G.H. Galbraith, and R.C. McLean. "Moisture Measurement in Building Materials: An Overview of Current Methods and New Approaches." Building Services Engineering Research and Technology 28, no. 4 (2007): 303-16.

Plassais, A., M.-P. Pomiès, N. Lequeux, P. Boch, J.-P. Korb, and D. Petit. "Micropore Size Analysis in Hydrated Cement Paste by NMR." Comptes Rendus de l'Académie des Sciences - Series IIC - Chemistry 4, no. 11 (2001): 805-08.

Polder, R.B. "Test Methods for on Site Measurement of Resistivity of Concrete — a Rilem Tc-154 Technical Recommendation." Construction and Building Materials 15, no. 2–3 (2001): 125-31.

Popovics, S. Strength and Related Properties of Concrete: A Quantitative Approach. Wiley, 1998.

Prado, P.J., B.J. Balcom, S.D. Beyea, R.L. Armstrong, and T.W. Bremner. "Concrete Thawing Studied by Single-Point Ramped Imaging." Solid State Nuclear Magnetic Resonance 10, no. 1 (1997): 1-8.

Prado, P.J., B.J. Balcom, S.D. Beyea, R.L. Armstrong, T.W. Bremner, and P.E. Grattan-Bellew. "Concrete/Mortar Water Phase Transition Studied by Single-Point MRI Methods." Magnetic Resonance Imaging 16, no. 5–6 (1998): 521-23.

Prado, P.J., B.J. Balcom, S.D. Beyea, T.W. Bremner, R.L. Armstrong, and P.E. Grattan-Bellew. "Concrete Freeze/Thaw as Studied by Magnetic Resonance Imaging." Cement and Concrete Research 28, no. 2 (1998): 261-70.

Rajabipour, F., and J. Weiss. "Electrical Conductivity of Drying Cement Paste." Mater. Struct. 40 (2007): 1143-60.

Ramezanianpour, A.A., A. Pilvar, M. Mahdikhani, and F. Moodi. "Practical Evaluation of Relationship between Concrete Resistivity, Water Penetration, Rapid Chloride Penetration and Compressive Strength." Construction and Building Materials 25, no. 5 (2011): 2472-79.

Rusch, H. "Researches toward a General Flexural Theory for Structural Concrete." Journal of the American Concrete Institute 57, no. 1 (1960): 1-28.

Safiuddin, M., and N. Hearn. "Comparison of ASTM Saturation Techniques for Measuring the Permeable Porosity of Concrete." Cement and Concrete Research 35, no. 5 (2005): 1008-13.

Safiuddin, M., H.B. Mahmud, and M.Z. Jumaat. "Efficacy of ASTM Saturation Techniques for Measuring the Water Absorption of Concrete." Arabian Journal for Science and Engineering 36, no. 5 (2011): 761.

Said, I., and J.G. MacGregor. "Sustained Load Strength and Short-Term Strain Behavior of High-Strength Concrete." Materials Journal 95, no. 5 (1998): 636-47.

Scrivener, K.L., A.K. Crumbie, and P. Laugesen. "The Interfacial Transition Zone (ITZ) between Cement Paste and Aggregate in Concrete." Interface Science 12, no. 4 (2004): 411-21.

Shang, H.S., Y.P. Song, and L.K. Qin. "Experimental Study on Strength and Deformation of Plain Concrete under Triaxial Compression after Freeze-Thaw Cycles." Building and Environment 43, no. 7 (2008): 1197-204.

Shang, H.S., T.H. Yi, and X.X. Guo. "Study on Strength and Ultrasonic Velocity of Air-Entrained Concrete and Plain Concrete in Cold Environment." Advances in Materials Science and Engineering (2014).

Shank, J.R. "Plastic Flow of Concrete at High Overload." Journal Proceedings 45, no. 2 (1949): 493-98.

Shi, C. "Effect of Mixing Proportions of Concrete on Its Electrical Conductivity and the Rapid Chloride Permeability Test (ASTM C1202 or ASHTO T277) Results." Cement and Concrete Research 34, no. 3 (2004): 537-45.

Shkoukani, H., and J. Walraven. "Sustained Tensile Strength of Concrete." In IABSE reports. Zurich, Switzerland: Swiss Federal Institute of Technology, 1991.

Smadi, M.M., F.O. Slate, and A.H. Nilson. "Shrinkage and Creep of High-, Medium-, and Low-Strength Concretes, Including Overloads." Materials Journal 84, no. 3 (1987): 224-34.

Spragg, R., Y. Bu, K. Snyder, D. Bentz, and J. Weiss. "Electrical Testing of Cement-Based Materials: Role of Testing Techniques, Sample Conditioning, and Accelerated Curing." West Lafayette, Indiana: Indiana Department of Transportation and Purdue University, 2013.

Spragg, R., C. Villani, K. Snyder, D. Bentz, J. Bullard, and J. Weiss. "Factors That Influence Electrical Resistivity Measurements in Cementitious Systems." Transportation Research Record: Journal of the Transportation Research Board, no. 2342 (2013): 90-98.

Stanish, K.D., R.D. Hooton, and M.D.A. Thomas. Testing the Chloride Penetration Resistance of Concrete: A Literature Review. Department of Civil Engineering, University of Toronto, Toronto, Ontario, Canada, 2000.

Stockl, S. "Strength of Concrete under Uniaxial Sustained Loading." Special Publication 34 (1972): 313-26.

Surendra, P.S., and C. Sushil. "Fracture of Concrete Subjected to Cyclic and Sustained Loading." Journal Proceedings 67, no. 10 (1970): 816-27.

Terzaghi, K., R.B. Peck, and G. Mesri. Soil Mechanics in Engineering Practice. 3rd ed. New York: Wiley, 1996.

Tumidajski, P.J. "Electrical Conductivity of Portland Cement Mortars." Cement and Concrete Research 26, no. 4 (1996): 529-34.

Tumidajski, P.J., A.S. Schumacher, S. Perron, P. Gu, and J.J. Beaudoin. "On the Relationship between Porosity and Electrical Resistivity in Cementitious Systems." Cem. Concr. Res. 26 (1996): 539.

Uno, T., K. Fujikake, S. Mindess, and H. Xu. "The Nitrogen Gas Tension Test of Concrete. Part 1: Effect of Boundary Conditions and Axial Strain Response." Materials and Structures 44, no. 4 (2011): 857-64.

Vivas, E., A. J. Boyd, H.R. Hamilton III, and M. Bergin. "Permeability of Concrete—Comparison of Conductivity and Diffusion Methods." FDOT, 2007.

Walter, H.P. "Factors Influencing Concrete Strength." Journal Proceedings 47, no. 2 (1951).

Wei, X., and L. Xiao. "Electrical Resistivity Monitoring and Characterisation of Early Age Concrete." Magazine of Concrete Research 65, no. 10 (2013): 600-07.

Weiss, J., K. Snyder, J. Bullard, and D. Bentz. "Using a Saturation Function to Interpret the Electrical Properties of Partially Saturated Concrete." Journal of Materials in Civil Engineering 25, no. 8 (2013): 1097-106.

Whittington, H.W., J. McCarter, and M.C. Forde. "The Conduction of Electricity through Concrete." Magazine of Concrete Research 33, no. 114 (1981): 48-60.

Winslow, D., and Di. Liu. "The Pore Structure of Paste in Concrete." Cement and Concrete Research 20, no. 2 (1990): 227-35.

Young, J.J., T.W. Bremner, M.D.A. Thomas, and B.J. Balcom. "Porous Materials." In NMR Imaging in Chemical Engineering, 285-303: Wiley-VCH Verlag GmbH & Co. KGaA, 2006.

Yu, X.T., Gao P., X. Wang, and Y.D. Liao. "The Properties of Cementitious Materials in Prolonged Curing " In Proceedings of the International Conference on Advanced Materials and Engineering Structural Technology (ICAMEST 2015), edited by Jong Wan Hu, 47–50. Qingdao, China, 2015.

Zaccardi, Y.A.V., J. Fullea García, P. Huélamo, and A.A. Di Maio. "Influence of Temperature and Humidity on Portland Cement Mortar Resistivity Monitored with Inner Sensors." Materials and corrosion 60, no. 4 (2009): 294-99.

Zi, G., H. Oh, and S.-K. Park. "A Novel Indirect Tensile Test Method to Measure the Biaxial Tensile Strength of Concretes and Other Quasibrittle Materials." Cement and Concrete Research 38, no. 6 (2008): 751-56.

Appendix A: Pressure Tension Specification Manual

The following is a summary of the specific pieces of equipment that comprise the Pressure Tension machine, with photos and links to the manufacturers website if available. There will be a brief description of the purpose of each component, in case the exact part is not available so a suitable replacement could be substituted.

1.1. Operating principle

The pressure tension machine (hereafter referred to as PT) operates on a simple principle of regulating the flow of compressed air into the concrete testing chamber to control the effective tension force the test specimen experiences up to failure. The following figure outlines the basic components of PT, as well as the basic relationships between the components in terms of controlled signals, electrical power, and air flow.

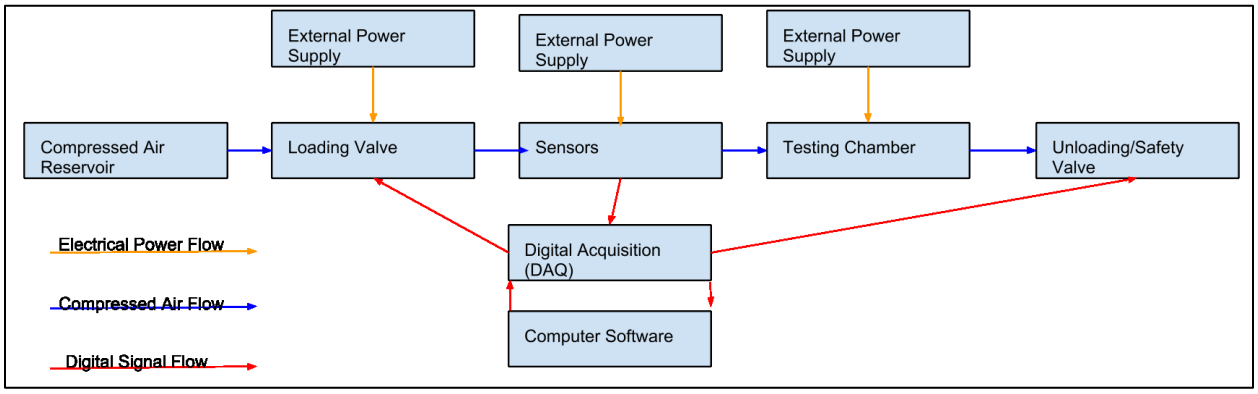

Figure 1- Schematic overview

1.2. Compressed air system

1.2.1. Air compressor

The pressure tension system uses ordinary atmospheric gasses which have been compressed as the basis of the pressure loading medium. This innovation sets it apart from previous configurations of this machine, which required dedicated nitrogen gas canisters that had to be replaced as they were discharged. To compress the gas, a commercially available air compressor ordinarily used for SCUBA tanks was repurposed for this application. There are two safety valves on the air compressor which must be closed before the air compressor will begin to pressurize the gas in the system.

The air compressor can be run during the operation of the system for testing purposes, so there is no downtime that would take the testing machine out of operation during a switching-out of tanks. This allows for long-term continuous testing to be performed such as creep studies that requires volumes of compressed gas beyond what the system configuration could nominally provide.

1.2.2. Compressed air reservoir

The compressed air reservoir consists of a compressed air tank which is connected via ¼" tubing to an electric air compressor. A regular SCUBA tank with a 3 L liquid capacity which has a nominal operating pressure of 2500 PSI (17 MPa) is of a sufficient volume and capacity for the operation of the PT machine.

There is a regulator on top of the tank which allows for a manual shutoff of the flow of air from the tank to prevent any leakages from the air system when it is not in operation. This regulator connects to a T junction between the tank, compressor and PT valves downstream.

1.3. Loading system

1.3.1. Blowout valve

Downstream from the reservoir is a safety blowout valve which vents to the atmosphere if the line pressure ever exceeds 13.7 MPa (2500 PSI). This has been installed to ensure that the sensitive valves downstream of the blowout valve will not be damaged by line pressures exceeding this threshold. Thus, the maximum possible tensile stress which the system can create corresponds to this value, and it would not be possible to test concrete specimens with tensile stresses higher then this threshold. The location of the blowout valve is found in Figure 2. The specific brand of blowout valve is a Kunkle Valve, Model number 0030-A01-KM, for a ¼" line and a blowout pressure of 2500 PSI (17 MPa).

Figure 2- Detail on the T-Junction including the tank regulator, quick connects, adaptor tubing and 17 MPa emergency blowout valve

1.3.2. ¼ turn safety valve

Downstream of the blowout valve along ¼" tubing is a manually operated ¼ turn valve off of a T-junction, connected to the tank via quick disconnect connections. Figure 3 shows this manual valve and the downstream line connection with the regulator valve.

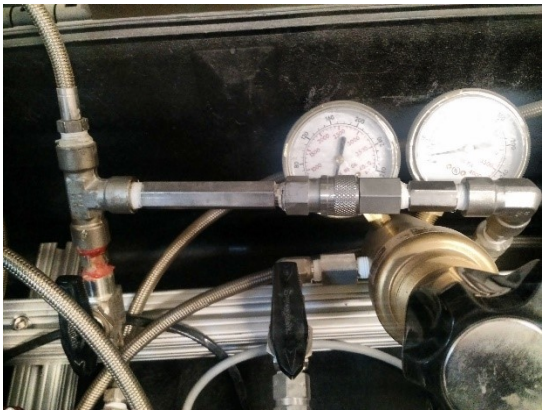

Figure 3- Manual ¼ valve and regulating valve to control the maximum pressure levels in the pressure tension machine

This ¼ turn valve in Figure 3 (the one on the left side of the figure) allows for a direct discharge of pressure into the atmosphere from the system that is independent of any other control mechanisms. This valve can be opened to immediately drain the tank of pressure if necessary.

1.3.3. Regulator valve

Downstream from this manual safety outlet is the regulator valve, shown in Figure 4, which allows an operator to manually set the "upstream pressure" at which the system will operate.

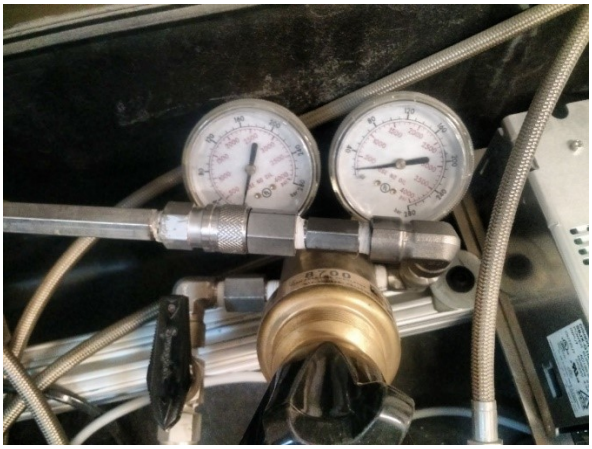

Figure 4-Regulator valve. The gauge on the right corresponds to the indicator that represents the current pressure of the compressed air within the tank. The gauge on the right indicates the

set point of the pressure tension machine and can be changed by rotating the dial on the regulator valve

The magnitude of the compressed air flow into the PT machine is directly proportional to this set point of the regulator valve, so in practice this set point should be set as close to the maximum failure pressure of the specimen as is possible. If this maximum anticipated pressure is unknown, a higher pressure may be used and the set point reset after the stress level sufficient to cause failure is ascertained. If the set point is below the tensile strength of the specimen, the test will not work correctly as the specimen will not fail in this configuration.

In addition, the pressure in the tank (the right golden-coloured gauge in Figure 4) should always be at a pressure higher than the regulating pressure, so that the pressure head is always constant while the automated system is operating. If the tank pressure is below the set point of the regulator valve, the maximum pressure of the system (and thus, the maximum stress on the specimen) will only be equal to the tank pressure, which will result in a system control that is more variable than designed for.

1.3.4. Downstream cut-off valves

Immediately downstream is a line cut-off valve that can be seen in Figure 4, which is another manually operated quarter turn valve. This valve can be opened and closed manually to control the flow of pressure into the system. In practice, this valve is closed whenever the system is not in use, which prevents any accidental pressure buildup downstream of the ¼ turn valve. In addition to this ¼ turn valve, there is redundant independently operated solenoid valve that performs the identical function as this ¼ turn valve. The solenoid valve, which is controlled via the safety interlock system, will shut off the flow of air automatically if the emergency stop

button is pressed, the safety circuits are otherwise disrupted or if there is a power loss to the system that would result in an uncontrolled flow of gas into the PT machine.

1.3.5. Flow regulating valve

Downstream from these two line-cut-off valves is a needle-tip valve which is used to manually restrict the flow rate of air through the line into the pressure chamber. Figure 5 shows the location of this valve on the line. This needle-tip valve is very important for the operation of the system, as an unrestricted flow through the pressure line results in rates of pressure change that are very difficult to control. In practice, this needle-tip vale will decrease the rate of flow into the system sufficiently to allow for a precise computer control. In practice, this needle-tip valve is set to be almost completely closed, with only a tiny fraction of the possible air flow being allowed into the rest of the system. If very high rates of loading, like impact loadings, are required, this needle-tip valve could be turned open, but this is not advised since a finer load rate control will not be possible in this configuration.

Figure 5- (left) solenoid cut-off valve and needle-tip valve. The automated actuator is the red box at the bottom, which operates a needle-tip valve that controls the flow rate into the PT machine

1.3.6. Automated needle valve and actuator

Figure 5 also shows the location of the computer controlled actuated needle valve, which is the primary method of automatically controlling the flow of compressed air through the system via computer input. The red box in Figure 5 is a prebuilt actuator valve system prepared by Hanbay Laboratory Automation, which consists of an MCJ 050AB multiturn actuator which controls a needle valve. The actuator is controlled via a digital acquisition (DAQ) output signal that is connected to a laptop computer with a USB cable. The actuator is capable of accepting signals of both 4-20 mA and 1-5 V, but our system uses the 1-5 V configuration.

The needle-tip valve that is used for the fine control of the pressure loading is identical to the manual needle-tip valve used to restrict the bulk flow into the system. The valve in use is an SS-1RS4 which was prepared by Hanbay and was shipped with the actuator box as a single unit. The specific valve was chosen for its turn-flow response being high, which is integral to the proper control of the flow into the system. A system response that is slow will result in an error in the

time it takes to open/close the valve, and thus the error between the desired pressure and the controlled pressure will increase. Thus, the rate of loading would not be properly automated.

The actuator requires a 12-24 volt DC power source to operate which can be seen in Figure 6. The actuators can be configured for a variety of valve turn times and torque, which result in different rate responses possible at different power levels and torque settings. The system configuration found to be optimal uses the highest possible turn rate setting to minimize the overall turning time of the valve, resulting in an optimal rate control response of the system. The computer signal is provided via one of the output channels in the DAQ system

Figure 6- 12 V DC power supplies. Each actuator runs on an independent supply, and the third unit supplies power for sensors

1.3.7. Pressure sensors

Immediately downstream from the actuator valve is a battery powered pressure sensor on the line to measure the magnitude of the line pressure. This pressure sensor can be seen in Figure 5 as the blue circular object in the center of the image. This sensor is included in case of power

failures to verify the safe discharge of pressure from the line, independent from the other electronic systems. This pressure sensor is also used to independently calibrate the digital pressure transducers used for the automatic measurement system.

A second digital pressure sensor is immediately downstream from the first digital sensor. This sensor is used to measure the pressure in the line and therefore the chamber. This digital signal is transmitted to the computer via DAQ. This sensor requires connection to one of the DC power supplies seen in figure 6 to function properly. The sensor outputs a 4-20 mA current signal that is read as an input in the DAQ which corresponds to a pressure range of between 0 and 34 MPa, or 0-5000 PSI. The software that runs the pressure tension machine requires a calibration of this digital signal to give accurate results. The software that runs the pressure tension machine takes 10 samples per second of this raw signal. Small amounts of electromagnetic interference from ambient conditions create a small error in this signal on the order of ± 0.05MPa (7 PSI). To adjust for this small error, the pressure tension software uses a running average of the last 10 samples (1 second) to provide an average pressure in the system at any given time.

Note that there will be a very small lag in the measured pressure at the gauge relative to the pressure within the chamber, since these two locations are not concurrent. The velocity of this flow is on the order of 10 m/s, and the distance between the gauge and the pressure chamber is considerably smaller than this, so this small lag error is considered negligible.

1.3.8. Pressure safety switch

At the same location as the digital pressure transducer, we have an independent pressure sensor which is activated at any pressures above 0.3MPa (50 PSI). This sensor, when activated by a

pressure greater than 0.3 MPa, engages the locking mechanism for the door unit, which automatically prevents this safety cover from being opened whenever there is any pressure within the system. The only way to disengage this lock is to completely discharge all the pressure from the system, which will cause this safety switch to deactivate.

1.3.9. DAQ

All the digital signals (for both input and output) are controlled via a National Instruments USB 6008 Digital Acquisition device, that hooks into a regular USB 2.0 port on a computer. In practice, an analog channel accepts the pressure transistor input of 4-20 mA, and two analog outputs are used to control the two actuators, with signals of 1-5 V outputted from the DAQ. The power signals for the DAQ are provided by through the USB connection, so no external power source is needed besides the laptop.

1.4. Testing chamber

1.4.1. Connections

The testing chamber is a custom fabricated piece of equipment that consists of the central steel cylindrical test chamber attached to the steel frame by way of a base plate. The central chamber is connected to the airflow line through a quick-release ¼" line connectors to allow for easy transportation of the chamber and frame. The chamber, both with and without a cylinder inside can be found in Figure 7. Figure 8 shows a cross section of the chamber with a sample inside.

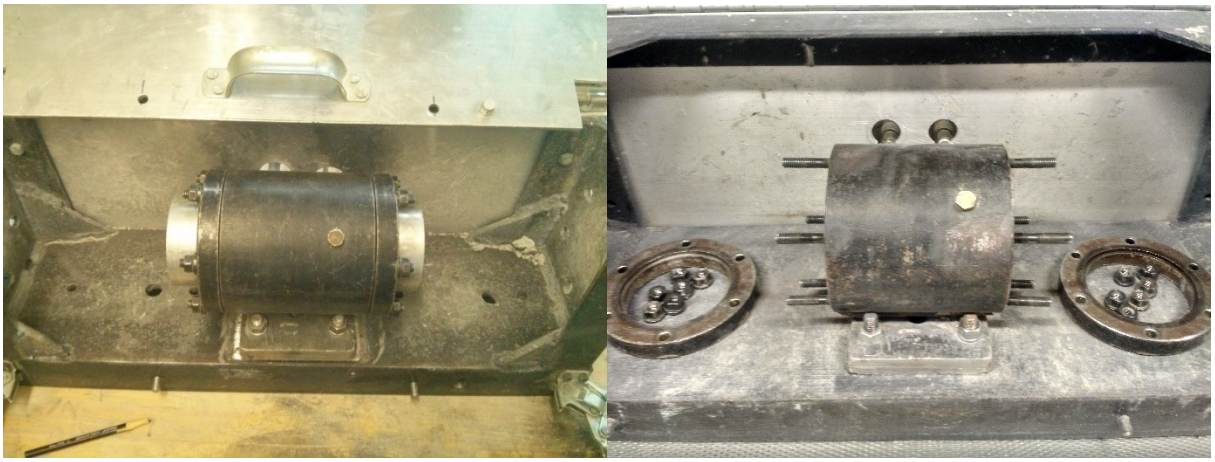

Figure 7- A) Pressure tension chamber loaded with simulated concrete cylinder B) chamber without sample. The two confinement rings, O-rings and the nuts and bolts to provide the sealing found in figure 7B.

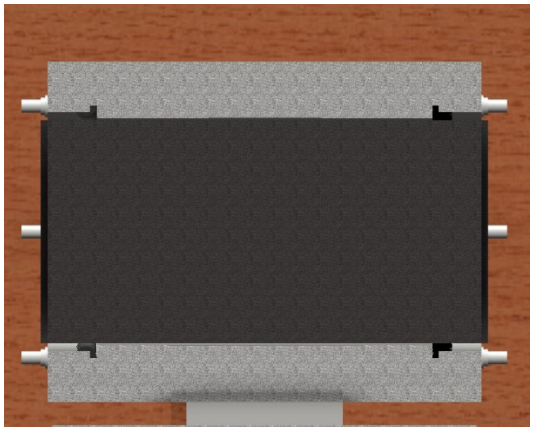

Figure 8- Cross section of pressure tension chamber with sample inside

1.4.2. Confining rings

The testing chamber itself consists of a hollow cylindrical tube that allows for a 100 mm x 200 mm concrete cylinder to be placed inside. Two hollow sealing rings with an interior corner bevel connect to this central chamber by tightening 6 hexagonal nuts onto threaded bolts. The order of torqueing these six nuts is an important factor in terms of providing a good seal in the pressure chamber. In practice, nuts on opposite sides of the chamber should be tightened sequentially so

that the pressure on the O-rings is symmetrical, and the ring remains parallel to the chamber. The exact torque on the confining ring should be sufficient to press the O-ring firmly onto the surface of the concrete cylinder. Tightening the bottom nut at the start of the tightening procedure will cause this compression of the O-ring to raise the whole sample up so it is not in physical contact with the bottom of the chamber, allowing a uniform pressure to develop around the whole cylinder during the testing.

1.4.3. O-rings

The seal between the test chamber and the atmosphere is provided by O-rings that have a compatible inner diameter with the sealing rings. The O-rings found to be effective are commercially available Buna O-rings with an interior diameter of 100 mm and a thickness greater than 5 mm. For samples with greater surface defects, the thicker O-rings provide a better seal. The O-rings are placed on the cylindrical surface of the concrete specimen and the hollow rings are then fitted and tightened via the bolts, which provides the seal for the gas. The torque should be sufficient to provide compression on the whole O-ring symmetrically. A large cause of leaks during testing procedures is an unsymmetrical configuration of the O-rings, so care should be taken on the operator's part to minimise this possible cause of leakage.

In the case of samples with extensive defects such as air bubbles which are concurrent with the location of the O-rings on the surface of the sample, a procedure to provide a seal has been developed after extensive experimentation. A high tensile strength tape with low surface friction characteristics, like a PVC or PTFE tape, can be wrapped in at least 2 layers at either end of the sample. Care is required to ensure that there are no air channels that develop between the tape and the concrete cylinder, and at least two layers are required so the tape can adhere to itself.

1.4.4. Testing chamber frame

To take the considerable force of impact from concrete fragments resulting from a successful test, the entire testing chamber is housed in a frame consisting of high-strength steel channels. Four triangular connecting plates are welded to these C-channels and the baseplate to provide additional shear connections between the impact plates and the base of the frame. The impact loading demand is extreme for this piece of equipment, particularly in terms of shear and repetitive fatigue damage from repeated use, so the design of this frame and baseplate was particularly conservative. The chamber itself is welded to a 1/2" thick baseplate which is bolted and welded to the steel frame to keep it in place.

The three other sides of the frame are sealed off with aluminum plates which form a retractable lid that has been attached to the base frame by means of threaded screws and washers. This lid prevents any debris from impacting areas other than the interior of the protective frame. The cover is integral to protect from any potential flying debris resulting from the test. There are two holes drilled in the front cover which correspond to the two studs in the steel frame, which act to prevent vertical movement during the impact events associated with the test. In addition, two clamps are attached via screws to the frame to provide further frictional sealing of the safety cover to the baseplate during the operation of the test.

1.4.5. Safety interlock system

The aluminum lid has a safety lock key on the side of it which interfaces with a locking mechanism on the baseplate, as seen in Figure 9. When the key is secured within the interlock mechanism, an operator must press the yellow button in Figure 9a to free the key and lid to access the test chamber. This yellow button must be depressed while the system is disarmed and when there is

power running through the system. If the system is armed for testing, or if there is no power, or if the operator attempts to open the lid without pressing this button, the lid is held in place with a sufficient force that prevents access to the chamber. This safety lockout is also connected to the 0.3 MPa safety pressure sensor by the chamber, which renders it effectively impossible to access the pressure chamber if there is any pressure buildup within the system.

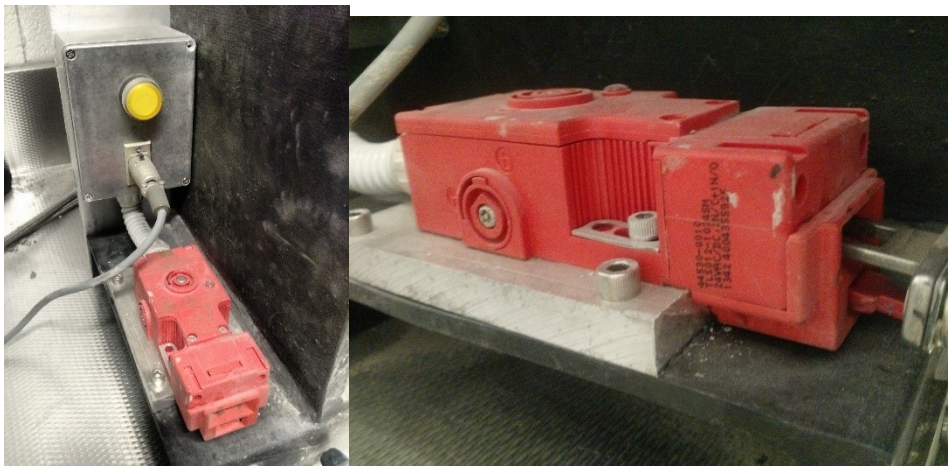

Figure 9- A) Safety interlock switch system and open button B) detail of safety lock key from lid

1.5. Unloading system

The line leading from the testing chamber to the exit valve is also attached to the testing chamber by way of a ¼" quick release connection. The 1/4" line is connected to two safety valves that will vent the pressure in the system, as well as the second controlled actuated unloading valve. The actuated unloading valve is identical to the loading valve, (Hanbay Laboratory Automation, which consists of an MCJ 050AB multiturn actuator with a Swagelok SS-1RS4needle valve). The valve is connected to the exit line by a T-junction, as seen in Figure 10. Like the loading valve, the actuator requires a 12-24 DC power source to operate.

Figure 10- Unloading system. Clockwise from upper left is the computer controlled actuator (red box), the quick disconnect, a ¼ turn valve for manual venting, and the solenoid valve (lower left) which opens the pressure line when the system is not armed

There are two safety valves which vent the pressure in the system, and ensure that no pressure buildup is possible during situations when the pressure chamber is accessible. The first is a manually operated ¼ turn valve that is controlled by the operator. Whenever the machine is not in use, this safety valve is kept open to ensure that no pressure can possibly build up within the testing chamber at any time. This valve is also integral in the case that electrical power is lost during a test and the system must be vented without computer input. This venting in the case of an electrical short is redundantly performed by the solenoid valve.

The second is a solenoid valve connected to the emergency stop button switch. It is an "active closed" valve, which means that the circuit between the power source must be complete for the valve to closed, which allows for a pressure buildup within the system. When the safety override button is activated, I.E. the key has been turned so that the system is not "locked out", this will activate both the active closed solenoid valve to prevent the system from venting pressure, as well as the other solenoid valve on the upstream line which will allow compressed air the system

in the first place. In the case of a power loss, this redundant safety system will automatically vent any pressure in the system as well as prevent the tank from discharging any extra gas. In practice, all the valves and safety systems must be properly configured and activated for the pressure tension test to be performed.

1.6. Safety systems

The pressure tension machine has several redundant safety systems in place. They can be summarized as follows

1.6.1. Redundant safety circuit

1.6.1.1. Emergency stop button

There is a master safety system that runs on a circuit independent from the manual or computer controlled systems, as seen in Figure 11. This system consists of a red 'emergency stop' button that can be down or up. When this emergency stop is down, the machine will not be able to build up pressure. The button must be twisted to allow it to move to the 'up' position. When the emergency stop button is up, the system is primed to be armed.

Figure 11- Emergency stop system. Red button is the emergency stop, which can be depressed or opened. At bottom is the green 'arming' button, which must be pressed while the emergency stop button is in the open configuration

1.6.1.2. Arming button

To arm the machine, which will allow pressure tension tests to be performed, both the emergency stop button must be in the up position, and the green button must be depressed. Depressing the green button will toggle the two solenoid valves into a configuration that will allow pressure to build up in the system.

The system cannot be armed in this manner if the key secured on the pressure chamber frame is not secure within its interlock box, I.E. when the lid to the testing frame is open. This ensures that the test can never be performed when the lid to the chamber is open. This emergency stop system also requires power to function properly. Any loss of power will cause the system to automatically disarm and discharge any pressure currently within the system.

1.6.1.3. Emergency safety valves

The green arming button is connected to the two solenoid valves on the pressure line, the upstream one being a "live open" and the downstream one being a "live closed". When the emergency stop button is depressed, the two valves will toggle into their deactivated positions, with the upstream one closing the system off from any air flow through the line, and the downstream one opening to allow any pressure within the system to be safely vented to the atmosphere. This 'disarmed' condition will remain the condition unless the proper procedure is followed to arm the system again. When the system is armed in this manner, the two solenoid valves will toggle to their respective live positions, where the upstream one allows pressure to

flow into the machine, and the downstream one being closed to allow pressure to build up. In the absence of power, the two solenoids will toggle to their disarmed positions.

1.6.1.4. Frame lid locking mechanism

Access to the testing chamber is moderated by the frame's lid locking mechanism. To disengage the lid from the secure interlock when it is closed, three conditions must be met. The first is that the power must be on and properly connected to the frame locking mechanism. The second is that the emergency stop button must be in the 'disarmed' position. The third is that the 'release' button must be depressed at the same time the lid is being pulled from the lock. If any one of these conditions is not satisfied, the lid will remain securely in place due to the interlock.

The emergency stop button is connected to the automatic door locking mechanism, which has two effects. The first effect is that it is impossible to operate the system if the safety door cover is not properly mounted within its lock. The second is that this door lock is impossible to disengage if the pressure sensor is reading any pressure above 50 PSI, preventing improper usage.

1.6.2. Computer controlled safety system

1.6.2.1. Automated load detection shutoff

The software that runs the pressure tension machine has several automated safety features built in. If the error between the theoretical signal and the measured signal from the pressure transducer exceeds 1 MPa, the computer controlled actuator valves will automatically close to prevent further air from entering the system. If this error grater than 1 MPa persists for 10 seconds, the system will automatically turn itself off. This feature is primarily designed to stop tests which have a rate of leakage that exceeds nominal parameters. This error shutoff feature

will also terminate the operation of the program after a tensile failure, since the measured pressure will drop to 0 while the load rate would not change. This will ensure that the actuated valves are shut after every successful test.

1.6.2.2. Manual override switch

An 'emergency close' button is prominently displayed on the user interface which override the automated signals to the actuators. When shut, the signal to the actuators will be set so they will close. In some cases, this emergency close override button can be quickly toggled to reset the actuated valves which may become stuck during the operation. When the valves are closed in this manner, the pressure in the system will not change due to the operation of the valves.

1.6.3. Manually operated ¼ turn valves

The pressure line has three manually operated ¼ turn valves installed which allow the operator to directly control the pressure within the system independently from any electronic or computer control.

1.6.3.1. Upstream discharge valve

The first ¼ turn valve is upstream of the regulator valve on this system. This valve will seal or discharge the pressure directly from the compressed air tank, upstream of any of the pressure tension control systems. After testing and after the valve on the tank has been shut to prevent further compressed discharge from the tank, this valve can be opened to vent any compressed gas in the line between the tank and the regulator valve. This valve must be closed for the test to operate. In addition, on the venting block there is another ¼ turn ball valve which allows the operator to manually discharge the pressurized line into the atmosphere.

1.6.3.2. Upstream cut-off valve

The second of the ¼ turn valves is directly below the regulator valve. When this valve is open, it allows the flow of compressed gas into the pressure tension machine. When closed, it will cut off any flow in between the tank and the rest of the pressure tension machine. This valve should be manually closed in conjunction with the first valve whenever the system is not armed for testing, as it will prevent any pressure loss from the tank into the atmosphere. If, for whatever reason, a test is unsuccessful, this valve should be closed to prevent any further pressurization of the chamber through the line.

1.6.3.3. Downstream discharge valve

This third ¼ turn valve is on the unloading system. When in the open configuration, the valve will discharge any pressure buildup directly into the atmosphere. This valve should be nominally open whenever the system is not armed for testing a specimen. After any test, this valve should be manually opened to ensure that there is no pressure buildup within the machine. When closed, this valve will allow for the buildup of pressure within the machine.

1.6.4. Maximum pressure blowout valve

A 2500 PSI blowout valve is installed adjacent to the compressed air tank. This valve will open automatically if the pressure in the line ever exceeds 2500 PSI or 13.7 MPa, which is the maximum pressure the system is designed to operate at. This blowout valve will ensure that the system can never be pressurized beyond this maximum level during the recharging of the air tank by the air compressor.

1.7. Software

The software used to control the testing procedure was created using National Instruments LabView software.

1.7.1. Operation input parameters

The whole system runs on a continuous control loop, with each control iteration and collected data point representing 1/10th of a second. The basic control parameters are inputted before the test begins, but they can also be changed during a run. The software can be configured to produce a monotonously increasing constant rate of stress in the form of a triangle wave, as well as a sinusoidal loading pattern for cyclic loading conditions. If the load rate is set to be zero, the system will maintain a constant pressure at an arbitrary stress level. This is the configuration used for long term constant duration studies such as creep. The maximum stress level and the loading rate are available as inputs in both metric and imperial units. There is a toggle to allow the operator to switch between either unit, and stress outputs are available in both unit schemes.

In practice, the loading rate should be set comparable to other destructive test methods, although a very wide range is available using the equipment. The common practice is to set the load rate at 0.05 MPa/second, or roughly 7 PSI/second. The maximum stress level should be set below the set point on the regulator valve, so that the software does not attempt to control the stress above a level which will be provided by the regulator valve.

A manual close valve override switch can be depressed on the control interface, which will close both computer controlled valves, disallowing any further control processes from the computer system.

1.7.2. Control loop

During each iteration of the software running, the sensor input is provided by the pressure transducer adjacent to the pressure chamber on the loading line. The pressure reading is then compared to the "theoretical" pressure, determined from the control inputs the user sets at the beginning of the trial. If the measured pressure is below the theoretical pressure, the system will attempt to compensate for this error by opening the actuated loading valve via an increase of this signal through the DAQ. If the measured signal is above the theoretical pressure, the system will attempt to compensate for this error by opening the unloading valve via an increase of the signal to the unloading valve actuator, thus venting excess gas to the atmosphere. The exact magnitude of this turning signal is directly proportional to the overall measured error.

For each $1/10^{th}$ of a second the test is running, the computer will decide whether to open the loading or unloading valves, and by exactly how much to adjust the turn of the valves by. Through this iterative process a great degree of loading control can be achieved.

There are fundamental limits to the signal response, since it takes a finite amount of time to open or close the valves via the actuators. This makes precise controlled loading rates beyond about 0.2 MPa/second infeasible. Beyond these limits, the system begins to resemble a staircase in terms of the pressure-time response. The computer will attempt to open the valves very quickly, but due to the comparatively long response of the actuators turning, they will effectively allow a large magnitude of pressure in the system at a high rate, only to immediately close, resulting in a constant pressure level until the error becomes sufficiently small to open the valves again, again allowing this stress to build up at a high rate.

1.7.3. Error detection

If the error between the input signal and the controlled rate ever reaches more than 1 MPa, the system will automatically close the loading valve to stop any uncontrolled system responses. Similarly, whenever the sample fails and there is a large pressure drop, the system will automatically close the valves to prevent further leakage out of the pressure tank. After 10 seconds of an error of this magnitude, the system will turn itself off.

1.7.4. Output

Both the loading rate and the system response update in real time while the system is running, with the red line representing the specified loading protocol, and the black line representing the system response as measured by the pressure transducer. This data can be directly exported an excel file. These excel files contain both the applied loading signal as well as the system response from the pressure transducers.

1.8. Operation

The exact test protocol involved in a pressure tension test is found below. Please note that the system requires training to be operated per standards.

1. **Sample Preparation**. The 4”x 8” (100 mm x 200 mm) concrete cylinders should be saturated, or as close to the saturation point as can reasonably be achieved. The curved surface of the cylinder, particularly in the region where the O-rings are located, should be free of defects and flaws that may cause the loss of the pressure seal. If these defects are too numerous, low friction tape can be applied in these regions to bridge these voids. At least two layers of tape should be applied on either side of the specimen in this manner, with care being taken to ensure there are no pathways for air to escape under the tape.

2. **Air system configuration**. Close the upstream discharge valve, upstream cut off valve, and open the downstream discharge valve. Open the compressed air tank regulator to charge the upstream part of the machine. Make sure that the tank pressure as read from the regulator valve is above the maximum pressure of the regulator valve. If the regulating pressure and the tank pressure are at the same level, recharge the pressure in the air tank via the air compressor attached to the system.
3. **Placing the sample into the pressure chamber.** The sample should be placed in the pressure chamber so that its midpoint is concurrent with the midpoint of the pressure chamber. There should be an equal amount of the sample hanging out of either end of the chamber. Make sure the surface in the region where the O-rings will sit is free of flaws and defects. Small adjustments can be made in the position of the sample within the chamber that will ensure the O-rings will not coincide with voids that can cause leaks. If voids are unavoidable, wrap the specimen with tape as specified in step 1.
4. **Placing the O-rings.** The two O-rings should be slipped on the sample and placed in a manner that they are bearing directly on the surface of the pressure chamber. Please note that these O-rings shouldn't be "rolled" into place, as this rolling can induce stresses in the O-ring which could lead to a loss of sealant at higher pressure. Ensure that the interface between the O-ring and the concrete surface is free of defects which could lead to a loss of pressure, this will be a critical step in determining whether the seal will hold throughout the test.
5. **Place the pressure rings on the sample.** The two bearing confining rings will slide overtop the concrete cylinder to be as close to the chamber as possible. Each pressure ring has a filet

groove which will accommodate the additional diameter of the O-ring, so make sure that the filet is oriented toward the respective O-ring.

6. **Place and tighten the bolts onto the pressure rings.** Each pressure ring has six holes concentrically arranged about the diameter which will allow the screws mounted on the pressure chamber to be drawn through. By tightening the bolts using a torque wrench or another appropriate tool, each ring should be properly secured to the chamber. The order of the bolt torqueing can be important, because asymmetries applied during torqueing can lead to a leak below the failure pressure. The first bolt that should be tightened is the one on the bottom of the chamber, because this will cause the sample to slightly lift in the chamber due to the compression on the O-ring. Subsequent bolts should be torqued on opposite sides of the chamber in order will lead to a more ideal sealing configuration, as seen in the accompanying figure. If ever there are leaks during the testing, a suggested first step is to reseat the pressure rings and ensure that the O-ring is being equally compressed from all sides. Consult the figure for a proper torqueing order to ensure a good seal

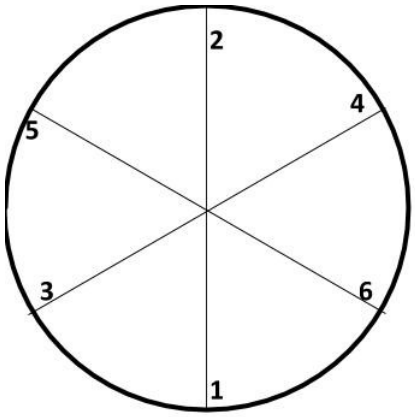

7. **Closing the chamber.** After the sample has been properly secured in the testing chamber, the aluminum safety door can be closed. Close the door and make sure the attached key is secured within the lock. After the door is properly seated, engage the two friction clamps on either end of the door to provide additional security for the door.
8. **Arm the system.** When the door is closed, put the emergency stop button in the 'up' system and press the green arming button.

9. **Close the manual override valves.** When the safety system is engaged, you can open the upstream cut-off valve and close the downstream vent valve. This will allow the pressure from the tank to flow into the system and subsequently build up.
10. **Set up the computer control parameters.** Set the desired loading rate, loading pattern and maximum expected pressure as inputs into the control software. The suggested default is: Linear loading, 5 PSI/s, 1000 PSI maximum.
11. **Begin the test.** Press the 'start' button on the computer software interface. This will give control of the actuator valves to the computer, which will begin ramping up the pressure at the specified loading rate. As the test progresses, both the control signal (in red) and the measured pressure signal (in black) will appear in charts demonstrating their current maximum pressure. This ramping will continue automatically until the material fails, at which point the actuators will automatically shut.
12. **Ending the test.** There will be a definite loss of pressure at the point of failure which should exceed the 1 MPa error and engage the actuator valve shutoffs. Open the downstream vent valve and shut the upstream cut-off valve to manually end flow of the system and vent any additional pressure left in the system. Depress the emergency stop button to disengage the solenoid valves.
13. **Open the door and cleanup.** After the pressure has discharged from the system, the pressure switch that locks the door will no longer be engaged. Press the release button before attempting to open the lid of the frame. You may now remove the bolts to remove the pressure rings and remove any debris left over from the test.

14. **Export the Data.** The results of the test will be automatically stored on the memory of the laptop in the LabView software interface, but to save the data, a manual export should be performed. Using the software interface, move the data window so that it covers the entire test from beginning to end. Right click this interface and select from the menu the option "Export to excel". The data will be exported as a Microsoft excel compatible .csv file. Save the file to an appropriate location.
15. **Turning the machine off.** When all tests are concluded, ensure the upstream cut-off valve is closed and the downstream vent valve is open. Close the regulator on the compressed air tank. Open the upstream discharge valve to remove any residual pressure in the system. Turn off the electrical power to the pressure tension machine and close the laptop.